



UNIVERSIDADE D
COIMBRA



Nieves María del Carmen Talavera Prieto

**THERMODYNAMIC CHARACTERIZATION OF
COTTON OIL AND BIODIESEL AND
MONITORING OF TRANSESTERIFICATION
REACTION**

**Ph.D. thesis in Chemical Engineering supervised by Doctor
António Alberto Torres Garcia Portugal and Doctor Abel Gomes
Martins Ferreira and submitted to the Department of Chemical
Engineering , faculty of Sciencies and Technology, University of
Coimbra.**

September 2018

Faculty of Sciences and Technology

THERMODYNAMIC CHARACTERIZATION OF COTTON OIL AND BIODIESEL AND MONITORING OF TRANSESTERIFICATION REACTION

Nieves María del Carmen Talavera Prieto

Ph.D. thesis in Chemical Engineering supervised by Doctor António Alberto Torres Garcia Portugal and Doctor Abel Gomes Martins Ferreira and submitted to the Department of Chemical Engineering, Faculty of Sciences and Technology, University of Coimbra.

September 2018



UNIVERSIDADE DE
COIMBRA



DEDICATION

This thesis is dedicated to my family. In particular to my mother Hortensia Prieto, for her understanding and wise advices and to my father Hector Talavera, for showing me that, all objectives could be achieved working hard and with perseverance.

I also dedicate it to my nephews, Lautaro, Cecy and Ignacio to whom I have missed during this time.

ACKNOWLEDGMENTS

The arduous way started a few years ago is now close to the end. This stage was marked by a lot of happiness times as well as some difficulties. In this road, many people have been involved in different ways and I should say that the completion of this doctoral thesis it could not has been possible without the support of them.

First of all, I would like to thank my supervisors, Dr. António Portugal and Dr. Abel Ferreira, who leaded me, so that I could reach the goal. Thanks for sharing your knowledge at our meetings and for inspired me the passion for science. We have had a lot of future ideas to continue working.

I also thank EADIC II - ERASMUS MUNDUS ACTION 2 LOT 13A UE Mobility Programme 2010-2401/001-001 - EMA2 for the awarded scholarship (2011-2014) and Dr. Oscar Orfeo and through him to CONICET for giving me the opportunity to finish this last stage of my doctoral thesis. Dr. Orfeo, thank you for your support and trust placed in me.

I thank people who helped me at laboratories. Engineers André F. Lopes, Joao Baptista and Rui Moreira, thanks for your friendliness and sympathy.

I thank all the staff of DEQ, who have make me feel as working at home and I also grateful to the employees who works for the Social Action Services of the University of Coimbra, thanks for the kindness and always look for the best possible solution to my needs.

I cannot forget to say thank to all people who, during the course of these years, have shown me true affection, becoming friends that I will never forget. Thank you Leonor, Telma, Carla, Paulo, Rui, Dra. Eugenia and Dr. Abel for all the support and help received. Thanks to my friends in Argentina who always gave me strength and encouraged me with a message or a call.

Finally, my deepest gratitude to my parents, my sister, brothers and brothers in law, who are always unconditionally supported me and accepted my absence. Without your support and containment this thesis would never have been possible.

ABSTRACT

In recent times, research on biodiesel has been increasing exponentially since it is an alternative to conventional diesel fuel, which is highly pollutant and whose prices have been raising considerably. The production of biodiesel from non-edible oils and even more, from raw material which are by-products of primary economic activity, like cottonseed oil whose main primary activity is the production of cotton fibbers, could provide some economic independence to regional economies and, at the same time, it would be a way to take full advantage of the main activity. In Argentina the law 26.093 “Regime of Regulation and Promotion for the Production and Sustainable Use of Biofuels” promotes the regional economies and industrialization of the farmland. Currently, the biodiesel is made almost entirely from soybean oil. However, the cotton productive and industrial sector could be interested to take advantage of by-product of ginning process for the biodiesel production in order to achieve significant changes in the regional economies.

This thesis is set to improve the industrial production of biodiesel from two different but interrelated perspectives; the knowledge of thermodynamic properties that have a significant influence on the process and facilities design and performance of the engine, and the monitoring of reaction, required to guarantee the quality of the final product.

The final characteristics of a biodiesel are largely determined by the characteristics of the raw material used. Giving the lack of information in fundamental thermodynamic properties, for oils and biodiesels, and even more scarce for cottonseed, new experimental data of density, viscosity, surface tension and speed of sound are reported. Density measurements were made in the temperature and pressure ranges, $T = (288 \text{ to } 358) \text{ K}$ and $p = (0.1 \text{ to } 30) \text{ MPa}$, respectively. The viscosity of cottonseed oil was measured at temperatures between 293 K and 373 K and for biodiesel the range was $T = (303 \text{ to } 348) \text{ K}$, in both cases at atmospheric pressure. The surface tension and speed of sound of cotton oil and biodiesel were measured at temperatures starting near 300 K up to 353 K, at atmospheric pressure. Based on this data, new models were developed and existent ones evaluated by statistical indicators. For each property, the most suitable models are reported. These contributions are very useful for the continuous update of databanks and

estimation of thermophysical properties and also for modelling and simulation of chemical processes.

This thesis also reports an off-line methodology to follow the course of the reaction through continuous measurements of the reaction medium density. It was possible to establish a correlation between the measured densities and the progress of the reaction, suitable for reactions at different temperatures and excesses of alcohol, and reaction times greater than five minutes. This work could be of great importance at industrial level allowing the easy monitoring of biodiesel production.

Keywords: biodiesel, cottonseed, thermodynamic properties, monitoring.

RESUMO

Últimamente o número de trabalhos sobre biodiesel aumentou exponencialmente, uma vez que se trata de uma alternativa ao diesel convencional, que é altamente poluente e cujos preços vêm subindo consideravelmente. A produção de biodiesel a partir de óleos não alimentares e também derivados de matérias-primas que são subprodutos da atividade econômica primária, como o óleo de algodão cujo objetivo principal é a produção de fibras de algodão, poderia proporcionar a independência econômica às economias regionais. Ao mesmo tempo, seria um modo de aproveitamento máximo da atividade principal. Na Argentina, a lei 26.093 “Regime de Regulação e Promoção da Produção e Uso Sustentável de Biocombustíveis” tem como meta promover as economias regionais e a industrialização das terras agrícolas. Atualmente, o biodiesel é produzido quase inteiramente a partir do óleo de soja. No entanto, o setor produtivo e industrial do algodão poderia estar interessado no aproveitamento do subproduto do processo de descaroçamento para a produção de biodiesel, a fim de alcançar mudanças significativas nas economias regionais.

Um dos objetivos desta tese é o de procurar melhorar a produção industrial de biodiesel utilizando duas perspectivas diferentes, inter-relacionadas: o conhecimento das propriedades termodinâmicas que influenciam significativamente o processo produtivo, o projeto das instalações e o desempenho do motor, e a monitorização da reação de transesterificação, necessária para garantir a qualidade do produto final e o desempenho conveniente do equipamento.

As características finais de um biodiesel são largamente determinadas pelas características da matéria-prima utilizada. Devido à falta de informações sobre as propriedades termodinâmicas fundamentais para óleos e biodieseis, ainda mais escassas para sementes de algodão, novos valores experimentais de densidade, viscosidade, tensão superficial e velocidade de som são reportados. As medidas da densidade foram feitas nas gamas de temperatura e pressão, $T = (288 \text{ a } 358) \text{ K}$ e $p = (0.1 \text{ a } 30) \text{ MPa}$, respectivamente. A viscosidade do óleo de algodão foi medida a temperaturas entre 293 K e 373 K enquanto que para o biodiesel o intervalo foi $T = (303 \text{ a } 348) \text{ K}$, em ambos os casos à pressão atmosférica. A tensão superficial e a velocidade do som do óleo de algodão e do biodiesel foram medidas a temperaturas situadas na proximidade de 300 K até

353 K e à pressão atmosférica. Com base nestes dados, foram desenvolvidos novos modelos e os já existentes foram avaliados através do cálculo de indicadores estatísticos. Para cada propriedade, realçam-se os modelos mais adequados. Estas contribuições são muito úteis para a atualização contínua de bancos de dados para estimar propriedades termofísicas e também para modelação e simulação de processos químicos.

Nesta tese também é desenvolvida uma metodologia off-line destinada a acompanhar o curso da reação através de medições contínuas da densidade do meio de reaccional. Foi possível estabelecer uma correlação entre as densidades medidas e o progresso da reação, adequada para reações a diferentes temperaturas e razões álcool/óleo, e para tempos de reação superiores a cinco minutos. Este assunto terá grande importância a nível industrial já que irá permitir a fácil monitorização da produção de biodiesel.

Palavras chave: biodiesel, semente de algodão, propriedades termodinâmicas, monitorização.

TABLE OF CONTENTS

LIST OF FIGURES.....	xvii
LIST OF TABLES	xxxii
1 CHAPTER.....	1
INTRODUCTION.....	1
1.1 Work aims and motivations.....	2
1.2 Document organization.....	3
2 CHAPTER.....	5
GENERAL CONTEXT.....	5
2.1 Introduction	6
2.2 The biodiesel as vehicular fuel	7
2.3 Theoretical concepts	11
2.3.1 Sources of biodiesel	11
2.3.2 Transesterification reaction	15
2.3.3 Industrial process.....	18
2.3.4 Quality control.....	19
2.4 Ethical and social implications	20
2.5 References	21
3 CHAPTER.....	25
DENSITY OF COTTONSEED OIL AND BIODIESEL	25
3.1 BIODIESEL DENSITY	26
3.1.1 Introduction	26
3.1.2 Experimental	28
3.1.2.1 Materials.....	28
3.1.2.2 Cottonseed biodiesel preparation	29

3.1.2.3	Biodiesel characterization.....	30
3.1.2.4	Experimental density measurement.....	30
3.1.3	Density database for biodiesels.....	32
3.1.4	Results and discussion.....	36
3.1.4.1	Density of cottonseed biodiesel.....	36
3.1.4.2	Density correlation	38
3.1.4.3	Density prediction	45
3.1.4.3.1	The group contribution methods (GCVOL).....	45
3.1.4.4	Degree of unsaturation	47
3.1.4.5	Predictive GMA.....	48
3.1.5	Mechanical coefficients.....	57
3.1.6	Conclusions	65
3.2	COTTONSEED OIL DENSITY	67
3.2.1	Introduction	67
3.2.2	Experimental section.....	67
3.2.2.1	Materials	67
3.2.2.2	Density measurement	68
3.2.3	Density models.....	68
3.2.3.1	GMA and GCVOL equations of state	68
3.2.3.2	Halvorsen's Model	69
3.2.3.3	Zong's Model	70
3.2.4	Results and discussion.....	71
3.2.4.1	Density of cottonseed oil	71
3.2.4.2	Density correlation	74
3.2.4.3	Density prediction	78

3.2.4.4	Mechanical coefficients	87
3.2.5	Conclusions	90
3.3	References	91
4	CHAPTER.....	99
	VISCOSITY OF COTTONSEED OIL AND BIODIESEL	99
4.1	Introduction	100
4.2	Experimental section	101
4.2.1	Materials.....	101
4.2.2	Viscosity measurements.....	101
4.3	Viscosity models.....	103
4.3.1	Correlation.....	103
4.3.2	Prediction	105
4.3.2.1	Zong method.....	105
4.3.2.2	Grunberg-Nissan.....	106
4.3.2.3	Yuan models.....	107
4.3.2.4	Ceriani's models.....	107
4.4	Results and discussion	108
4.4.1	Correlation of CSO and CSB viscosities.....	108
4.4.2	Prediction of CSO and CSB viscosity.....	117
4.4.3	Relation between viscosity and density	122
4.5	Conclusions	125
4.6	References	126
5	CHAPTER.....	129
	SURFACE TESIION OF COTTONSEED OIL AND BIODIESEL	129
5.1	Introduction	130

5.2	Experimental.....	131
5.3	Surface tension models.....	132
5.3.1	Correlation.....	132
5.3.2	Prediction	133
5.4	Result and discussion.....	139
5.4.1	Surface tension of CSO.....	139
5.4.2	Surface tension of CSB	146
5.4.3	Viscosity- Surface tension correlations.....	155
5.5	Conclusions	157
5.6	References	158
6	CHAPTER.....	163
	SPEED OF SOUND OF COTTONSEED OIL AND BIODIESEL	163
6.1	SPEED OF SOUND OF COTTONSEED BIODIESEL	164
6.1.1	Introduction	164
6.1.2	Experimental	167
6.1.2.1	Calibration liquids and fuels.....	167
6.1.2.2	Synthetic samples and cottonseed biodiesel preparation.....	168
6.1.2.3	Analytical methods.....	169
6.1.2.4	Sound speed measurement	169
6.1.3	Results and discussion.....	171
6.1.3.1	Speed of sound correlation	171
6.1.3.2	Molar compressibility.....	178
6.1.3.3	Prediction of speed of sound	188
6.1.4	Conclusions	192
6.2	SPEED OF SOUND OF COTTONSEED OIL	194

6.2.1	Experimental part	194
6.2.1.1	Measurements	194
6.2.2	Speed of sound models.....	197
6.2.2.1	Correlation	197
6.2.2.2	Prediction.....	198
6.2.3	Results and discussion.....	205
6.2.3.1	Auerbach relation	209
6.2.3.2	Molar compressibility.....	211
6.2.4	Conclusion.....	214
6.3	References	214
7	CHAPTER.....	219
	MONITORING OF THE TRANSESTERIFICATION REACTION	219
7.1	Introduction	220
7.2	Experimental part	222
7.2.1	Materials.....	222
7.2.2	Transesterification reaction.....	223
7.2.3	Density monitoring.....	223
7.2.4	¹ H NMR analysis.....	224
7.3	Results and discussion.....	225
7.3.1	Determination of cottonseed oil conversion to biodiesel	225
7.4	Conclusion	243
7.5	References	243
8	CHAPTER.....	247
	CONCLUSIONS.....	247
8.1	General Conclusions.....	248

8.2 Future works.....	250
APPENDIX.....	251
A Data for chapter 2.....	252
B Data for chapter 3.....	254
C Data for chapter 4.....	270
D Data for chapter 5.....	272
E Data for chapter 7.....	273

LIST OF FIGURES

Figure 2.1. Total primary energy supply by source (excludes electricity and heat trade) [2].....	6
Figure 2.2. World ethanol and biodiesel production (PJ) [1].....	7
Figure 2.3. Carbon cycle of biodiesel.....	8
Figure 2.4. Average emission impacts of biodiesel for heavy-duty highway engines [13].	9
Figure 2.5. Typical chemical structure of a triglyceride. R ₁ , R ₂ and R ₃ are long hydrocarbon chains.....	12
Figure 2.6. (a) Cotton boll parts [25] (b) Major components of whole cottonseed [26].....	15
Figure 2.7. Stepwise and overall transesterification reaction.....	16
Figure 2.8. Process flow for biodiesel production.....	19
Figure 3.1. Experimental setup for the measurement of liquid densities at high pressures: 1, Julabo FP-50 thermostatic bath; 2, DMA 60 (Anton Paar) device for measuring the period of oscillation; 3, measuring cell DMA 512P (Anton Paar); 4, syringe for sample introduction; 5, pressure generator model HIP 50-6-15; 6, PT probe; 7, pressure transducer WIKA, S-10; 8, NI PCI-8220 data acquisition board; 9, PC; 10, buffer.	32
Figure 3.2. Density (ρ) as a function of temperature at 0.1 MPa for the biodiesels in database: Δ , N5; ∇ , N6; \circ , N7; \square , N21; \diamond , N19 ; +, N20 ; \blacktriangle , N23; \blacktriangledown , N17; \times , N8; \times , N9; \triangleleft , R; \triangleright , P; \oplus , S; \star , SR; \boxplus , RP; \diamond , SP; \star , SRP; \bullet , CSB; \oplus , SCHB.....	33
Figure 3.3. Comparison between the densities of this work with values from the literature. (a) Δ , this work; \circ , Nogueira et al. [40]; +, Alptekin and Canakci [8]. (b) Deviations between the densities of this work (ρ_{this}) with values from the literature (ρ_{lit}). The line shows the deviations from density of Nogueira et al. [40] taking linear representations of data.....	38
Figure 3.4. Isotherms of $(2z-1)V_m^3$ versus the molar density (ρ_m) for cottonseed and Shedmann (SCHB) biodiesels calculated from GMA EoS. (a) CSB (experimental data of this work): Δ ,	

288.15 K; ▽, 298.15K; ○, 308.15 K; □, 318.15 K; ▲, 328.15 K; ▼, 338.15 K; ●, 348.15 K; ■, 358.15 K (b) SCHB: Δ, 288.12 K; ▽, 297.93 K; ○, 307.8 K; □, 317.6 K; ◇, 327.49 K ; ▲, 337.38 K; ▼, 347.26 K; ⊕, 357.13 K; ■, 367.03 K; ◆, 376.91; ☆, 386.84 K; +, 396.76 K. Full curves calculated from correlation with GMA EoS.....43

Figure 3.5. Relative density deviations between the calculated values with GMA EoS (ρ_{cal}) and the experimental values (ρ_{exp}). (a) CSB: Δ, 288.15 K; ▽, 298.15K; ○, 308.15 K; □, 318.15 K; ▲, 328.15 K; ▼, 338.15 K; ●, 348.15 K; ■, 358.15 K; (b) SCHB: Δ, 288.12 K; ▽, 297.93K; ○, 307.8 K; □, 317.6 K; ◇, 327.49 K ; ▲, 337.38 K ; ▼, 347.26 K; ●, 357.13 K; ■,367.03 K; ◆, 376.91 K; +, 386.84 K; ×, 396.76 K.....44

Figure 3.6. Density as function of the degree of unsaturation (DU) for some biodiesels in the database. At 293K and 0.1 MPa: Δ, [19]; ○, [20, 21]; at 353 K and 0.1 MPa: ▲, [19], ⊕, [20, 21].....47

Figure 3.7. Correlation between coefficients A_1 , A_2 , B_0 , B_1 and B_2 of the GMA EoS vs A_0 for biodiesels SR, SP, PR, SRP, N5, N8 N19, N23.....50

Figure 3.8. Relations for predictive 4PGMA EoS. (a) Coefficient A_0 as function of the molar density at 298 K from the revised GCVOL model ($\rho_{m,GVOL}^{298}$): □, path1; +, path2; ○, path 3; Δ, path4. The lines represent Eq. 3-14: (—) path 1; (---) path 2; (····) path 3; (----) path 4. (b) Degree of unsaturation parameter (DU) as function of mean molar mass (M) for the biodiesels studied. Lines correspond to the fittings with Eq. 3-16. Lines and symbols as in (a).....54

Figure 3.9. Thermal expansivity (α_p) for the SCHB calculated from GMA EoS. (a) α_p as function of temperature along isobars: Δ, 0.4 MPa; ▽, 19.8 MPa; ○, 39.8 MPa; □, 59.8 MPa; ◇, 79.8 MPa; +, 99.8 MPa; ×, 119.7 MPa. (b) α_p as a function of pressure along isotherms: Δ, 288.12 K; ▽, 307.80 K; ○, 327.49 K; □, 347.26 K; ◇, 367.03 K ; +, 386.84 K.59

Figure 3.10. Minimum and maximum values distribution of the mechanical coefficients for the biodiesels in the database. Triangles and circles refer to minima and maxima respectively and lines to the mean values. (a) Thermal expansivity; (b) isothermal compressibility; (c) internal pressure.....60

Figure 3.11. Isothermal compressibility (k_T) for the SCHB calculated from GMA EoS. (a) k_T as function of temperature along various isobars: Δ , 0.4 MPa; ∇ , 19.8 MPa; \circ , 39.8 MPa; \square , 59.8 MPa; \diamond , 79.8 MPa; $+$, 99.8 MPa; \times , 119.7 MPa. (b) k_T as function of pressure along isotherms: Δ , 288.12 K; ∇ , 307.80 K; \circ , 327.49 K; \square , 347.26 K; \diamond , 367.03 K; $+$, 386.84 K.62

Figure 3.12. Internal pressure (p_i) as function of temperature at 0.1 MPa for the biodiesels in the database. Δ , R; ∇ , P; \square , SP; \circ , SRP; \blacktriangle , N5; \blacktriangledown , N6; \blacksquare , N9; $+$, N21; \times , N23; \blacktriangleleft , CSB; \oplus , SCHB.64

Figure 3.13. Representative molecule of a mixed triglyceride. Oleic, linoleic and linolenic acids (OLiLn) are the fragments component of the TG..70

Figure 3.14. Comparison between the densities of this work for CSO with values from the literature. Δ , this work; \circ , Menzies et al. [76]; \blacktriangledown , Magne et al. [77]; ∇ , Arnold et al. [78]; \square , Demirbas [79]; $+$, Macovei [80]; \star , Eryilmaz et al. [81].72

Figure 3.15. Experimental density for CSO and CSB as function of pressure and temperature. Black symbols correspond to the oil and red ones to biodiesel: \star , 278.15 K; \blacktriangleleft , 288.15 K, Δ , 298.15 K; ∇ , 308.15 K; \circ , 318.15 K; \square , 328.15 K; \diamond , 338.15 K; \times , 348.15 K; $+$, 358.15 K. The lines represent the fittings with GMA EoS.74

Figure 3.16. Isotherms of $(2z-1)V_m^3$ versus the molar density (ρ_m) for CSO from GMA EoS. . Experimental: \star , 278.15 K; \blacktriangleleft , 288.15 K; ∇ , 298.15K; \circ , 308.15 K; \square , 318.15 K; \diamond , 338.15 K; \times , 348.15 K; $+$, 358.15 K. Full curves calculated from correlation with GMA EoS.76

Figure 3.17. Relative deviations between the calculated values with GMA EoS (ρ_{cal}) and the experimental values (ρ) for CSO: \star , 278.15 K; \blacktriangleleft , 288.15 K; Δ , 298.15 K; ∇ , 308.15 K; \circ , 318.15 K; \square , 328.15 K; \diamond , 338.15 K; \times , 348.15 K; $+$, 358.15 K.77

Figure 3.18. Relative density deviations between the calculated values with GMA EoS (ρ_{cal}) and the experimental values (ρ) from the literature for CSO. Δ , this work; \circ , Menzies et al. [76]; \blacktriangledown , Magne et al. [77]; ∇ , Arnold et al. [78]; \square , Demirbas [79]; $+$, Macovei [80]; \star , Eryilmaz et al. [81].77

Figure 3.19. Relative density deviations between the predicted (ρ_{cal}) and the experimental (ρ) values as function of pressure and temperature for CSO and GCVOL model: ☆, 278.15 K; ▲, 288.15 K; Δ, 298.15 K; ▽, 308.15 K; ○, 318.15 K; □, 328.15 K; ◇, 338.15 K; ×, 348.15 K; +, 358.15 K.81

Figure 3.20. Relative density deviations between the predicted (ρ_{cal}) and the experimental (ρ) values as function of pressure and temperature for CSO and GCVOL/HALV: ☆, 278.15 K; ▲, 288.15 K; Δ, 298.15 K; ▽, 308.15 K; ○, 318.15 K; □, 328.15 K; ◇, 338.15 K; ×, 348.15 K; +, 358.15 K.81

Figure 3.21. Relative density deviations between the predicted (ρ_{cal}) and the experimental (ρ) values as function of pressure and temperature for CSO with the GCVOL/ZONG(MTGA) (black) and GCVOL/ZONG(STGA) (red) methods: ☆, 278.15 K; ▲, 288.15 K; Δ, 298.15 K; ▽, 308.15 K; ○, 318.15 K; □, 328.15 K; ◇, 338.15 K; ×, 348.15 K; +, 358.15 K.82

Figure 3.22. RDs between the predicted (ρ_{cal}) and the experimental values (ρ) of CSO at atmospheric pressure using GCVOL EoS and the GCVOL extension of Halvorsen and Zong models. ▲, GCVOL; ▼, GCVOL/HALV; ●, GCVOL/ZANG(MTGA); ■, GCVOL/ZANG(STGA).82

Figure 3.23. Density differences, $\Delta\rho$, between oil and biodiesel as function of temperature. Comparison between data of this work for CSO and CSB with values from other oils/biodiesel. Δ, CSO/CSB at $p = 0.1$ MPa; ○, CSO/CSB at $p = 30$ MPa; mean values of density differences taken over the set (S, R and P) [19, 84]: ▲ at $p = 0.1$ MPa and ●, $p = 30$ MPa.84

Figure 3.24. Density deviations and relative deviations between the predicted and the experimental values as function of pressure and temperature for CSB, from DDT. Δ, 298.15 K; ▽, 308.15 K; ○, 318.15 K; □, 328.15 K; ◇, 338.15 K; ×, 348.15 K; +, 358.15 K.86

Figure 3.25. Thermal expansivity (α_p) as function of pressure for CSO (a) and CSB (b) predicted from GMA EoS. : ☆, 278.15 K; ▲, 288.15 K; Δ, 298.15 K; □, 308.15 K; ○, 318.15 K; □, 328.15 K; ◇, 338.15 K; ×, 348.15 K; +, 358.15 K.88

Figure 3.26. Isothermal compressibility (k_T) as function of pressure and temperature for CSO (a) and CSB (b) predicted from GMA EoS. : ☆, 278.15 K; ▲, 288.15 K; Δ, 298.15 K; ▽, 308.15 K; ○, 318.15 K; □, 328.15 K; ◇, 338.15 K; ×, 348.15 K; +, 358.15 K.....90

Figure 4.1. Viscosity of CSO as function of rotational speed. ○, $T=353\text{K}$; ⊕, $T= 363 \text{ K}$; ●, $T=373 \text{ K}$ 110

Figure 4.2. Dynamic viscosities, η , for CSO as function of temperature, T . ○, This work; ◻, Macovei [1]; Δ, Eryilmaz et al. [2]; Wakeham and Magne [3] (+, $IN=112$; +, $IN=101$; +, $IN=108$; +, $IN=6$). ☆, Rawitsch [29]; ◇, Boekenoogen [30]; Bauer and Markley [31] (×, $IN=7$, ×, $IN=46$; ×, $IN=56$). Full line corresponds to correlation with MYEGA Eq. 4-4..... 111

Figure 4.3. Logarithm of viscosity as function of $1/T$ for CSO and CSB. CSO: ○, This work; ◻, Macovei [1]; Δ, Eryilmaz et al. [2]; ☆, Rawitsch [29]; ◇, Boekenoogen [30]; Wakeham and Magne [3] (+, $IN=112$; +, $IN=101$; +, $IN=108$; +, $IN=6$); Bauer and Markley [31] (×, $IN=7$, ×, $IN=46$; ×, $IN=56$). CSB: ○, This work; Δ, Eryilmaz et al. [2]; □, Nogueira [4]. Upper symbols correspond to CSO and lower ones to CSB. Full lines correspond to correlation with MYEGA, dashed line correspond to prediction with CER..... 113

Figure 4.4. Relative deviations as function of temperature between the calculated viscosities of CSO based on fitted MYEGA, (η_{MYEGA}) and the experimental values (η). ○, This work; ◻, Macovey [1]; Δ, Eryilmaz et al. [2]; ☆, Rawitsch [29]; ◇, Boekenoogen [30]; Wakeham and Magne [3] (+, $IN=112$; +, $IN=101$; +, $IN=108$; +, $IN=6$); Bauer and Markley [31] (×, $IN=7$, ×, $IN=46$; ×, $IN=56$)..... 115

Figure 4.5. Relative deviations as function of temperature between the calculated viscosities of CSB based on MYEGA (η_{MYEGA}) and the experimental values (η). ○, this work; Δ, Eryilmaz et al. [2]; □, Nogueira et al. [4]. 116

Figure 4.6. Relative deviations as function of temperature between the calculated viscosities of CSO based on Zong model (η_{Zong}) and the experimental values (η). ○, This work; ◻, Macovey [1]; Δ, Eryilmaz et al. [2]; ☆, Rawitsch [29]; ◇, Boekenoogen [30]; Wakeham and Magne [3] (+, $IN=112$; +, $IN=101$; +, $IN=108$). (a) and (b) correspond to calculations with MTGA, STGA.... 117

Figure 4.7. Relative deviations as function of temperature between the calculated viscosities of CSO based on CER model ($\eta_{C_{er}}$) and the experimental values (η). \circ , This work; \blacksquare , Macovey [1]; Δ , Eryilmaz et al. [2]; \star , Rawitsch [29]; \diamond , Boekenoogen [30]; Wakeham and Magne [3] ($+$, $IN=112$; $+$, $IN=101$; $+$, $IN=108$). (a), (b) and (c) correspond to calculations with MTGA, STGA and PTGA. 119

Figure 4.8. Relative deviations as function of temperature between the calculated viscosities of CSB based on predictive models (η_{cal}) and the experimental values (η). \circ , This work; Δ , Eryilmaz et al. [2]; \square , Nogueira et al. [4]. Full and open symbols correspond to Ceriani et al. and Yuan models. 120

Figure 4.9. Relative deviations as function of temperature between the calculated viscosities of CSB based on predictive models (η_{cal}) with Grunberg and Nissan method with interaction term G_{ij} and the experimental values (η). \circ , This work; Δ , Eryilmaz et al. [2]; \square , Nogueira et al. [4]. B Red, blue and black symbols correspond to Ceriani with FA profile, Ceriani with FAMEs profile and Yuan models with FAME profile. 122

Figure 4.10. Density (ρ) as function of ($\eta^{-1/2}$) for CSO (left) and CSB (right). \circ , This work; \blacksquare , Macovei [1]; Δ , Eryilmaz et al.[2]; \square , Nogueira et al. [4]. Full lines correspond to linear correlation with Eq. 4-20. 123

Figure 4.11. RDs between viscosities calculated from Eq. 4-20 (η_{cal}) and that from literature (η) as function of temperature, for CSO. \circ , This work; \blacksquare , Macovei [1]; Δ , Eryilmaz et al. [2]. 124

Figure 4.12. RDs between viscosities calculated from Eq. 4-20 (η_{cal}) and that from literature (η) as function of temperature, for CSB. \circ , This work; Δ , Eryilmaz et al. [2]; \square , Nogueira et al. [4]. 124

Figure 5.1. Surface tension of CSO. \blacktriangledown , This work, Wilhelmy plate; \circ , Menzies et al. [33]; \star , Halpern [34]; \square , Dikko et al. [35]; \star , Zeitoun et al. [36]; $-\cdot-\cdot-$, Singleton and Benerito (crude CSO) [37]; $---$, Singleton and Benerito (refined CSO) [37]. Black full lines represent correlations of values with Eq. 5-1. 140

Figure 5.2. Surface tension as function of temperature of CSO compared with other oils. ▼, This work; Soy: ◻, Esteban et al. [38]; ◆,◇ Sahasrabudhe et al. [39]; +, Esteban et al. [38] (palm); ×, Esteban et al. [38] (rapeseed). 143

Figure 5.3. Prediction of surface tension of CSO. Experimental: ▼, This work, Wilhelmy plate; ○, Menzies et al. [33]. Prediction: —, Reid et al. [10], Eq. 5-8; - - -, Eqs. 5-11 and 5-13 using FA profile of the oil; ●, Allen et al. method; —, Sastri-Rao, $K = 0.158$ with critical parameters from Otobrise and Monago [25]; ⋯, Sastri-Rao, $K = 0.158$ with CSO critical parameters calculated by Neto et al. [28]. 146

Figure 5.4. Experimental surface tension of CSB as function of temperature: ▲, This work, 1st series; ▲, This work, 2nd series; ●, Al-Iwayzi et al. [41]; ☆, Wimala and Brown [42]. The lines represent the correlation of values with linear Eq. 5-1. 147

Figure 5.5. Experimental surface tension of CSB compared with biodiesel from other oils. Experimental (CSB): ▲, This work, 1st series; ▲, This work, 2nd serie; ●, Al-Iwayzi et al. [41]; ☆, Wimala and Brown [42]; Experimental (other biodiesels): ◻, Soy, Freitas et al. [19]; ×, Rapeseed, Freitas et al. [19]; □, Soy, Watts and Tate [47]; ■, Soy, Allen et al. [3]. 148

Figure 5.6. Prediction of surface tension of CSB. Experimental: ▲, This work, 1st series; ▲, This work, 2nd series; ●, Al-Iwayzi et al. [41]; ☆, Wimala and Brown [42]; Prediction: —, Reid et al.; - - -, Eqs. 5-11 and 5-13; —, Eqs. 5-10 and 5-12; — · — ·, Eqs. 5-17 to 5-19; —, Sastri-Rao, $K = 0.158$ and model parameters given by Neto et al. [28]; - - -, Sastri-Rao, $K = 0.158$ with FAME parameters given by Evangelista et al. [30]; — · — ·, Sastri-Rao, $K = 0.158$ with FAME parameters from predictive Constantinou and Gani [44]. ●, Allen et al. method [3]. 151

Figure 5.7. Predicted surface tension of CSB with Allen method. (a) Relative percent deviations between predicted and measured surface tension as function of temperature. (b) Parity plots for predicted and measured surface tension. ▲, 1st serie; ▲, 2nd serie; ☆, Wimala and Brown [42]. Dashed line corresponds to $RDs \pm 3\%$ 152

Figure 5.8. Predicted surface tension of CSB with Sastri and Rao method. (a) Relative percent deviations between predicted and measured surface tension as a function of temperature. (b)

Parity plots for predicted and measured surface tension. Δ , 1st serie; \blacktriangle , 2nd serie; \star , Wimala and Brown [42]. Dashed line corresponds to $RDs \pm 3\%$ 153

Figure 5.9. Surface tension of biodiesels and pure FAMES as function of temperature. Experimental (CSB): Δ , This work, 1st serie; \blacktriangle , This work, 2nd serie; \boxtimes , Soy, freitas et al. [19]; \times , Rapseed, Freitas et al. [19]. FAMES: — , C14:0; — , C16:0; — , C18:0; --- , C18:1; --- , C18:2; --- , C18:3; — , Reid et al. 154

Figure 5.10. Log plots of surface tension vs. viscosity for \blacktriangledown , CSO and \boxtimes , CSB. 156

Figure 5.11. Relative deviations between calculated values from Eq. 5-29 and experimental data of this work: \blacktriangledown , CSO; CSB, Δ first series, \blacktriangle , second series. 157

Figure 6.1. Scheme of speed of sound measurement system. (a) Ultrasound cell and peripheral equipment. (b) Ultrasound cell details 170

Figure 6.2. A-scan signal: (1) Emission signal; (2) receiving signal; (3) steel wall reflected signal. 171

Figure 6.3. Speed of sound (u) of methyl esters measured in this work as function of the temperature. \circ , MeC12:0; ∇ , MeC14 :0; Δ , MeC16:0; \square , MeC18:0; \diamond , MeC18:1; \odot , MeC18:2; +, melting points [20]. 174

Figure 6.4. Speed of sound (u) as function of the temperature and comparison of experimental data of this work with the previous literature data. Legend: (a) values for MeC12:0; (b) relative deviations for MeC12:0; (c) values for MeC14:0; (d) relative deviations for MeC14:0. In the relative deviations (u_{this}) represent this work's experimental data and (u_{lit}) the values from the literature. +, this work; \bullet , Tat and van Gerpen, NREL [2]; \odot , Gouw and Vlugter [3]; \bullet , Freitas et al. [5]; --- , Tat and van Gerpen [4]; \times , Daridon et al. [6]; Δ , Ndiaye et al. [7]. In (b, d) the symbol + represents the relative deviations between the fitted values with Eq. 6-2 and experimental data of this work. 175

Figure 6.5. Speed of sound (u) as function of the temperature (T) and comparison of experimental data of this work with the previous literature data. Legend: (a) values for MeC16:0;

(b) relative deviations for MeC16:0; (c) values for MeC18:0; (d) relative deviations for MeC18:0. In the relative deviations (u_{this}) represent this work's experimental data and (u_{lit}) the values from the literature. +, this work; ●, Tat and van Gerpen, NREL [2]; ⊕, Gouw and Vlugter [3]; (—), Tat and van Gerpen [4]; ☆, Tat and van Gerpen [4]; ×, Daridon et al. [6]; Δ, Ndiaye et al. [7]; ⊕, Ott et al. [8]; □, Freitas et al. [9]. In (b, d) the symbol + represents the relative deviations between the fitted values with Eq. 6-2 and experimental data of this work. 176

Figure 6.6. Speed of sound (u) as function of the temperature (T) and comparison of experimental data of this work with the previous literature data. Legend: (a) values for MeC18:1; (b) relative deviations for MeC18:1; (c) values for MeC18:2; (d) relative deviations for MeC18:2. In the relative deviations (u_{this}) represent this work's experimental data and (u_{lit}) the values from the literature. +, this work; ●, Tat and van Gerpen, NREL [2]; ⊕, Gouw and Vlugter [3]; ⊖, Freitas et al. [5]; (—), Tat and van Gerpen [4]; ×, Daridon et al. [6]; ☆, Tat and van Gerpen [4]; Δ, Ndiaye et al. [7]; ⊕, Ott et al. [8]; □, Freitas et al. [9]. In (b, d) the symbol + represents the relative deviations between the fitted values with Eq. 6-2 and experimental data of this work. .177

Figure 6.7. Speed of sound of biodiesel (u) as function of temperature. Legend: Δ, SCS; ∇, SBT ; ○, SPF; □, SYGI; +, SYGII; ▲, CSB; ×, Soy (S), Freitas et al. [5]; ☆, Palm (P), Freitas et al. [5]; (—) conventional diesel, Payri et al. [11]; (---), Rapeseed biodiesel, Payri et al. [11]; ◇, Huber et al.[10]. 178

Figure 6.8. Molar compressibility (k_m) of FAMES and biodiesel as function of temperature. (a) FAMES: ◇, MeC8:0; +, MeC10:0; Δ, MeC12:0; ∇, MeC14 :0 ; ○, MeC16:0; □, MeC18:0; ▣, MeC18 :1; ▤, MeC18:2; ▥, MeC18:3. (b) Biodiesel: Δ, soybean (S) [5]; ∇, rapeseed (R) [5] ; ○, palm (P) [5]; △, soybean+rapeseed (SR) [5]; ⊕, palm+rapeseed (PR) [5]; ▲, soybean+palm (SP) [5]; □, soybean+rapeseed+palm (SRP) [5]; +, sunflower (SF) [5]; ×, (soybean+rapeseed) GP [5]; ▣, SoyA [5] ; ◇, Sample A [10]; ▲,SCS; ▼, SBT; ●, SPF; ■, SYG1; ☆, SYG2, ◆, CSB. 182

Figure 6.9. Relation between molar compressibility (k_m) and molar mass (M). (a) FAMES: ☆, MeC8:0; Δ, MeC10:0; ∇ MeC12:0; ○, MeC14:0; ◇, MeC:16; □, MeC18:0; ▣, MeC18 :1; ▤, MeC18:2; ▥, MeC18:3. (b) Biodiesel: Δ, S [5]; ∇, R [5] ; ○, P [5]; △, SR [5]; ⊕, PR [5]; ▲, SP

[5]; □, SRP [5]; +, Sf [5]; ×, GP [5]; ▣, SoyA [5]; ◇, Sample A and ◆, Sample B [10];
 ▲,SCS; ▼, SBT; ●, SPF; ■, SYG1; ★, SYG2, ◆, CSB.....184

Figure 6.10. Deviation between the calculated speeds of sound from Eq. 6-14 applied to FAMES (u_{cal}) and experimental (u_{exp}). ▲, MeC7:0; △ MeC8:0; ▼, MeC9:0; ▽, MeC10:0; ●, MeC11:0; ○, MeC12:0; □, MeC13:0; ■, MeC14:0; ◆, MeC15:0; +, MeC16:0; ⊕, MeC17:0; ×, MeC18:0. ..189

Figure 6.11. Deviation between calculated speed of sound from Eq. 6-14 applied to biodiesel fuels (u_{cal}) and experimental (u_{exp}). Δ, S [12]; ▽, R [12]; ○, P [12]; △, SR [12]; ⊕, PR [12]; ▲, SP [12]; □, SRP [12]; +, Sf [12]; ×, GP [12]; ▣, SoyA[12]; ◇, Sample A and ◆, sample B [17];
 ▲,SCS; ▼, SBT; ●, SPF; ■, SYG1; ★, SYG2, ◆, CSB.....192

Figure 6.12. Schematic apparatus. 1: Double walled thermostated vessel; 2: Ultrasound cell; 3: Transducer Panametrics V305, 2.25 MHz; 4: Thermometer (Type K); 5: Magnetic stirrer; 6: pulser-receiver Panametrics (5072PR); 7: PCI data acquisition board (PCIe-9852), Addlink; 8: Data acquisition board (NI USB-6008); 9: PC.....195

Figure 6.13. Speed of sound of TGs as function of n , at 293.15 K (▲), 313.15 K (●) and 343.15 K (■).....201

Figure 6.14. Speed of sound of TGs as function of temperature. Symbols represent experimental data and lines calculated values from Eq. 6-37. Experimental data from Table 6.9: ▲tricaproin; ■, tricaprylin and ●, trilaurin; data from Hustad et al. [38]: Δ, tricaproin; □, tricaprylin; ○, trilaurin.....202

Figure 6.15. Speed of sound of representative TGs in oils as function of temperature. Symbols represent experimental data and lines calculated one from Eq. 6-37 and 6-38. Brown, black, red, blue, green and pink dashed lines correspond to trilaurin, tripalmitin, tristearin, triolein, trilinolein and trilinolenin, respectively. Black solid line corresponds to trimyristin. Experimental data: +, data from Table 6.9; ○, Hustad et al. [38].203

Figure 6.16. Relative deviations between calculated and experimental SOS in saturated TGs as function of temperature. Symbols (+) and (×) correspond to comparison with data from Table 6.9

and Hustad et al., respectively. Colors black, red, blue, pink, cyan and green correspond to tricaproin, tricaprylin, tricaprillin, trilaurin, tripalmitin and tristearin respectively.204

Figure 6.17. Relative deviations between calculated and experimental SOS in unsaturated TGs as function of temperature. The symbols correspond to comparison with data from Table 6.9: Δ , 1OPP; \circ , 2OPP; \square , 1POS; $+$, 1PSO; \diamond , 1OPS; \star , SOS; \blacktriangle , OOO; \bullet , LiLiLi.204

Figure 6.18. Differences between determination of speed of sound with methods 1 (u_{mtd1}) and 2 (u_{mtd2}). Open and full symbols correspond to absolute deviation and relative deviation, respectively.....206

Figure 6.19. Speed of sound of CSO and other oils. CSO: Δ , This work; \blacktriangle , Gouw and Vlугter [37]; \triangle , Ali and Ali [39]. Other oils: (sunflower) \square , González et al. [40]; \circ , Javanaud and Rahalkar [41]; $---$, McClements and Povey [36]; (Soy) \bullet , Oliveira et al. [42]; \circ , Javanaud and Rahalkar [41]; $---$, McClements and Povey [36]; (Rapseed) \blackline , McClements and Povey [36]; (Palm) $---$, McClements and Povey [36];.....207

Figure 6.20. Speed of sound as function of temperature. Symbols correspond to experimental data of this work. Black full line is the correlation with quadratic equation, Eq. 6-2. Black dashed line corresponds to prediction with ideal mixture, Eq. 6-31. Prediction with Auerbach relation: \blackline , with surface tension of this work; \blackline , surface tension of Menzies et al. [43]. Prediction with Auerbach relation with adjusted exponent: $---$, with surface tension of this work; $---$, with surface tension of Menzies et al. [43].209

Figure 6.21. Speed of sound as function of temperature. Symbols correspond to experimental data of this work. $---$, Zong/STGA and SOS of TGs with Eqs. 6-37 and 6-38; \blackline , Pseudo-experimental density and $\langle k_m \rangle$; $---$, pseudo-experimental density and k_m at 298 K.....212

Figure 7.1. Assembly for the monitoring of the transesterification reaction by the density variation. 1, Julabo F12-ED thermostatic bath; 2, DMA 60 (Anton Paar) device for measuring the period of oscillation; 3, measuring cell DMA 512P (Anton Paar); 4, PT probe; 5, NI PCI-6220 data acquisition board; 6, PC; 7, peristaltic pump; 8, reaction vessel; 9, condenser; 10, Digital thermometer (EUTHECNICS 4400).....224

Figure 7.2. Chemical shifts of protons for glycerides and for methyl esters.225

Figure 7.3. ¹H NMR spectra of CSO (a) and sample removed from the mixture of transesterification reaction (b).227

Figure 7.4. ¹H NMR spectra of samples removed from the transesterification reaction at different times. Reaction conditions: r = 4.5 and T = 323.15 K.228

Figure 7.5. Conversion of CSO (%C) as function of reaction time (t) from NMR analysis for different alcohol to oil ratios. At T = 323.15: Δ, r = 4.5; ○, r = 6.0; ♀, r = 7.5. At T = 343.15 K: □, r = 4.5; ◇, r = 6.0; ♂, r = 7.5.231

Figure 7.6. Evolution of density with reaction time, at 343.15° C and r = 6.0. Stages: (1+2) oil+MeOH mixture, dispersion of oil and slow rate; (3) minimum density; (4) fast reaction; (5) chemical equilibrium.233

Figure 7.7. Evolution of density, ρ, and oil conversion %C with reaction time, t, measured for two series of methanolysis reactions with catalyst concentration of 0.05 wt %: (a) 343.15 K; (b) 323.15 K. Black, red and blue refer to r = 4.5, 6.0 and 7.5 respectively.234

Figure 7.8. Evolution of density, ρ, with reaction time, t, and temperature T measured for two series of methanolysis reactions with catalyst concentration of 0.05 wt %: at 343.15 K and 323.15 K. Black, red and blue symbols refer to r = 4.5, 6.0 and 7.5 respectively.236

Figure 7.9. Density of the reaction mixture as function of oil conversion (%C). Symbols correspond to experimental data at time greater than t = 5 min. Circles and triangles correspond to T = 323.15 and T = 343.15 K, respectively and colours blue, red and black are relative to alcohol to oil ratios r = 4.5, 6.0 and 7.5, respectively. Dashed lines represent calculated data from the correlation with Eq. 7-6.238

Figure 7.10. Conversion of CSO (%C) as function of time, at 323.15 K. Δ, r = 4.5; ○, r = 6.0; ♀, r = 7.5. Lines represent %C calculated with density from Eq. 7-6.240

Figure 7.11. Conversion of CSO (%C) as function of time, at T = 343.15 K. □, r = 4.5; ◇, r = 6.0; ♂, r = 7.55. Lines represent %C calculated data from correlation with Eq. 7-6.241

Figure 7.12. Relative deviations of %C as function of reaction time. At $T = 323.15$: Δ , $r = 4.5$; \circ , $r = 6.0$; \circlearrowleft , $r = 7.5$. At $T = 343.15$ K: \square , $r = 4.5$; \diamond , $r = 6.0$; \circlearrowright , $r = 7.5$. The limits at $\pm 3\%$, corresponding to the *OARD*, are displayed.242

Figure 7.13. Parity plot for the conversion obtained from NMR analysis $(\%C)_{\text{NMR}}$ and from Eq. 7-6, taking density at time for which samples were taken for NMR analysis $(\%C)_{\rho}$. At $T=323.15$: Δ , $r = 4.5$; \circ , $r = 6.0$; $+$, $r = 7.5$. At $T= 343.15$ K: \square , $r = 4.5$; \diamond , $r = 6.0$; \times , $r = 7.5$. The limits at $\pm 3\%$, corresponding to the *OARD*, are displayed.....242

Figure B.1. Difference in density isolines ($\text{kg}\cdot\text{m}^{-3}$) obtained from GMA EoS as function of the temperature and pressure for the SCHB biodiesel. The isolines were calculated from the fitting of GMA EoS to pVT data in the restricted ranges (288 to 357) K and (0.4 to 50) MPa (dotted square).263

Figure B.2. Correlation between coefficients A_1 , A_2 , B_0 , B_1 and B_2 of the GMA EoS vs. A_0 for biofuels R, SR, N20 (path1).264

Figure B.3. Correlation between coefficients A_1 , A_2 , B_0 , B_1 and B_2 of the GMA EoS vs. A_0 for biofuels S, SRP, N5, N9, N17, N21 (path2).265

Figure B.4. Correlation between coefficients A_1 , A_2 , B_0 , B_1 and B_2 of the GMA EoS vs. A_0 for biofuels SR, SP, RP, SRP, N5, N8 N19, N23 (path3).266

Figure B.5. Correlation between coefficients A_1 , A_2 , B_0 , B_1 and B_2 of the GMA EoS vs. A_0 for biofuels P, S, SR, N7 (path4).267

Figure B.6. Difference of density isolines ($\text{kg}\cdot\text{m}^{-3}$) obtained from predictive 4PGMA EoS as function of the temperature and pressure. (a) N6; (b) CSB; (c) SCHB.268

Figure B.7. Relative deviations of thermal expansivity (a) and isothermal compressibility (b) found between GMA and Tait EoS as function of temperature for the set (R, P, S, SR, RP, SP, SRP) at 0.1 MPa and 40 MPa. At 0.1 MPa: Δ , R; ∇ , P; \circ , S; \square , SR; \diamond , RP ; SP ; $+$, SRP ; At 40 MPa : \blacktriangle , R; \blacktriangledown , P; \oplus , S; \boxplus , SR; \diamondplus ,RP; \oplus ,SP; \times , SRP.269

Figure E.1. Density, ρ , of the reaction medium as function of time, t , at $T = 323.15$ K. (a) $r = 4.5$; (b) $r = 6$ and (c) $r = 7.5$. Black, red and blue represent the 1st, 2nd and 3rd experiments, respectively. Thicker lines correspond to the selected experiments. – – – represent the mean density-time profile.276

Figure E.2. ¹H NMR conversion at $T = 323.15$ K. Symbols represent experimental data: Δ , $r = 4.5$; \circ , $r = 6$ and \square , $r = 7.5$. Black, red and blue correspond to 1st, 2nd and 3rd experiments, respectively. Full symbols were the selected experiment.277

Figure E.3. Density, ρ , of the reaction medium as function of time, t , at $T = 343.15$ K. (a) $r = 4.5$; (b) $r = 6$ and (c) $r = 7.5$. Black, red and blue represent the 1st, 2nd and 3rd experiments, respectively. Thicker lines correspond to the selected experiments. – – – represent the mean density-time profile.279

Figure E.4. ¹H NMR conversion at $T = 343.15$ K. Symbols represent experimental data: Δ , $r = 4.5$; \circ , $r = 6$ and \square , $r = 7.5$. Black, red and blue correspond to 1st, 2nd and 3rd experiments, respectively. Full symbols were the selected experiment.280

LIST OF TABLES

Table 2.1. Emission impacts for soybean-based biodiesel B20	9
Table 2.2. Ranking of producer countries of oils and fats [22].	13
Table 2.3. Major exporting countries of oils and fats [22].	13
Table 2.4. Approximate composition and typical producing yields from <i>G. hirsutum</i> [24].	14
Table 2.5. Specification for biodiesel (B100) [4].	20
Table 3.1. Sample material purities.	29
Table 3.2. Biodiesels used in this study: composition, degree of unsaturation (<i>DU</i>), density at 298K (GCVOL), <i>pVT</i> ranges of measurements, and EoS reported in the literature for <i>pVT</i> correlation.	34
Table 3.3. Experimental values of density data (ρ), for cottonseed biodiesel as a function of temperature (<i>T</i>), and pressure (<i>p</i>).	37
Table 3.4. Fitting parameters of GMA EoS applied to the correlation of experimental <i>PVT</i> data of biodiesel fuels with 95% confidence limits. The standard deviation (σ) correlation coefficient (<i>r</i>), and number of data points (N_p) are given. Also are referred the standard deviation in density (σ_ρ), and the average absolute deviation in density (<i>AARD</i>).	40
Table 3.5. Coefficients of Eq. 3-14 for the several predictive paths. The biodiesels used in each path are indicated for the paths.	51
Table 3.6. Parameters <i>a</i> and <i>b</i> of each of coefficients A_{1j} , A_{2j} , B_{0j} , B_{1j} , B_{2j} in Eq. 3-15 for path <i>j</i>	52
Table 3.7. Coefficients of Eq. 3-16, corresponding to the calculation of degree of unsaturation as function of the molar mass for the paths in 4PGMA.	55
Table 3.8. Average absolute relative deviation on density for the predictive methods applied to the biodiesels.	56

Table 3.9. Mass fractions (w_i) and molar fractions (x_i) of CSO and CSB.....	68
Table 3.10. Experimental density data (ρ) for CSO as a function of temperature (T), and pressure (p).	71
Table 3.11. Fitting parameters of GMA EoS applied to the correlation of experimental pVT data of cottonseed oil and biodiesel fuel.....	75
Table 3.12. Triglyceride profile for cottonseed oil [85].....	79
Table 3.13. Data for the application of PTGA to CSO.....	80
Table 3.14. Statistical results obtained from the application of the predictive models for the calculation of CSO densities.	80
Table 3.15. Coefficients of Eqs. 3-32 and 3-33.....	86
Table 3.16. Statistical results obtained from the application of the predictive models for the calculation of CSB densities.	87
Table 4.1. Experimental dynamic viscosity of CSO at temperature T and $p = 102.05$ kPa.s.....	109
Table 4.2. Kinematic and dynamic viscosity of CSB as a function of temperature.....	112
Table 4.3. Parameters of VFT and MYEGA equations fitted to the experimental CSO and CSB viscosity data, coefficient of determination, r^2 , average absolute relative deviation $AARD$ and standard deviation in viscosity, σ_η	115
Table 4.4. Average absolute relative deviations $AARD$ of viscosities for the predictive methods used in the calculation of viscosities of CSO.....	118
Table 4.5. Average absolute relative deviation $AARD$ of viscosities for the predictive methods used in the calculation of viscosities of CSB.....	121
Table 4.6. Parameters A and B of Eq. 4-20 and $AARD$ in density and viscosity for CSO and CSB.	124

Table 5.1. Correlation parameters m and c of Eq. 5-20 for FAs and FAMES [31].	139
Table 5.2. Surface tension of CSO as function of temperature.	139
Table 5.3. Quality parameters of CSO crude and refined used by Singleton and Benerito [37].	142
Table 5.4. Correlations parameters of CSO surface tension with Eq. 5-1 and derived surface entropy and enthalpy.	144
Table 5.5. Correlations parameters of CSO surface tension with Eqs. 5-2 and 5-3.	144
Table 5.6. Composition of CSO and CSB and Knotts' parachors, $P_{ch,1}$ [17]	145
Table 5.7. Surface tension of CSB as a function of temperature.	147
Table 5.8. Parameters for the correlations of surface tension of CSB with Eq. 5-1.	149
Table 5.9. Parameters for the correlations of surface tension of CSB with Eqs. 5-2.	149
Table 5.10. Average deviations, $AARD$ and $OARD$ for selected predictive methods applied to CSB.	152
Table 5.11. Parameters of Eq. 5-27 for CSO and CSB.	156
Table 6.1. Previous report of speed of sound data relative to FAMES and biodiesel studied in this section.	165
Table 6.2. Sample material purities of the calibration standards and FAMES.	168
Table 6.3. Biodiesel composition ($wt\%$) of biodiesel of this study.	169
Table 6.4. Experimental speed of sound (u) for FAMES, synthetic and produced biodiesels at atmospheric pressure.	172
Table 6.5. Parameters of equation 6-2 fitted to the (u , T) data of this study.	173
Table 6.6. Molar compressibility (k_m) for FAMES, synthetic and produced biodiesels.	180

Table 6.7. Fitting parameters and standard deviation (σ) of linear of equation fitted to the (k_m , T) data.	181
Table 6.8. Error analysis of predictions molar compressibility and speed of sound, by different methods.	187
Table 6.9. Experimental speed of sound of triglycerides.	199
Table 6.10. Coefficients of Eqs. 6-37 and 6-38.....	202
Table 6.11. Speed of sound of CSO as function of temperature using method 1.....	205
Table 6.12. Speed of sound of CSO as function of temperature using method 2.....	205
Table 6.13. Correlation parameter of speed of sound data, for CSO.	208
Table 6.14. Molar compressibility (k_m) of CSO as function of temperature. The mean molar compressibility ($\langle k_m \rangle$) taken over temperature range and corresponding standard deviation are presented.....	211
Table 6.15. Summary of results obtained with the prediction methods applied to SOS of CSO.	213
Table 7.1. Conversions of CSO to FAMES (%C) calculated by Gelbard et al. method [7], for all the experiences.	229
Table 7.2. Fitting parameters of Eq. 7-4. Coefficient of correlation and standard deviation are also indicated.....	230
Table 7.3. Density of main compounds existing in the reaction mixture at $T = 323.15$ K and 343.15 K, and atmospheric.....	232
Table 7.4. Characteristic parameters of density monitoring curves.	235
Table 7.5. Selected values for the conversion of CSO (% C) and densities of the reaction mixture as function of time (t), temperature (T) and methanol to oil ratio (r).....	237

Table 7.6. Fitting parameters of Eq. 7-5, with 95% confidence limits. Determination coefficient (r^2) and standard deviation in density (σ_ρ) are given.....	239
Table A.1. Fatty acid methyl esters (FAME) for diesel engines - Requirements and test methods. CEN EN 14214: 2008+A1:2009 [39].	252
Table B.1. Values of the mechanical coefficients α_p , k_T , γ_V and p_i at regular temperature and pressure intervals calculated from GMA EoS for CSB.....	254
Table B.2. Minimum and maximum values of mechanical coefficients for the biodiesels of database.	256
Table B.3. Rackett parameters for fatty acids of CSO.	257
Table B.4. Names and symbols for common fatty acids.	257
Table B.5. Mechanical coefficients of CSO calculated from GMA EoS.	258
Table C.1. Parameters of Zong model [9].	270
Table C.2. Parameters of Yuan model [11].	270
Table C.3. Parameter of Ceriani model [10].	271
Table D.1. Parameters of Eq. 5-3 for the surface tension of FA as function of temperature [13]	272
Table D.2. Parameters of Eq. 5-3 for the surface tension of FAMES as function of temperature [12].	272
Table E.1. Selection criteria for density and NMR monitoring.	273

ABBREVIATIONS

AAD: Average Absolute Deviation
AARD: Average Absolute Relative Deviation
AL: Alcoholic phase
ASTM: American Society for Testing and Materials
AV: Acid Value
BX: Blending fuel with X% of biodiesel (in volume)
CER: Ceriani
CFT: Collision Factor Theory
CG: Constantinou and Gani
CN: Cetane Number
CPA: Cubic Plus Association
CSB: Cottonseed Biodiesel
CSC: Corresponding States Correlations
CSO: Cottonseed Oil
DDPT: Density Differences Temperature Pressure Method
DDT: Density Differences Temperature Method
DG: Diglyceride
DI: Direct Injection
DSC: Differential Scanning Calorimetry
DU: Degree of Unsaturation
EoS: Equation of State
EPA: Environmental Protection Agency
EU: European Union
FAE: Fatty Acid Ester
FAEE: Fatty Acid Ethyl Ester
FAME: Fatty Acid Methyl Ester
FFA: Free Fatty Acid Ester
FID: Flame Ionization Detector
FT: Fourier Transform
GC: Gas Chromatography

GCVOL: Group Contribution Volume
GFL: Glass Forming Liquids
Gly: Glycerol
GMA: Goharshadi– Morsali–Abbaspour
GPC: Gel Permeation Chromatography
HC: Hydrocarbons
HPLC: High Performance Liquid Chromatography
HPTLC: High Performance Thin Layer Chromatography
HV: Heating Value
IN: Iodine Number
IR: infrared Spectroscopy
Me: Methanol
MG: Monoglyceride
MTGA: Mixed–TG Approach
MYEGA: Mauro-Yue-Ellison-Gupta-Allan
NBS: National Bureau of Standards
 N_{frag} : Number of fragments
NIR: Near Infrared
NIST: National Institute of Standards and Technology
NMR: Nuclear Magnetic Resonance
NO_x: Nitrogen Oxides
N_p: Number of data points
OARD: Overall Average Relative Deviation
P_{ch}: Parachor
PE: Pulse-Echo
PM: Particulate Materials
PTGA: Pseudo–TG Approach
pVT: Pressure–Volume–Temperature
RD: Relative Deviation
REFPROP: Reference Fluid Properties
RMSD: Root Mean Square Deviation

SAFT: Statistical Associating Fluid Theory
SEC: Size Exclusion Chromatography
SMD: Sauter Mean Diameter
Sn: Sterospecific Numbering
SOS: Speed of Sound
ST: Surface Tension
STGA: Simple–TG Approach
SV: Saponification Value
TG: Triglyceride
TLC: Thin Layer Chromatography
TMS: Tetramethylsilane
UM: Unsaponifiable Matter
ULSD: Ultra Low Sulphur Diesel
UNIFAC: Universal Functional Activity Coefficient
VFT: Vogel-Fulcher-Tammann
VTPR: Volume Translated Peng–Robinson
¹H NMR: Proton Nuclear Magnetic Resonance
4PGMA: 4 paths Goharshadi– Morsali–Abbaspour
%C: Percentage Conversion of CSO

LIST OF SYMBOLS

A : Pre-exponential factor

B : Actual volume of a molecule per mole

E^a : Activation energy

G_{ij} : Interaction parameter

K : Viscometer constant

k : Number of adjusted parameters

L : Distance between the transducer and the reflecting surface

M : Molar mass, Mean molar mass

m : Fragility parameter, Number of double bonds of fatty acid

m_{avg} : Average carbon number

n : Refractive index

N : rotational speed, Number of components

N_A : Avogadro's number

N_c : Total number of carbon atoms in the molecule

N_{cs} : Number of carbons of the alcohol side chain

N_i : Number of double bonds in the fatty acid chain

p : Pressure

p_c : Critical pressure

P_{ch} : parachor

p_{coh} : Cohesive pressure

p_i : Internal pressure

R : Ideal gas constant

r : Coefficient of correlation, Ratio of alcohol to oil

r^2 : Coefficient of determination

R_i : Molar speed of sound of i

S : Entropy, Collision factor

T : temperature

t : Flow time, Time

T_b : Normal boiling point

T_{br} : Reduced boiling temperature

T_c : Critical temperature
 T_g : Glass temperature
 T_r : Reduced temperature
 U : Expanded uncertainty, Internal energy
 u : Combined uncertainty, Speed of sound
 u_0 : Speed of sound at absolute zero
 u_i : Speed of sound of i
 V_m : Molar volume
 $wt\%$: Mass percentage
 w_i : Mass fraction
 x_i : Molar fraction
 Z : Acoustical impedance
 z : Compressibility factor, Number of carbon atoms
 z_{avg} : Average number of double bonds
 Z_{RA} : Rackett parameter

Greek symbols:

α_p : Thermal expansivity, isobaric expansibility
 γ : Surface tension
 γ_i : Surface tension of i
 γ_V : Thermal pressure coefficient
 Δ : Variation
 $\Delta_l^g H_m$: Molar enthalpy of vaporization
 $\Delta_l^g U_{coh}$: Molar cohesive energy
 η_∞ : High temperature viscosity limit
 η_g : Viscosity at glass transition temperature
 η : Dynamic viscosity
 η_i : Dynamic viscosity
 η_i^L : Dynamic viscosity of liquids
 k_S : isentropic compressibility
 κ_T : Isothermal compressibility

ν : Kinematic viscosity

ρ : Density

ρ_i : Density

ρ_m : Molar density

ρ_m^L : Liquid molar density

ρ_m^V : Vapor molar density

σ : Standard deviation

τ : Time of flight, Hagenbach-Couette kinetic energy correction,

ϕ : Volume fraction, Mass fraction

1 CHAPTER

INTRODUCTION

1.1 Work aims and motivations

In the last decades, the decrease of fossil fuel sources and the consequent increase in their prices has motivated a broad interest in the development of new energy alternatives. Moreover, the intensive use of petroleum based fuels is an important factor in air pollution and global warming, so it is essential to take measures to reduce greenhouse gases through the responsible use of energy and the development of new energy resources, clean, renewable and environmental friendly. In this context, biodiesel seems to be a promising alternative for fossil fuels. It is a liquid fuel derived from renewable sources, with physical properties similar to those of petroleum diesel and less pollutant than fossil fuels.

Since biodiesel can be obtained from a wide variety of sources and because that some important biodiesel properties, such as density, viscosity, surface tension and speed of sound depend on the composition of the raw material used, it is necessary to standardize the quality of the biodiesel to be considered as an option to diesel fuel. The knowledge of these properties is of high relevance to optimize the cost of biodiesel production, while allowing the fuel to meet the required quality standards. The traditional way of assesses these properties is by experimental measurements. However, due to technical difficulties and the high costs of the equipment necessary to carry out these determinations, the use of predictive methods is necessary.

On the other hand, adequate methods are required to monitor biodiesel production in order to avoid problems in the operation of production facilities and to guarantee the quality of the final product.

In this context, the aims of this thesis comprise two key-issues:

- 1) Developing correlation and prediction models of important thermo-physical properties, namely density, viscosity, surface tension and speed of sound, for cottonseed oil and cottonseed biodiesel.
- 2) Monitoring the transesterification reaction through the continuous measurement of the density in order to establish a correlation between the fatty acid methyl ester (FAME) content and the density to be used to estimate the degree of progress of the reaction.

Cottonseed oil was chosen as raw material not only for scientific and academic purposes, but also to provide an alternative use of agricultural resources available in the region where this work is framed, Province of Chaco, north of Argentina. In this region, biofuels are receiving more and more relevance, especially since the Law 26.093 "Regime of Regulation and Promotion for the

Production and Sustainable Use of Biofuels" was created to promote regional economies and the sustainable industrialization of the farmlands. Currently, biodiesel in Argentina is made almost entirely from soybean oil and is produced by around 30 PyMES (Small and Medium Businesses) that generate 9300 job positions over about seven large industries. Nevertheless, the cotton productive and industrial sector could be interested in the implementation of this alternative use of cottonseed that would allow achieving significant changes in the regional economies. Cotton is grown mainly for the production of fibbers, which constitute about 40% of the weight of the fruit, the rest is the seed, which can be used for animal feed, either directly (whole cottonseed) or, after extraction of the oil (expeller). For farmers far away from the ports and marketing centers, logistic costs are of high concern. Therefore, a solution for this situation would be to generate added value "in situ". This is the main reason to choose the cottonseed oil as raw material for the production of biodiesel since, besides being chemically suitable for this purpose it would allow the integral use of the cotton ginning process, thus improving the economic equation that this activity has in the province of Chaco.

1.2 Document organization

The present work is organized as follows:

Chapter 1 introduces the choice of thesis topic, main objectives and organization of the work.

Chapter 2 presents a general introduction on biodiesel as vehicular fuel, theoretical concepts on the transesterification reaction, as well as the importance of cottonseed oil as a raw material, in Argentina.

In Chapters 3 to 6 the measurements and correlations of important thermodynamic properties for cottonseed oil and cottonseed biodiesel are presented and the ability of models to predict them is studied. The properties discussed are density, viscosity, surface tension and speed of sound, which are organized in the corresponding chapters 3 to 6.

In Chapter 7, an innovative technique for the real time monitoring of the transesterification reaction through measurements of density variation of the reaction medium is described.

Finally, Chapter 8 addresses the general conclusions and future works.

2 CHAPTER

GENERAL CONTEXT

2.1 Introduction

Currently, the global energy supply mix is slowly changing. The trend towards burning cleaner fuels is growing around the world as a practical way to deal with the global warming. In almost all countries, there are strict regulations concerning to the emission of exhaust gases into the environment. However, oil, coal and natural gas are still accounting for the largest share of global primary energy supply, while biofuels account for a very small share of all primary energy commodities, as illustrate in Figure 2.1. The share of biofuels in the global fuel transportation have been increased since 2010, when it was about 2.7% to 4% in 2016 [1, 2]. Nevertheless, it continues to be very low compared to the total amount of fuels destined for the transport sector. Global production of fuel ethanol grew from 17 billion litres (349 PJ) in 2000 to 86.5 billion litres (1777 PJ) in 2010, an average annual growth of approximately 18%. In the same time frame, global production of biodiesel grew from 0.8 billion litres (28 PJ) to 18.5 billion litres (648 PJ), an average annual growth of approximately 37% (Figure 2.2). According to the International Energy Agency, this global production growth before 2010 slowed down 2% year-on-year due to structural challenges and policy uncertainty in key markets. However, biodiesel policy support remains robust and a production growth is expected [2].

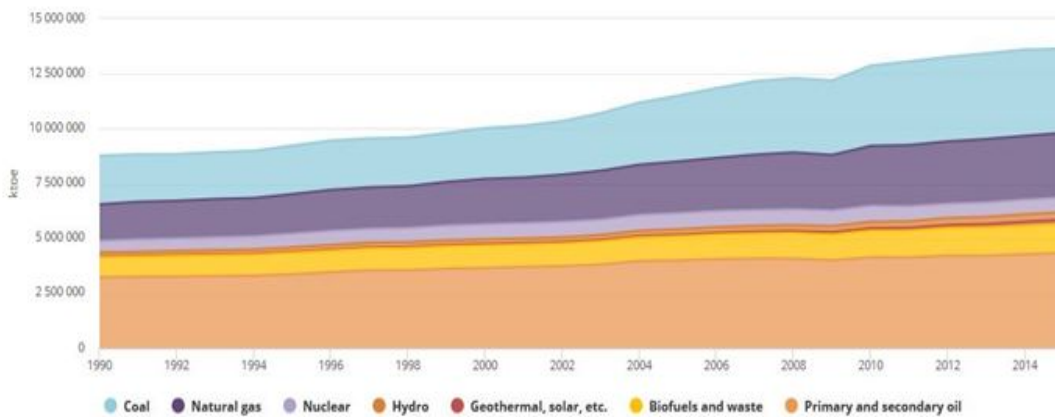


Figure 2.1. Total primary energy supply by source (excludes electricity and heat trade) [2].

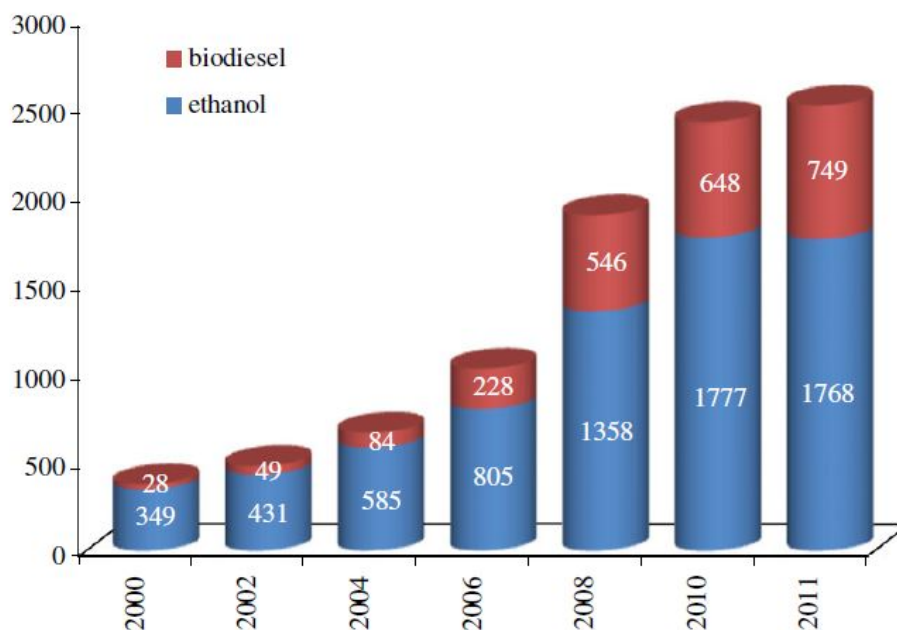


Figure 2.2. World ethanol and biodiesel production (PJ) [1].

The USA and several countries of the European Union are working to substitute petroleum-based fuel for alternative fuels, as well as many other countries, including Argentina. For example, in the EU, the share of fuels from renewable sources in the transport sector should amount to at least 10% of the total transport fuel use by 2020 [3]. According to the Kyoto Protocol, the European community committed to reducing greenhouse gas emissions by at least 5% by the year 2020, taking as reference the emissions of 1991. Argentina is not forced to meet the same goals, since it is a developing country, nevertheless ratified the Protocol, and it was committed to reducing emissions or, at least, not increasing them. A way to achieve this purpose is through the implementation of the law N° 26.093, which establishes the mandatory blending of diesel with biodiesel. This mandatory started with 5% in 2010, reached 10% in 2014 and currently 20% has been proposed.

2.2 The biodiesel as vehicular fuel

The name "biofuel" was created in the last 80th and refers to fuels derived from biomass resources, such as agricultural crops, animal waste, municipal waste, etc. In the transport sector,

the most commonly biofuels are bioethanol and biodiesel, both "eco-friendly" and are used as substitutes for gasoline and diesel, respectively, or in mixtures with them.

The ASTM (American Society for Testing and Materials) defines biodiesel as the “monoalkyl ester of long chain fatty acids, derived from renewable resources such as vegetable oils or animal fats, for use in compression-ignition (diesel) engine” [4], and it is usually obtained through a process called transesterification. When biodiesel is produced from vegetable oils, it has an added value, since the practice of agriculture extracts CO_2 from the atmosphere through the photosynthesis process and all the organic carbon present in the biofuel is of photosynthetic origin, thus contributing to the natural carbon cycle [5, 6] (see Figure 2.3).

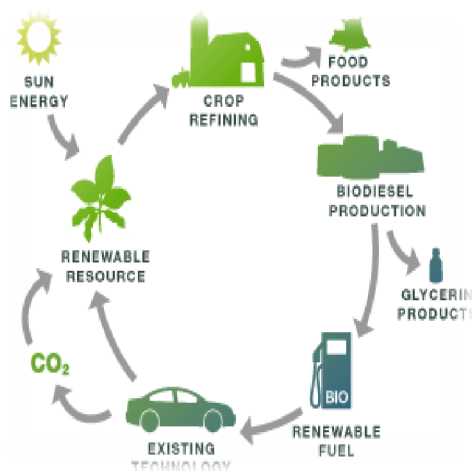


Figure 2.3. Carbon cycle of biodiesel.

From chemical point of view, biodiesel is composed mainly of alkyl esters and contains a significant quantity of oxygenated compounds; petrodiesel, on the other hand, is composed of approximately 64% aliphatic hydrocarbons, 35% aromatic hydrocarbons (including naphthenes and alkylbenzenes), 1-2% olefinic hydrocarbons and does not contain oxygenates [7]. From physical point of view, it has very similar characteristics and properties to conventional diesel, so that it is capable of operating in diesel engines with little or no modification, neat or blending with petroleum diesel in any proportion [6, 8-11]. These mixtures are usually designated with the acronym BX, where X is the volumetric percentage of biodiesel.

Biodiesel has cleaner combustion than conventional diesel as it contains 10-12% oxygen in its composition, which allows a more complete combustion [5, 6, 12]. According to the Environmental Protection Agency (EPA) [13], who have analyzed pre-existing data from various

emissions test programs to investigate these effects, a reduction of air pollutant gases have been observed, with exception of nitrogen oxides, which show a slight increase (see Figure 2.4) .

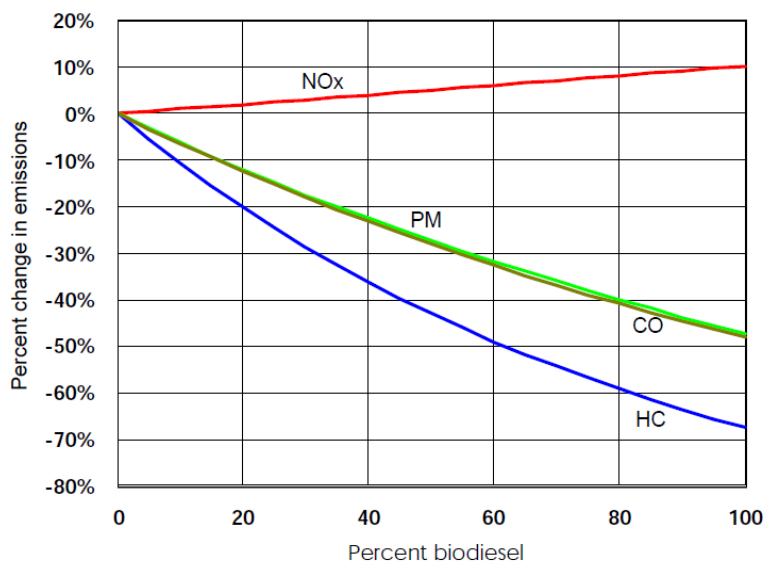


Figure 2.4. Average emission impacts of biodiesel for heavy-duty highway engines [13].

Particularly, for fuels containing 20% of soybean-based biodiesel and 80% of petroleum diesel (B20), the estimated emission impacts are shown in the next table, taking from EPA report.

Table 2.1. Emission impacts for soybean-based biodiesel B20 [13].

Emissions	B20 (%)
Hydrocarbons	-21.1%
Carbon monoxide	-11.0%
Nitrogen oxides	+2.0%
Particles	-10.1%

Similar results were found by Nabi et al. in tests carried out on diesel engines with mixtures of biodiesel obtained from cottonseed oil. In this study, for blending B30 a carbon monoxides reduction of 24% and an increase of 10% of nitrogen oxides were obtained, while for B10 a reduction of particulate materials and exhaust gases of 24% and 14% was found, respectively [12].

Biodiesel presents a set of technical, environmental and economic advantages, as well as some disadvantages.

Among the technical advantages it can be mentioned:

- It can run in diesel engines with little or no modification, neat or blending with diesel fuel [6, 8-11].
- It has high cetane number (CN) [12] and high flash point, making it safer to handle [8, 14].
- Excellent lubricating properties [15]. The sulphur-free diesel loses lubricating qualities and to overcome this shortcoming, additives must be used. Wadumesthrige et al. have been evaluated the lubricity of ULSD blended with different levels of cottonseed oil, soybean oil and poultry fat based biodiesels finding that the addition of biodiesel, even at low rate (2%), improve lubricating ability of diesel, reducing wear and increasing the useful life of the injection system and engine [16].

From the environmental point of view, it must be highlighted:

- It comes from renewable resources, biodegradable [5, 6, 14, 17] and essentially non toxic to aquatic organisms.
- The gases produced during combustion have lower amount of unburned fuel and carbon monoxide [11-14].
- The organic carbon present is of photosynthetic origin, thus does not contribute to the increase of carbon dioxide in the atmosphere and consequently to the effect of greenhouse gases [5, 6]. A life cycle analysis of biodiesel showed that overall CO₂ emissions were reduced by 78% compared with petroleum-based diesel fuel when neat biodiesel was used, and for a blend B20 the reduction on emission of CO₂ were 15.5%, even when biodiesel emits 4.7% more CO₂ than petroleum diesel at the tailpipe. The reduction is a direct result of carbon recycling in the plants [18].

Regarding to economic advantages, it can be mentioned:

- The conversion of the process is quite efficient.
- It grants independence to the lack of fossil fuels.
- The commercialization of its by-product (glycerol) is an accessory profitable business.
- In many countries the production of biodiesel is encouraged with important incentives and tax exemptions.

Among the disadvantages of biodiesel use it should be considered:

- The volumetric heating value (HV) is approximately 12% lower than diesel fuel (on a mass bases) [5, 6, 8, 14].

- Nitrogen oxides emissions are slightly higher compared to fossil diesel [6, 12-14].
- There are problems of fluidity at low temperatures due to the effect of temperature on the viscosity. For cottonseed biodiesel, blends B50 or greater can be used for temperatures in the range 20-40°C. However for temperatures below 20°C it is convenient to keep the biodiesel percentage to a minimum [12].
- Start-up and performance problems in cold weather because of formation of solid wax crystals at low temperatures. Cold flow properties of biodiesels depend on the degree of saturation and unsaturation of the raw material and also depend on the blend concentration. The greater degree of saturation, the higher the cloud point and pour point [19].
- Due to its better solvency capacity than petrodiesel, some polymeric species formed during the storage of biodiesel in controlled conditions are soluble in oxidized biodiesel, but become insoluble when oxidized biodiesel is mixture with diesel fuel, and create sediments that are sent by the fuel line, being able to clog the fuel filter. The solvency effects of biodiesel blends are more pronounced at low temperature than at room temperature [19].
- It degrades when it is stored for long periods of time. Biodiesel tends to suffer oxidative and / or thermal polymerization reactions due to the degree of unsaturation of the oil from which it is derived. This leads to the formation of insoluble products that can cause problems in the fuel line. Storage temperature, storage time, biodiesel blend level, and feedstock affect the mass of precipitate formed [19].

2.3 Theoretical concepts

2.3.1 Sources of biodiesel

Any substance containing fatty acids, either bonded to another molecule or free, can be used to produce biodiesel. Usually, biodiesel production is made from vegetable oils, which are constituted mainly by 95-98% of triglycerides (TG) and small proportions of monoglycerides (MG), diglycerides (DG), free fatty acid (FFA), phospholipids, phosphatides, carotenes, tocopherols and traces of water [20]. Even refined oils contain small amounts of FFA and water [21]. Triglycerides are esters composed by a glycerol (Gly) moiety and three fatty acid moieties, which may be the same or different (Figure 2.5). Triglycerides contain substantial amounts of oxygen in its structure.

Soybean, sunflower, palm, rapeseed, canola and jatropha oils are the most frequently oils used for biodiesel production; however other vegetable oils, used frying oils and animal fats can also be used. Factors like geography, climate and economic aspects of the place where biodiesel is produced determine the convenient feedstock.

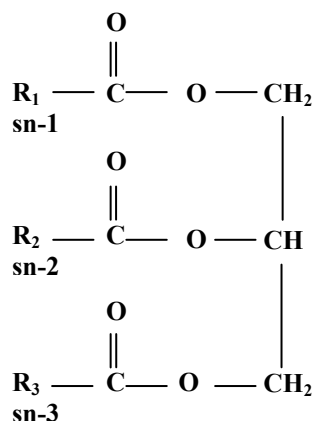


Figure 2.5. Typical chemical structure of a triglyceride. R_1 , R_2 and R_3 are long hydrocarbon chains.

According to data from The Oil World Statistics, in 2017 Argentina was the sixth producer of vegetable oils and fats worldwide, with a production of 10231 kt and was the third larger exporter in the world, after Indonesia and Malaysia and closely followed by Brazil (see Table 2.2 and Table 2.3). From total oil production, 87% corresponds to soybean followed by sunflower (11%) and other minor raw materials (peanuts, cotton, rapeseed, safflower and linseed). From soybean oil 70% is exported and 30% is used mainly to supply the national biodiesel production, whereas in the case of sunflower oil, 40% is exported and the remainder is used almost exclusively for culinary purposes.

Table 2.2. Ranking of producer countries of oils and fats [22].

		2014/2015	2016/2017	Estimated annual
		(kt)	(kt)	increment (%)
1°	Indonesia	37664	39902	5.9
2°	China	26584	27285	3.0
3°	EU	23960	23933	-0.1
4°	Malaysia	22300	21355	- 4.2
5°	USA	17604	19826	12.6
6°	Argentina	9259	10231	10.5
7°	Brazil	10241	10127	-1.1
8°	India	8540	9569	12.0
	Others	47812	52074	8.9
	Total world	203864	214302	5.1

Table 2.3. Major exporting countries of oils and fats [22].

		2014/2015	2016/2017	Estimated annual
		(kt)	(kt)	increment (%)
1°	Indonesia	28667	27887	-2.7
2°	Malaysia	18963	17951	-5.3
3°	Argentina	5832	6623	13.6
4°	Ukraine	4043	5605	38.6
	Others	24650	26242	6.5
	Total world	82155	84308	2.6

The use of autochthonous feedstock in the north of Argentina for biodiesel production, such as cottonseed oil, presents some advantages: is a by-product of cotton ginning, it is not used for food, generates jobs positions and enhance the regional economy.

Traditionally, cotton grow is of great importance for Chaco, since it is one of the main crops on which its economy is based. In spite of this, the cotton production in the country has been decreasing in the last years due to different factors such as low yield compared with soybeans, price volatility, restrictions on foreign trade, increasing production cost, among others. However, in December 2017, different actors of the productive sector have been inquired about this issue and the expectation for the 2017-2018 planting area is a generalized growth, both at country level and for the Chaco, according to data from Argentina Cotton Chamber [23].

Cotton plant belongs to the *Gossypium* genus of the Malvaceae family. There are more than 40 species of *Gossypium*, but only four are cultivated for commercial cotton fibers; *G. arboreum*, *G. barbadense*, *G. herbaceum* and *G. hirsutum*. Currently 95% of the fiber production is derived from *G. hirsutum* [24]. The fiber is the main product of the plant and secondarily, the seed (see Figure 2.6(a)); around 1.5–1.6 kg of cottonseed result from each kilogram of fiber produced [24]. The seed has three main destinations: oil production, forage for cattle and seed for sowing. The industrialization of cottonseed in cotton producing areas is an alternative to strengthen the sustainability of the agroindustrial chain of cotton.

The raw cottonseed is made up of three parts, as can be observed in Table 2.4, 1) linters (ca. 13%), which are short fibers still clinging to the seed; 2) hulls (ca. 32%), a tough, protective coating for the kernel; and 3) the protein and oil rich kernel itself (ca. 55%). Figure 2.6(b) illustrates the major components of whole cottonseed. The composition of the seed varies between different species, and even within the species, with the climatic and cultivation conditions. Typically, moisture-free kernels of *G. hirsutum* contain 26–43% of crude oil and 26–41% of protein. The oil is extracted from the seeds after the remove the lint, yielding ca. 15-16% on average [24].

Table 2.4. Approximate composition and typical producing yields from *G. hirsutum* [24].

Seed component	Mass fraction (%)	Protein content (%)	Oil content (%)
Seed analysis*			
Linters	12.7	3.7	0.9
Hull	31.8	3.6	0.8
Kernels	55.5	38.6	34.8
Product yields			
Linters	9		
Hull	25	5	1.0
Oils	16		
Meal	46	41-44	2.2
Misc. (debris/lost mass)	4		

*Moisture-free basis.



Figure 2.6. (Left) Cotton boll parts [25]; (Right) Major components of whole cottonseed [26].

Traditionally, cottonseed oil is used almost entirely in the production of edible products. However, in Argentina it is not used for human consumption as pure oil, rather as an aggregate in processed foods, sauces, prepared for condiments, snacks and in products for body care. Another use that has been considered in the last years, mainly in the cotton producing areas, is as a raw material to produce biodiesel, since it is suitable for that purpose according to many research [12, 27, 28].

The fatty acid profile of cottonseed oil is typical of the oleic–linoleic group of vegetable oils, since these two unsaturated fatty acids make up almost 75% of the total fatty acids. Roughly, 52% is linoleic acid and 16–20% is oleic acid. Palmitic acid, a saturated fatty acid makes up around 24% of the total and stearic acid is present at 2–3%. Several minor fatty acids are also present in the oil, including myristic, palmitoleic, malvalic, sterculic, linolenic, arachidic and behenic acids. In cottonseed oil, the saturated fatty acids are primarily found on the ends of the glycerol backbone – that is, at the sn-1 and sn-3 glycerol positions – and the sn-2 position usually carries an unsaturated fatty acid [24].

2.3.2 *Transesterification reaction*

In 1970, it was discovered that the viscosity of oils can be reduced by a simple chemical process called transesterification. Through this reaction the size of the oil molecule is reduced roughly one-third of its original size, thus decreasing its viscosity and making it similar to diesel fuel [5].

The transesterification reaction consists in reacting TG with a low molecular weight alcohol, usually methanol or ethanol, in presence of a catalyst, to obtain a mixture of fatty acids esters (FAMEs or FAEEs) and glycerol as final products. The process takes place in three consecutive and reversible reactions, in which TGs are transformed into DGs, then these are converted into MGs and finally into Gly, releasing an alkyl ester molecule of fatty acid in each stage [29]. The set of consecutive and reversible reaction and the global one are shown in Figure 2.7.

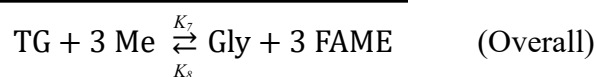
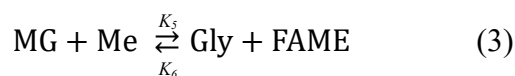
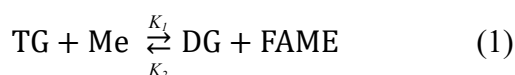


Figure 2.7. Stepwise and overall transesterification reaction.

According to the stoichiometry of the reaction, three moles of alcohol are required for each mole of triglyceride to yield three molecule of FAME and one molecule of glycerol. However, due to the reversibility of the reaction, an excess of alcohol is added to shift the equilibrium to the right side obtaining the maximum generation of products (biodiesel and glycerol).

Several factors affect the yield of the transesterification reaction, including temperature, molar ratio of alcohol to oil, type of catalyst and the quality of vegetable oil. These reaction variables have been studied by many researchers for conventional processes using basic and acid catalysts [27, 30-32]. Some important factors are described as follow:

- Effect of the presence of free fatty acids and water: In conventional transesterification of fats/vegetable oils for biodiesel production, FFA and water always produce negative effects. Basic catalysis is greatly affected by the presence of FFA and moisture. When the acidity is higher than 0.5%, part of the catalyst is consumed by reacting with the carboxyl groups of the FFA, forming the salt of the same acid usually called "soap" and decrease the catalyst efficiency. Further, the resulting soap causes gels formation and hinders the separation of biodiesel and

glycerine phases [32], all of which result in a low conversion. Relative to moisture, this causes the hydrolysis of triglycerides forming carboxylic acids and consequently soap. Acid catalysis is more tolerant to FFA because they can be converted to alkyl esters [32, 33]. However, water is produced by this reaction and affects the ester-formation, even more than in basic catalysis. It was demonstrated that 0.1 wt % of water in the reaction mixture affect the esterification and 5 wt % almost completely inhibited it [32]. When FFA and water are present in the reaction system at the same time, they had a synergistic negative effect on the reaction [31].

- Effect of the molar ratio of alcohol to oil: this variable is related with the type of catalyst used. Acid catalysis requires higher molar ratios than basic catalysis to achieve the same yield at a given reaction time [30, 32]. According to Freedman, a relation of alcohol to oil of 30:1 and 69 hs of reaction it was necessary to reach high yields of methyl esters (at temperature of ca. 65°C) [30]. Generally, higher molar ratios of alcohol to oil result in a higher conversion in less time. However, large excess tends to prevent the separation of glycerol [5]. The effect of the molar ratio of alcohol to oil for basic catalysis will be discussed with detail in Chapter 7.

- Effect of type of catalyst: transesterification reaction can be performing by different type of catalyst, such as basic, acidic or enzymatic catalysts. Alkali metal alkoxides are more effective transesterification catalysts compared to the acidic catalysts [5, 30]. However, if the raw material contains high amount of FFA, acid catalysis is preferred. Enzymatic biodiesel production using lipases as catalyst has also been researched with the purpose to overcome issues related to recovery and treatment of the by-product. However, its application on an industrial scale is not feasible because of its high cost of lipases [34]. In the industrial production the basic catalysis is broadly used.

- Effect of the reaction temperature: as expected, the reaction rate is strongly influenced by the reaction temperature. However, given enough time, the reaction will proceed to near completion even at room temperature. Generally, the operating temperature is limited by the boiling point of the alcohol used. This effect will be discussed in Chapter 7.

- Effect of the stirring speed: in the transesterification reaction, alcohol and oil form a two-phase liquid system and the reaction is diffusion-controlled. High stirring speed is required to form an emulsion of alcohol drops dispersed in the oil phase, thus improving the mixture and increasing the reaction rate. The mixing effect is most significant at the beginning of the reaction [35, 36].

2.3.3 *Industrial process*

Industrial processes for biodiesel production are usually alkali-catalyzed, although other approaches have been proposed, including acid catalysis [32, 33] and enzymatic catalysis [34, 37, 38]. The acid catalysis is slower than alkaline-catalysis [30, 32, 33] however, it has been found useful for pre-treatment of oils with high FFA, since esterification is relative fast. Enzymes have shown good tolerance for the free fatty acid level and/or water content of the feedstock, but have not been adopted industrially because of their high cost. Immobilization of the enzyme can improve better opportunities in this area [34]. Relative to the alkaline homogeneous catalysis, the optimum conditions of temperature, time and molar ratio of methanol to oil to achieve maximum conversion, are not consensual.

Figure 2.8 shows a schematic diagram of the processes involved in biodiesel production by alkaline catalysis. The reaction takes place in a stirred reactor tank where alcohol, catalyst and oil are fed and react each other for approximately 1 hour at 60°C. A molar ratio of alcohol to oil of 6:1 is normally used in industrial processes to obtain methyl ester yields higher than 98% by weight [5]. Once the reaction time have been attained, the mixture constituted by a phase rich in glycerol and an organic phase rich in esters, is pumped to a settling tank or a centrifuge to remove glycerol from esters. The non reacted alcohol is distributed in both phases. After separation from the glycerol, the methyl esters stream pass through a methanol stripper, usually a vacuum flash process before washing process. For this process, acidified water is used to remove any remaining catalyst, soap, salts, methanol, or free glycerol from the biodiesel. The acid neutralizes the catalyst and split the soap that may have formed during the transesterification reaction. Soap reacts with acid to form water soluble salts and FFAs; the salts will be removed during the water washing step and the free fatty acids will stay in the biodiesel. After wash process, the biodiesel is dried through a vacuum flash process up to the standard required value. The glycerol stream leaving the separator is only about 50% glycerol. It contains some of the excess methanol and most of the catalyst and soap. The refining steps include acidification, separation of FFA and recovery of alcohol. At this point, the glycerol should have a purity of approximately 85% and is typically sold to a glycerol refiner [39]. The methanol removed from the methyl ester and glycerol stream may contain some water, so it must go through a distillation process before being reused in the reaction.

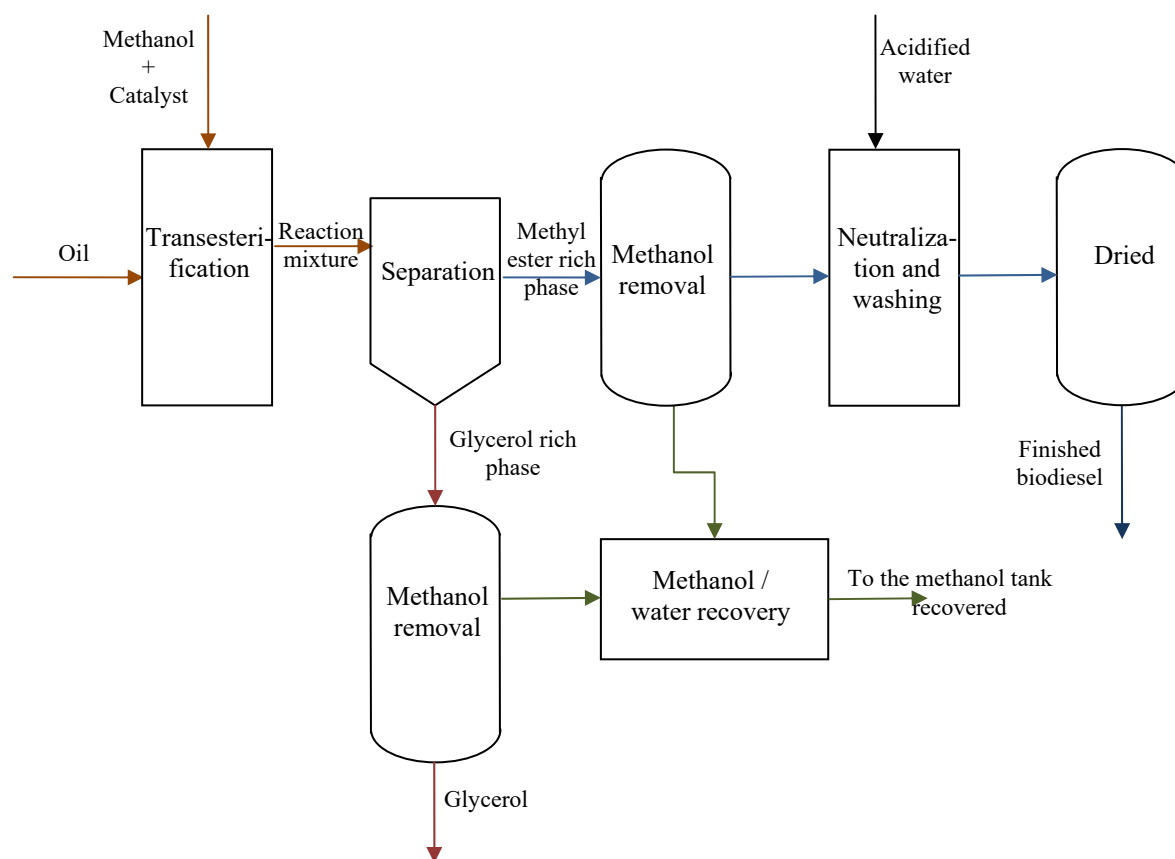


Figure 2.8. Process flow for biodiesel production.

When low quality oils are used, usually with high FFA content, a process that involves two stages can be performed. First the FFA are converted to FAME by an acid catalyzed pre-treatment and in the second step transesterification is completed by using alkaline catalyst [40, 41].

2.3.4 Quality control

Biodiesel can be obtained from diverse feedstock having different composition, degree of unsaturation and impurities leading to biodiesels with different characteristics and properties. For optimal engine performance and quality exhaust emission, biodiesel must comply a set of quality parameters, which are established in the standards EN 14214 in Europe and ASTM D6751 in USA. In Argentina, limits and specification for biodiesel are set in the Resolution 129/01

(Ministry of Energy and Mining), based on ASTM standard. Table 2.5 shows the specifications included in the USA norm and the European norm is presented in Table A.1 [42].

Table 2.5. Specification for biodiesel (B100) [4].

Properties	Test method	Limits	Units
Ca & Mg, combined	EN 14538	5 maximum	ppm ($\mu\text{g/g}$)
Flash Point (closed cup)	D 93	93 minimum	degrees C
Alcohol Control (One of the following must be met)			
Methanol Content	EN 14110	0.2 maximum	% mass
Flash Point	D 93	130 minimum	degrees C
Water & sediments	D 2709	0.05 maximum	% vol.
Kinematic Viscosity, 40 °C	D 445	1.9 – 6.0	$\text{mm}^2/\text{sec.}$
Sulphated Ash	D 874	0.02 maximum	% mass
Sulphur			
S 15 Grade	D 5453	0.0015 max (15)	% mass (ppm)
S 500 Grade	D 5453	0.05 maximum (500)	% mass (ppm)
Copper Strip Corrosion	D 130	No. 3 maximum	
Cetane	D 613	47 minimum	
Cloud point	D 2500	report	degrees C
Carbon residue 100% sample	D 4530*	0.05 maximum	% mass
Acid Number	D 664	0.5 maximum	mg KOH/g
Free Glycerine	D 6584	0.02 maximum	% mass
Total Glycerine	D 6584	0.24 maximum	% mass
Phosphorus Content	D 4951	0.001 maximum	% mass
Distillation, T90 AET	D1160	360 maximum	degrees C
Sodium/Potassium, combined	EN 14538	5 maximum	ppm
Oxidation Stability at 110°C	EN 14112	3 minimum	hours
Cold Soak Filtration	Annex to D6751	360 maximum	seconds
For use in temperatures below -12	Annex to D6751	200 maximum	seconds

Bold=BQ-9000 Critical specification Testing Once Production Process Under Control.

* The carbon residue shall be run on the 100% sample.

2.4 Ethical and social implications

The increasing global demand of energy and depletion of fossil fuel reserves has generated a growing interest in the development of renewable energies. In this context, the use of biomass as a resource to produce energy seems to be very promising, but it is essential to keep in mind that

production and consumption of energy, although renewable, are strongly linked to social and ethical issues and not only to technical aspects. The proposal of use plants to produce the so-called agrofuels have both, positive and negative socio-economic implications, we should know that farmlands are not an inexhaustible source of resources and it is necessary to follow the agro-ecological principles for the sustainability, like crops rotation system, with all the complexity that this represents. Also, Europe and the USA look at South America's countries as suppliers of raw materials; if this is not properly regulated and managed, it can put at risk the food security of less developed countries, depriving millions of people of food crops.

Political incentives for biofuels production must be carefully analyzed; they cannot be carried out at the expense of deforestation and expansion of farmlands with disappearance of biodiversity. For this reasons the production of biofuels should not be based on food crops neither the farmlands can be deviated to the production of crops for biofuel. Regarding to this, it is important to highlight the privilege situation of Argentina in comparison with other countries, where the competition of crops for energy production versus crops for food purposes is strong due to the less availability of farmland. In the north of Argentina, the use of cottonseed as raw material for the production of biodiesel does not represent the diversion of a food crop, but rather the use of a by-product of the cotton ginning, given that it is grown mainly for the production of fibber. This has a positive social impact, since it generate new job positions and contribute to strengthening the economy of Chaco without affecting environment.

2.5 References

1. Timilsina GR. Biofuels in the long-run global energy supply mix for transportation. *Philosophical Transaction of Royal Society A*. 2014;372(2006):20120323.
2. International Energy Agency. *Trackin Clean Energy Progress 2017*. Available from <https://www.iea.org/tcep/>. a2017.
3. Parliament European Union CotE. Directive (EU) 2015/1513 of the European Parliament and of the Council of 9 September 2015 Amending Directive 98/70/EC Relating to the Quality of Petrol and Diesel Fuels and Amending Directive 2009/28/EC on the Promotion of the Use of Energy from Renewable Sources. *Official Journal of the European Union*. 2015;239:1-29.

4. American Society for Testing and Materials Testing. Standard Specification for Biodiesel Fuel Blend Stock (B100) for Middle Distillate Fuels. ASTM International; 2012.
5. Srivastava A, Prasad R. Triglycerides-based diesel fuels. *Renewable and sustainable energy reviews*. 2000;4(2):111-33.
6. Singh S, Singh D. Biodiesel production through the use of different sources and characterization of oils and their esters as the substitute of diesel: a review. *Renewable and sustainable energy reviews*. 2010;14(1):200-16.
7. ASTDR. Toxicological profile for fuel oils. Atlanta, Georgia 30333: Agency for Toxic Substances & Disease Registry, Services USDoHaH; 1995.
8. Clark S, Wagner L, Schrock M, Piennaar P. Methyl and ethyl soybean esters as renewable fuels for diesel engines. *Journal of the American Oil Chemists Society*. 1984;61(10):1632-8.
9. Peterson C, Thompson J, Taberski J, Reece D, Fleischman G. Long-range on-road test with twenty-percent rapeseed biodiesel. *Applied Engineering in Agriculture*. 1999;15(2):91.
10. Peterson CL, Reece DL, Thompson JC, Beck SM, Chase C. Ethyl ester of rapeseed used as a biodiesel fuel—a case study. *Biomass and Bioenergy*. 1996;10(5-6):331-6.
11. Wang W-G, Lyons DW, Clark NN, Gautam M, Norton P. Emissions from nine heavy trucks fueled by diesel and biodiesel blend without engine modification. *Environmental science & technology*. 2000;34(6):933-9.
12. Nabi MN, Rahman MM, Akhter MS. Biodiesel from cotton seed oil and its effect on engine performance and exhaust emissions. *Applied Thermal Engineering*. 2009;29(11-12):2265-70.
13. EPA. A comprehensive analysis of biodiesel impacts on exhaust emissions. Environmental Protection Agency, 2002.
14. Knothe G, Krahl J, Van Gerpen J. *The biodiesel handbook*: Elsevier; 2015.
15. Hu J, Du Z, Li C, Min E. Study on the lubrication properties of biodiesel as fuel lubricity enhancers. *Fuel*. 2005;84(12-13):1601-6.
16. Wadumesthrige K, Ara M, Salley SO, Ng KS. Investigation of lubricity characteristics of biodiesel in petroleum and synthetic fuel. *Energy & Fuels*. 2009;23(4):2229-34.
17. Zhang X, Peterson C, Reece D, Haws R, Möller G. Biodegradability of biodiesel in the aquatic environment. *Transactions of the ASAE*. 1998;41(5):1423.

18. Sheehan J, Camobreco V, Duffield J, Graboski M, Shapouri H. Life cycle inventory of biodiesel and petroleum diesel for use in an urban bus. Final report. National Renewable Energy Lab., Golden, CO (US), 1998.
19. Tang H, Salley SO, Ng KS. Fuel properties and precipitate formation at low temperature in soy-, cottonseed-, and poultry fat-based biodiesel blends. *Fuel*. 2008;87(13-14):3006-17.
20. Aluyor E, Ozigagu C, Oboh O, Aluyor P. Chromatographic analysis of vegetable oils: A review. *Scientific Research and Essay*. 2009;4(4):191-7.
21. Ma F, Hanna MA. Biodiesel production: a review. *Bioresource technology*. 1999;70(1):1-15.
22. Calzada J. 6° en el mundo, Argentina produce más aceite que Brasil. *Bolsa de Comercio de Rosario*. Year XXXV; Edition 1820. June 2017.
23. Ing. Agr. Fernández HL. Campaña Algodonera 2017/2018. Perspectivas para la superficie de siembra. *Cámara Algodonera Argentina*. 2017 Diciembre 2017.
24. Gunstone F. *Vegetable oils in food technology: composition, properties and uses*: John Wiley & Sons; 2011.
25. Available from: <https://thesoilhuggersjourney.wordpress.com/2014/08/12/pick-a-plant-day-our-cotton->.
26. Poore M. Alternative feeds for beef cattle. Available from: <https://slideplayer.com/slide/4740462/>.
27. Rashid U, Anwar F, Knothe G. Evaluation of biodiesel obtained from cottonseed oil. *Fuel Processing Technology*. 2009;90(9):1157-63.
28. Azcan N, Danisman A. Alkali catalyzed transesterification of cottonseed oil by microwave irradiation. *Fuel*. 2007;86(17-18):2639-44.
29. Freedman B, Butterfield RO, Pryde EH. Transesterification kinetics of soybean oil 1. *Journal of the American Oil Chemists' Society*. 1986;63(10):1375-80.
30. Freedman B, Pryde E, Mounts T. Variables affecting the yields of fatty esters from transesterified vegetable oils. *Journal of the American Oil Chemists Society*. 1984;61(10):1638-43.
31. Ma F, Clements L, Hanna M. The effects of catalyst, free fatty acids, and water on transesterification of beef tallow. *Transactions of the ASAE*. 1998;41(5):1261.

32. Canakci M, Van Gerpen J. Biodiesel production via acid catalysis. Transactions of the ASAE. 1999;42(5):1203.
33. Lotero E, Liu Y, Lopez DE, Suwannakarn K, Bruce DA, Goodwin JG. Synthesis of biodiesel via acid catalysis. Industrial & engineering chemistry research. 2005;44(14):5353-63.
34. Shimada Y, Watanabe Y, Samukawa T, Sugihara A, Noda H, Fukuda H, et al. Conversion of vegetable oil to biodiesel using immobilized *Candida antarctica* lipase. Journal of the American Oil Chemists' Society. 1999;76(7):789-93.
35. Nouredini H, Zhu D. Kinetics of transesterification of soybean oil. Journal of the American Oil Chemists' Society. 1997;74(11):1457-63.
36. Vicente G, Martínez M, Aracil J, Esteban A. Kinetics of sunflower oil methanolysis. Industrial & Engineering Chemistry Research. 2005;44(15):5447-54.
37. Nelson LA, Foglia TA, Marmer WN. Lipase-catalyzed production of biodiesel. Journal of the American Oil Chemists' Society. 1996;73(9):1191-5.
38. Li J, Li L, Tong J, Wang Y, Chen S. Research development on lipase-catalyzed biodiesel. Energy procedia. 2012;16:1014-21.
39. Van Gerpen J. Biodiesel processing and production. Fuel processing technology. 2005;86(10):1097-107.
40. Canakci M, Van Gerpen J. Biodiesel production from oils and fats with high free fatty acids. Transactions of the ASAE. 2001;44(6):1429.
41. Zhang Y, Dube M, McLean D, Kates M. Biodiesel production from waste cooking oil: 1. Process design and technological assessment. Bioresource technology. 2003;89(1):1-16.
42. Automotive fuels - Fatty acid methyl esters (FAME) for diesel engine - Requirements and test methods. BS EN 14214:2008.

3 CHAPTER

DENSITY OF COTTONSEED OIL AND BIODIESEL

This chapter reports experimental density data of CSB and CSO measured at temperatures from (288.15 to 358.15) K and (278.15 to 358.15) K, respectively and pressures from 0.1 MPa up to 30.0 MPa. The measurement densities were correlated with the Goharshadi–Morsali–Abbaspour equation of state (GMA EoS) and from these result, some mechanical coefficients were calculated. For biodiesel, the predictive group contribution method (GCVOL) for high pressure was applied, and two new models to predict density as function of temperature and pressure were developed. For cotton oil, the GCVOL, Halvorsen and Zong fragment-based methods were applied for density prediction. In all case, the ability of the models was evaluated by statistical indicators.

In this chapter, density data regarding to biodiesel have already been published in *Fuel* 2015, 141, 23-38 and the data relative to cottonseed oil was published in the *Journal of Chemical and Engineering Data* 2018, 63 (9), 3438–3448.

3.1 BIODIESEL DENSITY

3.1.1 Introduction

Density is an important property for any process and it is related to other properties such as viscosity, surface tension, and speed of sound.

Biodiesel density affects the injection system of diesel engines, which is one of the most important parameters for high performance. An appropriate quantity of fuel must be delivered into the engine cylinder and mixed with air to achieve proper combustion mixture. In diesel engines, this operation is carried out under pressure, usually at $p \approx (15\text{--}50)$ MPa and moderate temperature $T \approx (300\text{--}350)$ K, and is strongly affected by the fuel density [1-3]. With the common rail injection technology the pressure can reach up 100–120 MPa [4, 5]. Therefore the simulation of biodiesel production, blending, and design of injection systems requires accurate knowledge of volumetric properties over wide ranges of pressure and temperature.

Literature usually reports biodiesel density measurements made close to the ambient temperature (285 – 295) K and atmospheric pressure [6-12] and few measurements of this property have been reported in wider temperature ranges [13-18]. The inclusion of pressure has been made in the works by Pratas et al. [19], Tat and Van Gerpen [20-22], Nikolic et al. [23], Aparício et al. [24], Dzida and Prusakiewicz [25], and recently by Chhetri and Watts [26] and Schedemann et al. [27]. Since density depends on the raw material from which biodiesel was produced, FAMEs profile is crucial for applying the correlation and prediction models to that property, which also has not been provided by authors [23-25].

To correlate pure FAME and biodiesel densities the Tait equation of state (EoS) [28] has been used [19, 24, 27]. Pratas et al. [19] used this EoS to correlate density of pure FAME (methyl laurate, myristate, and oleate), methyl biodiesels from palm (P), soybean (S), and rapeseed (R) oils, binary (RP, SP, SR) mixtures, and ternary mixture (SRP) for temperatures from 283 K to 333 K and pressures up to 45 MPa. Schedemann et al. [27] used Tait equation to correlate data for methyl linoleate at temperatures between 278 K to 367 K and pressures between 0.4 MPa and 130 MPa. The relative deviations in density obtained from those correlations have been usually lower than 0.01%. Cubic equations of state such as the cubic-plus-association equation of state (CPA EoS) [29, 30], and the volume translated Peng–Robinson (PR) equation of state (VTPR EoS) [31] have been applied to density correlation and prediction. The CPA EoS combines a

physical contribution from a cubic density EoS (Soave-Redlich Kwong EoS) with an association term accounting for intermolecular hydrogen bonding and solvation effects, which disappears for non-associating components, such as esters. The VTPR EoS uses the cubic Peng–Robinson EoS in which the predictive UNIFAC group contribution method developed by Dortmund [32] is employed for calculation of the needed parameters. Pratas et al. [19] applied the CPA EoS to correlate pure FAME density, and the calculated pure component parameters were applied to predict the density of methyl biodiesels, with deviations ranging from 0.79% to 2.5%. Schedemann et al. [27] used the VTPR method to predict density data of methyl linoleate and biodiesel. For the biodiesel deviations $\approx 1\%$ were found at 396.8 K and pressures up to 55 MPa whereas at temperatures lower than 396.8 K and pressures up to 130 MPa deviations ranged from -1% to -7%. More complex EoS such as variants of SAFT EoS were also used. The SAFT EoS is based on a clear physical molecular model, assuming that a molecule is composed of chains of freely jointed spherical segments and several intermolecular forces are taken in consideration [33]. Recently Oliveira et al. [34] applied the soft-SAFT EoS to density prediction of FAMES and of biodiesels measured by Pratas et al. [19] and obtained mean deviations of 0.49%. Dong et al. [35] were the first to apply the PC-SAFT equation of state using group contribution methods for the calculation of parameters and prediction of FAMES and biodiesel densities. For FAMES at atmospheric pressure, deviations in density were less than 0.5%, and for biodiesels studied by Pratas et al. [19] predicted densities were all within 1% deviation. Pratas et al. [36] extended a group contribution method developed for the prediction of molar volume (GCVOL) under high pressure. The prediction of biodiesel density with this method was made with relative deviations between 0.2% and 0.7%. Recently Meng et al. [37] revised the modified Rackett equation proposed by Spencer and Danner [38] to predict biodiesel densities over wide temperature range (298–523) K at atmospheric pressure. The revised Rackett equation allowed the density prediction for three biodiesels with a maximum deviation of 0.42%. An attempt was made to use fundamental relations of thermodynamics in particular the Helmholtz free energy [14] to model thermodynamic properties of biodiesel. Using this approach, biodiesel density was predicted within 0.6% deviation for temperatures between 278 K and 333 K. A new interesting approach and never applied to biodiesel for the correlation of density is provided by the Goharshadi–Morsali–Abbaspour equation of state (GMA EoS), which was found valid for polar, non-polar, and H-bonded fluids [39]. The GMA EoS equation is based on the theory of the average potential

energy and it has shown linear behaviour for various thermodynamic properties. The existence of such regularities is very important because they can be used for safe extrapolation in the density calculation for high pressures.

Density data regarding cottonseed biodiesel is very scarce in the literature, compared with other FAME diesels. Nogueira et al. [40] presented density data at temperatures between 293.15 and 373.15 K at atmospheric pressure, and Alptekin and Canakci [8] presented the value at 288.15 K. As far as it is known, no high-pressure results were presented so far for this biodiesel.

In this study, cottonseed oil was transesterified into biodiesel and its density was measured at temperatures between 288.15 K and 358.15 K and pressures between 0.1 MPa and 30 MPa, Aiming to gather a sufficiently large amount of data, and for the sake of statistical significance for biodiesel density correlation and prediction, the measured densities for CSB were combined with literature data relative to other 18 biodiesels. The built database was used to test the correlation of density with temperature and pressure using the Goharshadi– Morsali–Abbaspour equation of state (GMA EoS) and the predictive GCVOL for high pressure [36]. The information regarding all biodiesels was also used to test and develop two new full predictive models. As far as it is known, this is the first time that density measurements of CSB are presented under high pressures, and the GMA EoS used to model biodiesel density.

3.1.2 Experimental

3.1.2.1 Materials

The detailed specifications of all materials are summarized in Table 3.1. The terminology (C_m:n) was used for FAMEs, where m is the number of carbon atoms and n the number of double bonds of the related fatty acid.

Table 3.1. Sample material purities.

Material	Supplier	Cas No	Sample purity (wt %)	Properties
Sodium methoxide	Fluka	124-41-4	≥97	
Methanol	Carlo Herba	67-56-1	≥99.9	
Methyl mirystate (C14:0)	Fluka	124-10-7	≥99	
Methyl Pentadecanoate (C15:0)	Fluka	7132-64-1	≈99	
Methyl palmitate (C16:0)	Fluka	112-39-0	≥99	
Methyl stearate (C18:0)	Sigma	112-61-8	≈99	
Methyl oleate (C18:1)	Aldrich	112-62-9	≈99	
Methyl linoleate (C18:2)	Acros Organics	112-63-0	≈99	
Methyl linolenate (C18:3)	Fluka	301-00-8	≥99	
Methyl heptadecanoate (C17:0)	Fluka	1731-92-6	≥99	
N-Heptane	Sigma Aldrich	142-82-9	99	
Cottonseed oil	Acros Organics	17711	Fatty acid composition: MeC14:0 and lower: ca. 1.5%; MeC16:0 ca. 25%; MeC18:0 ca. 3%; MeC18:1, 16 to 24%; MeC18:2, 50 to 55%; MeC18:3 and higher < 1.5%.	$AV \leq 0.5 \text{ mg KOH}\cdot\text{g}^{-1}$ $SV = 185 - 198 \text{ mg KOH}\cdot\text{g}^{-1}$ $IN = 95 \text{ to } 115 \text{ g I/100g}$ $UM < 1.5\%$ $n = 1.4720 \text{ to } 1.4730$ (20°C, 589 nm)

AV = acid value; SV = Saponification value; IN = Iodine number; UM = unsaponifiable matter; n = refractive index.

3.1.2.2 Cottonseed biodiesel preparation

The transesterification of cottonseed oil was carried out in a 50 ml three-necked double wall jacketed reactor. The reactor was equipped with a reflux condenser to avoid methanol losses, a magnetic stirrer, a digital thermometer (ERTCO-EUTECHNICS Model 4400 Digital thermometer with an uncertainty of 0.01K) and one stopper to feed the raw materials. The reactor was initially charged with a known amount of oil. A solution of known amount of catalyst sodium methoxide was prepared in the required amount of methanol and was added to the oil sample. After proper closing of the flask the temperature in the reactor was maintained constant by circulating water from a thermostatic bath (Digiterm 100 JP SELECTA). The system was also

kept airtight preventing the loss of alcohol. The reaction mix was held at a temperature just above the boiling point of the alcohol i.e. around 65°C to speed up the reaction. The reaction time was two hours. Excess alcohol was normally used to ensure total conversion of the oil to its esters. After the methyl ester formation process is completed, the heating was stopped and the products transferred to a separating funnel. The ester layer containing mainly FAMES and methanol, and the glycerol layer containing mainly glycerol and methanol were separated. The biodiesel was washed three times; ones of them with acidified water to neutralize the catalyst and then was dried under vacuum (50mbar at 40°C) to remove traces of moisture, until the water content met the specification. This determination was carried out by Karl Fischer.

3.1.2.3 Biodiesel characterization

The FAMES of biodiesel produced from cottonseed oil, were analyzed by gas chromatography in a TRE METRICS 9001 gas chromatograph equipped with a fused silica capillary column DB-225 (J & W Scientific, Agilent) of 30 m in length, 0.15 µm film and internal diameter of 0.25 mm. A sample (1 µL) was injected at temperature of 280 °C and without split. Helium was used as the carrier gas at a flow rate of 1 ml min⁻¹ and also used as auxiliary gas for the FID. The following temperature ramp was used: initial temperature of 70 °C during 1 min, followed by an increase of 10 °C· min⁻¹ up to 180 °C, and then 3 °C· min⁻¹ up to 220 °C maintained for 15 min. The biodiesel components were quantified by using heptadecanoate methyl ester as an internal standard. Calibration curves were developed using different concentrations of each methyl ester in n-heptane with addition of internal standard. The composition (wt %) of the cottonseed biodiesel (CSB) was found from three injections: methyl myristate (0.93±0.28)%, methyl palmitate (26.76±1.56)%, methyl stearate (2.81±0.29)%, methyl oleate (17.89±1.71)%, and methyl linoleate (51.61±2.99)%.

3.1.2.4 Experimental density measurement

Cottonseed biodiesel densities were determined using an Anton Paar DMA 60 digital vibrating tube densimeter, with a DMA 512P measuring cell. Figure 3.1 shows the installation of the DMA 512P cell and the peripheral equipment used. The temperature in the vibrating tube cell was measured with a platinum resistance probe (PT100). A Julabo F12-ED thermostatic bath with

ethylene glycol was used as circulating fluid in the thermostat circuit of the measuring cell and the temperature was held constant to ± 0.01 K. The required pressure was generated and controlled using a Pressure Generator model 50-6-15, High Pressure Equipment Co., with acetone as hydraulic fluid. The diameter of the metallic tube was 1.59×10^{-3} m and the buffer had more than 1 m length, which guaranteed the inexistence of hydraulic liquid diffusion in the liquid contained within the densimeter cell. Pressures were measured with a pressure transducer (Wika Transmitter S-10, WIKA Alexander Wiegand GmbH & Co.). A PCI-6220 data acquisition board (DAQ) from National Instruments (NI) was used for real time collection of period, temperature, and pressure values. For this task a Labview application was developed. Modules of temperature (NI SCCFT01) and pressure (NI SCC-CI20) were installed into a NI SC- 2345 bus and connected to the DAQ board. The measuring setup and the calibration of the vibrating tube densimeter were described with detail in a previous paper [41]. The performance of the densimeter was checked against water (Milli-Q) at temperatures (298.15, 318.15, 328.15, 338.15, 358.15) K and for each temperature different pressures (0.1, 10, 20, 30) MPa were considered. At each (T, p) coordinate the density was measured five times in increasing pressure direction, and other five times in decreasing pressure one. The repeatability in density was better than $0.1 \text{ kg}\cdot\text{m}^{-3}$. The measured densities compared with the reference NIST data [42] showed relative deviations in the range (0.03–0.07)%, except for 358.15 K were deviations reached 0.15%. The influence of viscosity on density uncertainty (damping effects on the vibrating tube) for liquids with viscosities less than $100 \text{ mPa}\cdot\text{s}$ can be important. An approximate value of such uncertainty was obtained using the method proposed by Anton Parr [43] for the DMA 512P densimeter. From densities and viscosities presented by Nogueira et al. [40] for babassu, soybean and cottonseed biodiesels the obtained uncertainty was $0.03 \text{ kg}\cdot\text{m}^{-3}$ thus contributing with a negligible value to the combined standard uncertainty. The expanded uncertainties, U , were calculated with confidence level 95% (with coverage factor $k = 2$) for temperature, pressure, and density. The uncertainties in temperature and pressure were $u(T) = 0.02$ K and $u(p) = 0.02$ MPa, respectively. The combined standard uncertainty of the density measurements, estimated taking into account the influence of uncertainties associated with calibration equation [41], temperature, pressure, period of oscillations (six-digit frequency counter), viscosity, and density data of calibrating fluids was estimated as $0.81 \text{ kg}\cdot\text{m}^{-3}$. Hence, the expanded uncertainty in the measurement of density by this method was estimated to be $U(\rho) = 1.6 \text{ kg}\cdot\text{m}^{-3}$.

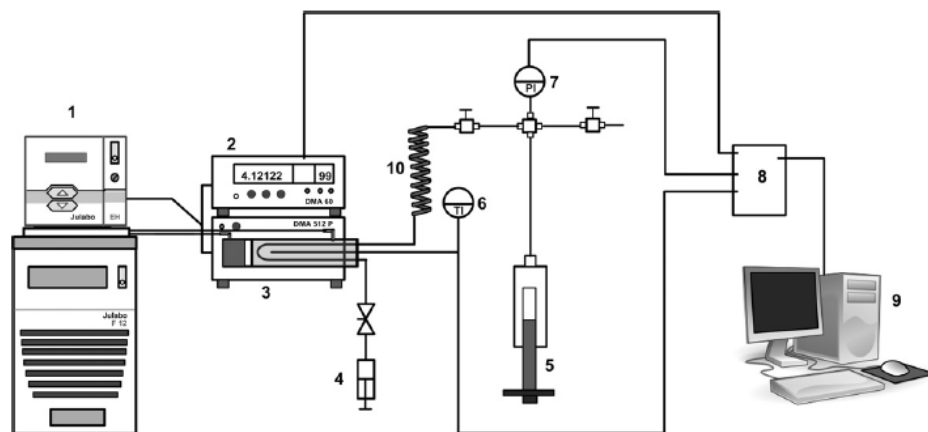


Figure 3.1. Experimental setup for the measurement of liquid densities at high pressures: 1-Julabo FP-50 thermostatic bath; 2-DMA 60 (Anton Paar) device for measuring the period of oscillation; 3-Measuring cell DMA 512P (Anton Paar); 4-Syringe for sample introduction; 5-Pressure generator model HIP 50-6-15; 6-PT probe; 7-Pressure transducer WIKA, S-10; 8-NI PCI-8220 data acquisition board; 9-PC; 10-Buffer.

3.1.3 Density database for biodiesels

The information concerning to biodiesel densities under high pressures with detailed FAMES profile is available in literature as explained in Section 3.1.1. Pratas et al. [36] have shown that discrepancies in density data reported by different authors are usually due to differences in the oil composition, and not caused by experimental errors during measurements. Thus, detailed composition of biodiesels must be known for reliable prediction of their densities.

The database used for the development of density models contain 19 biodiesels and was built using measurements made by Pratas et al. [19], Tat and Van Gerpen [20, 21], Schedemann et al. [27] and the CSB densities measured in this work. The information relative to these biodiesel and the equations of state used for density correlation by those authors are presented in Table 3.2. Tat et al. [22] presented density values at 294 K and up to 35 MPa for methyl soy biodiesel. However, access to the values is difficult and uncertain because they are presented in graphic form. Their biodiesel had practically the same composition of N21 biodiesel, which was also measured up to 35 MPa for temperatures between 293 K and 373 K. Dzida and Prusakiewicz [25] measured density from 273 K up to 363 K at atmospheric pressure and the values at pressures up to 100 MPa in the range (293–318) K were calculated following a numerical procedure proposed by Sun et al. [44]. However, the FAMES profile was not presented, also neither by Nikolic' et al. [23], who made density measurements for rapeseed biodiesel at 293 K and up to 160 MPa, and

presented density data in graphic form, which for our purpose was useless. Density as a function of temperature at atmospheric pressure for all fuels in the database is plotted in Figure 3.2.

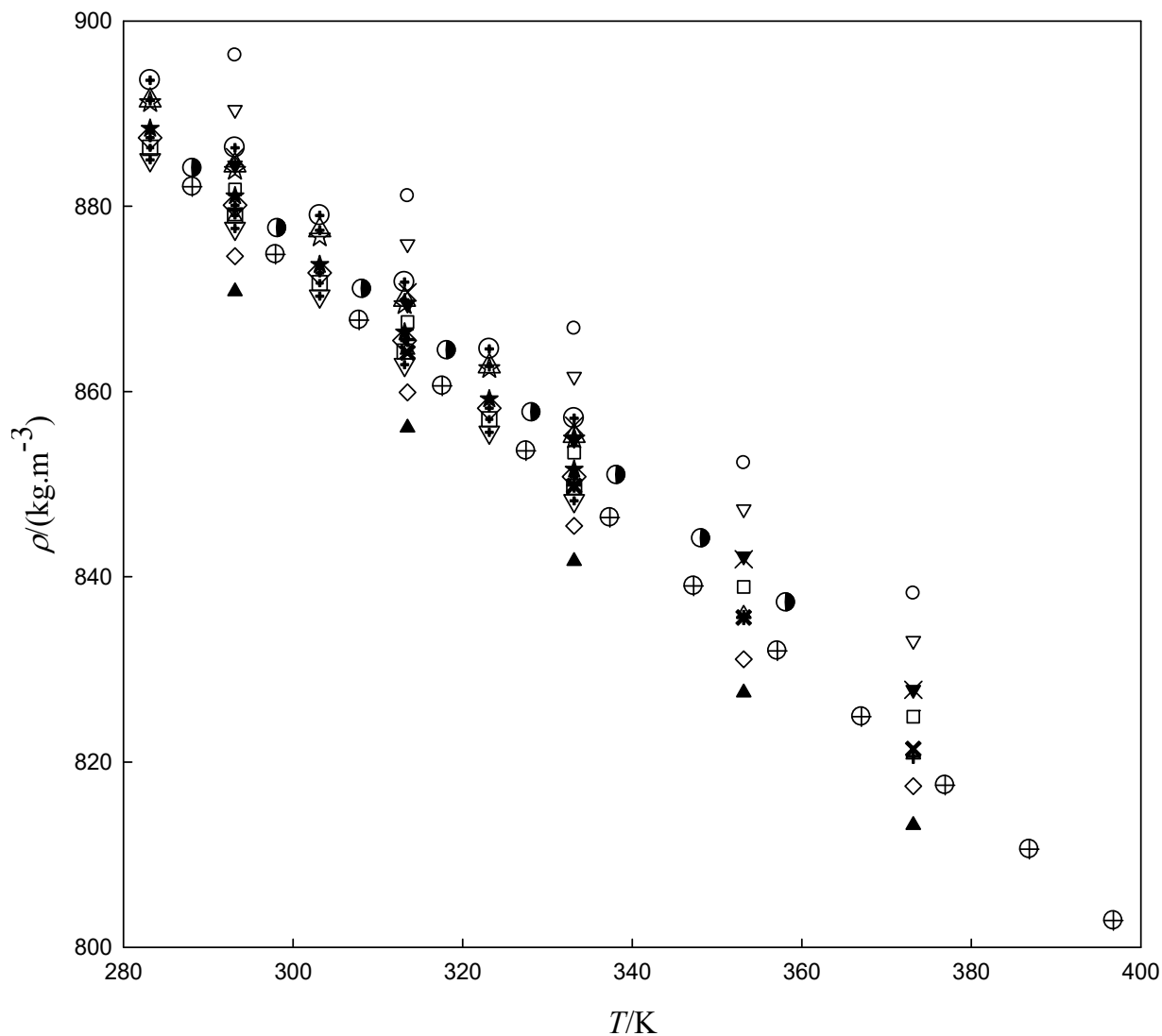


Figure 3.2. Density (ρ) as a function of temperature at 0.1 MPa for the biodiesels in database: Δ , N5; ∇ , N6; \circ , N7; \diamond , N19; $+$, N20; \square , N21; \blacktriangle , N23; \blacktriangledown , N17; \times , N8; \times , N9; \triangleleft , R; \triangleright , P; \oplus , S; \star , SR; \boxplus , RP; \diamond , SP; \star , SRP; \bullet , CSB; \oplus , SCHB.

As can be seen from the Figure 3.2, density decreases as temperature increases, as expected. In this figure can also be observed that, lower and upper density limits for the envelope density in the database correspond to N23 (methyl tallow) and N7 (methyl linolenate) fuels studied by Tat and Van Gerpen [20, 21], respectively. This was expected since density increases with increasing

content in unsaturated FAMES and unsaturation level. According to the biodiesel composition, the degree of unsaturation (DU) can be calculated taking into account the amount of monounsaturated and polyunsaturated FAMES ($wt\%$) present in the biodiesel by the empirical expression [45-47].

$$DU = (\text{monounsaturated } C_n: 1 ; wt\%) + 2(\text{polyunsaturated } C_n: 2; 3 ; wt\%) \quad \text{Eq. 3-1}$$

Table 3.2. Biodiesels used in this study: composition ($wt\%$), degree of unsaturation (DU), density at 298K (GCVOL), pVT ranges of measurements, and EoS reported in the literature for pVT correlation.

FAME	S	R	P	SR	PR	SP	SRP	N5	N6	N7
C10	0	0.01	0.03	0	0.02	0.01	0.01	0	0	0
C12	0	0.04	0.24	0.03	0.2	0.18	0.14	0	0	0
C14	0.07	0.07	0.57	0.09	0.54	0.01	0.38	3.0	0	0
C16	10.76	5.22	42.45	8.9	23.09	25.56	18.97	6.5	1.4	7.4
C16:1	0.07	0.2	0.13	0.15	0.17	0.11	0.14	4.1	0	0
C17:0	0	0	0	0	0	0	0	1.5	0	0
C18	3.94	1.62	4.02	2.76	3.02	4.04	3.28	1.9	0.7	3.7
C18:1	22.96	62.11	41.92	41.82	52.92	33.13	42.51	64.8	5.2	24.8
C18:2	53.53	21.07	9.8	37.51	15.47	31.72	27.93	9.1	86.5	2.9
C18:3	7.02	6.95	0.09	7.02	3.08	3.58	4.66	9.0	6.2	61.2
C20	0.38	0.6	0.36	0.46	0.49	0.39	0.45	0	0	0
C20:1	0.23	1.35	0.15	0.68	0.67	0.2	0.52	0	0	0
C22	0.8	0.35	0.09	0.46	0.24	0.32	0.33	0	0	0
C22:1	0.24	0.19	0	0.12	0.09	0.12	0.14	0	0	0
C24	0	0.22	0.15	0	0	0.63	0.53	0	0	0
DU	144.6	120.0	62.0	131.8	91.0	104.2	108.5	105.1	190.6	153.0
$\rho_{m,GVOL}^{298}$	3.0037	2.9721	3.0652	2.9929	3.0198	3.0277	3.0114	3.0127	3.0044	3.0325
M	292.77	295.08	284.32	293.43	289.49	289.20	290.86	290.79	294.1	291.97
T_{\min}	283.15	283.15	283.15	283.15	283.15	283.15	283.15	293.15	293.15	293.15
T_{\max}	333.15	333.15	333.15	333.15	333.15	333.15	333.15	373.15	373.15	373.15
p_{\min}	0.1	0.1	0.1	0.1	0.1	0.1	0.1	0.1	0.1	0.1
p_{\max}	45.0	45.0	45.0	45.0	45.0	45.0	45.0	34.5	34.5	34.5
ρ_{\min}	857.1	855.2	848.2	854.9	849.7	850.8	851.6	820.8	833.1	838.2
ρ_{\max}	916.0	913.8	907.4	913.6	909.1	909.9	911.0	897.7	909.6	914.9
EoS	Tait	TVG	TVG	TVG						

Continued									
FAME	N8	N9	N17	N19	N20	N21	N23	CSB	SCHB
C10	0	0	0	0	0	0	0	0	0
C12	0	0	0	0.1	0	0	0.1	0	0
C14	0	0	0	1.5	0	0.1	3.4	0.93	0.5
C16	38.6	20.9	15.2	25.5	4.0	11.0	26.3	26.76	7.9
C16:1	0	0	0	3.2	0.2	0.1	3.5	0	0.2
C17:0	0	0	0	0.5	0	0	1.6	0	0
C18	44.1	28.2	5.3	12.6	1.9	4.0	22.3	2.81	2.2
C18:1	4.8	15.3	57	46.3	65.4	23.4	39.9	17.89	58.6
C18:2	2.4	7.7	22.5	10.2	19.1	53.2	2.3	51.61	20.6
C18:3	10.1	28.0	0	0.1	9.4	7.8	0.6	0	8.1
C20	0	0	0	0	0	0	0	0	0.5
C20:1	0	0	0	0	0	0	0	0	1.1
C22	0	0	0	0	0	0	0	0	0.1
C22:1	0	0	0	0	0	0	0	0	0.1
C24	0	0	0	0	0	0	0	0	0.1
<i>DU</i>	29.8	86.7	102.0	70.1	122.6	145.5	49.2	121.1	117.4
$\rho_{m,GVOL}^{298}$	3.0372	3.0218	2.9973	3.0346	2.9789	3.0124	3.0422	3.0494	2.9854
<i>M</i>	286.26	289.95	291.88	287.39	294.57	291.99	286.09	287.53	293.75
<i>T</i> _{min}	313.15	293.15	293.15	293.15	293.15	293.15	293.15	288.15	288.12
<i>T</i> _{max}	373.15	373.15	373.15	373.15	373.15	373.15	373.15	358.15	396.76
<i>p</i> _{min}	0.1	0.1	0.1	0.1	0.1	0.1	0.1	0.1	0.4
<i>p</i> _{max}	34.5	34.5	34.5	34.5	34.5	34.5	34.5	30.0	129.8
ρ _{min}	821.4	827.8	827.8	817.4	820.6	824.9	813.2	837.2	802.9
ρ _{max}	884.8	903.5	902.9	893.5	898.6	900.5	890.0	899.7	938.5
EoS	TVG	-	-						

Compositions of the biodiesels studied, in mass percentage; Biofuels by letters refer to Pratas et al. [19] (S=methyl soy, R=methyl rapeseed, P=methyl palm, SR=soy+rapeseed; PR=palm+rapeseed, SP=soybean+palm, SRP=soy+rapeseed+palm); N(number) refers to the biodiesels studied by Tat and Van Gerpen [20, 21] (N5=methyl oleate, N6=methyl linoleate, N7=methyl linolenate, N8=2:1 methyl stearate/methyl linseed, N9= 2:1 methyl linseed/methyl stearate, N17=Oxidized methyl soy, N19= methyl lard, N20=methyl canola, N21=methyl soy, N23=methyl tallow); CSB is the cottonseed fuel produced in this work; SCHB is the biodiesel specimen studied by Schedemann et al. [27]. $\rho_{m,GVOL}^{298}$ /(mol·dm⁻³); *M*/(g·mol⁻¹); *T*/K; *p*/MPa; ρ /(kg·m⁻³). TVG: Empirical EoS by Tat and Van Gerpen [21].

From Table 3.2 the degree of unsaturation of N23 and N7 biodiesels were 49 and 153, respectively. The set encompassing the biodiesels presented by Pratas et al. [19], the cottonseed biodiesel and the fuel measured by Schedemann et al. [27] showed intermediate behaviour in density as function of temperature compared with N7 and N23 biodiesels (see Figure 3.2). All the fuels in that set, presented lower contents in C18:3 than N7 biodiesel and the C18:3 content ranges from a minimum of 0.09% (P fuel, $DU = 62.0$) to a maximum of 8.0% (SCHB fuel, $DU = 117.4$). The cottonseed biodiesel showed a density value well in the middle of the (temperature, density) plot (Figure 3.2), corresponding to an intermediate DU . The degree of unsaturation is strongly dependent on the C18:2 and C18:3 contents, which have a great influence in the density, and therefore it is expected that DU might be important in density calculations. For this reason this parameter was used to develop a predictive model of density.

3.1.4 Results and discussion

3.1.4.1 Density of cottonseed biodiesel

Cottonseed biodiesel pVT data measured in this work is reported in Table 3.3 for temperatures between 288.15 K and 358.15 K and pressures between 0.1 MPa and 30.0 MPa. The experimental data showed that biodiesel density behaved as expected, meaning that density decreases as temperature increases and pressure drops. The density at 288.15 K and atmospheric pressure is $884.1 \text{ kg}\cdot\text{m}^{-3}$ and, thus it is well within the limits between 860 and $900 \text{ kg}\cdot\text{m}^{-3}$ required by the EN 14214 standard [48].

Table 3.3. Experimental values of density data (ρ), for cottonseed biodiesel as a function of temperature (T), and pressure (p).

p^c /MPa	ρ^a / ($\text{kg}\cdot\text{m}^{-3}$) at T^b / K							
	288.15	298.15	308.15	318.15	328.15	338.15	348.15	358.15
0.1	884.1	877.6	871.1	864.4	857.7	851.0	844.1	837.2
1.0	884.6	878.2	871.6	865.0	858.3	851.6	844.8	837.9
2.0	885.1	878.7	872.2	865.7	859.0	852.3	845.5	838.7
3.0	885.7	879.3	872.9	866.3	859.7	853.1	846.3	839.5
4.0	886.2	879.9	873.5	867.0	860.4	853.8	847.0	840.3
5.0	887.3	880.9	874.5	867.9	861.3	854.6	847.9	841.0
6.0	887.4	881.1	874.7	868.3	861.8	855.2	848.6	841.8
7.0	887.9	881.7	875.3	868.9	862.5	855.9	849.3	841.8
8.0	888.5	882.3	876.0	869.6	863.1	856.6	850.0	842.6
9.0	889.0	882.8	876.5	870.2	863.8	857.3	850.7	843.4
10.0	889.6	883.4	877.1	870.8	864.4	858.0	851.4	844.1
15.0	892.2	886.1	880.0	873.9	867.6	861.3	854.9	848.4
20.0	894.8	888.9	882.9	876.8	870.7	864.5	858.2	851.8
25.0	897.2	891.4	885.6	879.6	873.6	867.5	861.4	855.2
30.0	899.7	894.0	888.3	882.4	876.5	870.5	864.4	858.3

^a $U(\rho) < 1.6 \text{ kg}\cdot\text{m}^{-3}$; ^b $u(T) = 0.02 \text{ K}$; ^c $u(p) = 0.02 \text{ MPa}$.

Comparing the density of CSB with those from other fuel in the database, it was interesting to note that N21 had comparable values in the same temperature and pressure ranges. This was very likely due to the similar content in C18:2, which is known to have an important contribution in density. The density measurements of CSB were comparable with those presented by Nogueira et al. [40], whose measurements were made at (293.15, 313.15, 333.15, 353.15, and 373.15) K, and the ones presented by Alptekin and Canakci [8] at 288.15 K, all data at atmospheric pressure (see Figure 3.3). Taking linear representations of density data on the temperature obtained for the present work and data presented by Nogueira et al. [40], calculated deviations were between 0.1% and -0.4%. No explanation was found for the differences between our values and those presented by Nogueira et al. since the measurement techniques were similar and the FAMES profile of the samples were almost the same, resulting in comparable molar mass (CSB: $M = 287.53$, Nogueira et al.: $M = 288.33$) and degrees of unsaturation (CSB: $DU = 121.1$, Nogueira et al.: $DU = 129.7$).

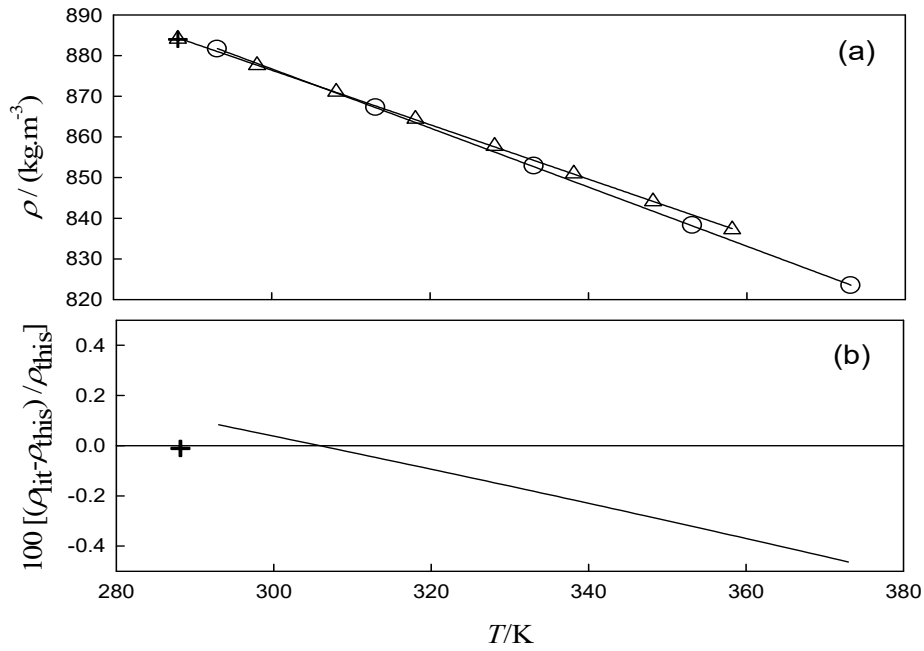


Figure 3.3. Comparison between the densities of this work with values from the literature. (a) Δ , this work; \circ , Nogueira et al. [40]; $+$, Alptekin and Canakci [8]. (b) Deviations between the densities of this work (ρ_{this}) with values from the literature (ρ_{lit}). The line shows the deviations from density of Nogueira et al. [40] taking linear representations of data.

3.1.4.2 Density correlation

In the present work the GMA EoS was used to correlate density with temperature and pressure of cottonseed and all the other biodiesels in the database built for this work. The GMA EoS is conveniently given by [39]:

$$(2z - 1)V_m^3 = A(T) + B(T)\rho_m \quad \text{Eq. 3-2}$$

where z , V_m , and ρ_m are the compressibility factor, molar volume, and molar density, respectively. The temperature dependent parameters $A(T)$ and $B(T)$ are given by the following equations [39]:

$$A(T) = A_0 - \frac{2A_1}{RT} + \frac{2A_2 \ln T}{R} \quad \text{Eq. 3-3}$$

$$B(T) = B_0 - \frac{2B_1}{RT} + \frac{2B_2 \ln T}{R} \quad \text{Eq. 3-4}$$

where A_0 - A_2 and B_0 - B_2 are the fitting parameters, and R is the gas constant. Density at different temperatures and pressures was calculated from:

$$B(T)\rho_m^5 + A(T)\rho_m^4 + \rho_m - 2p/RT = 0 \quad \text{Eq. 3-5}$$

The coefficients A_0 - A_2 and B_0 - B_2 of the GMA EoS regressed by fitting Eqs. 3-2 to 3-4, to the pVT data through least-squares method with confidence limits of 95% are given in Table 3.4. Standard deviation, σ , correlation coefficient r , number of data points N_p , are also indicated. The average absolute relative deviation, $AARD$, and the standard deviation for density, σ_ρ , calculated respectively by:

$$AARD\% = 100 \sum_{i=1}^{N_p} |1 - \rho_{calc}/\rho_{exp}|_i / N_p \quad \text{Eq. 3-6}$$

$$\sigma_\rho = \left[\sum_{i=1}^{N_p} (\rho_{cal} - \rho_{exp})_i^2 / (N_p - k) \right]^{1/2} \quad \text{Eq. 3-7}$$

are also presented in Table 3.4. In Eqs. 3-6 and 3-7, ρ_{cal} and ρ_{exp} are the densities calculated from Eq. 3-5 and those experimentally determined for the measurement i , respectively, and $k = 6$ is the number of adjusted parameters. The statistical indicators allowed to conclude that GMA EoS gives an excellent pVT data correlation for biodiesels, since the standard deviation in density is generally less than $0.2 \text{ kg}\cdot\text{m}^{-3}$ and the $AARD$ is less than 0.02%.

Table 3.4. Fitting parameters of GMA EoS applied to the correlation of experimental *PVT* data of biodiesel fuels with 95% confidence limits. The standard deviation (σ), correlation coefficient (r) and number of data points (N_p) are given. Also are referred the standard deviation in density (σ_ρ) and the average absolute relative deviation in density (*AARD*).

Parameter	R	P	S	SR	PR	SP	SRP	N5
A_0^a	156.6408	155.02365	-191.31330	-203.12707	-19.90696	88.19071	-76.56096	-11.65220
A_1^b	57.4777	54.62277	-9.48038	-10.92667	21.34827	43.52531	12.35306	23.78009
A_2^c	-0.0916	-0.090737	0.1232171	0.1308369	0.0167058	-0.0490859	0.0525300	0.0121614
B_0^d	-49.4897	-44.08269	69.27326	74.10448	12.63065	-22.26999	32.08480	10.02161
B_1^e	-17.4004	-15.45037	5.47409	6.09774	-4.71302	-11.88194	-1.60108	-5.56848
B_2^f	2.9599×10^{-2}	2.6243×10^{-2}	-4.3751×10^{-2}	-4.6842×10^{-2}	-8.56398×10^{-3}	1.2664×10^{-2}	-2.0847×10^{-2}	-7.164697×10^{-3}
σ^g	0.001653	0.000960	0.001426	0.001633	0.000928	0.000918	0.002572	0.001888
σ_ρ^h	0.09	0.06	0.13	0.14	0.06	0.06	0.15	0.14
r	0.9993	1.0000	0.9999	0.9999	1.0000	1.0000	0.9997	0.9999
N_p	84	84	84	84	84	84	84	30
<i>AARD</i> %	0.008	0.006	0.013	0.013	0.005	0.005	0.010	0.012
Parameter	N6	N7	N8	N9	N17	N19	N20	N21
A_0	130.32820	-28.91800	117.74356	230.08141	-365.23193	146.2366	-12.2901	168.1241
A_1	51.95599	19.70029	49.70914	74.50985	-45.43698	54.5771	25.0475	60.8676
A_2	-0.074832	0.0226279	-0.0664370	-0.1343981	0.2292324	-0.0846	0.0128	-0.0974
B_0	-35.802429	18.70439	-29.83708	-65.78690	136.99403	-39.8071	10.7011	-49.1615
B_1	-14.65893	-3.54271	-13.51784	-21.47494	19.30164	-15.2526	-5.9416	-17.7889
B_2	0.0209081	-0.012448	0.017005	0.038765	-0.085119	0.023366	$-7.6505e^{-3}$	0.028891
σ	0.001772	0.002621	0.002117	0.002045	0.005443	0.001481	0.001989	0.001553
σ_ρ^h	0.14	0.22	0.16	0.14	0.39	0.12	0.73	0.11
r	0.9999	0.9995	0.9997	0.9998	0.9989	0.9999	0.9999	0.9999
N_p	30	30	24	30	30	30	30	30
<i>AARD</i> %	0.011	0.018	0.014	0.012	0.032	0.010	0.064	0.009

Continued

Parameter	N23	CSB	SCHB
A_0	112.1672	93.75307	31.96439
A_1	47.5108	45.51811	34.23931
A_2	-0.0637	-0.05195	-0.014476
B_0	-28.5269	-25.7089	-4.14103
B_1	-12.9304	-12.9335	-8.94477
B_2	0.016435	0.014473	0.0015429
σ	0.003008	0.001458	0.005861
σ_ρ^h	0.22	0.10	0.37
r	0.9997	0.9998	0.9998
N_p	30	120	324
AARD %	0.018	0.007	0.033

^a $A_0/(\text{dm}^9 \cdot \text{mol}^{-3})$; ^b $A_1/(\text{MPa} \cdot \text{dm}^{12} \cdot \text{mol}^{-4})$; ^c $A_2/(\text{MPa} \cdot \text{dm}^{12} \cdot \text{mol}^{-4} \cdot \text{K}^{-1})$; ^d $B_0/(\text{dm}^{12} \cdot \text{mol}^{-4})$; ^e $B_1/(\text{MPa} \cdot \text{dm}^{15} \cdot \text{mol}^{-5})$; ^f $B_2/(\text{MPa} \cdot \text{dm}^{15} \cdot \text{mol}^{-5} \cdot \text{K}^{-1})$; ^g $\sigma/(\text{dm}^9 \cdot \text{mol}^{-3})$; ^h $\sigma_\rho / (\text{kg} \cdot \text{m}^{-3})$;

Under isothermal conditions, the quantity $(2z - 1)V_m^3$ showed a linear behaviour with the molar density. The isotherms of $(2z - 1)V_m^3$ versus molar density are presented in Figure 3.4 for cottonseed and Schedemann et al. [27] biodiesels selected from the database, having in consideration the differences in temperature and pressure ranges at which density measurements were made. The linearity held well for all isotherms and was slightly improved when shorter temperature and pressure ranges were considered, like in the cottonseed case. Good results were also obtained for the other biodiesels from the database. The linearity seems to be very important for safe extrapolation of density at high temperatures and pressures.

Proceeding with the evaluation of the GMA EoS capacity to correlate the density data for all temperatures and pressures, the relative deviations between experimental and calculated values with Eq. 3-2 were evaluated. In Figure 3.5, the relative deviation as a function of temperature and pressure is shown for cottonseed and Schedemann biodiesels. Due to more restricted temperature and pressure ranges of the fitting for cottonseed biodiesel the relative deviations were very small, usually in the range $\pm 0.02\%$ (less than $\pm 0.2 \text{ kg}\cdot\text{m}^{-3}$), while for the biofuel measured by Schedemann et al. [27] the deviations were usually less than $\pm 0.05\%$ (less than $\pm 0.5 \text{ kg}\cdot\text{m}^{-3}$). For the other biodiesels in the database the deviations were in the same range as found for cottonseed biodiesel. The relative deviations in density resulting from correlation with the GMA EoS for all the biodiesels in the database at considered temperatures and pressures are given as supplementary material of the published paper relative to cottonseed biodiesel [55].

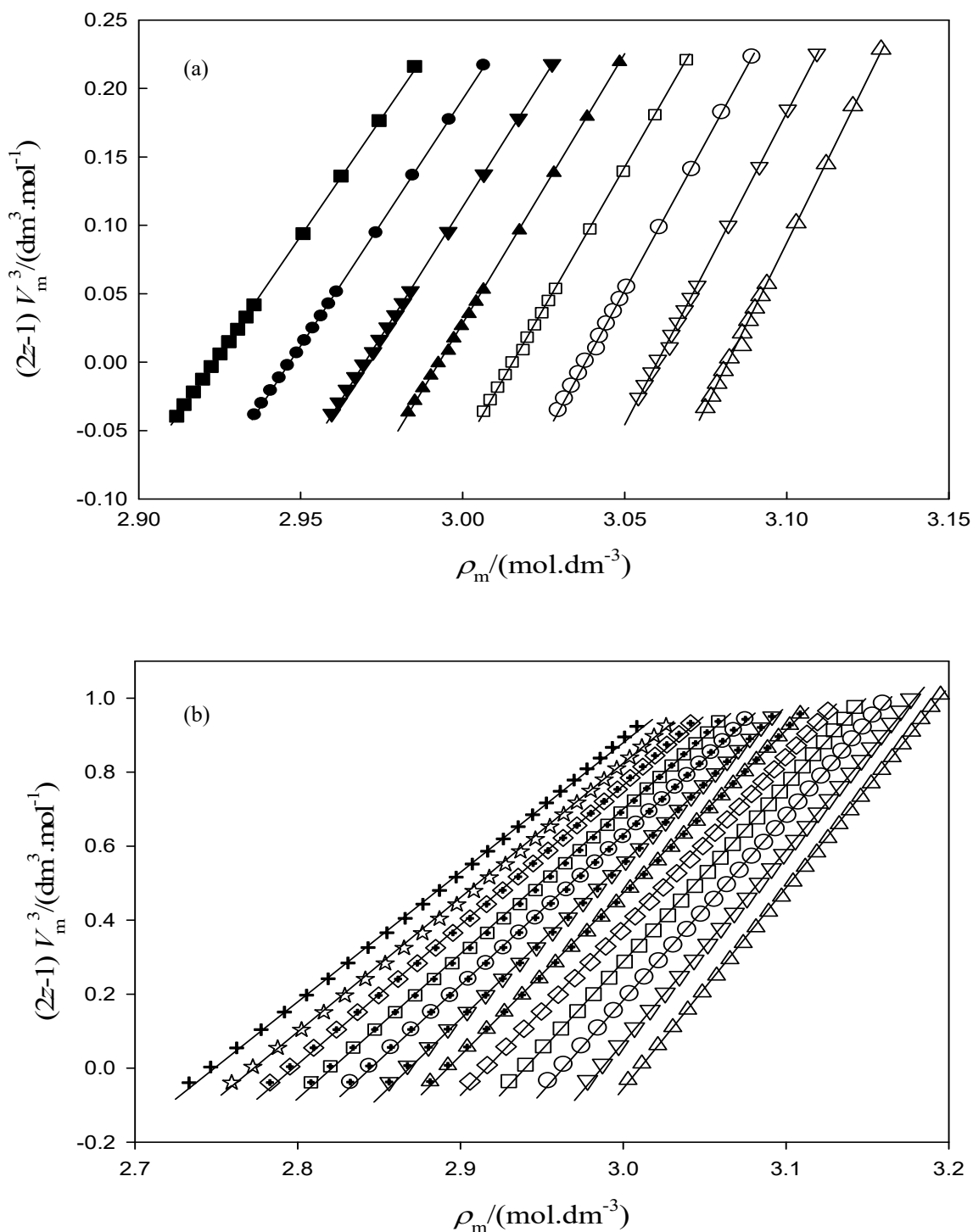


Figure 3.4. Isotherms of $(2z-1)V_m^3$ versus the molar density (ρ_m) for cottonseed and Shedmann (SCHB) biodiesels calculated from GMA EoS. (a) CSB (experimental data of this work): Δ , 288.15 K; ∇ , 298.15K; \circ , 308.15 K; \square , 318.15 K; \blacktriangle , 328.15 K; \blacktriangledown , 338.15 K; \bullet , 348.15 K; \blacksquare , 358.15 K (b) SCHB: Δ , 288.12 K; ∇ , 297.93 K; \circ , 307.8 K; \square , 317.6 K; \diamond , 327.49 K; \blacktriangle , 337.38 K; \blacktriangledown , 347.26 K; \oplus , 357.13 K; \boxplus , 367.03 K; \diamond , 376.91; \star , 386.84 K; $+$, 396.76 K. Full curves calculated from correlation with GMA EoS.

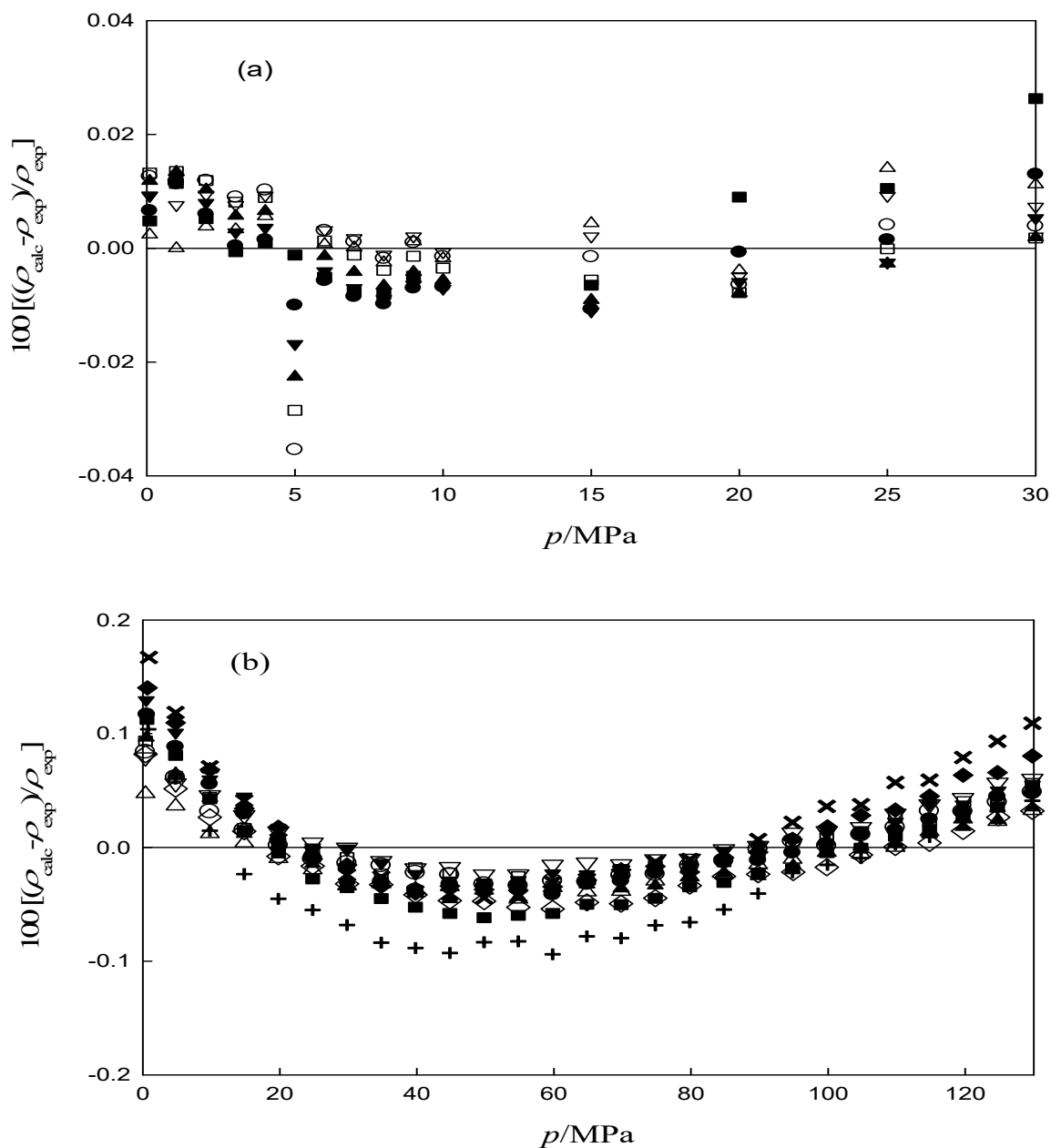


Figure 3.5. Relative density deviations between the calculated values with GMA EoS (ρ_{cal}) and the experimental one (ρ_{exp}). (a) CSB: Δ , 288.15 K; ∇ , 298.15K; \circ , 308.15 K; \square , 318.15 K; \blacktriangle , 328.15 K; \blacktriangledown , 338.15 K; \bullet , 348.15 K; \blacksquare , 358.15 K; (b) SCHB: Δ , 288.12 K; ∇ , 297.93K; \circ , 307.8 K; \square , 317.6 K; \diamond , 327.49 K; \blacktriangle , 337.38 K; \blacktriangledown , 347.26 K; \bullet , 357.13 K; \blacksquare , 367.03 K; \blacklozenge , 376.91 K; $+$, 386.84 K; \times , 396.76 K.

3.1.4.3 Density prediction

3.1.4.3.1 The group contribution methods (GCVOL)

A group contribution method (GCVOL) for the prediction of liquid densities as a function of temperature from the triple point to the normal boiling point was presented by Elbro et al. [49]. In that method (original GCVOL) the molar volume was calculated by:

$$V_m = \sum_i n_i \Delta v_i \quad \text{Eq. 3-8}$$

where n_i is the number of group i in the substance and Δv_i is a temperature dependent group molar volume given by

$$\Delta v_i = A_i + B_i T + C_i T^2 \quad \text{Eq. 3-9}$$

where the group volume parameters A_i , B_i , and C_i were obtained by Elbro et al. [49], whose original model presented 36 different group parameters for a large variety of chemical substances including alkanes, alkenes, aromatic, alcohols, ketones, aldehydes, esters, ethers, chlorides, and siloxanes. The densities for strongly polar solvents were predicted by this method with an average relative deviation of 1% approximately.

In 2003, Ihmels and Gmehling [50] added 24 new groups to the 36 existing ones using the Dortmund Data Bank for Pure Component Properties (DDB-Pure). With this extension (extended GCVOL) densities of tertiary alcohols, alkynes, carboxylic acids, allenes, cycloalkanes, fluorides, bromides, iodides, thiols, sulfides, sulfates, amines, nitriles, and nitro compounds were calculated with an average mean deviation of 1.5% for a database of 1040 compounds. Pratas et al. [51, 52] applied the original CGVOL to density prediction of pure FAMES present in biodiesel in greater content, and those existing in minority. They concluded that for the majority FAMES the density can be predicted within an *AARD* of 0.5%, except for the methyl linoleate since the model describes poorly the effect of unsaturation on density. For the case of minority FAMES and FAEEs the density could be predicted within a deviation of 1.5%, except for the linolenate esters at high temperatures, again due to the poor description of the polyunsaturation effect on densities. Pratas et al. [36] also applied the original and the extended GCVOL models to 18 biodiesel samples of soy, rapeseed, palm, cottonseed, jatropha, and mixtures thereof at temperatures

between 273.15 and 373.15 K and densities from 815 to 898 kg·m⁻³, and obtained overall *AARDs* of 0.6% and 2.7% for the original and the extended GCVOL, respectively. To solve the precision lack for the polyunsaturation ester effect, Pratas et al. [36] found new parameter values A_i , B_i , and C_i relative to the double bond (–CH=) contribution, based on density data measured for FAMES [51, 52]. This revised variant of GCVOL was applied to the 18 biodiesels leading to a decrease in the overall *AARDs* to 0.25% in density, corresponding to ≈ 2 kg·m⁻³ [36]. Pratas et al. extended the revised GCVOL to high pressures using the equation [36],

$$\rho(T, p) = \frac{M}{V_m(T)(1+Ap)} \quad \text{Eq. 3-10}$$

where ρ is the density in g·cm⁻³, M is the molar mass in g·mol⁻¹, $V_m(T)$ is the molar volume in cm³·mol⁻¹ predicted by revised GCVOL, and p is the absolute pressure (MPa). For biodiesel the mean molar mass is:

$$M = \sum_i x_i M_i \quad \text{Eq. 3-11}$$

where x_i and M_i are the molar fraction and the molar mass of FAME i in the fuel, respectively. Pratas et al. obtained $A = -5.7 \times 10^{-4}$ MPa⁻¹ [36] by fitting Eq. 3-10 to high pressure densities for laurate, myristate, and oleate methyl esters, reported by Pratas et al. [51, 52]. The Eq. 3-10 correlates the high pressure densities of these methyl esters with an *AARD* of 0.3% and the high pressure densities for 8 biodiesel fuels were predicted with *AARDs* from 0.23 to 0.74% [36]. We have recalculated the constant A in Eq. 3-10 by fitting to the densities of methyl palmitate [53], methyl oleate [19, 54], and methyl linoleate [27, 54], since they are the most abundant FAMES in the biodiesels. The fitting of Eq. 3-10 gives $A = (-5.46 \times 10^{-4} \pm 4.35 \times 10^{-6})$ MPa⁻¹ with standard deviation of 5.0 kg·m⁻³ and *AARD* = 0.43%. The *AARDs* resulting from application of Eq. 3-10 to the prediction of high-pressure densities for the nineteen biodiesels in the database are given in Table 3.8. Some of the biodiesels measured by Tat and Van Gerpen as N7, N8, N9, N17 showed *AARDs* higher than 1%. These biodiesels could be considered as outliers from the point of view of the dominant FAMES profile, since N7 had a very high C18:3 content, N8 and N9 showed high values of C18:0, and N17 presented a very high content of C18:1. A huge advantage of this method is its simplicity and straightforward density estimation. The detailed information about

the deviations in density resulting from Eq. 3-10 applied to all the biodiesels in the database is given in supplementary material of the published paper relative to this chapter [55].

3.1.4.4 Degree of unsaturation

The density data for several biodiesels measured by Pratas et al. [19] and by Tat and Van Gerpen [20, 21] are represented as a function of the degree of unsaturation at 293.15 K, and 353.15 K and atmospheric pressure in Figure 3.6.

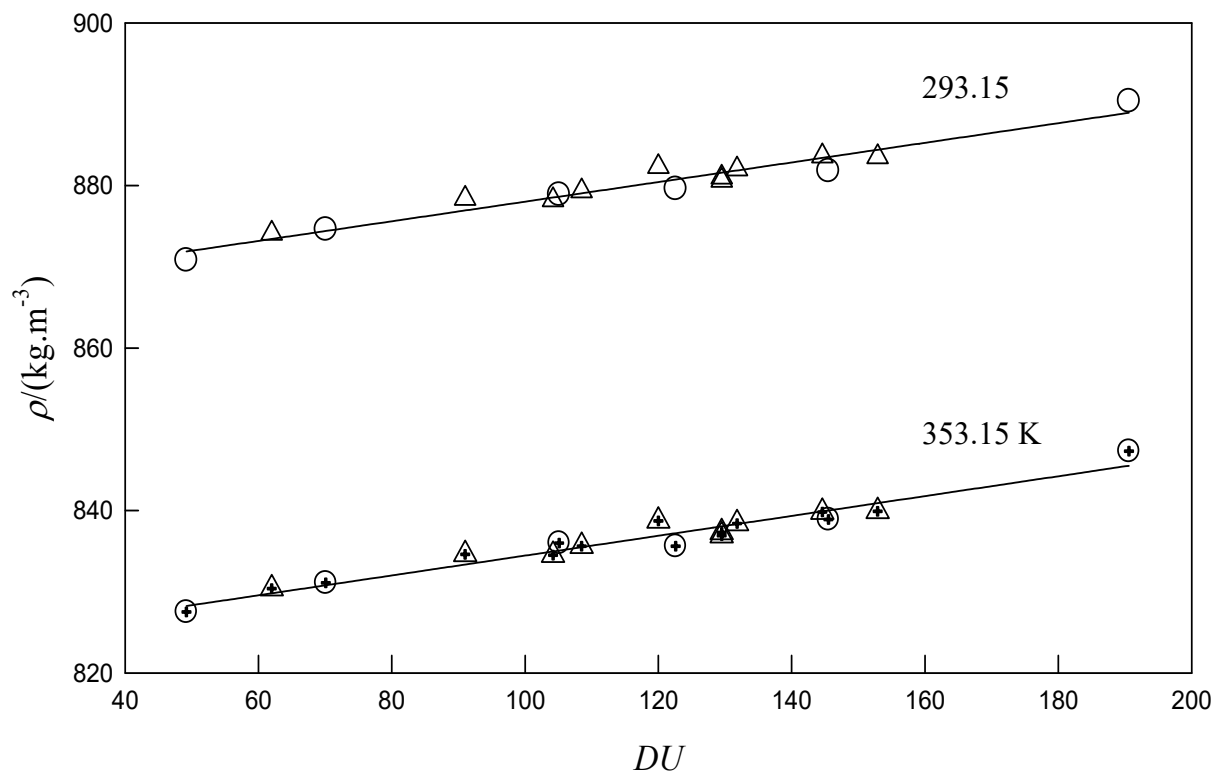


Figure 3.6. Density as function of the degree of unsaturation (DU) for some biodiesels in the database. At 293K and 0.1 MPa: Δ , [19]; \circ , [20, 21]; at 353 K and 0.1 MPa: \triangle , [19], \oplus , [20, 21].

Clearly, for each temperature the density was a linear function of the DU . For this reason and taking into account that density is a linear function of temperature with a slight curvature at high pressures [23, 27], the equation:

$$\rho = (d_1 + d_2T + d_3p + d_4p^2) + (d_5 + d_6T + d_7p + d_8p^2)DU \quad \text{Eq. 3-12}$$

is proposed to represent the biodiesel density within wide ranges of temperatures and pressures.

The biodiesels (S,R,P) reported by Pratas et al. [19] and (N6,N20,N23) studied by Tat and Van Gerpen [20, 21] were used as the training set to fitting of Eq. 3-12 and the other thirteen biodiesels were included in the validation set. The training set was selected to fulfil the following: (i) biodiesels having a linear dependence on DU ; (ii) biodiesels covering a wide range of DU (the range of DU is between 49.2 (N23) to 190.6 (N6)); (iii) biodiesels from different authors should spread in wide ranges of density. The parameters of Eq. 3-12 for 95% confidence limits were $d_1=(1088.017\pm 3.359)$, $d_2=(-0.74348\pm 0.01054)$, $d_3=(0.50665\pm 0.06776)$, $d_4=(1.6074\times 10^{-3}\pm 1.6572\times 10^{-3})$, $d_5=(0.02599\pm 0.02719)$, $d_6=(2.7723\times 10^{-4}\pm 8.485\times 10^{-5})$, $d_7=(8.8455\times 10^{-4}\pm 5.6863\times 10^{-3})$, $d_8=(-2.1255\times 10^{-5}\pm 1.4024\times 10^{-5})$, with correlation coefficient and standard deviation of 0.996 and $1.7 \text{ kg}\cdot\text{m}^{-3}$, respectively. Eq. 3-12 gives $OARD$ of 0.19% for the training set and 0.36% for the validation set. Detailed results for density calculations of all the biodiesels are presented in Table 3.8. The minimum ($AARD = 0.09\%$) and the maximum ($AARD = 1.10\%$) deviations in the validation set were observed for SR and N7 biodiesels, respectively. The overall average relative deviation of 0.36% corresponding to less than $4\text{kg}\cdot\text{m}^{-3}$ can be regarded as a good indicator for the density prediction. Eq. 3-12 gives better density predictions than more complex methods including those based in SAFT or CPA equations of state. The $AARD = 0.36\%$ obtained for the validation set was close to the value 0.49% reported by Oliveira et al. [34] with soft-SAFT EoS applied to the density prediction of FAMEs and biodiesels measured by Pratas et al. [19]. Detailed information about deviations in density resulting from Eq. 3-12 applied to all the biodiesels in the database is given in supplementary material of the published paper [55].

3.1.4.5 Predictive GMA

Taking the advantage of the large ranges of temperature and pressure available for the density data of Schedemann (SCHB), it was evaluated the possibility of predicting plausible values for the density at temperatures and pressures significantly higher and out of the (T, p) ranges used in the fitting of the GMA EoS. As the biodiesel density measurements have usually been made for temperatures lower than 373.15 K and pressures up to 50 MPa, the GMA EoS was tested under

restrictive temperature and pressure ranges considering two approaches: (i) for $T = (288 \text{ to } 357)$ K and $p = (0.4 \text{ to } 5)$ MPa; (ii) $T = (288 \text{ to } 357)$ K and $p = (0.4 \text{ to } 50)$ MPa. The approach (i) was based on the fact that the density measurements in some studies just were evaluated up to 5 MPa [26]. It was concluded that approach (i) gave good predictions of density up to 40 MPa and temperatures up to 397 K. With procedure (ii) it should be possible to extend the good prediction of density to higher temperatures and pressures. The density deviations were only about 3 Kg.m^{-3} near the maximum temperature ($T = 397 \text{ K}$) and pressure ($p = 130 \text{ MPa}$) and the predictions were in excellent agreement with the experimental values up to 75 MPa even at 397 K (see Figure B.1). These results are certainly important for density prediction in fuel injection and combustion simulations for diesel engines operating at high pressure.

A new predictive method for the determination of biodiesel density as function of temperature and pressure was derived from GMA EoS using the following procedure. Starting with the fitted A_0 - A_2 and B_0 - B_2 parameters of biodiesel fuels studied by Pratas et al. [19] and by Tat and Van Gerpen [20, 21] listed in Table 3.4, it was found that the parameters A_i ($i=1,2$) and B_i ($i=0,2$) were linear functions in A_0 as displayed in Figure 3.7. Thus, once A_0 is known all the other parameters follow.

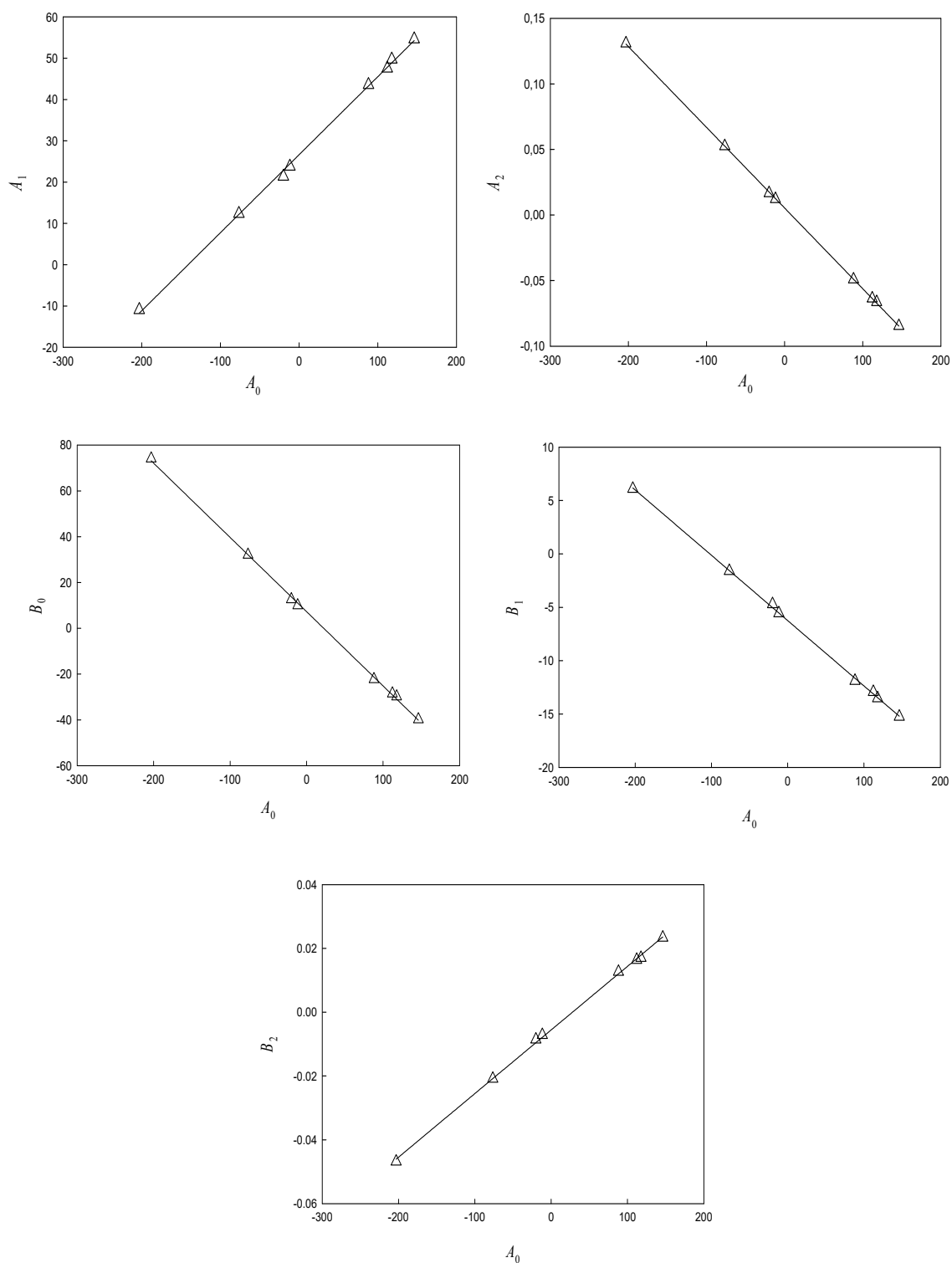


Figure 3.7. Correlation between coefficients A_1 , A_2 , B_0 , B_1 and B_2 of the GMA EoS vs. A_0 for biodiesels SR, SP, PR, SRP, N5, N8 N19, N23.

Next step, a correlation was established between A_0 and a fuel property of easy calculation, namely the molar density at 298.15 K obtained via GCVOL method, $\rho_{m,GVOL}^{298}$, calculated by:

$$\rho_{m,GVOL}^{298} = \frac{1}{V_{m,GVOL}^{298}} \quad \text{Eq. 3-13}$$

where $V_{m,GVOL}^{298}$ is the biodiesel molar volume calculated from the revised GCVOL from Eqs. 3-8 and 3-9. It was found that,

$$A_0 = A_{00} + A_{01}\rho_{m,GVOL}^{298} \quad \text{Eq. 3-14}$$

For the selected biodiesels, a distribution that follow four paths in the $(\rho_{m,GVOL}^{298}, A_0)$ plot was found, as displayed in Figure 3.8(a). It was also observed that three paths intercept close the SR biodiesel position in the diagram. The coefficients A_{00} , A_{01} and the corresponding correlation coefficients and standard deviations for the paths are presented in Table 3.5. As mentioned before, the parameters A_i ($i = 1, 2$) and B_i ($i = 0, 2$) are linear functions of A_0 . The linear plots for all paths are given in Figures B.2 to B.5. For each path j ($j = 1, 4$), the coefficients A_{ij} and B_{ij} are linearly correlated with A_{0j} through the Eq. 3-15

$$(A_{ij} \text{ or } B_{ij}) = a_{ij} + b_{ij}A_{0j} \quad \text{Eq. 3-15}$$

The intercepts a_{ij} and slopes b_{ij} , for each path are given in Table 3.6.

Table 3.5. Coefficients of Eq. 3-14 for the several predictive paths. The biodiesels used in each path are indicated for the paths.

Path	A_{00}	A_{01}	r	σ
1 (R, SR, N20)	50126.241± 8426.018	-16819.896± 2826.240	0.986	42.18
2 (S, SRP, N5, N9, N17, N21)	-74576.7736± 13663.295	24763.645± 4539.462	0.939	85.55
3 (SR, SP, PR, SRP, N5, N8, N19, N23)	-21247.607± 2458.569	7036.696± 813.476	0.962	35.23
4 (P, S, SR, N7)	-15644.7775± 1249.6898	5152.0630± 413.296	0.994	23.297

Table 3.6. Parameters a and b of each of coefficients $A_{1j}, A_{2j}, B_{0j}, B_{1j}, B_{2j}$ in Eq. 3-15 for path j .

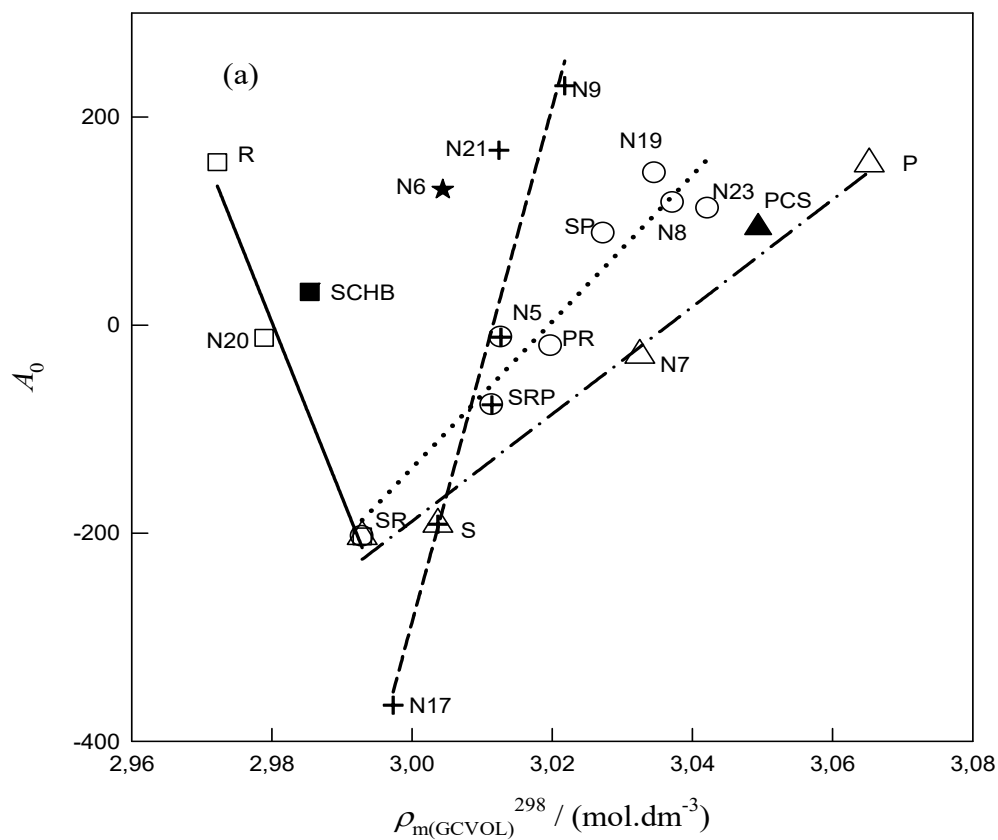
Parameter	$j = 1$	$j = 2$	$j = 3$	$j = 4$
A_{1j}				
a	27.5906	27.6408	26.6213	25.7892
b	0.1901	0.1998	0.1888	0.18351
σ	0.2534	1.0627	0.8551	0.7416
r	1.000	1.000	0.999	1.000
A_{2j}				
a	5.2303×10^{-3}	5.7578×10^{-3}	5.3296×10^{-3}	5.0017×10^{-3}
b	-6.1835×10^{-4}	-6.1173×10^{-4}	-6.1549×10^{-4}	-6.1840×10^{-4}
σ	8.916×10^{-6}	0.0005	0.0005	0.0003
r	1.000	1.000	1.000	1.000
B_{0j}				
$a/$	5.0461	8.3032	7.2557	7.5176
b	-0.3433	-0.3391	-0.3243	-0.32769
σ	1.7597	4.0022	0.9725	1.4906
r	1.000	0.999	1.000	1.000
B_{1j}				
a	-7.0268	-6.3924	-6.2496	-5.8746
b	-6.5267×10^{-2}	-6.7720×10^{-2}	-6.1213×10^{-2}	-5.9914×10^{-2}
σ	0.3469	0.7927	0.1855	0.4970
r	1.000	0.999	1.000	0.999
B_{2j}				
a	-4.1383×10^{-3}	-6.3474×10^{-3}	-5.5601×10^{-3}	-5.6124×10^{-3}
b	2.1232×10^{-4}	2.0743×10^{-4}	1.9945×10^{-4}	2.0255×10^{-4}
σ	0.0011	0.0025	0.0008	0.0009
r	1.000	0.999	1.000	1.000

It was also observed that biodiesel degree of unsaturation (DU) is related to the mean molar mass, and also three paths intercept close to SR position, as shown in Figure 3.8(b). The fuels in path 1 exhibited a linear (DU, M) behaviour, while the other paths were parabolic. The biodiesels that follows path 3, present considerable lower degree of unsaturation compared with those having the same molar mass, but follow path 4. In path 2, DU increases strongly with the molar mass in the small range considered for this property and the representative line for this path crosses paths 3 and 4. The fuels of path 2 have molar mass in the range $M = (289.95-292.77)$

$\text{g}\cdot\text{mol}^{-1}$ corresponding to an average of $291.37 \pm 1.02 \text{ g}\cdot\text{mol}^{-1}$. The corresponding degree of unsaturation as a function of molar mass is given by the general equation:

$$DU = d_0 + d_1M + d_2M^2 \quad \text{Eq. 3-16}$$

The parameters d_0 , d_1 , d_2 , the corresponding correlation coefficients and standard deviations for the paths 1-4 are given in Table 3.7.



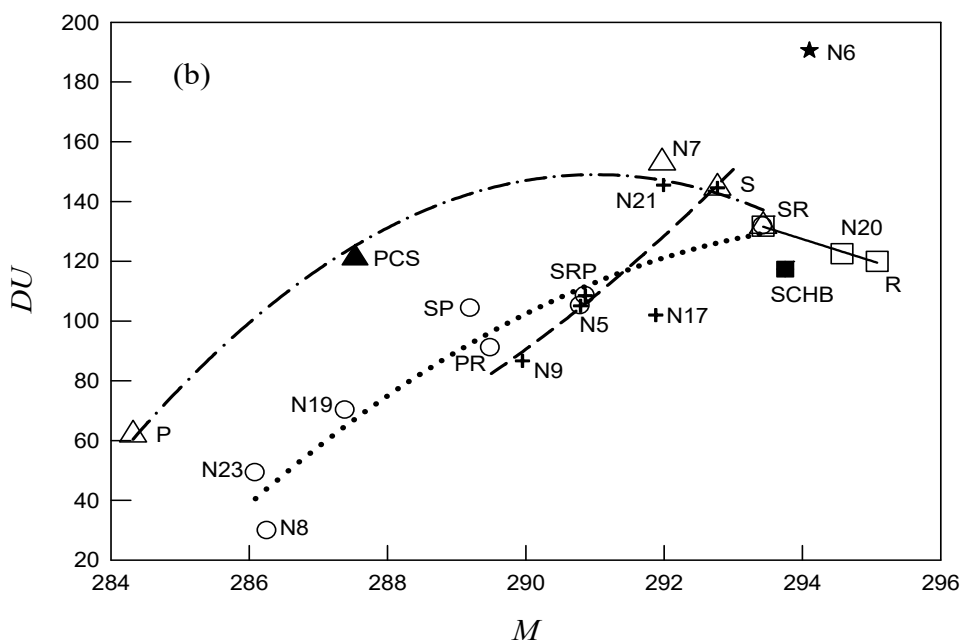


Figure 3.8. Relations for predictive 4PGMA EoS. (a) Coefficient A_0 as function of the molar density at 298 K from the revised GCVOL model ($\rho_{m,GVOL}^{298}$): \square , path1; $+$, path2; \circ , path 3; Δ , path4. The lines represent Eq. 3-14: (—) path 1; (---) path 2; (\cdots) path 3; (-·-·-) path 4. (b) Degree of unsaturation parameter (DU) as function of mean molar mass (M) for the biodiesels studied. Lines correspond to the fittings with Eq. 3-16. Lines and symbols as in (a).

The density prediction by GMA EoS considering the four paths (4PGMA) was made using the following criteria. From biodiesel composition, values of DU , M , and $\rho_{m,GVOL}^{298}$ were calculated using Eqs. 3-1, 3-11 and 3-13. If the molar mass was in the range of $291.37 \pm 1.02 \text{ g}\cdot\text{mol}^{-1}$ (path 2) or whether $2.970 < \rho_{m,GVOL}^{298} < 2.993$ (path 1), Eqs. 3-14 and 3-15 were used. When $\rho_{m,GVOL}^{298} > 2.993$, Eq. 3-16 was used to evaluate DU and this value was compared with the one from Eq. 3-1. Then, the selection between paths 3 and 4 was made following the lower difference in DU . For biodiesels with high degree of unsaturation ($DU > 150$, such as N6), path 2 should be used. Once the coefficients A_0 - A_2 and B_0 - B_2 were calculated using Eqs. 3-14 and 3-15, the density was obtained from Eq. 3-5.

Table 3.7. Coefficients of Eq. 3-16, corresponding to the calculation of degree of unsaturation as function of the molar mass for the paths in 4PGMA.

Path	d_0	d_1	d_2	r	σ
1 (R, SR, N20)	2275.27	-7.306	0	0.996	0.8
2 (S, SRP, N5, N9, N17, N21)	-85989.44	-609.23	1.0794	0.836	17.1
3 (SR, SP, PR, SRP, N5, N8, N19, N23)	-94629.5	641.76	-1.0865	0.968	10.2
4 (P, S, SR, N7)	-168458.48	1158.86	-1.9912	0.992	6.5

For predictive GMA the biodiesels (N6, CSB, SCHB) were chose as validation set, since these biodiesels were not used in the development of the predictive method. The other biodiesels in database were used to establish the linear correlation between coefficient A_0 and $\rho_{m,GCVOL}^{298}$ and linear correlations between (A_1, A_2) and (B_0-B_2) with A_0 . Nevertheless all the biodiesels from the database could be considered as belonging to the validation set of the predictive GMA because their densities were not used directly in the fittings. The 4PGMA results are presented in Table 3.8 and detailed information regarding the RDs in density, resulting from the predictive 4PGMA model, for all the biodiesels in database and for all the temperatures and pressures, are given as supplementary material [55]. With the exceptions of the biodiesels (N7, N8, N9) all $AARD$ values for the biodiesels were lower than 0.35% (less than $3\text{kg}\cdot\text{m}^{-3}$). The contour plots for the density differences as a function of temperature and pressure for the set (N6, CSB, SCHB) not included in 4PGMA development, are presented in Figure B.6. The N6 fuel, essentially C18:2 (0.865 by mass) with the higher degree of unsaturation ($DU=191$) presented the lower density deviations. However N6 has a composition far from that usually found in biodiesel. For CSB and SCHB biodiesels, the density deviations in predictions were low in the recommended (p, T) values for operation of injection systems ($T \approx 344\text{ K}$, $p = 12\text{-}22\text{ MPa}$) [1-3]. For CSB the predicted density at the recommended injection (p, T) conditions were practically the measured ones. The maximum $OARD$ of only 0.25% ($\approx 2\text{kg}\cdot\text{m}^{-3}$) obtained for path1 indicates that 4PGMA could provide excellent density predictions at high pressure. The pVT data presented by Schedemann in more extensive temperature and pressure ranges were predicted with $AARD = 0.34\%$. The 4PGMA provides much better predictions of density than SAFT and CPA equations of state requiring comparatively less computation effort.

Table 3.8. Average absolute relative deviation on density for the predictive methods applied to the biodiesels.

Biodiesel	Eq. 3-10 (GCVOL)	Eq. 3-12 (<i>DU</i>)	4PGMA EoS
			<i>AARD</i> (path)
S	0.55	(0.06) ^a	0.04(2); 0.03(4)
R	0.61	(0.13) ^a	0.19(1)
P	0.49	(0.13) ^a	0.21(4)
SR	0.44	0.09	0.16(1); 0.04(3); 0.18(4)
PR	0.34	0.12	0.02(3)
SP	0.32	0.16	0.03(3)
SRP	0.37	0.12	0.09(2); 0.02(3)
<i>AARD</i> ^b	0.45	0.12 ^c	0.18(1); 0.07(2), 0.03 (3); 0.14(4)
N5	0.39	0.21	0.26(2); 0.13(3)
N7	1.15	1.09	0.48(4)
N8	1.30	1.05	0.70(3)
N9	1.07	0.84	0.59(2)
N17	1.15	0.56	0.22(2)
N19	0.38	0.25	0.14(3)
N20	0.29	(0.36) ^a	0.31(1)
N21	0.34	0.36	0.31(2)
N23	0.32	(0.33) ^a	0.34(3)
<i>AARD</i> ^c	0.68	0.62 ^c	0.35(2); 0.33(3)
N6	0.80	(0.12) ^a	0.10(2)
CSB	0.50	0.16	0.17(4)
SCHB	0.67	0.50	0.34 (1)
<i>AARD</i> ^d	0.66	0.33 ^e	
<i>OARD</i> ^f	0.60	0.36 ^c	0.25(1); 0.23(2); 0.18(3); 0.21(4)

^a Biodiesels used in the training set;

^b Total *AARD* for the biodiesels from Pratas et al. [19];

^c Total *AARD* for the biodiesels from Tat and Van Gerpen [21];

^d Total *AARD* for the biodiesels N6 [20, 21], cottonseed, and SCHB [27]

^e *AARD* for the subsets from the validation set;

^f $OARD = \frac{\sum_i AARD_i}{i}$ $i = 19$ for Eq. 3-10; $i = 13$ for Eq. 3-12; $i = 4$ for path1; $i = 7$ for path 2; $i = 8$ for path 3; $i = 5$ for path 4.

3.1.5 Mechanical coefficients

The thermal expansivity, $\alpha_p = -(1/\rho)(\partial\rho/\partial T)_p$, and the isothermal compressibility, $k_T = (1/\rho)(\partial\rho/\partial p)_T$ can be calculated from the GMA EoS as [56]:

$$\alpha_p = \frac{(2B_1+2B_2T)\rho_m^5+(2A_1+2A_2T)\rho_m^4+2p}{5\rho_m^5(RT^2B_0-2B_1T+2B_2T^2 \ln T)+4\rho_m^4(RT^2A_0-2A_1T+2A_2T^2 \ln T)-RT^2\rho_m} \quad \text{Eq. 3-17}$$

$$k_T = \frac{2}{\rho_m RT+5\rho_m^5(RTB_0-2B_1+2B_2T \ln T)+4(RTA_0-2A_1+2AT \ln T)} \quad \text{Eq. 3-18}$$

The internal pressure $p_i = (\partial U/\partial V)_T$, where U is the internal energy, can be calculated according to the relationship

$$p_i = (\partial U/\partial V)_T = T(\partial p/\partial T)_V - p = T \cdot \gamma_V - p \quad \text{Eq. 3-19}$$

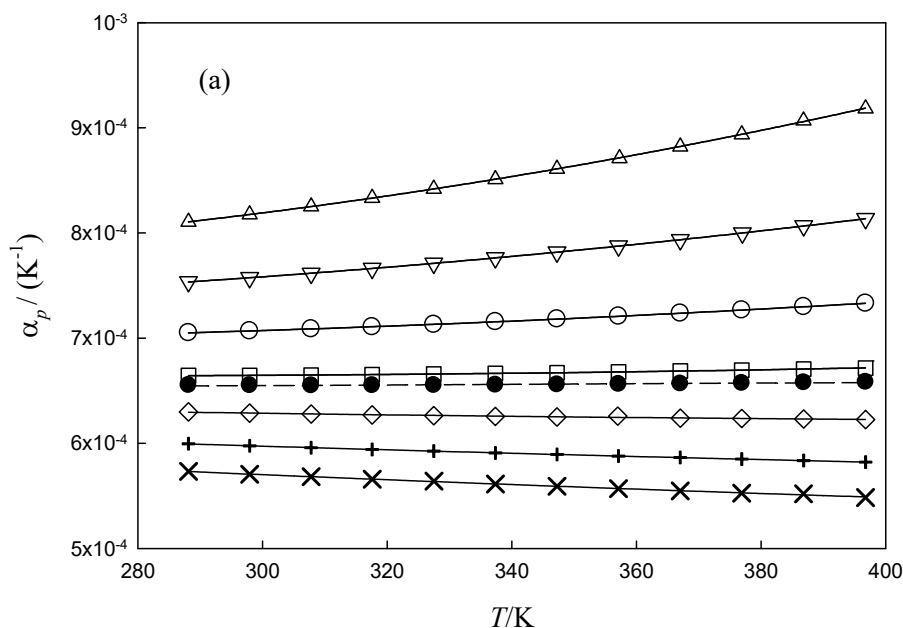
where γ_V is the thermal pressure coefficient $\gamma_V = \alpha_p/k_T$.

Based on the excellent results for the density description by the GMA EoS, the thermal expansivity, α_p , isothermal compressibility, k_T , and internal pressure p_i , were calculated from Eqs. 3-17 to 3-19 at temperatures from 283.15 K to 373.15 K and pressures between 0.1 MPa and 40 MPa using the coefficients presented in Table 3.4. The values of the mechanical coefficients for all biodiesels included in the database are given in Table B.1 and B.2.

Density variations along isothermic or isobaric paths are usually smooth functions of temperature and pressure. However, the mechanical coefficients are quite sensitive to subtle changes in the density. The pressure behaviour of α_p isotherms has been a matter of interest due to the characteristic crossings observed for this property at high pressure and reflects a change in the effective intermolecular potential with pressure [57]. As the density measurements by Schedemann et al. [27] were made up to 130 MPa, these data will be suited for the detailed study on the mechanical coefficients behaviour in extended ranges of pressure.

The dependences of the thermal expansivity on temperature along isobars, $(\alpha_p, T)_p$ and thermal expansivity on pressure along isotherms, $(\alpha_p, p)_T$, for the biodiesel studied by Schedemann et al. [27] are represented in Figure 3.9. The observed behaviour of α_p , as a function of pressure was consistent with the expected, i.e. it decreases with the increase in pressure at isothermal

conditions (see Figure 3.9(b)). The α_p isotherms show a clear intersection point nearly 65 MPa. This point obey the condition $(\partial\alpha_p/\partial T)_p = 0$, meaning that α_p was independent of temperature at that pressure. This can be observed in Figure 3.9(a) where α_p is represented as a function of temperature for isobaric conditions. At 64.8 MPa the thermal expansivity was almost independent of temperature with value $(6.562\pm 0.011)\times 10^{-4} \text{ K}^{-1}$. In the figure it is shown that for pressures lower than 65 MPa the thermal expansivity behaved normally, i.e. it increased as temperature rises at isobaric conditions, particularly at low pressures. However, a small decreasing of α_p with temperature was observed, for pressures higher than 65 MPa. The intersection of the α_p isotherms was observed for many liquids and was first described by Bridgman [58]. Some recent studies revealed that this behaviour seems to be a general property of liquids and that such intersection are common to occur usually at pressures below 200 MPa as indicated by the data collected by Taravillo et al. [59].



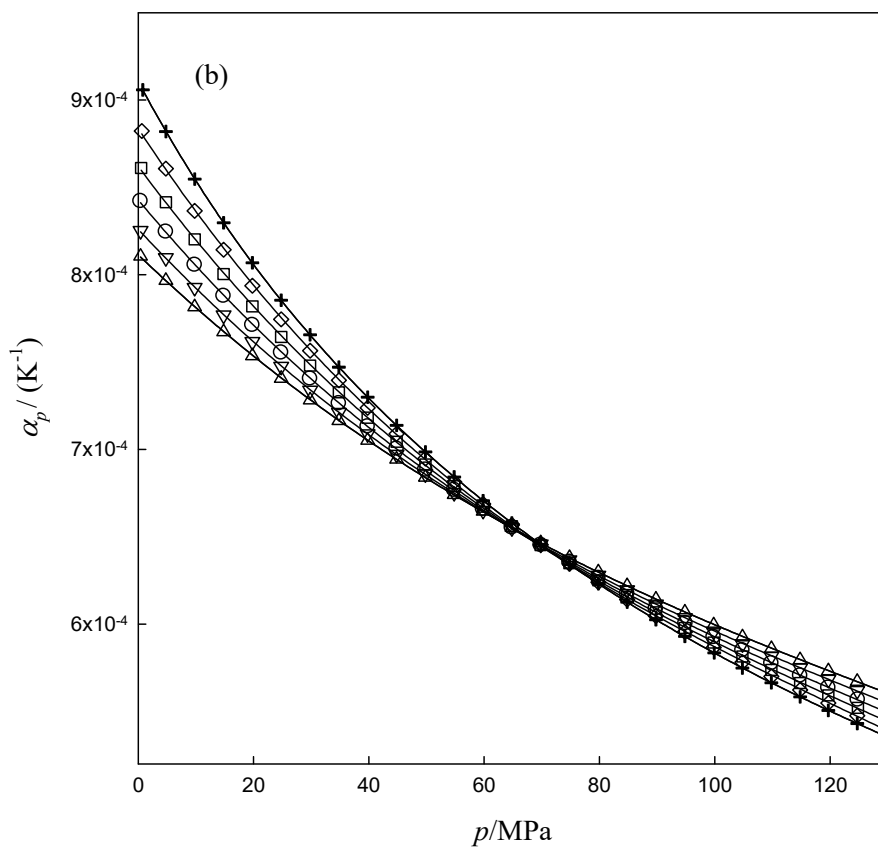


Figure 3.9. Thermal expansivity (α_p) for the SCHB calculated from GMA EoS. (a) α_p as function of temperature along isobars: Δ , 0.4 MPa; ∇ , 19.8 MPa; \circ , 39.8 MPa; \square , 59.8 MPa; \diamond , 79.8 MPa; $+$, 99.8 MPa; \times , 119.7 MPa. (b) α_p as a function of pressure along isotherms: Δ , 288.12 K; ∇ , 307.80 K; \circ , 327.49 K; \square , 347.26 K; \diamond , 367.03 K; $+$, 386.84 K.

The calculations of α_p , for the database fuels in the ranges 283.15 K to 373.15 K and 0.1 MPa to 40 MPa shows minimum and maximum values as presented in Figure 3.10 (a). The averages for minimum and maximum values were, $(6.802 \pm 0.304) \times 10^{-4} \text{ K}^{-1}$ and $(9.103 \pm 0.747) \times 10^{-4} \text{ K}^{-1}$, respectively. For S and SR fuels the α_p maximum values showed markedly higher deviations from the average. The α_p values for the 19 fuels gave an average of $(8.237 \pm 0.249) \times 10^{-4} \text{ K}^{-1}$ at ($T=298.15\text{K}$, $p=0.1 \text{ MPa}$), which is practically the same value measured for the biodiesels set presented by Pratas et al. [36]. That value was near to the one obtained for Diesel D-2 ($8.03 \times 10^{-4} \text{ K}^{-1}$), from the density data measured by Tat and Van Gerpen [21] at the same (T , p) conditions. Santos et al. [60] presented almost the same thermal expansivity for diesel ($8.36 \times 10^{-4} \text{ K}^{-1}$) and corn biodiesel ($8.39 \times 10^{-4} \text{ K}^{-1}$) obtained from density measurements in the range 283.15 K to 323.15 K at atmospheric pressure. However, Aparício et al. [24] concluded that diesel had greater

thermal expansivity than rapeseed biodiesel with differences increasing with temperature (7% at 288.15 K, 16% at 308.15 K and 22% at 328.15 K).

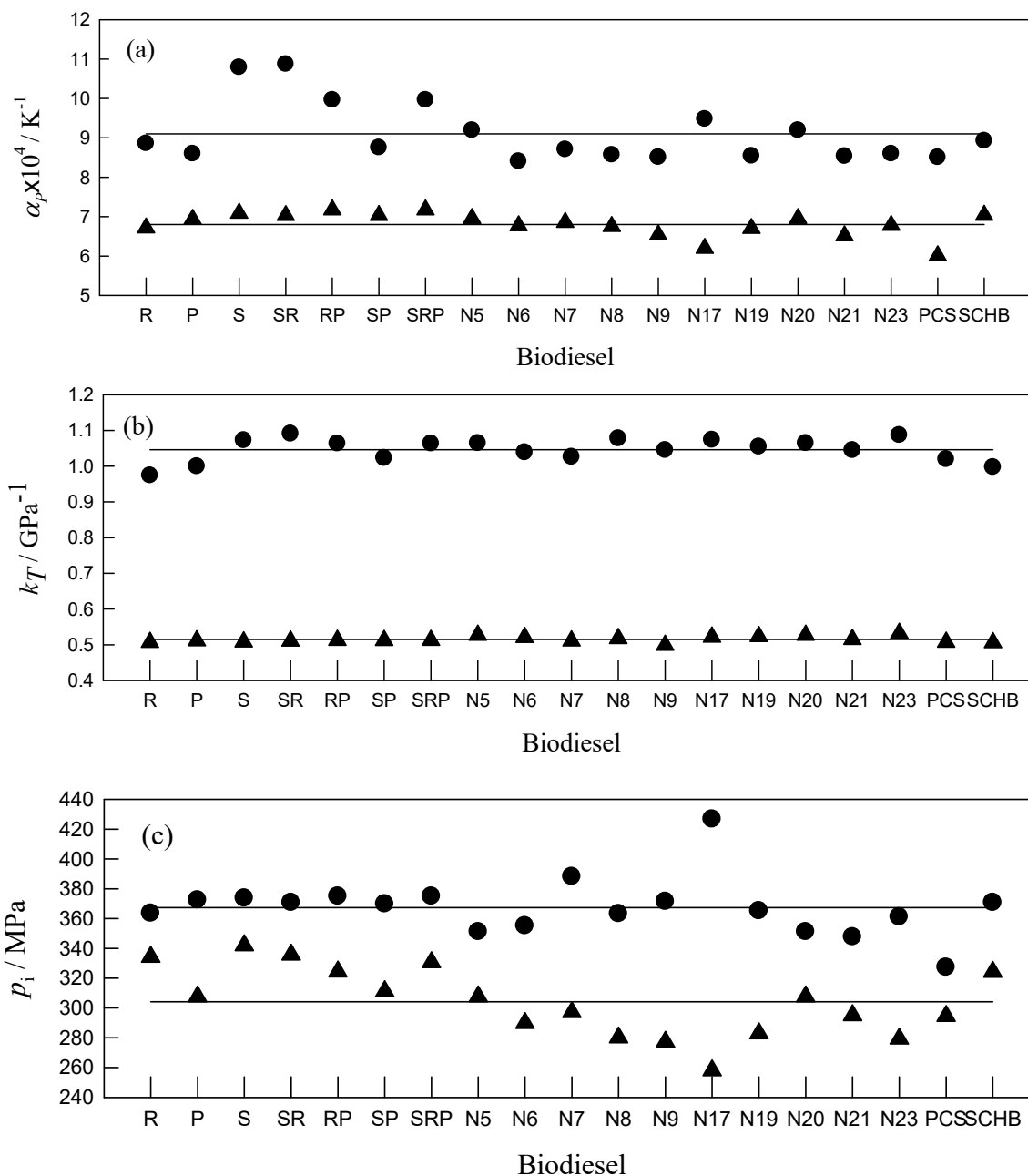


Figure 3.10. Minimum and maximum values distribution of the mechanical coefficients for the biodiesels in the database. Triangles and circles refer to minima and maxima respectively and lines to the mean values. (a) Thermal expansivity; (b) isothermal compressibility; (c) internal pressure.

Considering water and ethanol as standards at 298.15 K and 0.1 MPa, the thermal expansivity values of biodiesels were significantly higher than the one of water and lower than the corresponding value for ethanol (water: $2.57 \times 10^{-4} \text{ K}^{-1}$ [61]; ethanol $1.07 \times 10^{-3} \text{ K}^{-1}$ [62]). The thermal expansivity is related to the engine power loss due to the fuel heating [19]. The higher the thermal expansivity, the greater the power loss. From the results obtained for the several biodiesels in database and for diesel, significant differences in power due to corresponding differences in α_p are not expected. The thermal expansivity values for the biodiesel set (R, P, S, RP, RS, SP, SRP) obtained in this work with GMA EoS were compared in Figure B.7(a) with the ones from Tait EoS at pressures of 0.1 MPa and 40 MPa used for correlation by Pratas et al. [19]. The values calculated from the two EoS were in good agreement, differing within $\pm 2\%$ (less than $2 \times 10^{-5} \text{ K}^{-1}$).

Concerning to k_T , the observed behaviour for variations in temperature and pressure was according to the expected as illustrated in the $(k_T, T)_p$ and $(k_T, p)_T$ plots given in Figure 3.11 for the biodiesel studied by Schedemann et al. [27]. Parabolic bends are observed for k_T as the temperature increases, particularly at low pressure. A pronounced parabolic decrease of k_T as pressure increases at fixed temperature was observed especially at the higher pressures. The minimum and maximum k_T values for the 19 fuels in the ranges 283.15 K to 373.15 K and 0.1 MPa to 40 MPa, are shown in Figure 3.10(b). The average values for minimum and maximum of k_T were $(0.515 \pm 0.008) \text{ GPa}^{-1}$ and $(1.046 \pm 0.032) \text{ GPa}^{-1}$, respectively. It is interesting to note the very small deviations from the average values. At 298.15 K and 0.1 MPa the average $(0.68 \pm 0.01) \text{ GPa}^{-1}$ was obtained for the biodiesels in database. For Diesel D-2, the data from Tat and Van Gerpen gives $k_T = 0.73 \text{ GPa}^{-1}$. Both values were intermediate to the ones observed for water and ethanol (water: 0.452 GPa^{-1} [64] ethanol: 1.40 GPa^{-1} [62]). The isothermal compressibility values for the biodiesel set (R, P, S, RP, RS, SP, SRP) obtained with GMA EoS were compared with the values from Tait EoS [19] (see Figure B.7(b)). At 0.1 MPa the values from GMA were systematically 2% lower (ca 0.02 GPa^{-1}) than those reported by Pratas et al. while at 40 MPa GMA produces values systematically higher with deviations usually less than 2%.

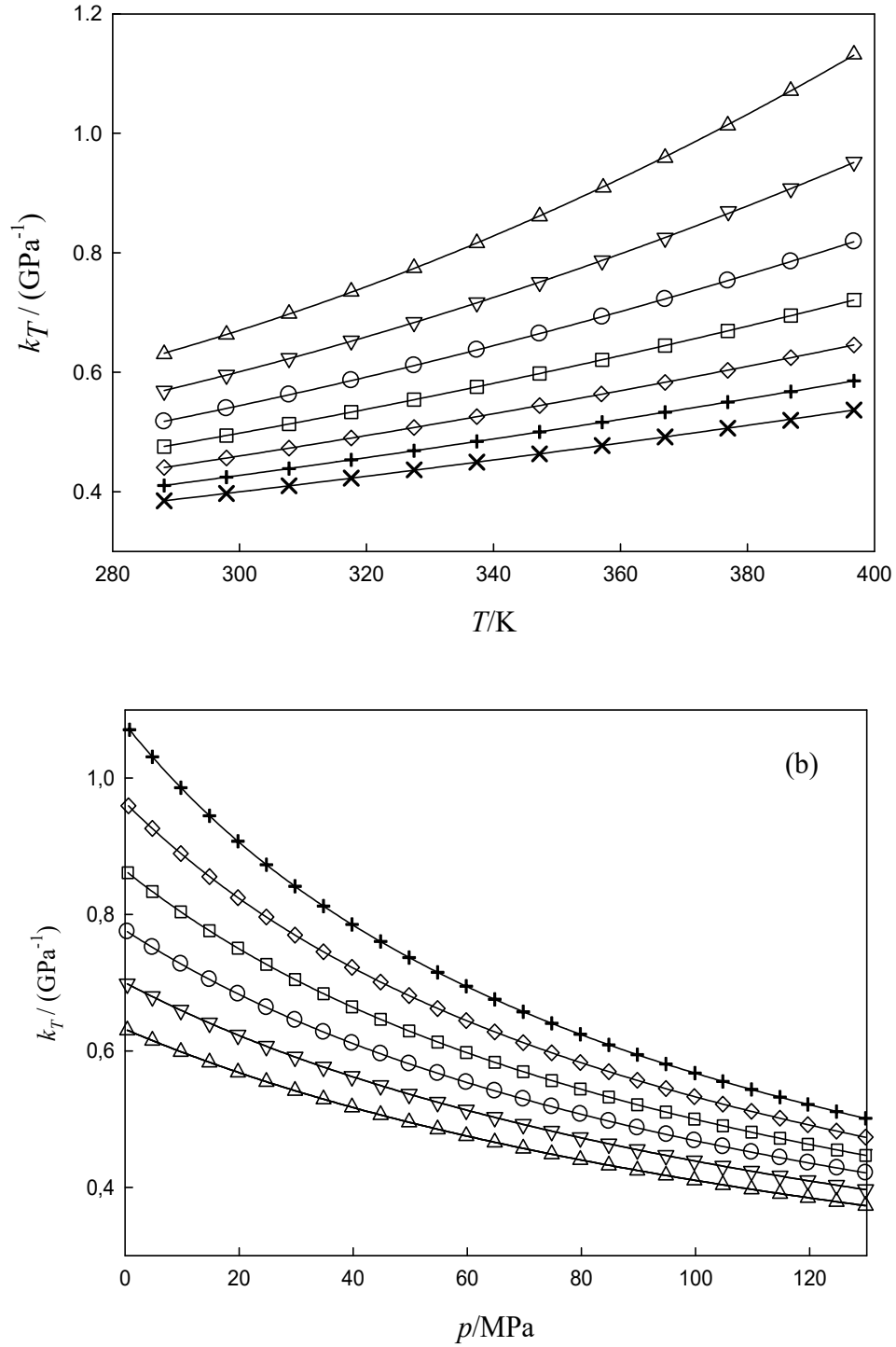


Figure 3.11. Isothermal compressibility (k_T) for the SCHB calculated from GMA EoS. (a) k_T as function of temperature along isobars: Δ , 0.4 MPa; ∇ , 19.8 MPa; \circ , 39.8 MPa; \square , 59.8 MPa; \diamond , 79.8 MPa; $+$, 99.8 MPa; \times , 119.7 MPa. (b) k_T as function of pressure along isotherms: Δ , 288.12 K; ∇ , 307.80 K; \circ , 327.49 K; \square , 347.26 K; \diamond , 367.03 K; $+$, 386.84 K.

Although rarely used in biodiesel researches, the internal pressure p_i provides a useful basis for understanding the nature of molecular interactions in liquid state. As far as it is known, only Schedemann et al. [27] presented values for this coefficient relative to methyl linoleate. The internal pressure is a macroscopic property used for estimating the cohesion of liquids, reflecting the molecular ordering, and it measures the change in the internal energy as the liquid experiences a slight isothermal expansion. From the results obtained in this study for biodiesels, p_i had low sensitivity to the pressure and temperature variations. For temperatures between 283.15 K and 373.15 K and pressures up to 40 MPa the p_i minimum and maximum averages for the 19 fuels were (304±23) MPa and (367±19) MPa, respectively (see Figure 3.10(c)). For pure liquids below their boiling points, p_i is from 200 to 800 MPa, for non-associated and associated liquids, respectively [63]. The normal boiling temperature for the considered biodiesels were in the range $T_{nb} = (611 \text{ to } 642) \text{ K}$ [64, 65]. Therefore, biodiesel presents internal pressures near the lower limit for pure non-associated liquids. An isothermal decrease with pressure was always observed, however for temperature the behaviour was variable, depending on the fuel nature. The behaviour of p_i as a function of the temperature at 0.1 MPa is shown in Figure 3.12 for selected biodiesels. The most general behaviour was a p_i decreasing with temperature and for some fuels the decrease was more evident in the range of temperatures studied, especially for the fuels prepared by Tat and Van Gerpen [20, 21]. The cottonseed biodiesel produced in this work had the lowest internal pressure between all the studied 19 fuels. From the values of thermal expansion and isothermal compressibility given before at 298.15 K and atmospheric pressure, the internal pressure of diesel D-2 is 327 MPa and is in close agreement with what was found for biodiesel.

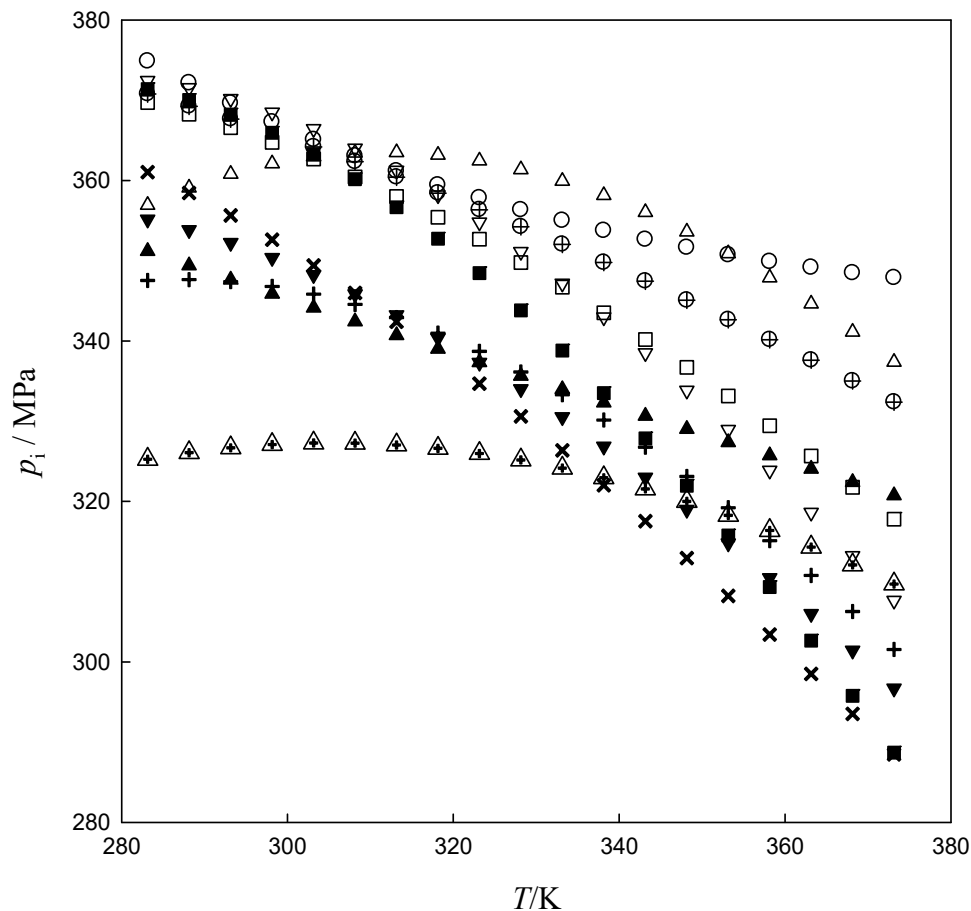


Figure 3.12. Internal pressure (p_i) as function of temperature at 0.1 MPa for the biodiesels in the database. Δ , R; ∇ , P; \square , SP; \circ , SRP; \blacktriangle , N5; \blacktriangledown , N6; \blacksquare , N9; $+$, N21; \times , N23; \triangleleft , CSB; \oplus , SCHB.

Given the molecular structure of the FAMES that composing the biodiesel, the attractive dispersion forces are the most important. They arise from induced dipoles and their strength is related with the polarizabilities of the molecules, which for different FAMES in biodiesel are similar, no matter the alkyl chain length [66]. Although the presence of a carbonyl group provides some polarity to molecules, the two oxygen atoms of the ester functional group and the absence of electropositive hydrogen within the FAME molecules prevent hydrogen bonding. The relative importance of the various molecular interactions (dispersion, polar, hydrogen bond) present in the liquid can be evaluated by comparing the internal pressure with the cohesive pressure. If the gas phase intermolecular interactions are excluded (perfect gas behaviour assumed), the cohesive pressure (or cohesive energy density) p_{coh} is given by [67],

$$p_{coh} = \frac{\Delta_l^g U_{coh}}{V_m} \cong \frac{(\Delta_l^g H_m - RT)}{V_m} \quad \text{Eq. 3-20}$$

where $\Delta_l^g U_{coh}$, $\Delta_l^g H_m$, and V_m are the molar cohesive energy, the molar enthalpy of vaporization, and molar volume (all usually taken at 0.1 MPa), respectively.

According to Ivanov and Abrosimov [67], the existence of strong intermolecular interactions in a liquid substantially increases the cohesive pressure relative to the internal pressure, while for liquids without such strong intermolecular interactions the internal pressure is comparable to the cohesive pressure. Taking water and ethanol as examples at 298.15 K and atmospheric pressure, and from the thermal expansion and isothermal compressibility values mentioned before, the internal pressures are 170 MPa and 234 MPa, respectively. At the same (T, p) conditions the cohesive pressure is increased to 2400 MPa and 700 MPa [68] for water and ethanol, respectively. These values reflect the strong hydrogen bonding, especially for water. For rapeseed biodiesel, Yuan [69] reported the value $297 \text{ J}\cdot\text{g}^{-1}$ for the enthalpy of vaporization at 373.15 K and Lee and Hansen [70] the value $320 \text{ J}\cdot\text{g}^{-1}$ for soybean biodiesel. From those values and density values by Pratas et al. [36], the corresponding cohesion pressures calculated with Eq. 3-20 are 236 MPa and 274 MPa for rapeseed and soybean fuels. For rapeseed biodiesel Zhang et al. [66] and Cataldo et al. [71] reports $p_{coh} = 308 \text{ MPa}$ and $p_{coh} = 277 \text{ MPa}$, respectively. Therefore, the internal pressure of biodiesel fuel is of the same magnitude order as the cohesion pressure, meaning that it behaves as non-associated liquid without strong molecular interactions.

3.1.6 Conclusions

New density experimental data for cottonseed biodiesel at temperatures between 288 K and 358 K and pressures up to 30 MPa were measured with an estimated combined uncertainty of $0.81 \text{ kg}\cdot\text{m}^{-3}$. As far as it is known these are the first measurements for cottonseed biodiesel under high pressure.

The pVT data of cottonseed biodiesel were combined with similar information from other 18 biodiesels collected from literature, this way constituting a statistically significant database that was used to test the correlation of the GMA EoS. This equation was used for the first time to correlate biodiesel density revealing excellent results, with standard deviations less than $0.5 \text{ kg}\cdot\text{m}^{-3}$, corresponding to mean relative deviations less than 0.05%. Regarding to the prediction

ability of GMA EoS, at the (p, T) conditions found in high efficient and high pressure injection systems, reliable extrapolated densities for high temperatures and pressures were obtained. Using the coefficients obtained from correlation, in the restricted ranges of temperature (up to 357 K) and pressure (up to 50 MPa) usually used in measurements, good density predictions could be obtained up to 400 K and 130 MPa (maximum deviations of $\approx 3 \text{ kg}\cdot\text{m}^{-3}$).

Two new predictive equations of state for density, namely the DU and 4PGMA were developed and tested. Both EoS are simple to use and its application needs only the FAMEs profile of biodiesel. From the tests carried out in the 19 biodiesels from the database an overall average deviation of 0.36% corresponding to about $\approx 3 \text{ kg}\cdot\text{m}^{-3}$ was found with DU method. For 4PGMA, the predicted maximum density deviation was 0.25% ($\approx 2 \text{ kg}\cdot\text{m}^{-3}$). These results represent notable improvements in the prediction of biodiesel density in large temperature and pressure ranges where important operations in biodiesel processing take place. The isothermal compressibility increased with temperature at constant pressure, and decrease as pressure goes up for constant temperature as expected. The behaviour of the thermal expansivity as a function of pressure was also the predictable i.e. a decreasing is observed for increasing pressure at isothermal conditions. The α_p isotherms showed an evident intersection point nearly 65 MPa and therefore, at this pressure α_p was independent from temperature. The internal pressure for all tested fuels was low and slightly higher than the cohesive pressure. This means that the biodiesel behaves as a non-associated liquid with weak molecular interactions.

Supplementary material

Supplementary data associated to the published article, on which this section was based, it can be found in <http://dx.doi.org/10.1016/j.fuel.2014.09.113>.

3.2 COTTONSEED OIL DENSITY

3.2.1 Introduction

CSO is used in many areas as food processing, new chemical developing and for biodiesel production [72]. The used of triglyceride oils in synthesis of alkyd resins has been studied in recent times. This is due to environmental and eco-friendliness of this product. Alkyd resins are conventional binders used in the production of paints, varnishes and other coating products. Among other oils, that contain carbon-carbon double bonds as the functional groups, cottonseed oil is widely used in synthesis and characterization of alkyd resins [73-75]. In all the aforementioned areas the knowledge of density of CSO plays an important role in the development, performance and behaviour analysis in the applications.

The density of CSO was measured at atmospheric pressure by Menzies et al. [76], Magne et al. [77], Arnold et al. [78], Demirbas [79], Macovey [80] and by Eryilmaz et al. [81]. As far as it is known, inclusion of pressure in density of CSO was never made. To address this limitation, in this section the densities of CSO were measured in the range $T = (278.15-358.15)$ K and pressures $p = (0.1-30.0)$ MPa. The Goharshadi–Morsali–Abbaspour equation of state (GMA EoS) was used to correlate the new experimental data with temperature and pressure. The group contribution method GCVOL revised by Pratas et al. [36], the Halvorsen et al. method [82] and the fragments method of Zong [83] were evaluated for prediction of densities. Also, a comparison of CSO density with experimental data available in literature was performed and, a new simple and efficient method for prediction of biodiesel density from the available density of the oil was proposed.

3.2.2 Experimental section

3.2.2.1 Materials

The specification details of the CSO used and fatty acid profile were already given in Table 3.1. The mass and molar composition of CSO and CSB are presented in Table 3.9.

Table 3.9. Mass fractions (w_i) and molar fractions (x_i) of CSO and CSB.

Component	CSO		CSB	
	w_i (wt %) ^a	x_i	w_i (wt %) ^b	x_i
Myristic C14:0	1.45	0.0174	0.93±0.28	0.0110
Palmitic C16:0	24.15	0.2579	26.76±1.56	0.2845
Stearic C18:0	2.90	0.0279	2.81±0.29	0.0271
Oleic acid C18:1	19.32	0.1873	17.89±1.71	0.1735
Linoleic acid C18:2	50.72	0.4952	51.61±2.99	0.5039
Linolenic acid C18:3	1.45	0.0143		

^a Values considering the mass fraction of free fatty acids (FFA) reported in Table 3.1. The mean values of mass fractions of oleic and linoleic acids were considered in the calculations and normalization procedure was realized.

^b From Gas Chromatography.

3.2.2.2 Density measurement

Cottonseed oil densities were determined using the Anton Paar DMA 60 digital vibrating tube densimeter, with a DMA 512P measuring cell. The accessory equipment, the measuring setup, the calibration and performance of the vibrating tube densimeter were described with detail in section 3.1.2.4.

3.2.3 Density models

3.2.3.1 GMA and GCVOL equations of state

The GMA EoS [39] used to correlate the measured densities with temperature and pressure, and the GCVOL method [36, 49], used for the prediction of liquid densities as a function of temperature and pressure, have been described previously for CSB (Section 3.1.4.2 and 3.1.4.3).

For oils, the molar fractions, x_i , and molar mass, M_i , in Eq. 3-11 and the number of group i , n_i , and the respective contributions, Δv_i , in Eq. 3-8 are relative to fatty acids.

Freitas et al. [84] fitted the revised GCVOL [36] (Eq. 3-10), to pVT data of three vegetable oils (palm, soybean and *Jatropha curcas*) in the ranges (283.15 to 363.15) K and (0.1 to 45.0) MPa, finding $A = -5.99 \times 10^{-4} \text{ MPa}^{-1}$. The model described by Eq. 3-10 will be labelled here as GCVOL.

3.2.3.2 Halvorsen's model

One of the most used models for the calculation of oil densities is due to Halvorsen et al. [82]. It combines the fatty acid critical properties and the composition of oil (fatty acids content) to predict the density of oils using the modified Rackett equation:

$$\rho_{\text{oil}}(T, p = 1\text{atm}) = \frac{\sum x_i M_i}{R \left(\sum_i \frac{x_i T_{ci}}{p_{ci}} \right) \left(\sum_i x_i Z_{RAi} \right) \left[(1 + (1 - T_r))^{2/3} \right]} + F_c \quad \text{Eq. 3-21}$$

where x_i , M_i , T_{ci} and p_{ci} are the molar fraction, molar mass, critical temperature and critical pressure of the fatty acid i , respectively. T_r is the reduced temperature, R is the ideal gas constant, Z_{RA} is the Rackett parameter, a correlating parameter unique to each compound and F_c is the correction factor that take into account for the triglyceride form of the fatty acid in the oil. F_c is independent of the temperature and depends solely on the oil type.

The molar mass of oil, M_{oil} , is calculated from:

$$M_{\text{oil}} = 3 \sum x_i M_i + 38.0488 \quad \text{Eq. 3-22}$$

$$T_r = \frac{T}{T_{c,\text{mix}}} \quad \text{Eq. 3-23}$$

$$T_{c,\text{mix}} = \sum_i x_i T_{ci} \quad \text{Eq. 3-24}$$

$$F_c = 0.0236 + k|875 - M_{\text{oil}}| \quad \text{Eq. 3-25}$$

where $k = 0.00082$ and $k = 0.000098$ for molar mass higher than 875 g/mol^{-1} and lower than 875 g/mol^{-1} , respectively. The values of T_c and p_c , Z_{RA} and the molar mass of the fatty acids present in CSO are given in Table B.3. More detailed information about the model is given by Halvorsen et al. [82]. Using Eq. 3-21 for calculation of $V_{\text{m,oil}}(T)$ with M_{oil} calculated from Eq. 3-22, Freitas et al. [84] fitted GCVOL (Eq. 3-10) to pVT data of vegetable oils in the ranges of temperature and pressure mentioned before and they found $A = -4.29 \times 10^{-4} \text{ MPa}^{-1}$. The model that combines Eq. 3-10 using this value of A and Eq. 3-21 will be labelled here as GCVOL/HAL.

3.2.3.3 Zong's model

Zong et al. [83] developed a model to estimate the thermophysical properties of triglyceride mixtures. They divided each TG molecule into four parts, one glycerol fragment and three fatty-acid fragments (F), and then correlated experimental data to obtain the contribution of each fragment to the overall property.

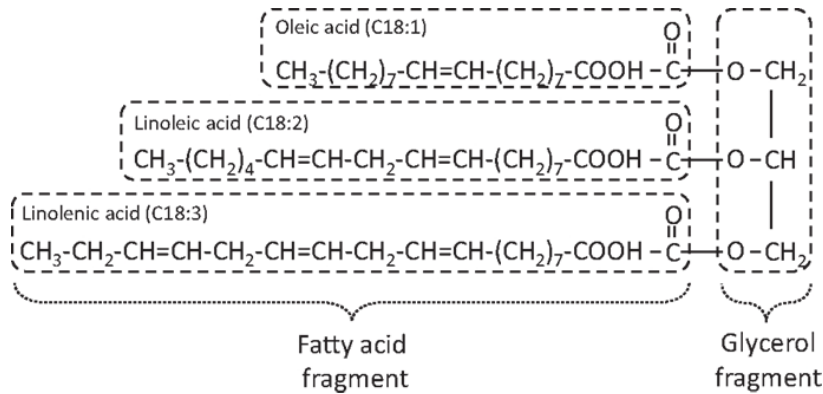


Figure 3.13. Representative molecule of a mixed triglyceride. Oleic, linoleic and linolenic acids (OLiLn) are the fragments component of the TG.

From Zong et al. [83], the density of oil can be calculated by,

$$\frac{1}{\rho_{\text{oil}}} = \sum_i w_i \frac{1}{\rho_i} \quad \text{Eq. 3-26}$$

where ρ_{oil} is the oil density, ρ_i and w_i are the density and the mass fraction of triglyceride i , respectively. This approach requires the knowledge of representative triglyceride molecules. Then, the density of each triglyceride molecule is estimated from its molar volume ($V_{m,i}$) using:

$$V_{m,i} = \sum_A N_{\text{frag},A} V_{m,A}(T) \quad \text{Eq. 3-27}$$

where $V_{m,A}(T)$ is the liquid molar volume contribution of fragment A (in $\text{cm}^3 \cdot \text{mol}^{-1}$) at temperature $T(\text{K})$ and $N_{\text{frag},A}$ is the number of fragment A in the triglyceride i . The temperature dependency of liquid molar volume, $V_{m,A}$, is [83]:

$$V_{m,A} = \frac{1+B_{2,A}T}{B_{1,A}} \quad \text{Eq. 3-28}$$

where $B_{1,A}$ and $B_{2,A}$ are the temperature dependent parameters of fragment A, which values were given by Zong et al. [83]. Using Eq. 3-26 to 3-28, Freitas et al. [84] fitted CGVOL, (Eq. 3-10) to pVT data of the three vegetable oils mentioned before and they found $A = -2.80 \times 10^{-4} \text{ MPa}^{-1}$. The model that combines Eq. 3-10 using this value of A and Zong's equations will be labelled here as GCVOL/ZONG.

3.2.4 Results and discussion

3.2.4.1 Density of cottonseed oil

Cottonseed oil pVT data are reported in Table 3.10 for temperatures between 278.15 K and 358.15 K and pressures between 0.1 MPa and 30.0 MPa. The experimental data showed that the oil density behaved as expected, meaning that density decreases as temperature increases and pressure drops.

Table 3.10. Experimental density data (ρ) for CSO as a function of temperature (T), and pressure (p).

$p/$ MPa	$\rho / (\text{kg} \cdot \text{m}^{-3})$ at T / K										
	278.15	283.15	288.15	293.15	298.15	308.15	318.15	328.15	338.15	348.15	358.15
0.1	927.8	924.3	920.8	917.3	913.9	907.3	900.9	894.7	888.7	883.0	877.4
1.0	928.2	924.5	920.9	917.3	914.3	907.9	901.6	895.4	889.4	883.6	877.8
2.0	928.7	924.8	921.1	917.8	914.8	908.4	902.1	895.9	890.0	884.2	878.6
3.0	929.1	925.4	921.8	918.3	915.4	909.0	902.8	896.7	890.7	884.9	879.2
4.0	929.6	925.8	922.2	918.9	915.9	909.6	903.4	897.3	891.4	885.6	879.9
5.0	930.1	926.4	922.8	919.3	916.5	910.2	904.0	897.9	892.0	886.3	880.7
6.0	930.5	926.7	923.2	919.9	917.0	910.8	904.6	898.6	892.7	886.9	881.2
7.0	931.0	927.5	923.9	920.3	917.5	911.3	905.1	899.1	893.3	887.5	881.9
8.0	931.3	927.6	924.1	920.9	918.0	911.8	905.7	899.7	893.9	888.2	882.6
9.0	931.8	928.1	924.7	921.3	918.4	912.4	906.4	900.4	894.4	888.4	882.4
10.0	932.3	928.5	925.0	921.8	919.0	912.9	906.8	900.9	895.1	889.4	883.9
15.0	934.4	930.8	927.4	924.3	921.7	915.5	909.5	903.7	898.0	892.5	887.1
20.0	936.4	933.0	929.7	926.7	924.1	918.1	912.2	906.5	900.9	895.5	890.2
25.0	938.5	935.1	931.9	928.9	926.5	920.6	914.8	909.2	903.7	898.4	893.3
30.0	940.6	937.2	934.1	931.2	928.9	923.0	917.3	911.8	906.4	901.2	896.1

^a $U(\rho) < 1.6 \text{ kg} \cdot \text{m}^{-3}$; ^b $u(T) = 0.02 \text{ K}$; ^c $u(p) = 0.02 \text{ MPa}$.

The density of CSO were measured at atmospheric pressure by Menzies et al. [76] at (293 to 503) K, Magne et al. [77] at (273 to 374) K, Arnold et al. [78] at (298 to 343) K, by Demirbas [79] at $T = 311.15$ K, Macovei [80] in the extensive range (253 to 523) K and by Eryilmaz et al. [81] at (298 to 373) K. These measurements were compared with determinations of this work in Figure 3.14.

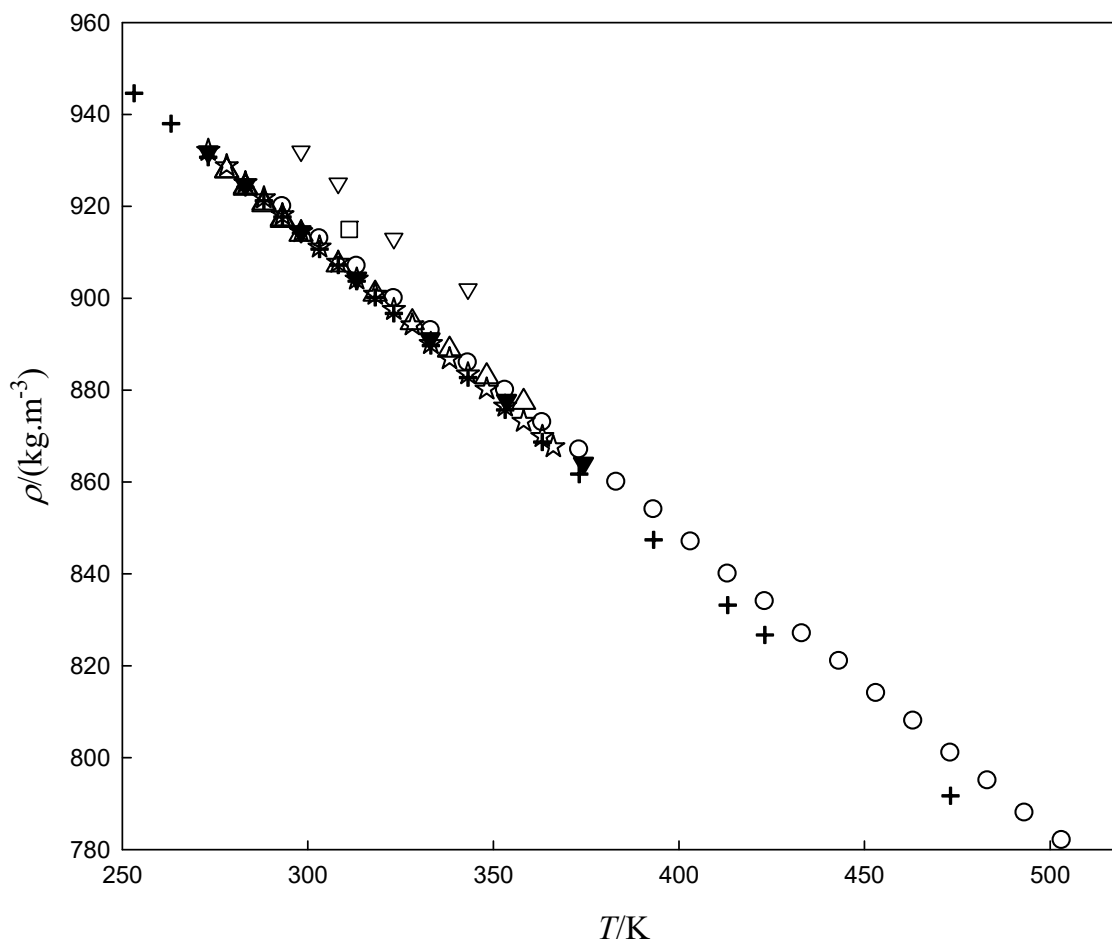
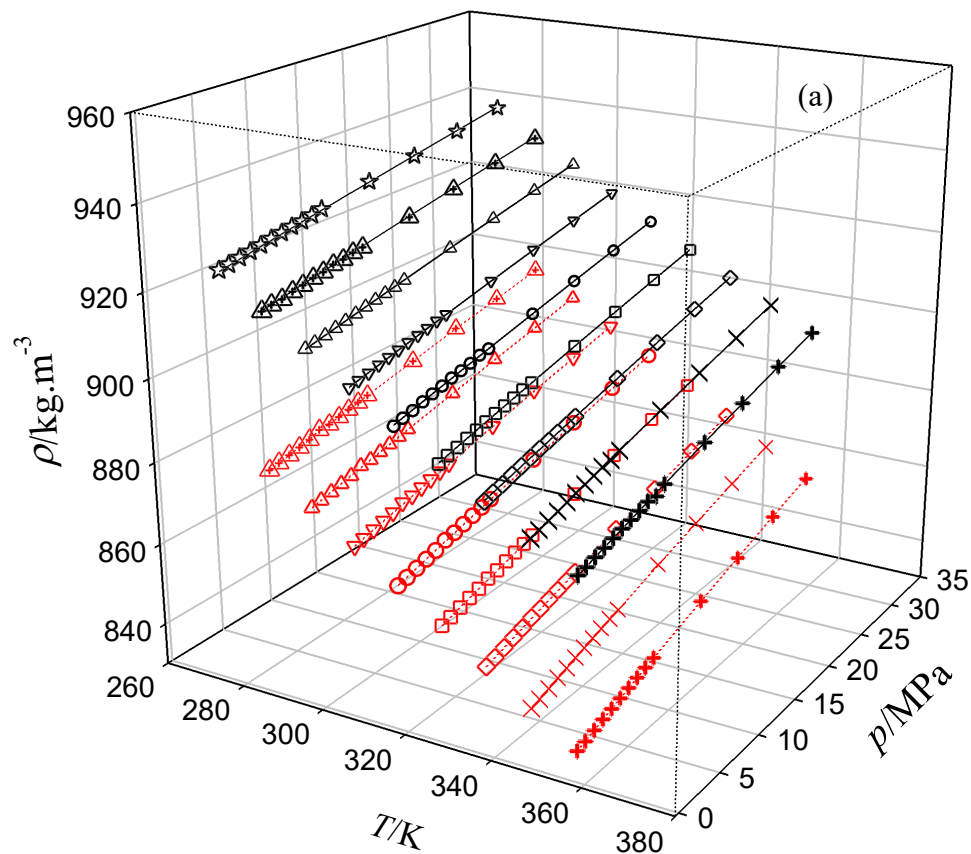


Figure 3.14. Comparison between the densities of this work for CSO with values from the literature. Δ , this work; \circ , Menzies et al. [76]; ∇ , Magne et al. [77]; ∇ , Arnold et al. [78]; \square , Demirbas [79]; $+$, Macovei [80]; \star , Eryilmaz et al. [81].

Taking linear representations of density data obtained in this work at atmospheric pressure, maximum relative deviation of ca. 0.3% is obtained from the values measured by Menzies et al [76], up to 313 K and deviations decrease up to zero at 358 K. Beyond these value of temperature, the measurements made by Menzies et al. follow the same trend as ours, as temperature increases. Relative deviations ranging between 0.01% and 0.25% are obtained by

comparing values of this work with the measurements made by Magne et al. [77], Macovei [80], and Eryilmaz et al. [81] and 1.8% for the values of Arnold et al. [78].

The information concerning to CSB at temperatures $T = (288 \text{ to } 358) \text{ K}$ and pressures $p = (0.1 \text{ to } 30.0) \text{ MPa}$, previously published [55] is compared here with the densities of CSO in Figure 3.15. Figure 3.15(a) shows a 3D representation of density and in Figure 3.15(b) the two-dimensional plot is provided. It can be seen that for each isotherm the density of oil runs almost parallel with density of biodiesel. The differences $\Delta\rho = (\rho_{\text{oil}} - \rho_{\text{bd}})$, between the densities of the oil and corresponding biodiesel are comprise between $34.4 \text{ kg}\cdot\text{m}^3$ at $(288.15 \text{ K}, 30.0 \text{ MPa})$ and $40.2 \text{ kg}\cdot\text{m}^3$ at $(358.15 \text{ K}, 0.1 \text{ MPa})$.



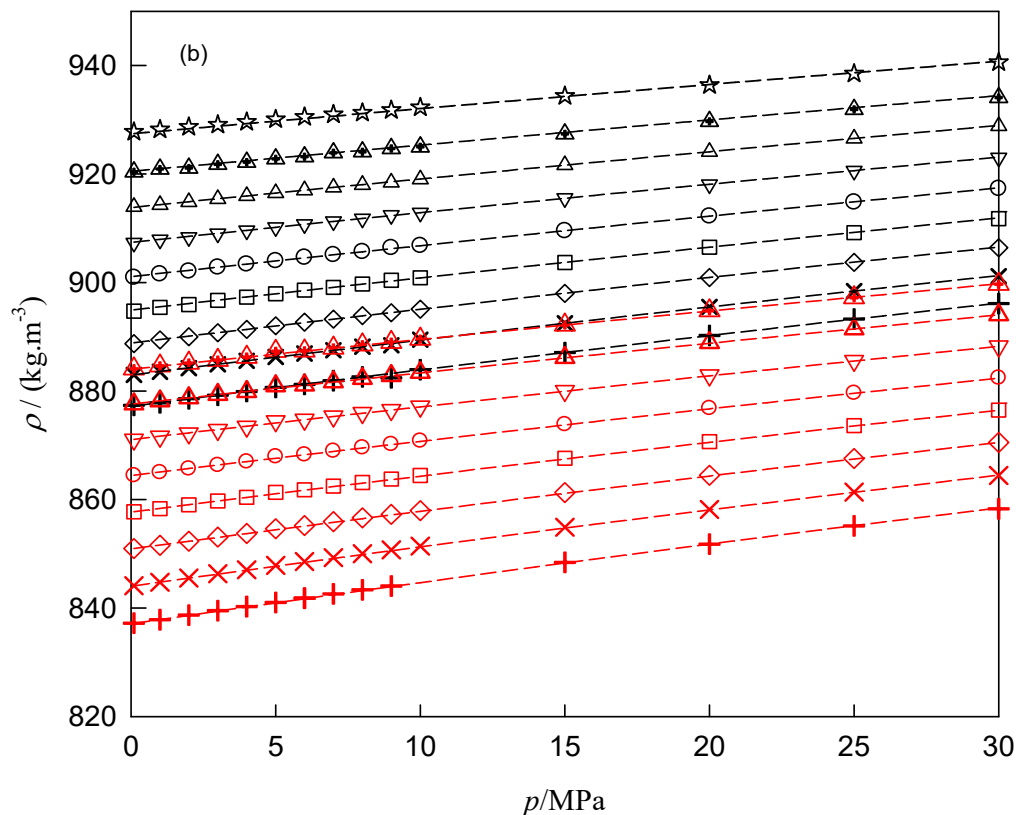


Figure 3.15. Experimental density for CSO and CSB as function of pressure and temperature. Black symbols correspond to the oil and red ones to biodiesel: ☆ , 278.15 K; ▲, 288.15 K, △, 298.15 K; ▽, 308.15 K; ○, 318.15 K; □, 328.15 K; ◇, 338.15 K; ×, 348.15 K; +, 358.15 K. The lines represent the fittings with GMA EoS.

3.2.4.2 Density correlation

The calculation of molar volume and molar density in GMA EoS involves the molar mass, M . From the FA profile of CSO (see Table 3.9), Eq. 3-22 gives $M_{oil} = 859.4 \text{ g.mol}^{-1}$ and was used in this work. This value is close to 849.4 g.mol^{-1} estimated by Ceriani and Meirelles [85].

The coefficients A_0 - A_2 and B_0 - B_2 of the GMA EoS obtained by fitting Eqs. 3-2 to 3-4, to the pVT data through least-squares, with confidence limits of 95%, are given in Table 3.11. The statistical indicators and the standard deviation for density from Eq. 3-7 are also given. The results obtained previously for CSB are given for comparison purposes.

Table 3.11. Fitting parameters of GMA EoS applied to the correlation of experimental pVT data of cottonseed oil and biodiesel fuel.

Parameter	Oil	Biodiesel
A_0^a	-9757.00018±3151.7994	93.75307±27.1477
A_1^b	468.5901±616.2269	45.51811±5.4239
A_2^c	6.5798±1.9377	-0.051795±0.01662
B_0^d	12520.5111±2976.0709	-25.7089±8.9420
B_1^e	414.2958±579.9925	-12.9335±1.7818
B_2^f	-8.1256±1.8309	0.014473±0.005479
σ^g	0.2558	0.001458
σ_ρ^h	0.211	0.10
r^2	0.9990	0.9998
N_p	165	120
$AARD\%$	0.018	0.007

^a $A_0/(\text{dm}^9 \cdot \text{mol}^{-3})$; ^b $A_1/(\text{MPa} \cdot \text{dm}^{12} \cdot \text{mol}^{-4})$; ^c $A_2/(\text{MPa} \cdot \text{dm}^{12} \cdot \text{mol}^{-4} \cdot \text{K}^{-1})$; ^d $B_0/(\text{dm}^{12} \cdot \text{mol}^{-4})$; ^e $B_1/(\text{MPa} \cdot \text{dm}^{15} \cdot \text{mol}^{-5})$; ^f $B_2/(\text{MPa} \cdot \text{dm}^{15} \cdot \text{mol}^{-5} \cdot \text{K}^{-1})$; ^g $\sigma/(\text{dm}^9 \cdot \text{mol}^{-3})$; ^h $\sigma_\rho / (\text{kg} \cdot \text{m}^{-3})$;

The statistical indicators allowed to conclude that GMA EoS gives an excellent pVT data correlation for CSO, since the standard deviations in density are low (lower than the combined uncertainty) and extremely lower $AARDs$ were obtained. In Table 3.11 it can be seen that some variances are high when they are compared with the corresponding parameters themselves, but it must keep in mind that the standard deviations of the coefficients indicate the range over which a parameter value could extend without affect the model fit adversely for a given confidence level. For the same set of data ($T, p, (2z-1)V_m^3$), different values of A_i and B_i parameters can be obtained with the same standard deviation.

Under isothermal conditions, the quantity $(2z-1)V_m^3$ must have a linear behaviour with the molar density as it is expected by inspection of Eq. 3-2. The isotherms of $(2z-1)V_m^3$ versus molar density ρ_m are presented in Figur 3.16 for CSO. The linearity holds well for all isotherms. The linearity is very important for safe extrapolation of density at high temperatures and pressures.

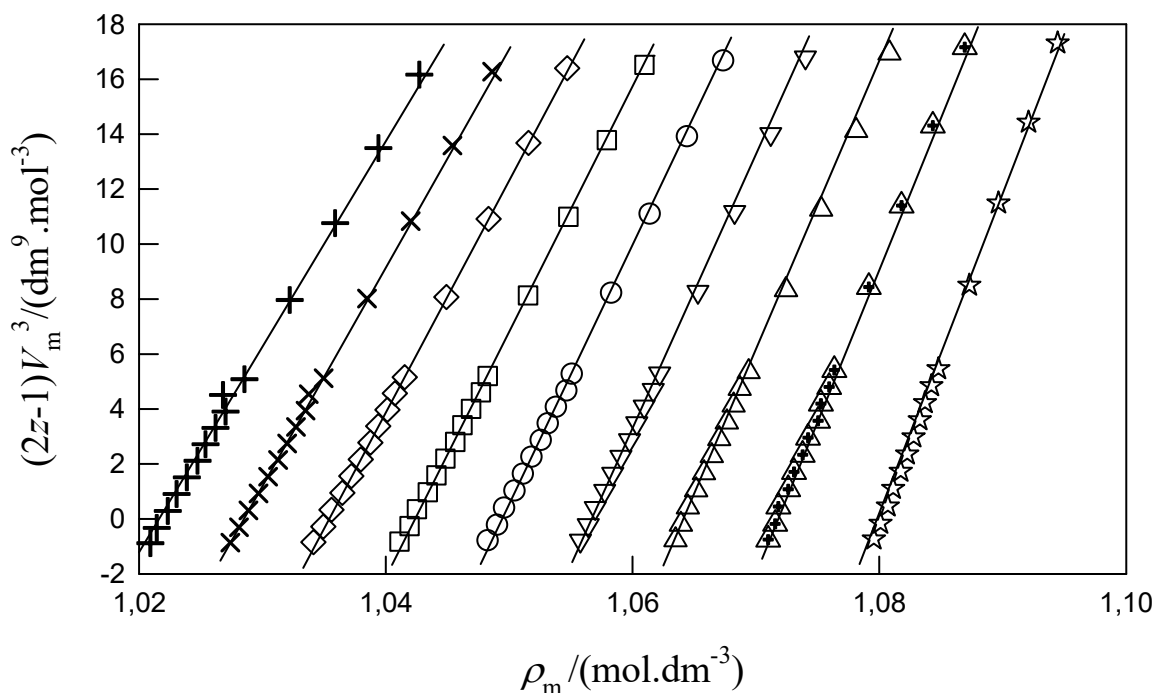


Figure 3.16. Isotherms of $(2z-1)V_m^3$ versus the molar density (ρ_m) for CSO from GMA EoS. Experimental: ☆ , 278.15 K; ▲ , 288.15 K; Δ, 298.15 K; ∇, 308.15 K; ○, 318.15 K; □, 328.15 K; ◇, 338.15 K; ×, 348.15 K; +, 358.15 K. Full curves calculated from correlation with GMA EoS.

Proceeding with the evaluation of the GMA EoS capacity to correlate the density data for all temperatures and pressures, the relative deviations were evaluated. As is shown in Figure 3.17, the *RDs* as a function of temperature and pressure were very small, usually in the range 0.04% (less than $\pm 0.4 \text{ kg}\cdot\text{m}^{-3}$) for CSO. Also, the densities reported for CSO at atmospheric pressure and different temperatures, by the authors mentioned before, were compared with values obtained from GMA EoS in Figure 3.18 where the *RDs* are plotted as a function of temperature.

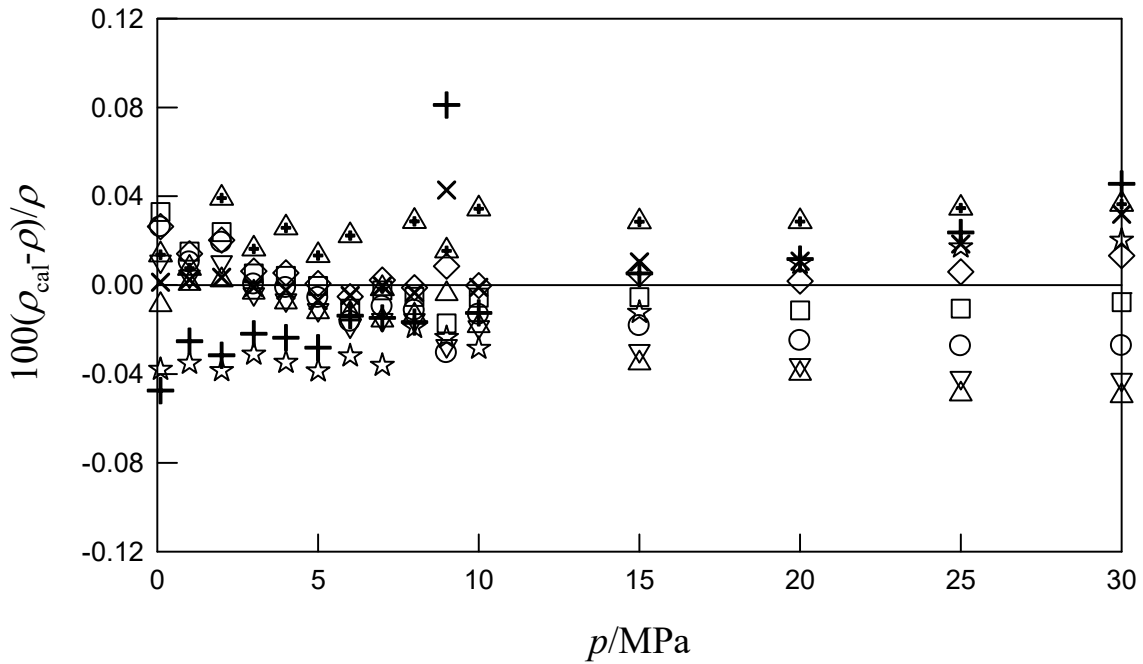


Figure 3.17. Relative deviations between the calculated values with GMA EoS (ρ_{cal}) and the experimental values (ρ) for CSO: ☆, 278.15 K; ▲, 288.15 K; △, 298.15 K; ▽, 308.15 K; ○, 318.15 K; □, 328.15 K; ◇, 338.15 K; ×, 348.15 K; +, 358.15 K.

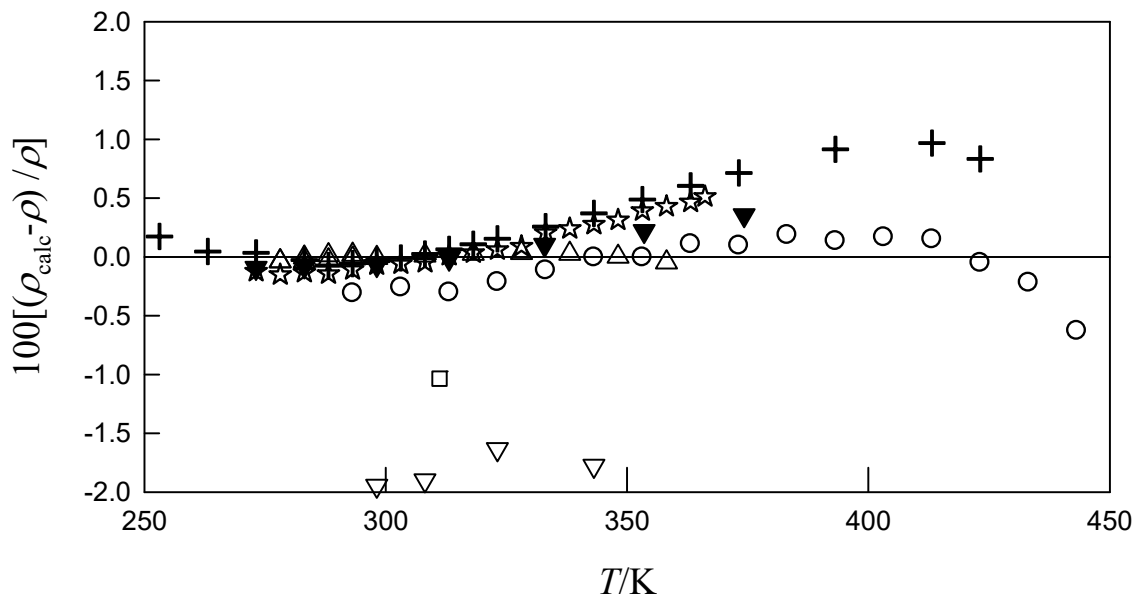


Figure 3.18. Relative density deviations between the calculated values with GMA EoS (ρ_{cal}) and the experimental values (ρ) from the literature for CSO. △, this work; ○, Menzies et al. [76]; ▼, Magne et al. [77]; ▽, Arnold et al. [78]; □, Demirbas [79]; +, Macovei [80]; ☆, Eryilmaz et al. [81].

The densities calculated from GMA EoS deviate less than 0.3% (less than $1 \text{ kg}\cdot\text{m}^{-3}$) from data reported by Menzies et al. in the range 293 K to 433 K. For this reason, it can be said that the GMA EoS has excellent extrapolation ability outside the temperature domain used in its establishment (between 273 K and 358 K). Data reported by Magne et al. [77] are also in excellent agreement with GMA EoS results, especially at temperatures up to 333 K (*RD* less than 0.1%). The densities reported by Macovey [80] and Eryilmaz et al. [81] are also in very good agreement with densities derived from the GMA EoS. Data reported by Macovey [80] is in excellent agreement at 253 K and 273 K proving the ability of GMA EoS for low temperature extrapolation. The values reported by Arnold et al. [78] and Dermibas [79], deviate 1% or more from GMA EoS.

3.2.4.3 Density prediction

The density estimation of oils with Zong's method is made from the densities of individual triglyceride molecules. Thus, the knowledge of the triglyceride profile representing the fatty acid fragments of the oil is needed. The studies in the literature that present oil properties and the corresponding oil composition in terms of TGs, DGs, MGs, and FFAs are scarce and the feed oil analysis is represented usually by the fatty acids composition. Chang and Liu [86] proposed three approaches to characterize feed oils: the mixed-TG approach (MTGA) where detailed TG composition is considered, the simple-TG approach (STGA) and the pseudo-TG approach (PTGA), where FFA composition is used.

For MTGA, the TG composition of CSO reported by Ceriani et al. [85] is given in Table 3.12, where the TG molar mass are also given. The calculations allow to obtain a fatty acid profile for CSO close to that presented by ACROS: MeC14:0 and lower: 1.0% (ACROS: ca 1.5%), MeC16:0: 26.4% (ACROS: ca 25%), MeC18:0: 2.1% (ACROS: ca 3%), MeC18:1: 18.0% (ACROS: 16 to 24%), MeC18:2: 50.0% (ACROS: 50 to 55%), MeC18:3: 0.4% (ACROS: < 1.5%). Therefore, we have considered the TG profile from Ceriani et al. [85] for MTGA.

For STGA the oil is represented by a mixture of simple-TG, that means each TG molecule is composed by the same FFA fragments and it is present with the corresponding FFA fraction.

For the PTGA approach the oil is represents by a simple-TG molecule with the same weighted-average number of CH_2 groups in the FA chain and the same weighted-average number of $\text{CH}=\text{CH}$ groups as the original oil mixture based on the mole fraction of each FA component.

The weighted-average numbers of CH₂ groups (n) and CH=CH groups (m) in the oil were calculated with the equations:

$$n = \sum_i^N x_i n_i \quad \text{Eq. 3-29}$$

$$m = \sum_i^N x_i m_i \quad \text{Eq. 3-30}$$

where N is the number of fatty acids present in the feed oil, x_i is the mole fraction of each fatty acid and n_i and m_i indicate the total numbers of CH₂ groups and CH=CH groups, respectively, in each simple-TG component. Table 3.13 lists the corresponding n_i and m_i values and FA composition of the pseudo-TG.

Table 3.12. Triglyceride profile for cottonseed oil [85].

Triglyceride ^a	M /gmol ⁻¹	wt %	mol %	Triglyceride	M /gmol ⁻¹	wt %	mol %
LOP	776	0.09	0.11	POLi	856	14.30	14.29
PPoP	804	0.62	0.66	SOLi	884	1.31	1.27
POP	832	3.67	3.77	OLiA	912	0.09	0.09
POS	860	0.54	0.54	LLiLi	798	0.23	0.25
POA	888	0.07	0.06	MLiLi	826	1.11	1.15
LLiP	774	0.26	0.29	PLiLi	854	26.58	26.62
MLiP	802	1.16	1.23	SLiLi	882	4.75	4.60
PLiP	830	13.74	14.16	LiLiA	910	0.17	0.16
PLiS	858	3.91	3.90	PoLiLi	852	1.30	1.31
PLiA	886	0.39	0.37	OLiLi	880	10.43	10.14
LOLi	800	0.19	0.20	LiLiLi	878	12.88	12.56
PPoLi	828	1.93	1.99	LiLiLn	876	0.28	0.28

^a Symbols for the FA are listed in Table B. 4.

Table 3.13. Data for the application of PTGA to CSO.

Fatty Acid	molar fraction, x_i^a	n_i	m_i
Myristic acid C14:0	0.0174	36	0
Palmitic acid C16:0	0.2579	42	0
Stearic acid C18:0	0.0279	48	0
Oleic acid C18:1	0.1873	42	3
Linoleic acid C18:2	0.4952	36	6
Linolenic acid C18:3	0.0143	30	9
Pseudo- TG		$n = 38.9$	$m = 3.7$

^a Values considering the mean values of mass fractions of oleic and linoleic acids.

The predicted densities of CSO obtained from the application of the models, in terms of the statistical indicators are given in Table 3.14, relative to the studied ranges of temperature and pressure of this work. The *RDs* between calculated and experimental data are provided in Figure 3.19 to Figure 3.21.

Table 3.14. Statistical results obtained from the application of the predictive models for the calculation of CSO densities.

Model	<i>AARD</i> (%)	<i>AAD</i> ^a /kg·m ⁻³	<i>RMSD</i> ^b /kg·m ⁻³
GCVOL	1.18	10.81	11.41
GCVOL/HALV	0.16	1.42	2.18
GCVOL/ZONG(MTGA)	0.74	6.79	7.23
GCVOL/ZONG(STGA)	0.89	8.15	8.58

$$^a AAD = \frac{1}{N} \sum_{i=1}^N |\rho_{calc} - \rho_{exp}|; \quad ^b RMSD = \sqrt{\sum_{i=1}^N \frac{(\rho_{calc} - \rho_{exp})^2}{N}}$$

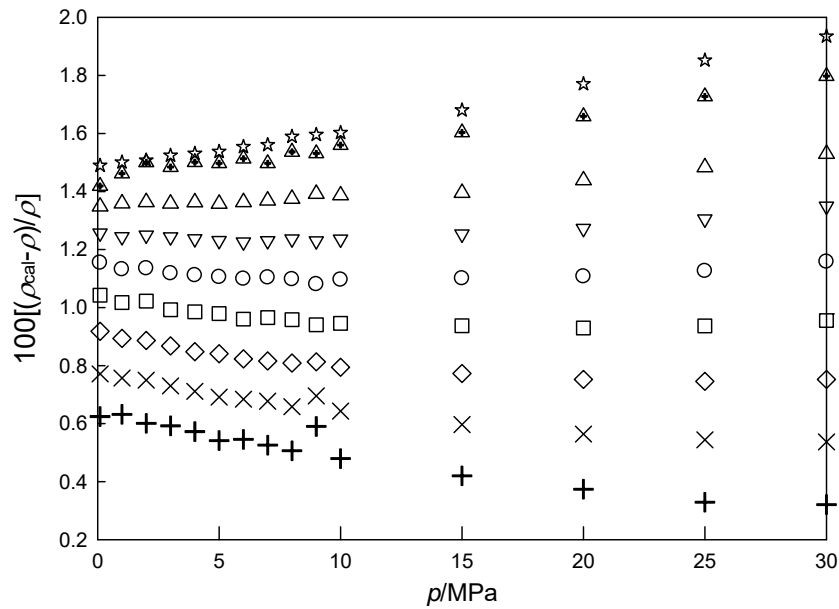


Figure 3.19. Relative density deviations between the predicted (ρ_{cal}) and the experimental (ρ) values as function of pressure and temperature for CSO and GCVOL model: ☆, 278.15 K; ▲, 288.15 K; △, 298.15 K; ▽, 308.15 K; ○, 318.15 K; □, 328.15 K; ◇, 338.15 K; ×, 348.15 K; +, 358.15 K.

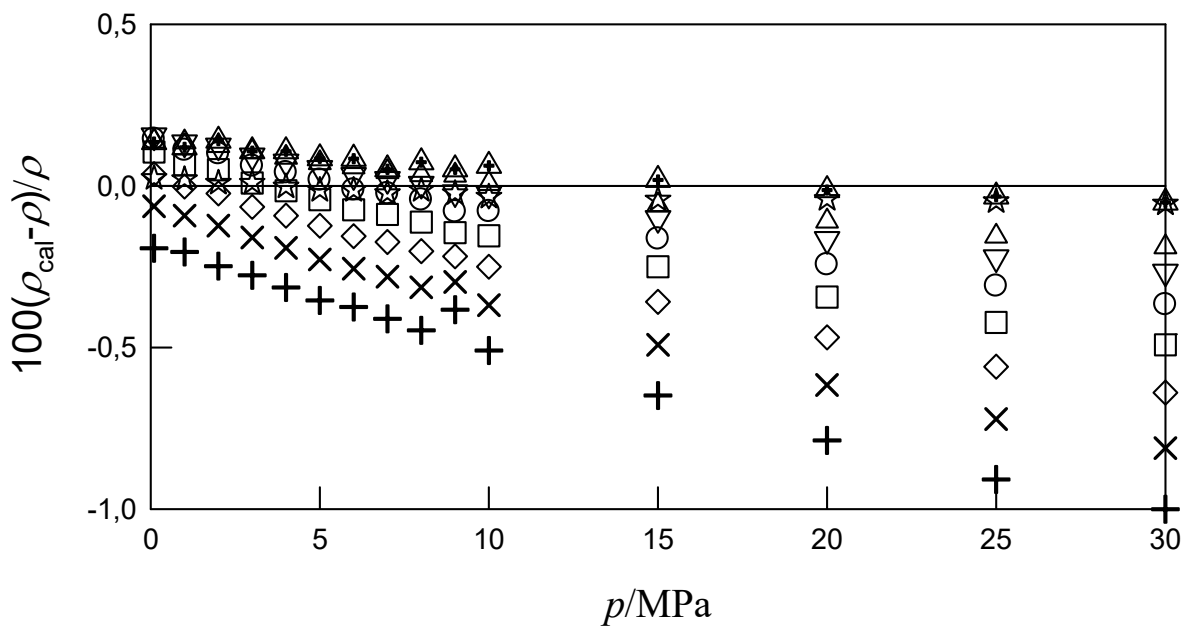


Figure 3.20. Relative density deviations between the predicted (ρ_{cal}) and the experimental (ρ) values as function of pressure and temperature for CSO and GCVOL/HALV: ☆, 278.15 K; ▲, 288.15 K; △, 298.15 K; ▽, 308.15 K; ○, 318.15 K; □, 328.15 K; ◇, 338.15 K; ×, 348.15 K; +, 358.15 K.

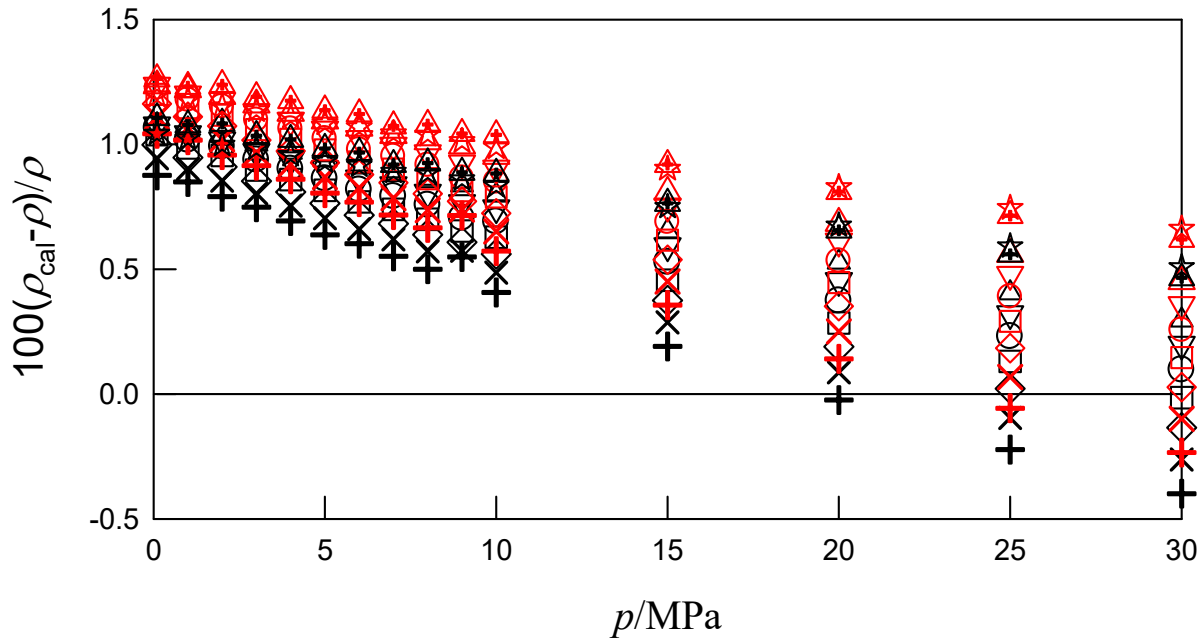


Figure 3.21. Relative density deviations between the predicted (ρ_{cal}) and the experimental (ρ) values as function of pressure and temperature for CSO with the GCVOL/ZONG(MTGA) (black) and GCVOL/ZONG(STGA) (red) methods: ☆, 278.15 K; ▲, 288.15 K; △, 298.15 K; ▽, 308.15 K; ○, 318.15 K; □, 328.15 K; ◇, 338.15 K; ×, 348.15 K; +, 358.15 K.

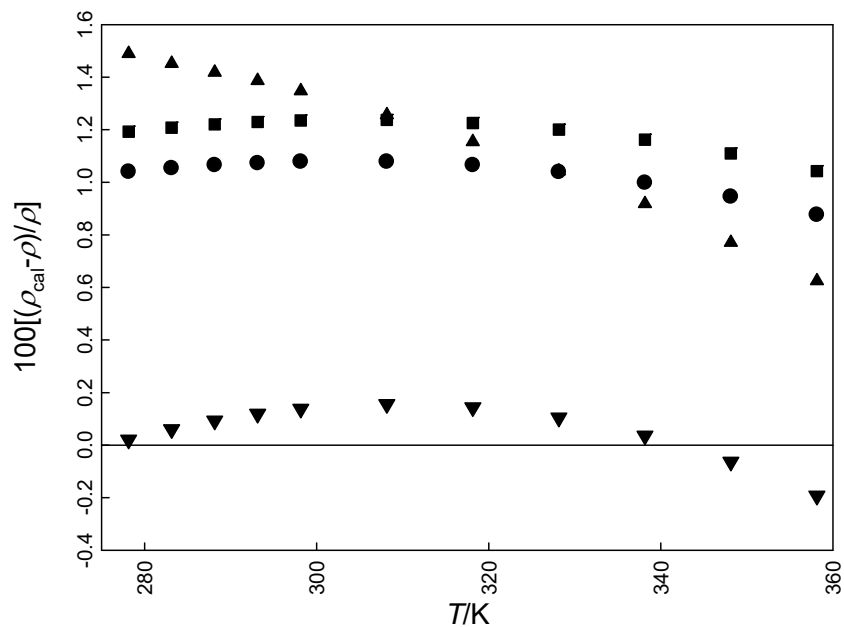


Figure 3.22. RDs between the predicted (ρ_{cal}) and the experimental values (ρ) of CSO at atmospheric pressure using GCVOL EoS and the GCVOL extension of Halvorsen and Zong models. ▲, GCVOL; ▼, GCVOL/HALV; ●, GCVOL/ZONG(MTGA); ■, GCVOL/ZONG(STGA).

From Figure 3.19, it can be seen that the *RDs* resulting from the application of GCVOL model to CSO are temperature-dependent, with a maximum of 1.9% at 278.15 K and 30 MPa and a minimum of 0.3% at 358.15 K at the same pressure. The overall *AARD* is 1.18%, which correspond to a very high *RMSD*. The predicted values of densities show always very high positive deviations. The relative deviations at atmospheric pressure are displayed in Figure 3.22. In spite of the high *RDs* obtained, the big advantage of this method is its simplicity and straightforward density estimation.

For GCVOL/HAL the densities are predicted with a very good level with overall *AARD* = 0.16% and low *RMSD* = 2.2 kg·m⁻³. a value which is close to the uncertainty of the measurements. From Figure 3.20, a temperature-dependence of *RDs* is observed again with maximum deviation of -1.0% at 358.15 K and 30 MPa and a minimum close to zero at 338.15 K and pressures lower than 10 MPa. From Figure 3.22 it can be concluded that deviations are in the range $\pm 0.2\%$.

From Figure 3.21, it can be seen that GCVOL/ZONG method with MTGA methodology, predicts density with a reasonable level of accuracy with overall *AARD* = 0.74% and accuracy of 7.23 kg/m³. A maximum deviation of 1.1% at 298.15 K and 0.1 MPa and a minimum of -0.01 at 338.15 K and 30.0 MPa are observed for the *RDs*. In Figure 3.22, deviations ranging between 0.9 and 1% (*AARD*=1.03%) are observed at atmospheric pressure. The results with STGA used in GCVOL/ZONG method are also displayed in Figure 3.21. They are similar to those obtained with MTGA (see Table 3.14). The predictions from PTGA method are not provided because they are similar to those obtained from MTGA. The advantages of using PTGA methodology is that it allows the prediction of density with the FFA oil profile, which is much easier to access and it is usually supplied in the analysis of the oils.

The densities of CSO and CSB were combined to develop a new predictive method as follow. Freitas et al. [84] reported experimental data on density for soybean (S), rapeseed (R) and palm (P) oils at temperatures $T = (283.15 \text{ to } 363.15) \text{ K}$ and $p = (0.1 \text{ to } 45.0) \text{ MPa}$ and Pratas et al. [19] measured the densities of the corresponding biodiesels in the ranges $T = (283.15 \text{ to } 333.15) \text{ K}$ and $p = (0.1 \text{ to } 45.0) \text{ MPa}$. Combining these data, the differences between the densities of the oil and corresponding biodiesel, $\Delta\rho = (\rho_{\text{oil}} - \rho_{\text{Bd}})$, were calculated as a function of temperature and pressure at overlapping (T, p) values for oil and biodiesel: $T = (293.15, 303.15 \text{ and } 323.15) \text{ K}$ and $p = (0.1 \text{ and } 30) \text{ MPa}$. Next, the mean value of differences of $\Delta\rho$ taken over the set (S, R and P)

oils was calculated at each (T, p) . In Figure 3.23 these mean values and the values corresponding at the differences density of CSO/CSB are represented at atmospheric pressure and at $p = 30.0$ MPa. In the same figure the error bars corresponding to the standard deviations for each mean value are displayed.

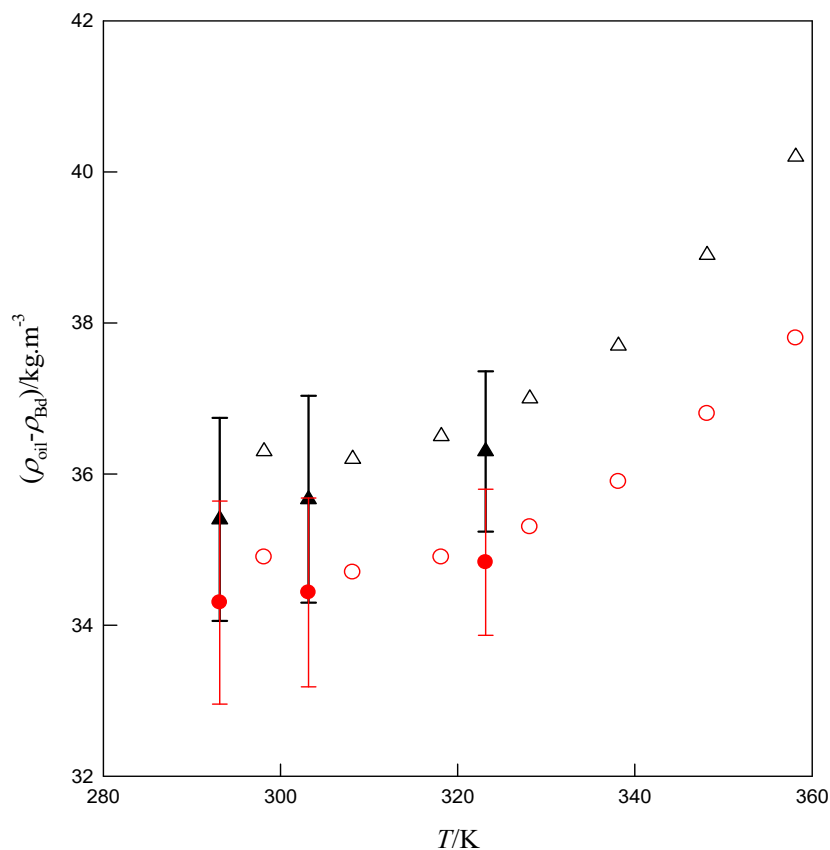


Figure 3.23. Density differences, $\Delta\rho$, between oil and biodiesel as function of temperature. Comparison between data of this work for CSO and CSB with values from other oils/biodiesel. Δ , CSO/CSB at $p = 0.1$ MPa; \circ , CSO/CSB at $p = 30$ MPa; mean values of density differences taken over the set (S, R and P) [19, 84]: \blacktriangle at $p = 0.1$ MPa and \bullet $p = 30$ MPa.

From Figure 3.23 it can be observed that the differences $\Delta\rho$ increase with temperature following a slightly parabolic trend. The increase of pressure from 0.1 MPa to 30 MPa decreases the difference in density by a maximum $1.5 \text{ kg}\cdot\text{m}^{-3}$ at 323.15 K. Data obtained for CSO and CSB show a general good agreement with the data for other oils (inside the errors of determinations). The error bars corresponding to the standard deviations of mean values indicate uncertainties of the order of the expanded uncertainty in the measurement of density in this work ($1.6 \text{ kg}\cdot\text{m}^{-3}$).

Figure 3.23 suggests that density of biodiesels can be estimated with good accuracy, within $\pm 2 \text{ kg}\cdot\text{m}^{-3}$ (uncertainty of about 0.2%), from measurements of oil density. As the influence of pressure in $\Delta\rho$ is small, it could be considered, at first approximation, that $\Delta\rho$ is function of temperature only. From the mean values of $\Delta\rho$, taken over the oil set (S, R and P) at atmospheric pressure the following equation is obtained:

$$\frac{\Delta\rho(p=0.1\text{MPa},T)}{\text{Kg}\cdot\text{m}^{-3}} = 42.394 - 7.272 \cdot 10^{-2}(T/K) + 1.6667 \cdot 10^{-4}(T/K)^2 \quad \text{Eq. 3-31}$$

The prediction of biodiesel densities from the densities reported for the oil, made with Eq. 3-31 will be labelled as simple density differences method (DDT). For consideration of pressure and temperature in $\Delta\rho$ other two models were built. In the first one, (DDTP1) the equation proposed by Pratas et al. [36] was considered:

$$\Delta\rho(T, p) = \frac{\Delta\rho(p=0.1\text{MPa},T)}{1+a(p-0.1)} \quad \text{Eq. 3-32}$$

where a is a parameter derived from least squares and p is the pressure, in MPa. In the second model (DDTP2), the modified Tait-Tammann equation was tested:

$$\Delta\rho(T, p) = \frac{\Delta\rho(p = 0.1\text{MPa}, T)}{1 - c \ln[(B + p)/(B + 0.1)]} \quad \text{Eq. 3-33}$$

where $B = b_0 + b_1T$. The parameters c , b_0 and b_1 are obtained by fitting Eq. 3-33 to $\Delta\rho$.

Eqs. 3-31 to 3-33 could be applied to predict CSB density from the density values available for the oil, and in a more general context they could be useful to predict biodiesel density at given (p, T) coordinates, from the corresponding density of the oil at the same conditions. In Table 3.15 the parameters of Eqs. 3-32 and 3-33 are given, as well as the coefficient of regression and the standard deviation.

Table 3.15. Coefficients of Eqs. 3-32 and 3-33.

	DDTP1	DDTP2
a / MPa^{-1}	1.243×10^{-3}	
c		0.5188
b_0 / MPa		-1174.2661
$b_1 / \text{MPa} \cdot \text{K}^{-1}$		2.4208
r^2	0.9847	0.9916
$\sigma_\rho / \text{kg} \cdot \text{m}^{-3}$	0.072	0.055

The statistical indicators of those models for the prediction of CSB densities, as function of pressure and temperature, are given it Table 3.16 and the deviations between the calculated and experimental CSB densities resulting from application of DDT method are displayed in Figure 3.24.

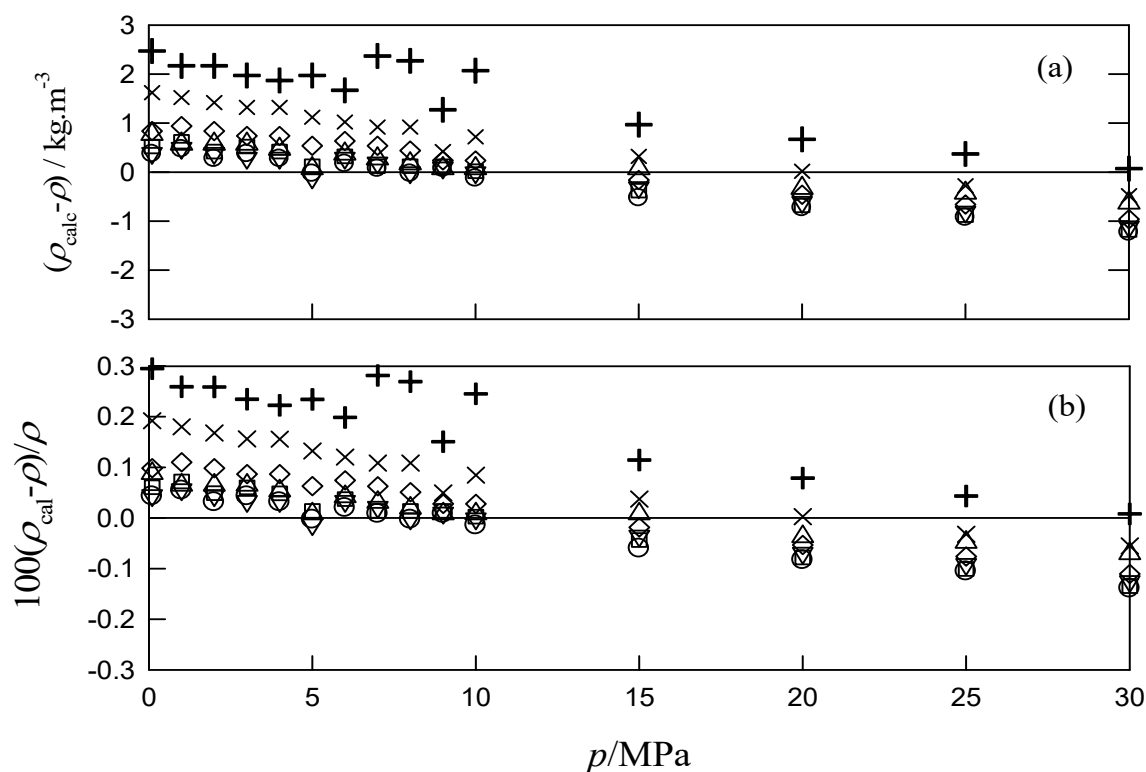


Figure 3.24. Density deviations and relative deviations between the predicted and the experimental values as function of pressure and temperature for CSB, from DDT. Δ , 298.15 K; ∇ , 308.15 K; \circ , 318.15 K; \square , 328.15 K; \diamond , 338.15 K; \times , 348.15 K; $+$, 358.15 K.

Table 3.16. Statistical results obtained from the application of the predictive models for the calculation of CSB densities.

Model	<i>AARD</i> (%)	<i>AAD</i> /kg.m ⁻³	<i>RMSD</i> /kg.m ⁻³
DDT	0.08	0.66	0.89
DDTP1	0.10	0.82	1.03
DDTP2	0.10	0.88	1.10

From the Figure 3.24 and from data available in Table 3.16 it can be concluded that DDT provide a good method for prediction of CSB densities. The prediction of densities can be made with $AARD = 0.08\%$ and $RMSD = 0.89 \text{ kg}\cdot\text{m}^{-3}$. It can be seen that only a minor part of CSB density data present deviations above $1 \text{ kg}\cdot\text{m}^{-3}$: 81% of predicted values deviates less than this value. Similar results were obtained using the measurements made by Freitas et al. for sunflower oil [84] and for sunflower biodiesel [87]. For this pair SFO/SFB the statistical measures were $AARD = 0.11\%$, $AAD = 0.95 \text{ kg}\cdot\text{m}^{-3}$ and $RMSD = 1.18 \text{ kg}\cdot\text{m}^{-3}$. The DDT method can be very useful to predict the biodiesel density from previous densities determinations of the original oil before the transesterification reaction. As it can be seen from Table 3.16, the DDTP1 and DDTP2 methods that take into account the correction for the pressure for $\Delta\rho$ gives almost the same good predictions as DDT method.

3.2.4.4 Mechanical coefficients

Some important mechanical properties, like the thermal expansivity, $\alpha_p = - (1/\rho)(\partial\rho/\partial T)_p$, and isothermal compressibility, $k_T = (1/\rho)(\partial\rho/\partial p)_T$, derived from the GMA equation of state [56], have been calculated and compared with the one obtained for biodiesel in the previous section.

The calculated mechanical coefficients, α_p and k_T , given by Eqs. 3-17 and 3-18 for CSO, are presented in Table B.5. In Figure 3.25(a) α_p of CSO decreases with the increase of pressure at isothermal conditions as expected but it decreases with temperature at isobaric conditions which is unusual. The α_p of CSO behaves abnormally until temperatures near 338 K. At this temperature the behaviour inversion occurs at 4 MPa and α_p increases with the temperature as expected. As far as it is know this behaviour was not reported for vegetable oils perhaps due to the scarcity of pVT measurements for these liquid substances.

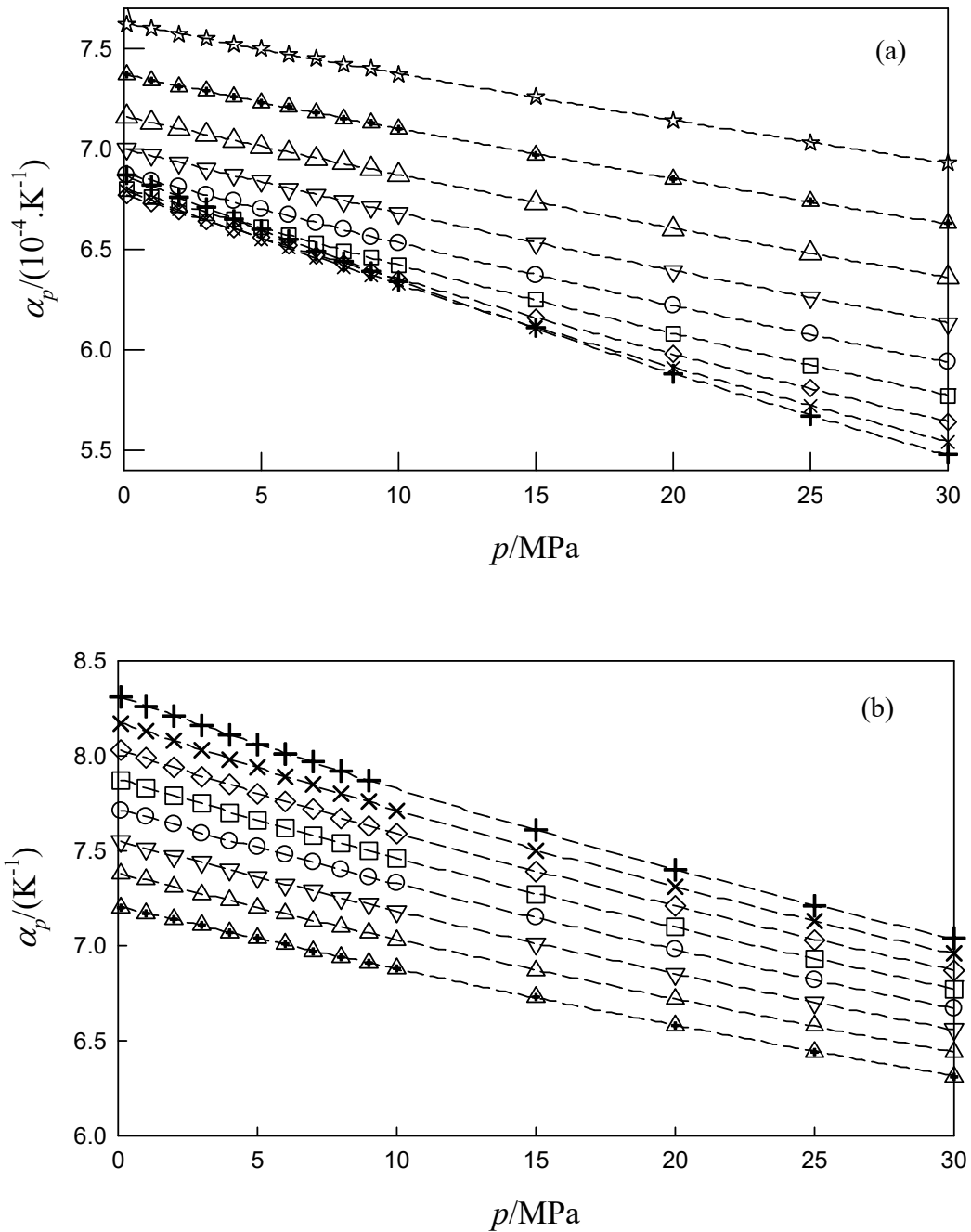


Figure 3.25. Thermal expansivity (α_p) as function of pressure for CSO (a) and CSB (b) predicted from GMA EoS: \star , 278.15 K; \blacktriangle , 288.15 K; \triangle , 298.15 K; \square , 308.15 K; \circ , 318.15 K; \square , 328.15 K; \diamond , 338.15 K; \times , 348.15 K; $+$, 358.15 K.

In the previous section for biodiesel, it have found that the values of α_p , behaved normally, i.e., increasing as temperature rises at isobaric conditions, particularly at low pressures (see

Figure 3.25(b)). However, at 65 MPa isotherms $(\alpha_p, p)_T$ intersect and after, a small decrease of α_p with temperature was observed, for pressures higher than 65 MPa as explained in section 3.1.5.

The value of α_p at standard conditions ($T = 298.15$ K, $p = 0.1$ MPa) for CSO and CSB are similar, $7.16 \times 10^{-4} \text{ K}^{-1}$ and $7.38 \times 10^{-4} \text{ K}^{-1}$, respectively. For CSB the value at those conditions is lower than the mean $\langle \alpha_p \rangle = (8.237 \pm 0.249) \times 10^{-4} \text{ K}^{-1}$ calculated over 19 biodiesels in a previous section and also is lower than the α_p value of Diesel D-2 $(8.20 \pm 0.16) \times 10^{-4} \text{ K}^{-1}$ calculated from the density data measured by Tat and Van Gerpen [21] and Santos et al. [60].

The thermal expansivity is related to the engine power loss due to the fuel heating [19]. Thus, from the results obtained for CSB and for diesel, some performance differences in power due to corresponding differences in α_p should be expected.

For k_T the observed variations with temperature and pressure of CSO and CSB are in according to the expected, as illustrated in the $(k_T, p)_T$ plots given in Figure 3.26. Some parabolic bends are observed in k_T as the temperature increases, particularly at low pressure. The value of k_T at standard conditions for CSO and CSB are 0.57 GPa^{-1} and 0.67 GPa^{-1} , respectively indicating that biodiesel is more compressible than the oil. This should be explained by the difference in molecular structure of the liquids, being FAMEs molecules more flexible than TGs ones. The value of k_T of CSB is close to the mean $\langle k_T \rangle = (0.68 \pm 0.01) \text{ GPa}^{-1}$ found in previous section taking into consideration 19 biodiesels. For Diesel D-2 the value 0.73 GPa^{-1} was calculated from the density data measured by Tat and Van Gerpen [21]. Biodiesel has compressibility close to Diesel which is advantageous in terms of the compression of diesel blends with biodiesel to be used in the injection.

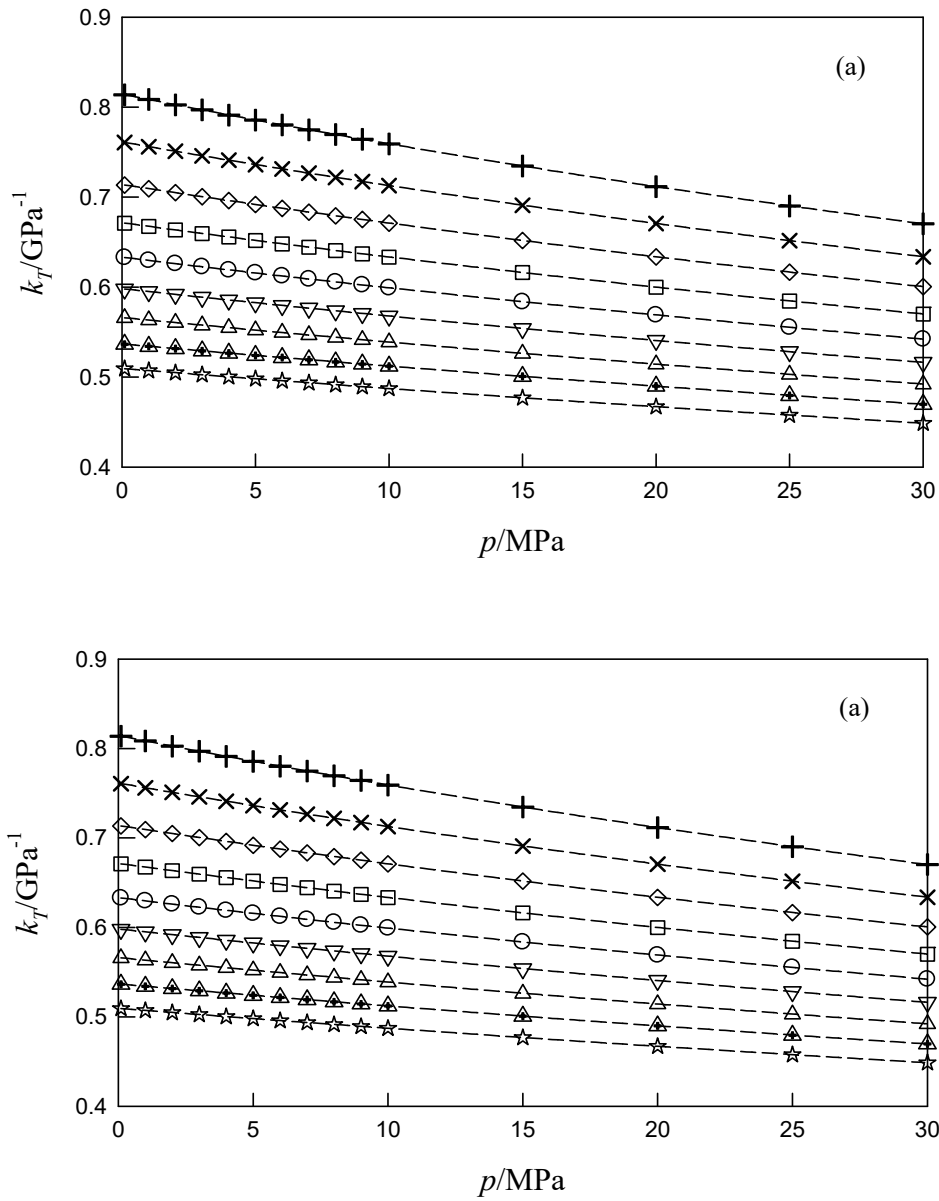


Figure 3.26. Isothermal compressibility (k_T) as function of pressure and temperature for CSO (a) and CSB (b) predicted from GMA EoS. : \star , 278.15 K; \blacktriangle , 288.15 K; \triangle , 298.15 K; ∇ , 308.15 K; \circ , 318.15 K; \square , 328.15 K; \diamond , 338.15 K; \times , 348.15 K; $+$, 358.15 K.

3.2.5. Conclusions

The experimental densities of cottonseed oil were measured in the range $T = (278.15 - 358.15)$ K and pressures $p = (0.1 - 30.0)$ MPa. The measured data were very well correlated with the Goharshadi–Morsali–Abbaspour equation of state with $AARD = 0.018\%$ which is only somewhat

higher than the value obtained for density data correlation of cottonseed biodiesel ($AARD = 0.007\%$). The group contribution method GCVOL combined with Halvorsen model and Zong fragment-based approaches (MTGA and STGA) are adequate for prediction of CSO density data: the temperature and pressure dependencies of experimental density data are described with $AARDs$ of 0.16%, 0.74% and 0.89%, respectively.

The density of CSO runs almost parallel with density of CSB for each isotherm with differences between $34.4 \text{ kg}\cdot\text{m}^{-3}$ to $40.2 \text{ kg}\cdot\text{m}^{-3}$. The densities of CSB can be predicted from CSO densities with very low density deviations ($AARD = 0.08\%$) using a new simple method (DDT) found in this work and which may possibly to be extended to most part of biodiesel fuels obtained from edible oils.

The behaviour of the thermal expansivity as a function of pressure was the predictable, i.e., a decreasing is observed for increasing pressures at isothermal conditions for oil and biodiesel. However, for the oil the same property decreased with increasing temperature at isobaric conditions which is unusual. This behaviour is reversed at 338 K. The isothermal compressibility behaves as expected i.e. an isobaric increase with temperature and an isothermal decrease with pressure was observed for oil and biodiesel.

3.3 References

1. Patil S, Akarte M. Effect of injection pressure on CI engine performance fuelled with biodiesel and its blends. *International Journal of Scientific & Engineering Research*. 2012;3(3):1-4.
2. Çelik BM, Şimşek D. The determination of optimum injection pressure in an engine fuelled with soybean biodiesel/diesel blend. *Thermal science*. 2014;18(1):229-38.
3. Liu H-P, Strank S, Werst M, Hebner R, Osara J, editors. Combustion emissions modeling and testing of neat biodiesel fuels. ASME 2010 4th International Conference on Energy Sustainability; 2010: American Society of Mechanical Engineers.
4. Ghurri A, Kim J-D, Kim HG, Jung J-Y, Song K-K. The effect of injection pressure and fuel viscosity on the spray characteristics of biodiesel blends injected into an atmospheric chamber. *Journal of mechanical science and technology*. 2012;26(9):2941-7.
5. Seykens X, Somers L, Baert R. Modelling of common rail fuel injection system and influence of fluid properties on injection process. *Proceedings of VAFSEP*. 2004:6-9.

6. Torres-Jimenez E, Svoljšak-Jerman M, Gregorc A, Lisec I, Dorado MP, Kegl B. Physical and chemical properties of ethanol– biodiesel blends for diesel engines. *Energy & Fuels*. 2009;24(3):2002-9.
7. Enweremadu C, Alamu O. Development and characterization of biodiesel from shea nut butter. *International Agrophysics*. 2010;24(1):29-34.
8. Alptekin E, Canakci M. Characterization of the key fuel properties of methyl ester–diesel fuel blends. *Fuel*. 2009;88(1):75-80.
9. Alptekin E, Canakci M. Determination of the density and the viscosities of biodiesel–diesel fuel blends. *Renewable energy*. 2008;33(12):2623-30.
10. Doll KM, Sharma BK, Suarez PA, Erhan SZ. Comparing biofuels obtained from pyrolysis, of soybean oil or soapstock, with traditional soybean biodiesel: density, kinematic viscosity, and surface tensions. *Energy & Fuels*. 2008;22(3):2061-6.
11. Dos Santos I, De Carvalho S, Solleti J, de La Salles WF, de La KTdS, Meneghetti S. Studies of *Terminalia catappa* L. oil: characterization and biodiesel production. *Bioresource technology*. 2008;99(14):6545-9.
12. Tiwari AK, Kumar A, Raheman H. Biodiesel production from jatropha oil (*Jatropha curcas*) with high free fatty acids: an optimized process. *Biomass and bioenergy*. 2007;31(8):569-75.
13. Baroutian S, Aroua MK, Raman AA, Sulaiman NM. Viscosities and densities of binary and ternary blends of palm oil+ palm biodiesel+ diesel fuel at different temperatures. *Journal of Chemical & Engineering Data*. 2009;55(1):504-7.
14. Huber ML, Lemmon EW, Kazakov A, Ott LS, Bruno TJ. Model for the thermodynamic properties of a biodiesel fuel. *Energy & Fuels*. 2009;23(7):3790-7.
15. Baroutian S, Aroua MK, Raman AA, Sulaiman NMN. Density of palm oil-based methyl ester. *Journal of Chemical & Engineering Data*. 2008;53(3):877-80.
16. Baroutian S, Aroua MK, Raman AA, Sulaiman NMN. Densities of ethyl esters produced from different vegetable oils. *Journal of Chemical & Engineering Data*. 2008;53(9):2222-5.
17. Tate R, Watts K, Allen C, Wilkie K. The densities of three biodiesel fuels at temperatures up to 300 C. *Fuel*. 2006;85(7-8):1004-9.
18. Tat ME, Van Gerpen JH. The specific gravity of biodiesel and its blends with diesel fuel. *Journal of the American Oil Chemists' Society*. 2000;77(2):115-9.

19. Pratas MJ, Oliveira MB, Pastoriza-Gallego MJ, Queimada AJ, Pineiro MM, Coutinho JA. High-pressure biodiesel density: experimental measurements, correlation, and cubic-plus-association equation of state (CPA EoS) modeling. *Energy & Fuels*. 2011;25(8):3806-14.
20. Tat ME, Van Gerpen JH. Speed of sound and isentropic bulk modulus of alkyl monoesters at elevated temperatures and pressures. *Journal of the American Oil Chemists' Society*. 2003;80(12):1249-56.
21. Tat ME, Van Gerpen JH. Measurement of Biodiesel Speed of Sound and Its Impact on Injection Timing: Final Report; Report 4 in a Series of 6. National Renewable Energy Lab., Golden, CO.(US), 2003.
22. Tat ME, Van Gerpen JH, Soylu S, Canakci M, Monyem A, Wormley S. The speed of sound and isentropic bulk modulus of biodiesel at 21 C from atmospheric pressure to 35 MPa. *Journal of the American Oil Chemists' Society*. 2000;77(3):285-9.
23. Nikolić BD, Kegl B, Marković SD, Mitrović MS. Determining the speed of sound, density and bulk modulus of rapeseed oil, biodiesel and diesel fuel. *Thermal Science*. 2012;16(suppl. 2):505-14.
24. Aparicio C, Guignon B, Rodríguez-Antón L, Sanz P. Determination of rapeseed methyl ester oil volumetric properties in high pressure (0.1 to 350 MPa). *Journal of thermal analysis and calorimetry*. 2007;89(1):13-9.
25. Dzida M, Prusakiewicz P. The effect of temperature and pressure on the physicochemical properties of petroleum diesel oil and biodiesel fuel. *Fuel*. 2008;87(10-11):1941-8.
26. Chhetri A, Watts K. Densities of canola, jatropha and soapnut biodiesel at elevated temperatures and pressures. *Fuel*. 2012;99:210-6.
27. Schedemann A, Wallek T, Zeymer M, Maly M, Gmehling J. Measurement and correlation of biodiesel densities at pressures up to 130 MPa. *Fuel*. 2013;107:483-92.
28. Dymond J, Malhotra R. The Tait equation: 100 years on. *International journal of thermophysics*. 1988;9(6):941-51.
29. Kontogeorgis GM, Michelsen ML, Folas GK, Derawi S, von Solms N, Stenby EH. Ten years with the CPA (Cubic-Plus-Association) equation of state. Part 1. Pure compounds and self-associating systems. *Industrial & engineering chemistry research*. 2006;45(14):4855-68.

30. Kontogeorgis GM, Michelsen ML, Folas GK, Derawi S, von Solms N, Stenby EH. Ten years with the CPA (Cubic-Plus-Association) equation of state. Part 2. Cross-associating and multicomponent systems. *Industrial & Engineering Chemistry Research*. 2006;45(14):4869-78.
31. Schmid B, Gmehling J. From van der Waals to VTPR: The systematic improvement of the van der Waals equation of state. *The Journal of Supercritical Fluids*. 2010;55(2):438-47.
32. Weidlich U, Gmehling J. A modified UNIFAC model. 1. Prediction of VLE, hE, and γ_{∞} . *Industrial & engineering chemistry research*. 1987;26(7):1372-81.
33. Gross J, Sadowski G. Application of perturbation theory to a hard-chain reference fluid: an equation of state for square-well chains. *Fluid Phase Equilibria*. 2000;168(2):183-99.
34. B Oliveira M, V.D. Freitas S, Llovel F, Vega L, A.P. Coutinho J. Development of simple and transferable molecular models for biodiesel production with the soft-SAFT equation of state 2014.
35. Dong NH, Thuy NT, Tho V. Predicting the temperature/pressure dependent density of biodiesel fuels. *Petrovietnam J*. 2012;10:46-58.
36. Pratas MJ, Freitas SV, Oliveira MB, Monteiro SC, Lima AS, Coutinho JA. Biodiesel density: Experimental measurements and prediction models. *Energy & Fuels*. 2011;25(5):2333-40.
37. Meng X, Jia M, Wang T. Predicting biodiesel densities over a wide temperature range up to 523K. *Fuel*. 2013;111:216-22.
38. Spencer CF, Danner RP. Improved equation for prediction of saturated liquid density. *Journal of Chemical & Engineering Data*. 1972;17(2):236-41.
39. Goharshadi EK, Morsali A, Abbaspour M. New regularities and an equation of state for liquids. *Fluid phase equilibria*. 2005;230(1-2):170-5.
40. Nogueira Jr CA, Feitosa FX, Fernandes FA, Santiago RIS, de Sant'Ana HB. Densities and viscosities of binary mixtures of babassu biodiesel+ cotton seed or soybean biodiesel at different temperatures. *Journal of Chemical & Engineering Data*. 2010;55(11):5305-10.
41. Ferreira CE, Talavera-Prieto NM, Fonseca IM, Portugal AT, Ferreira AG. Measurements of pVT, viscosity, and surface tension of trihexyltetradecylphosphonium tris (pentafluoroethyl) trifluorophosphate ionic liquid and modelling with equations of state. *The Journal of Chemical Thermodynamics*. 2012;47:183-96.

42. NIST. Thermophysical properties of fluids. Accessed in June 2014. Available from: <http://webbook.nist.gov/chemistry/fluid/>.
43. Private communication from Parr A. 2005.
44. Sun TF, Ten Seldam CA, Kortbeek PJ, Trappeniers NJ, Biswas SN. Acoustic and Thermodynamic Properties of Ethanol from 273.15 to 333.15 K and up to 280 MPa. *Physics and Chemistry of Liquids*. 1988: 107-16.
45. Ramos MJ, Fernández CM, Casas A, Rodríguez L, Pérez Á. Influence of fatty acid composition of raw materials on biodiesel properties. *Bioresource Technology*. 2009;100(1):261-8.
46. Mohibbe Azam M, Waris A, Nahar NM. Prospects and potential of fatty acid methyl esters of some non-traditional seed oils for use as biodiesel in India. *Biomass and Bioenergy*. 2005;29(4):293-302.
47. Islam M, Magnusson M, J. Brown R, Godwin A, Nabi M, Heimann K. Microalgal Species Selection for Biodiesel Production Based on Fuel Properties Derived from Fatty Acid Profiles. *Energies*. 2013;6(11): 5676-702.
48. EN 14214: 2012+ A1: 2014. Liquid petroleum products Fatty acid methyl esters (FAME) for use in diesel engines and heating applications Requirements and test methods.
49. Elbro HS, Fredenslund A, Rasmussen P. Group contribution method for the prediction of liquid densities as a function of temperature for solvents, oligomers, and polymers. *Industrial & engineering chemistry research*. 1991;30(12):2576-82.
50. Ihmels EC, Gmehling J. Extension and Revision of the Group Contribution Method GCVOL for the Prediction of Pure Compound Liquid Densities. *Industrial & Engineering Chemistry Research*. 2003;42(2):408-12.
51. Pratas MJ, Freitas S, Oliveira MB, Monteiro SC, Lima AS, Coutinho JA. Densities and viscosities of fatty acid methyl and ethyl esters. *Journal of Chemical & Engineering Data*. 2010;55(9):3983-90.
52. Pratas MJ, Freitas S, Oliveira MB, Monteiro SC, Lima AS, Coutinho JA. Densities and viscosities of minority fatty acid methyl and ethyl esters present in biodiesel. *Journal of Chemical & Engineering Data*. 2011;56(5):2175-80.
53. Ndiaye EHI, Habrioux M, Coutinho JAP, Paredes MLL, Daridon JL. Speed of Sound, Density, and Derivative Properties of Ethyl Myristate, Methyl Myristate, and Methyl

- Palmitate under High Pressure. *Journal of Chemical & Engineering Data*. 2013;58(5):1371-7.
54. Outcalt SL. Compressed-Liquid Density Measurements of Methyl Oleate and Methyl Linoleate. *Journal of Chemical & Engineering Data*. 2011;56(11):4239-43.
55. Prieto NM, Ferreira AG, Portugal AT, Moreira RJ, Santos JB. Correlation and prediction of biodiesel density for extended ranges of temperature and pressure. *Fuel*. 2015;141:23-38.
56. Goharshadi E, Moosavi M. Thermodynamic properties of some ionic liquids using a simple equation of state. *Journal of Molecular Liquids*. 2008;142(1-3):41-4.
57. Randzio SL. An attempt to explain thermal properties of liquids at high pressures. *Physics Letters A*. 1986;117(9):473-6.
58. Bridgman PW. *Physics of High Pressure*. New York: Dover Publications Inc.; 1970.
59. Taravillo M, Baonza VG, Cáceres M, Núñez J. Thermodynamic regularities in compressed liquids: I. The thermal expansion coefficient. *Journal of Physics: Condensed Matter*. 2003;15(19):2979.
60. Santos DQ, de Lima AL, de Lima AP, Neto WB, Fabris JD. Thermal expansion coefficient and algebraic models to correct values of specific mass as a function of temperature for corn biodiesel. *Fuel*. 2013;106:646-50.
61. Chen CT, Fine RA, Millero FJ. The equation of state of pure water determined from sound speeds. *The Journal of Chemical Physics*. 1977;66(5):2142-4.
62. Gonçalves F, Trindade A, Costa C, Bernardo J, Johnson I, Fonseca I, et al. PVT, viscosity, and surface tension of ethanol: New measurements and literature data evaluation. *The Journal of Chemical Thermodynamics*. 2010;42(8):1039-49.
63. Zorębski E. Internal pressure studies of alcohols on the basis of ultrasonic measurements. *Molecular and Quantum Acoustics*. 2005;26:317-26.
64. Goodrum J. Volatility and boiling points of biodiesel from vegetable oils and tallow. *Biomass and Bioenergy*. 2002;22(3):205-11.
65. Yuan W, Hansen A, Zhang Q. Vapor pressure and normal boiling point predictions for pure methyl esters and biodiesel fuels. *Fuel*. 2005;84(7-8):943-50.
66. Zhang Y, Mallapragada SK, Narasimhan B. Dissolution of waste plastics in biodiesel. *Polymer Engineering & Science*. 2010;50(5):863-70.

67. Ivanov E, Abrosimov V. Relationship between the internal pressure and cohesive energy density of a liquid nonelectrolyte. Consequences of application of Dack's concept. *Journal of Structural Chemistry*. 2005;46(5):856-61.
68. Cabane B, Vuilleumier R. The physics of liquid water. *Comptes Rendus Geoscience*. 2005;337(1):159-71.
69. Yuan W, Hansen AC, Zhang Q. Computational modelling of NO_x emissions from biodiesel combustion. *International journal of vehicle design*. 2007;45(1-2):12-32.
70. Chia-fon FL, Hansen AC. Investigation of Bio-Diesel Fueled Engines under Low-Temperature Combustion Strategies. FINAL REPORT DE-FC26-05NT42634. Board of Trustees of the University of Illinois, submitted to U.S. Department of Energy, National Energy Technology Laboratory.
71. Cataldo F, Ursini O, Angelini G. Biodiesel as a plasticizer of a SBR-based tire tread formulation. *ISRN Polymer Science*. 2013. Article ID 340426, 9 pages <http://dx.doi.org/10.1155/2013/340426>.
72. Rashid U, Anwar F, Knothe G. Evaluation of biodiesel obtained from cottonseed oil. *Fuel Processing Technology*. 2009;90(9):1157-63.
73. Isaac IO, Ekpa OD. Fatty acid composition of cottonseed oil and its application in production and evaluation of biopolymers. *American Journal of Polymer Science*. 2013;3(2):13-22.
74. Cruz-Aldaco K, Flores-Loyola E, Aguilar-González CN, Burgos N, Jiménez A. Synthesis and Thermal Characterization of Polyurethanes Obtained from Cottonseed and Corn Oil-Based Polyols. *Journal of Renewable Materials*. 2016;4(3):178-84.
75. Shakina J, Muthuvinothini A. Synthesis and Characterization of Cotton Seed Oil based Biodegradable Thermosetting Polymers. *Journal of Academia and Industrial Research (JAIR)*. 2015;3(10):520.
76. Menzies AWCK, WG, Bingham, EC. Determination of specific heat, density, surface tension, viscosity, and lubricating value of typical oils. Bingham, E. C. *Cutting fluids. Technologic Papers of Bureau of Standards*, 1922, T 204. 247-9. <https://archive.org/details/cuttingfluids1922204bing>. (accessed April 2018)..
77. Magne FC, Hughes EJ, Skau EL. Density-composition data for cottonseed oil-solvent mixtures. *Journal of the American Oil Chemists Society*. 1950;27(12):552-5.

78. Arnold LK, Juhl WG, Arvidson HC. Densities and viscosities of trichloroethylene miscellas of cottonseed oil, fish oil, and beef tallow. *Journal of the American Oil Chemists' Society*. 1954;31(9):393-4.
79. Demirbas A. Relationships derived from physical properties of vegetable oil and biodiesel fuels. *Fuel*. 2008;87(8-9):1743-8.
80. Macovei VM. Culegere de caracteristici termofizice pentru biotehnologie și industria alimentară : Tabele și diagrame. Română: Alma Galați; 2000.
81. Eryılmaz T, Yeşilyurt M, Yumak H, Arslan M, Şahin S. Determination of the Fuel Properties of Cottonseed Oil Methyl Ester and Its Blends with Diesel Fuel/Pamuk Tohumu Metil Esteri Ve Dizel Yakıt İle Karışımlarının Yakıt Özelliklerinin Belirlenmesi. *International Journal of Automotive Engineering and Technologies*. 2014;3(2):79-90.
82. Halvorsen J, Mammel W, Clements L. Density estimation for fatty acids and vegetable oils based on their fatty acid composition. *Journal of the American Oil Chemists' Society*. 1993;70(9):875-80.
83. Zong L, Ramanathan S, Chen C-C. Fragment-based approach for estimating thermophysical properties of fats and vegetable oils for modeling biodiesel production processes. *Industrial & engineering chemistry research*. 2009;49(2):876-86.
84. Freitas SV, e Silva FA, Pastoriza-Gallego MJ, Piñeiro MM, Lima AIS, Coutinho JoA. Measurement and Prediction of Densities of Vegetable Oils at Pressures up to 45 MPa. *Journal of Chemical & Engineering Data*. 2013;58(11):3046-53.
85. Ceriani R, Meirelles AJ. Predicting vapor–liquid equilibria of fatty systems. *Fluid Phase Equilibria*. 2004;215(2):227-36.
86. Chang A-F, Liu Y. Integrated process modeling and product design of biodiesel manufacturing. *Industrial & Engineering Chemistry Research*. 2009;49(3):1197-213.
87. Ivaniš GR, Radović IR, Veljković VB, Kijevčanin ML. Biodiesel density and derived thermodynamic properties at high pressures and moderate temperatures. *Fuel*. 2016;165:244-51.

4 CHAPTER

VISCOSITY OF COTTONSEED OIL AND BIODIESEL

In this chapter, the viscosities of CSO and CSB were measured at atmospheric pressure and temperatures from (293 to 373) K and (303 to 348) K, respectively. The Vogel-Fulcher-Tammann (VFT) and Mauro (MYEGA) equations were selected to represent the temperature dependence of the experimental data, giving deviations within the experimental uncertainties. The prediction of CSO and CSB viscosities was made with the Ceriani and Zong models for CSO and the Grunberg-Nissan equation coupled with Ceriani and Yuan models for CSB. The influence of interaction parameter (G_{ij}) in Grunberg-Nissan equation was studied.

4.1 Introduction

Viscosity is one of the most important properties of a biodiesel that must be in accordance with the standards. Viscosity affects the spray quality of fuels in direct-injection diesel engines. Fuels with high viscosity tends to form larger droplets upon injection, which may result in a poor fuel atomization, increasing the engine deposits and affects the quality of fuel/air mixture and, consequently, the exhaust emissions from the engine. It is also important to verify the viscosity behaviour with temperature variation since an increase in temperature between the fuel pump and the fuel injector it is expected, thus affecting the injection system design. Reducing viscosity is the major reason why vegetables oil or fats are transesterified to biodiesel. Moreover, in the synthesis process, the knowledge of physical properties such as viscosity is of great importance. Design of pipes, reactors, pumps, mixers, settlers and other equipment involved in biodiesel production is highly dependent on the viscosity of both, oil and biodiesel.

The viscosity of CSO has been measured by different authors with different methodologies and with different purposes. Beyond the measurements made by several authors at one temperature, viscosity data as function of this variable are due to Macovei [1], Eryilmaz et al. [2] and Wakeham and Magne [3]. The viscosity data of CSB is scarce from the literature. The few studies over extensive ranges of temperature were made by Eryilmaz et al. [2] and Nogueira et al. [4].

This chapter aims to provide experimental viscosity data of CSO and CSB at atmospheric pressure and temperatures in the range $T = (293 \text{ to } 373) \text{ K}$ and $T = (303 \text{ to } 348) \text{ K}$, respectively. Viscosity data were correlated with Vogel-Fulcher-Tammann (VFT) [5-7] and Mauro (MYEGA) [8] equation. The predictive ability of Zong's fragment-based [9] and Ceriani [10] models were evaluated for CSO, and the Ceriani [10] and Yuan's model revised by Freitas et al. [11], were applied to CSB. The importance of the use of interaction contributions parameter in Grunberg and Nissan [12] equation in viscosity of CSB were quantitatively studied.

4.2 Experimental section

4.2.1 Materials

The detailed specifications of the CSO used in viscosity measurements were summarized in Table 3.1.

The details of CSO transesterification to produce the biodiesel and its characterization were given in section 3.1.2.2 and 3.1.2.3, respectively. The molar and mass compositions of CSO and CSB are presented in Table 3.9.

4.2.2 Viscosity measurements

Dynamic viscosity measurements of CSO were made over the temperature (293 to 373) K at atmospheric pressure using a Brookfield Thermosel system with a rotational DV-II+ (model LVDV- II) viscometer. Temperature was controlled to better than ± 0.01 K, which was considered as the uncertainty of temperature measurements. The stirring action of the rotating spindle, plus the small sample volume helped to keep the temperature gradient across the sample to a minimum. For each measurement, the temperature was measured by a platinum resistance thermometer ERTCO-Eutechnics High Precision Digital Thermometer certified in the ITS90 with an uncertainty of 0.01K. The spindle SC4-18 was used for the viscosity measurements with a sample volume of 8.0 ml and rotational speeds from (10 to 200) RPM was used. This measurements are accurate to within $\pm 1\%$ of the full-scale viscosity range for a given spindle/speed combination and the reproducibility is within $\pm 0.2\%$ [13]. For SC4-18, spindle factor is $30/N$ where N is the rotational speed (RPM). The full-scale range of viscosity corresponding to any spindle/speed combination is the factor multiplied by 100. As the same accuracy of $\pm 1\%$ applies to the readings in the range, the accuracy of viscosity measurement will increase as the reading approaches 100% of full-scale. Thus it is possible to measure almost the same viscosity value with different error levels at different speeds. Whenever possible, measurements were made at speeds corresponding to the higher percentage readings for the spindle. At each temperature the viscosity was measured several times and the mean value of measurements and corresponding standard deviation (usually less than 0.5% relative to the mean value) were derived providing a good precision of measurements. Prior to measurements, the viscometer was checked with a Brookfield viscosity standard certified by NIST, with viscosity

49.9 mPa·s at 298.15 K. The measured value for this standard was $\eta = (50.9 \pm 0.1)$ mPa·s. Taking into account the uncertainties of temperature and repeatability of measurements, the combined uncertainty of viscosity was estimated to be better than 2.0%.

Kinematic viscosities of CSB were determined by using an Ubbelohde viscometer (Schott type 53203/0c) with a Schott–Geräte automatic measuring unit (Model AVS-470), for which the uncertainty in the flow time of measurement is 0.01 s. The visco-system AVS-470 was coupled to an optical viscoPump II and a heater controller bath CT52, all from Shott instruments. The temperature was monitored by a digital thermometer with an uncertainty of ± 0.01 K. The kinematic viscosity (ν) is obtained by using the equation:

$$\nu = K(t - \tau) \tag{Eq. 4-1}$$

where, K is the viscometer constant, t is the flow time in seconds, and τ is the Hagenbach-Couette kinetic energy correction, which value is given by the manufacturer. This correction is given for each capillary tube and depends on the flow time. The viscometer constant (K) is given in an enclosed production certificate and was validated and checked with pure compounds (methanol and 1-propanol) viscosity measurements from (273.15 to 323.15) K. For each sample, at least five individual measurements were made, allowing the calculation of the average viscosity as well as the associated standard deviation, which was of the order of $0.01 \text{ mm}^2 \cdot \text{s}^{-1}$. The kinematic viscosity measurements were made over the range (303.15 to 348.15) K and were transformed into dynamic viscosity ($\eta = \rho\nu$) using the values of density (ρ) at atmospheric pressure calculated from the GMA EoS [14]. Considering the uncertainties in the measured time and density, the combined standard uncertainty in the dynamic viscosity, $u_c(\eta)$ is estimated as 0.01 mPa·s.

The measurement of the atmospheric pressure was made using a calibrated pressure transducer (AFRISO Euro-Index, DMU03). Taking the observed values covering the years 2013-2014, the mean value was $p = (102.05 \pm 0.19)$ kPa.

4.3 Viscosity models

4.3.1 Correlation

Modelling of the temperature effect on the dynamic viscosity of vegetable oils has been investigated by various researchers as Kapseu et al. [15], Nouredini et al. [16], Lang et al. [17], Toro-Vazquez et al. [18] and more recently by Yilmaz [19]. Usually, the effect of temperature in viscosity of oils is given through the Arrhenius-type relationship:

$$\eta = Ae^{E^a/RT} \quad \text{Eq. 4-2}$$

where, η is dynamic viscosity, A the pre-exponential factor, E^a the activation energy, R the gas constant and T the absolute temperature. The factor A corresponds to the value of the viscosity at the high temperature limit, $A = \ln \eta_\infty$.

An issue that has been raised recently and which remains open is the possibility of determining the glass transition temperature of vegetable oils, T_g . Thermal analysis methods such as differential scanning calorimetry (DSC) can be used to detect the glass transition of materials with low amorphous content. Abdulkarim and Ghazali studied the possibility of such detection for several oils using HyperDSC techniques at very fast scan rates [20] and they detected glass transitions in canola, sunflower and cocoa butter. However, these transitions show a large temperature range and exact temperature values were not reported.

To represent the temperature dependence of viscosity in wide temperature ranges three parameters equations have been used. Among them, one of the most commonly used is the Vogel-Fulcher-Tammann (VFT) equation [5-7]:

$$\ln \eta = A_{\text{VFT}} + \frac{B_{\text{VFT}}}{T - T_0} \quad \text{Eq. 4-3}$$

where, $A_{\text{VFT}} = \ln \eta_\infty$ is the pre-exponential factor. The constants A_{VFT} , B_{VFT} and T_0 are the fitting parameters. T_0 is the Vogel temperature, also called “ideal glass transition temperature” at which all movements of the constituent elements of a liquid are considered to be totally frozen. However, the temperature dependence of viscosity of supercooled liquids cannot be described over the entire range of temperature with a single VFT equation [21, 22] and thus other equations

can be preferred for data correlation over large ranges of temperatures. For this purpose, Mauro et al. [8] proposed a new model (MYEGA) for the viscosity of glass forming liquids (GFL):

$$\ln \eta = A_{\text{MYEGA}} + \left(\frac{B_{\text{MYEGA}}}{T} \right) e^{(C_{\text{MYEGA}}/T)} \quad \text{Eq. 4-4}$$

where, $A_{\text{MYEGA}} = \ln \eta_{\infty}$, B_{MYEGA} and C_{MYEGA} are fitting parameters.

The viscosity departure from an Arrhenius temperature-dependence of GFLs is described by the ‘fragility’ parameter, m : [23]:

$$m = \left[\frac{d \log \eta}{d (T_g/T)} \right]_{T=T_g} \quad \text{Eq. 4-5}$$

Small values of m (ca. 20) correspond to strong materials and high values ($m \approx 100$) to fragile systems.

Eqs. 4-3 and 4-4 can be rewritten as equivalent equations in terms of T_g , m , $\ln \eta_{\infty}$, and the viscosity at T_g , $\ln \eta_g$. From Eq. 4-5, taking into account ($x = T_g / T$) the Eqs. 4-3 and 4-4 are:

VFT:

$$\ln \eta = \ln \eta_{\infty} + \frac{[\ln(\eta_g/\eta_{\infty})]^2}{[2.3m(x^{-1}) + \ln(\eta_g/\eta_{\infty})]} \quad \text{Eq. 4-6}$$

where

$$B_{\text{VFT}} = T_g \frac{[\ln(\eta_g/\eta_{\infty})]^2}{\ln(10) m} \quad \text{Eq. 4-7}$$

$$T_o = T_g \left[1 - \frac{\ln(\eta_g/\eta_{\infty})}{\ln(10) m} \right] \quad \text{Eq. 4-8}$$

MYEGA:

$$\ln \eta = \ln \eta_{\infty} + x \ln \left(\frac{\eta_g}{\eta_{\infty}} \right) \exp \left[\left(\frac{\ln(10) m}{\ln(\eta_g/\eta_{\infty})} \right) (x - 1) \right] \quad \text{Eq. 4-9}$$

where

$$B_{\text{MYEGA}} = T_g \ln(\eta_g/\eta_{\infty}) \exp \left[1 - \frac{\ln(10) m}{\ln(\eta_g/\eta_{\infty})} \right] \quad \text{Eq. 4-10}$$

$$C_{\text{MYEGA}} = T_g \left[\frac{\ln(10)}{\ln(\eta_g/\eta_{\infty})} - 1 \right] \quad \text{Eq. 4-11}$$

4.3.2 Prediction

4.3.2.1 Zong method

Zong et al. [9] developed a predictive fragment-based method for the calculation of dynamic viscosity of vegetable oils. As for liquid molar volume, each TG molecule is divided into four parts, one glycerol fragment and three fatty acid fragments. The viscosity of oil, η_{oil} , is [9]:

$$\ln \eta_{oil} = \sum_i w_i \ln \eta_i \quad \text{Eq. 4-12}$$

where, η_i and w_i are the viscosity and mass fraction of triglyceride i , respectively. The viscosity of each liquid triglyceride specie (η_i) is [9]:

$$\ln \eta_i = \sum_A N_{frag,A} \ln \eta_A(T) \quad \text{Eq. 4-13}$$

where, η_A is the viscosity contribution of fragment A (in Pa.s) and $N_{frag,A}$ is the number of fragment A in the TG molecule. The temperature dependency of viscosity, η_A , is [9]:

$$\ln \eta_A = C_{1,A} + \frac{C_{2,A}}{T} + C_{3,A} \ln T \quad \text{Eq. 4-14}$$

where, $C_{1,A}$, $C_{2,A}$ and $C_{3,A}$ are the temperature dependency parameters of fragment A and T is the temperature (K). The values of parameters $C_{1,A}$, $C_{2,A}$ and $C_{3,A}$ are reported in Table C.1 for the fragments involved in CSO.

The application of Eqs. 4-12 to 4-14 need the knowledge of the triglyceride profile of the oil and thus, MTGA, STGA and PTGA approximations can be used in this context, as explained for density (Section 3.2.4.1).

4.3.2.2 Grunberg-Nissan

One of the most suitable equations for the calculation of viscosity of FAME mixtures, η_{mix} , is the Grunberg-Nissan equation [12]:

$$\ln \eta_{mix} = \sum_i x_i \ln \eta_i + \sum_{i=1}^N \sum_{j=1}^N x_i x_j G_{ij} \quad \text{Eq. 4-15}$$

where, η_i (mPa.s) is the viscosity of the FAME i , x_i and x_j are the molar fractions of the i^{th} and j^{th} components, G_{ij} is the interaction parameter (mPa.s), and N is the number of components in the mixture. Given that biodiesel fuels are non-associated liquids (i.e. they have essentially a dispersive interaction between the individual components) composed of mixtures of FAMEs with similar structures, their dynamic viscosity can be estimated from Eq. 4-15 considering $G_{ij} = 0$, obtaining:

$$\ln \eta_{mix} = \sum_i x_i \ln \eta_i \quad \text{Eq. 4-16}$$

However, neglecting G_{ij} is the main reason for underestimating mixture viscosity [24]. Existing data suggest that for alkane solutions G_{ij} is constant, independent of temperature and this approximation could be extended to the mixtures of non-polar molecules as FAMEs.

For the calculation of the viscosity of individual FAME, η_i , different methods will be used as described in the following sections.

4.3.2.3 Yuan models

Yuan model [24] use the Vogel-Tammann-Fulcher equation to describe the viscosity temperature relationship of pure FAMES. Freitas et al. [11] refitted the parameters of VFT equation using new and more accurate data for viscosity of FAMES reported by Pratas et al. [25, 26]. The parameters are given in Table C.2.

4.3.2.4 Ceriani's model

Ceriani et al. [10] proposed a group contribution method to predict the viscosity of fatty acid compounds. A compound or a mixture of compounds is treated as a solution of groups, and its properties are the averaged sum of contributions of each group. The calculation of dynamic viscosity of mixture component i is [10]:

$$\ln \eta_i = \sum_k N_k A_{1k} + \frac{\sum_k N_k B_{1k}}{T + \sum_k N_k C_{1k}} + \left[M_i \left(\sum_k N_k A_{2k} + \frac{\sum_k N_k B_{2k}}{T + \sum_k N_k C_{2k}} \right) \right] + Q \quad \text{Eq. 4-17}$$

$$Q = \xi_1 q + \xi_2 \quad q = \alpha + \frac{\beta}{T + \gamma} \quad \xi_1 = f_0 + N_c f_1 \quad \xi_2 = s_0 + N_{cs} s_1 \quad \text{Eq. 4-18}$$

where N_k is the number of groups k in the molecule i ; M_i is molar mass of the compound; A_{1k} , B_{1k} , C_{1k} , are first order parameters and A_{2k} , B_{2k} , and C_{2k} are second order parameters, obtained from the regression of the experimental data, k represents the groups in component i , Q is a correction term, f_0 , f_1 , s_0 , and s_1 are optimized constants, α , β , γ , and δ are also optimized parameters obtained by regression of the viscosity databank as a whole, N_c is the total number of carbon atoms in the molecule, and N_{cs} is the number of carbons of the alcohol side chain. The parameter values found by Ceriani et al. [10] are given Table C.3. Ceriani et al. obtained *AARDs* of 4.81% for applications of Eq. 4-17 to TGs, with maximum *RD* = 33% and minimum *RD* = 0.03%.

4.4 Results and discussion

4.4.1 Correlation of CSO and CSB viscosities

The viscosities of the CSO measured in this work at atmospheric pressure in the range $T = (293 \text{ to } 373) \text{ K}$ are presented in Table 4.1. At each temperature, the viscosity as function of shear rate represented by the rotational speed is shown. From this table, it can be concluded that CSO can be considered as Newtonian fluid for temperatures lower than 373.15 K because the viscosity is almost constant and independent of shear rate. In Figure 4.1 the viscosity is plotted against the rotational speed at temperatures $T = (353.15; 363.15 \text{ and } 373.15) \text{ K}$. At 373.15 K thinning behaviour is clearly observed: a rapid decrease of viscosity with shear rate at low shear, followed by a Newtonian plateau for rotational speeds higher than 60 rpm up to 200 rpm. At temperatures lower than 373.15 K, the Newtonian behaviour is seen after $N=10 \text{ rpm}$ or $N=20 \text{ rpm}$. Therefore, we have considered the average of viscosities calculated over the rotational speeds higher than those limits, as indicated Table 4.1. Rheological studies on vegetable oils have been made by Silva et al. [27] who studied cotton, canola, corn, sunflower, and soybean oils at 30, 45 and 60 °C and concluded that all of them displayed a Newtonian behaviour. The same conclusion were found by Macedo et al. [28] who studied the rheology of canola, corn, sunflower, sunflower and soybean oils.

Table 4.1. Experimental dynamic viscosity of CSO at temperature T and $p = 102.05$ kPa.s.

T/K	N/rpm	$\eta/(\text{mPa}\cdot\text{s})$	$\langle\eta\rangle /$ ($\text{mPa}\cdot\text{s}$)	$\sigma /$ ($\text{mPa}\cdot\text{s}$)	T/K	N/rpm	$\eta/(\text{mPa}\cdot\text{s})$	$\langle\eta\rangle /$ ($\text{mPa}\cdot\text{s}$)	$\sigma /$ ($\text{mPa}\cdot\text{s}$)
292.65	10	72.60			332.97	150	17.00	16.89	0.07
292.65	20	72.90			343.00	10 ^b	14.40		
292.65	30	72.50			343.00	20 ^b	12.90		
292.65	40	72.40	72.60	0.22	343.00	30	13.20		
297.73	10 ^b	58.50			343.00	40	13.10		
297.73	20	57.80			343.00	60	13.10		
297.73	30	57.50			343.00	80	13.20		
297.73	40	57.40	57.57	0.21	343.00	100	13.20		
301.55	10 ^b	47.40			343.00	120	13.20		
301.55	20	46.80			343.00	150	13.20	13.17	0.06
301.55	30	46.80			353.02	10 ^b	12.30		
301.55	40	46.90			353.02	20 ^b	10.70		
301.55	60	46.90	46.85	0.06	353.02	30	10.50		
312.65	10 ^b	32.40			353.02	40	10.50		
312.65	20	32.10			353.02	60	10.50		
312.65	30	32.10			353.02	80	10.50		
312.65	40	32.20			353.02	100	10.50		
312.65	60	32.20			353.02	120	10.50		
312.65	80	32.20	32.16	0.05	353.02	150	10.50		
322.97	10 ^b	24.30			353.02	200	10.60	10.51	0.04
322.97	20 ^b	23.40			363.10	10 ^b	9.30		
322.97	30	22.90			363.10	20 ^b	8.70		
322.97	40	23.00			363.10	30	8.50		
322.97	60	23.00			363.10	40	8.70		
322.97	80	22.90			363.10	60	8.50		
322.97	100	23.00	22.96	0.05	363.10	80	8.51		
332.97	10 ^b	18.40			363.10	100	8.49		
332.97	20 ^b	17.40			363.10	120	8.50		
332.97	30	16.80			363.10	150	8.50		
332.97	40	16.80			363.10	200	8.52	8.53	0.07
332.97	60	16.90			372.99	10 ^b	12.60		
332.97	80	16.90			372.99	20 ^b	9.45		
332.97	100	16.90			372.99	30 ^b	8.95		
332.97	120	16.90			372.99	40 ^b	8.29		

Continued

372.99	60	7.65		
372.99	80	7.60		
372.99	100	7.23		
372.99	120	7.20		
372.99	150	7.14		
372.99	200	7.14	7.33	0.23

^a Standard uncertainties are $u(T) = 0.1$ K, $u(p) = 0.19$ kPa and the combined uncertainty is $u_c(\eta) < 2\%$.

^b Not considered to the calculation of average viscosity because they belong to the thinning behaviour.

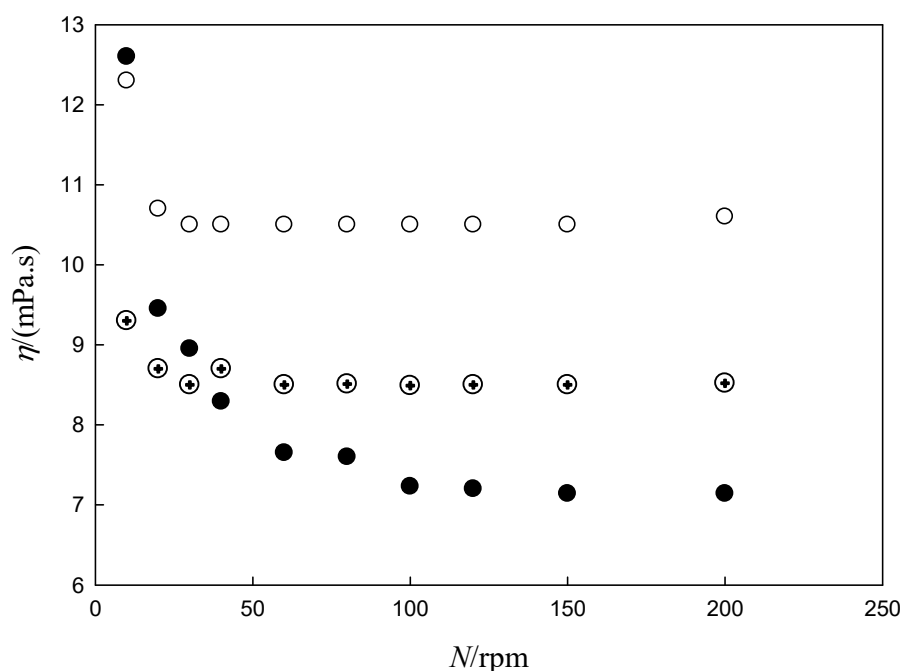


Figure 4.1. Viscosity of CSO as function of rotational speed. \circ , $T = 353$ K; \otimes , $T = 363$ K; \bullet , $T = 373$ K.

Data for the viscosity of CSO from the literature are presented in Figure 4.2 and can be summarized as follows. Macovey [1] measured the dynamic viscosity in the range 288.15 to 373.15 K. Eryilmaz et al. [2] measured the kinematic viscosity of CSO in the range 298.15 K to 373.15 K and the dynamic viscosity were obtained from the densities calculating by GMA EoS which parameters were giving in Table 3.10. Wakeham and Magne [3] studied the dynamic viscosity of deodorized cottonseed oil and hydrogenated cottonseed oils. They reported also the iodine number (IN) of the samples, which is a measure on unsaturated level. Measurements were

done in the range 302 K to 517 K and IN between 6 and 112. Some other values are available at point temperatures for example at 40°C as fixed by international standards.

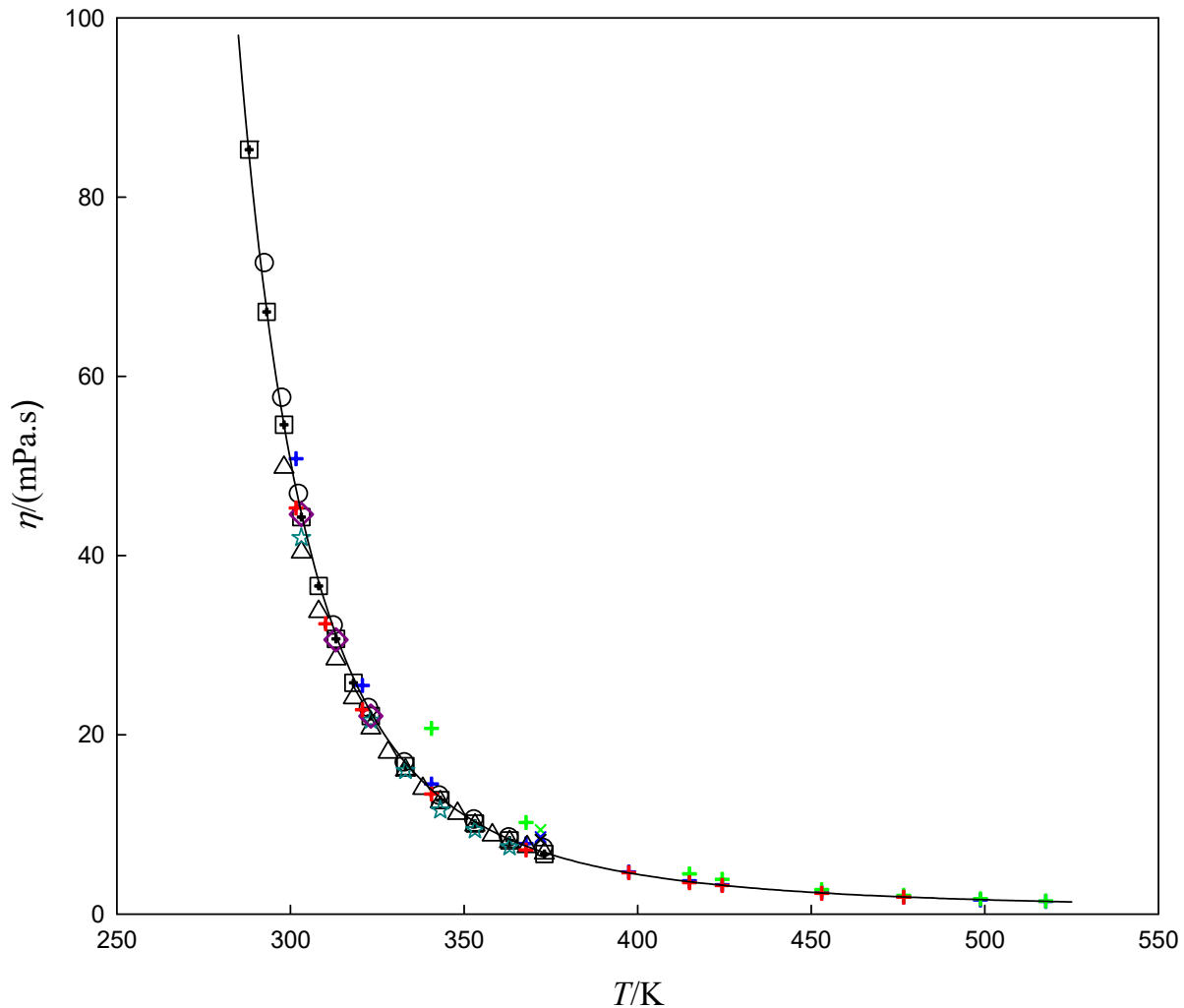


Figure 4.2. Dynamic viscosities, η , for CSO as function of temperature, T . \circ , This work; \boxtimes , Macovei [1]; Δ , Eryilmaz et al. [2]; Wakeham and Magne [3] ($+$, $IN=112$; $+$, $IN=101$; $+$, $IN=108$; $+$, $IN=6$). \star , Rawitsch [29]; \diamond , Boekenooen [30]; Bauer and Markley [31] (\times , $IN=7$; \times , $IN=46$; \times , $IN=56$). Full line corresponds to correlation with MYEGA Eq. 4-4.

From Figure 4.2, it can be seen the general good agreement of data of this work with those from the literature. The agreement between values of this work and the values measured by Wakeham and Magne for $IN = 112$ (non-hydrogenated CSO) is clearly observable. The data from the different authors can be compared with those from this work in the overlapping ranges of

temperature by calculating de *AARD*. The data deviate from the values reported by Macovey [1], Erylmaz et al. [2] and Wakeham and Magne [3] by 4.5%, 8% and 7%, respectively.

The viscosity of the CSB measured in this work at atmospheric pressure in the range $T = (303.15 \text{ to } 348.15) \text{ K}$ is presented in Table 4.2. The dynamic viscosity was obtained from kinematic viscosity using the relation $\eta = \rho v$, with values of densities calculated from GMA EoS and reported in Prieto et al. [14]. Erylmaz et al. [2] reported viscosity in the range (298 to 373) K and Nogueira [4] from (293 to 373) K.

Table 4.2. Kinematic and dynamic viscosity of CSB as a function of temperature.

T/K	$v/(\text{mm}^2\cdot\text{s}^{-1})$	$\eta/(\text{mPa}\cdot\text{s})$	T/K	$v/(\text{mm}^2\cdot\text{s}^{-1})$	$\eta/(\text{mPa}\cdot\text{s})$
303.15	5.738	5.017	333.15	3.300	2.819
308.15	5.118	4.458	338.15	2.926	2.490
313.15	4.608	3.998	338.15	2.921	2.486
318.15	4.178	3.612	343.15	2.925	2.479
323.15	3.792	3.265	348.15	2.770	2.338
328.15	3.470	2.976			

^aStandard uncertainties are $u(T) = 0.01 \text{ K}$, $u(p) = 0.23 \text{ kPa}$, $u(t) = 0.01 \text{ s}$. $u_c(v) = 0.01 \text{ mm}^2\cdot\text{s}^{-1}$ and $u_c(\eta) = 0.01 \text{ mPa}\cdot\text{s}$.

In Figure 4.3, the logarithm of viscosity is represented as a function of the reciprocal of temperature (Arrhenius plot) for CSO and CSB. It can be concluded that non-Arrhenius behaviour is observable.

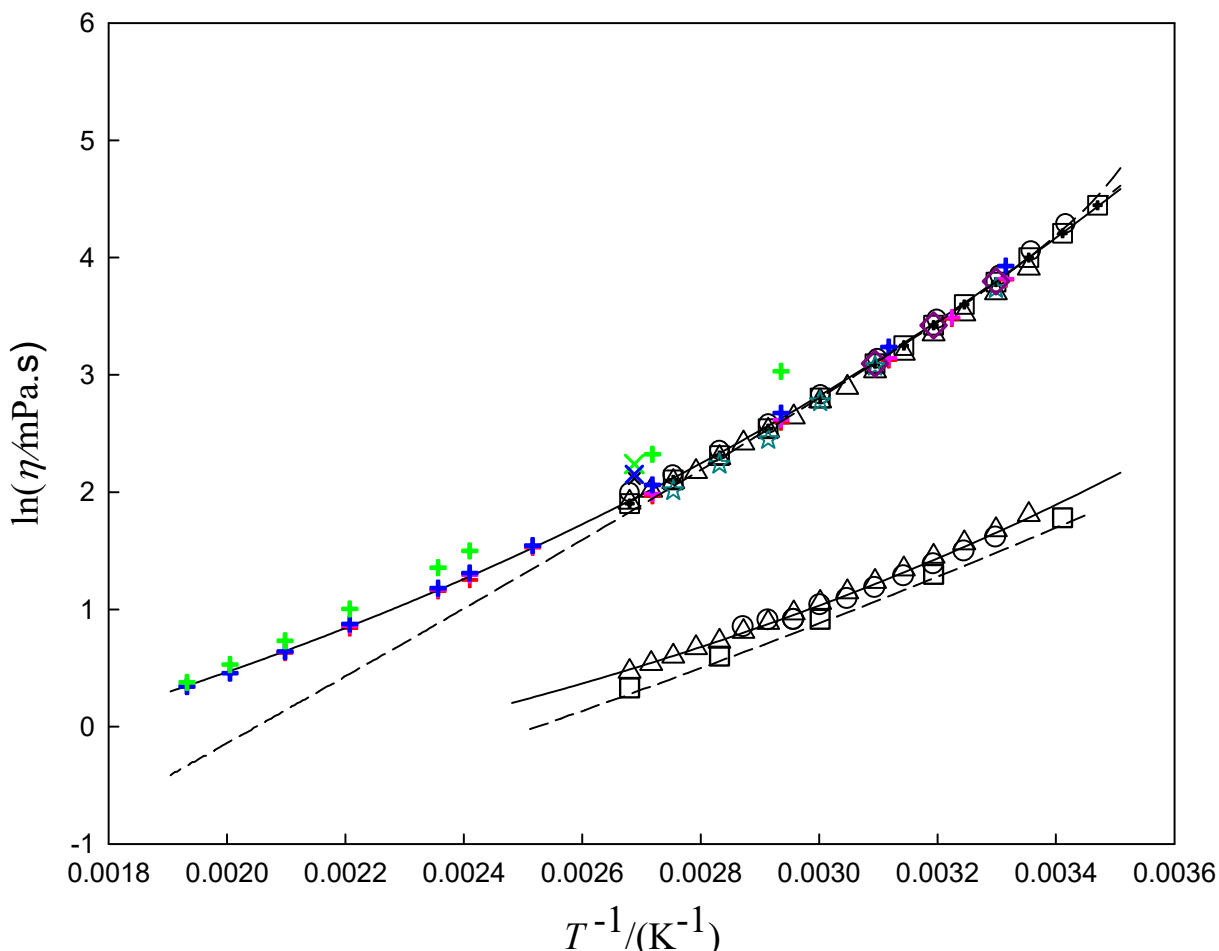


Figure 4.3. Logarithm of viscosity as function of $1/T$ for CSO and CSB. CSO: \circ , This work; \blacksquare , Macovei [1]; Δ , Eryilmaz et al. [2]; \star , Rawitsch [29]; \diamond , Boekenoogen [30]; Wakeham and Magne [3] ($+$, $IN=112$; $+$, $IN=101$; $+$, $IN=108$; $+$, $IN=6$); Bauer and Markley [31] (\times , $IN=7$, \times , $IN=46$; \times , $IN=56$). CSB: \circ , This work; Δ , Eryilmaz et al. [2]; \square , Nogueira [4]. Upper symbols correspond to CSO and lower ones to CSB. Full lines correspond to correlation with MYEGA, dashed line correspond to prediction with CER.

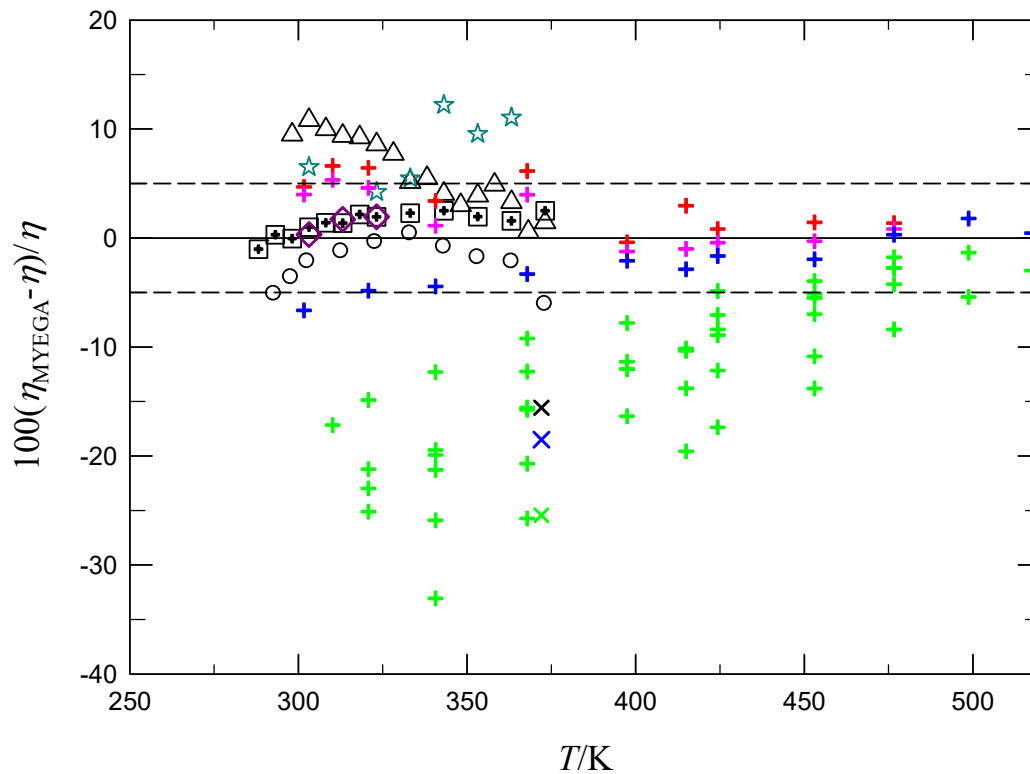
In Figure 4.3 the dynamic viscosity of CSB from this work are compared with the measurements made by Eryilmaz et al. [2] and Nogueira et al. [4] in the overlapping ranges of temperature, obtaining *AARDs* of 5% and 11% , respectively.

The *IN* of CSO used in this work is in the range (95 – 115) g I/100g and is comparable to the higher values of *IN* reported by Wakeham and Magne [3] ($IN=101, 108, 112$) g I/100g. Therefore, their dynamic viscosities were combined with those from this work to fit the correlation models VFT and MYEGA. The fitted parameters are presented in Table 4.3. From this table, it can be seen that the predicted high temperature limiting of viscosities are similar for

VFT and MYEGA $\eta_{\infty} = (10^{-3.9}$ and $10^{-3.7})$ Pa.s, which can be compared with $\eta_{\infty} = 10^{-5 \pm 2.1}$ Pa.s usually mentioned in the literature [32]. At the glass transition, the estimates of viscosities from VFT and MYEGA are of order of $10^{8.9}$ Pa.s and $10^{9.6}$ Pa.s, respectively, which are lower than the value taken as standard (10^{12} Pa.s) [8]. As far as it is known, the glass transition temperatures of vegetable oils was rarely measured or predicted. In the literature only two studies were found. Abdulkarim and Ghazali [20] detected glass transition of canola (CLO), sunflower (SFO), palm olein (PO), rice bran oils (RBO), and cocoa butter (CB) using hyperDSC™ scan rates (100 °C to 200 °C/min). The glass transition region starts at ca. 208 K and extends by more than 20 K. In another study, Cieřła et al. [33] obtained $T_g = (193.55$ to $201.95)$ K for a SFO. VFT equation predicts $T_g = 183$ K for CSO which is not far from the value of Cieřła et al., while the value 157 K, predicted with MYEGA, is low compared with the literature. The values of fragility index, m , obtained from VFT and MYEGA are different but still allow considering that CSO has an intermediate behaviour: the change in viscosity in the glass transition region will be not as steep as for a fragile liquid neither so weak as for a strong one. Both equations, VFT and MYEGA provides an excellent correlation of dynamic viscosity of CSO in the range $T = (292 - 518)$ K with $AARD = 2.7\%$, standard deviation of 1.2 mPa.s and high correlation coefficients (see Table 4.3). The correlation of viscosity with MYEGA equations is compared with experimental data in Figure 4.2 and Figure 4.3 and excellent agreement is observed. For the fitting with VFT equation, similar results were obtained. To evaluate the correlation ability of the models, the RDs between the calculated and experimental viscosities were calculated and they are presented in Figure 4.4 for MYEGA. It can be seen that RDs of the data used for the fitting are usually in the range $\pm 5\%$ corresponding to the $AARD = 2.7\%$. For excluded data, with the exception of data from Macovey [1] and Boekenoogen [30] the viscosities deviate more than 5%. The values of Wakeham and Magne [3] and Bauer and Markley [31], corresponding to IN values lower than 101 display very high relative deviations (-20% to -30%) especially at temperatures between 300 K and 400 K. These deviations correspond to the increase of viscosity with the decrease in IN .

Table 4.3. Parameters of VFT and MYEGA equations fitted to the experimental CSO and CSB viscosity data, coefficient of determination, r^2 , average absolute relative deviation $AARD$ and standard deviation in viscosity, σ_η .

Eqs.	$A=\ln(\eta_\infty/$ mPa.s)	T_0/K	B	C	$\ln(\eta_g/$ mPa.s)	m	T_g /K	$AARD$ (%)	$\sigma_{\ln \eta}$	$\sigma_\eta/$ (mPa.s)	r^2
CSO											
VFT											
Eq. 4-6	-2.0861	153.24	882.73		27.4738	78.71	183.10	2.6	0.034	1.1	0.9991
MYEGA											
Eq. 4-9	-1.6228		519.315	349.371	28.9551	42.82	157.06	2.7	0.035	1.2	0.9992
CSB											
VFT											
Eq. 4-6	-1.8362	163.72	486.63		23.5796	105.42	182.87	2.4	0.030	0.1	0.9939
MYEGA											
Eq. 4-9	-1.3714		207.272	450.804	26.4696	48.41	150.08	2.5	0.030	0.1	0.9938


Figure 4.4. Relative deviations as function of temperature between the calculated viscosities of CSO based on fitted MYEGA, (η_{MYEGA}) and the experimental values (η). \circ , This work; \boxtimes , Macovey [1]; Δ , Erylmaz et al. [2]; \star , Rawitsch [29]; \diamond , Boekenoogen [30]; Wakcham and Magne [3] ($+$, $IN=112$; $+$, $IN=101$; $+$, $IN=108$; $+$, $IN=6$); Bauer and Markley [31] (\times , $IN=7$, \times , $IN=46$; \times , $IN=56$).

For CSB, given the good agreement between viscosities of this work with the measurements made by of Eryilmaz et al. [2] they were combined to fit the VFT and MYEGA equations. The results of fittings are displayed in Figure 4.3. Both equations represent the selected data with good accuracy: the *AARD* is 2.4% and the standard deviation is very low (0.1 mPa.s). The coefficient of determinations is only somewhat lower than for CSO. In the Figure 4.5, relative deviations between the calculated viscosities with MYEGA and the data from literature are displayed. The relative deviations of the data used in the fittings are in the range $\pm 5\%$ corresponding to the *AARD* = 2.5%. The data reported by Nogueira et al. [4] deviates by more than 10% (*AARD* = 14.3%). Relative deviations with VFT equation were not represented because they are almost as those obtained with MYEGA.

For CSB, the mean value of the predicted high temperature viscosity limit is ca. $\eta_{\infty} \approx 10^{-3.7}$ Pa.s a value which is comparable with the value obtained for CSO ($\eta_{\infty} \approx 10^{-3.8}$ Pa.s). The predicted glass transition temperature was not too different from those found for the oil. The estimates of viscosities at glass transition from VFT and MYEGA are of the order of $10^{7.2}$ Pa.s and $10^{8.5}$ Pa.s. As far as it known, no glass transition temperatures values were reported in literature for biodiesels.

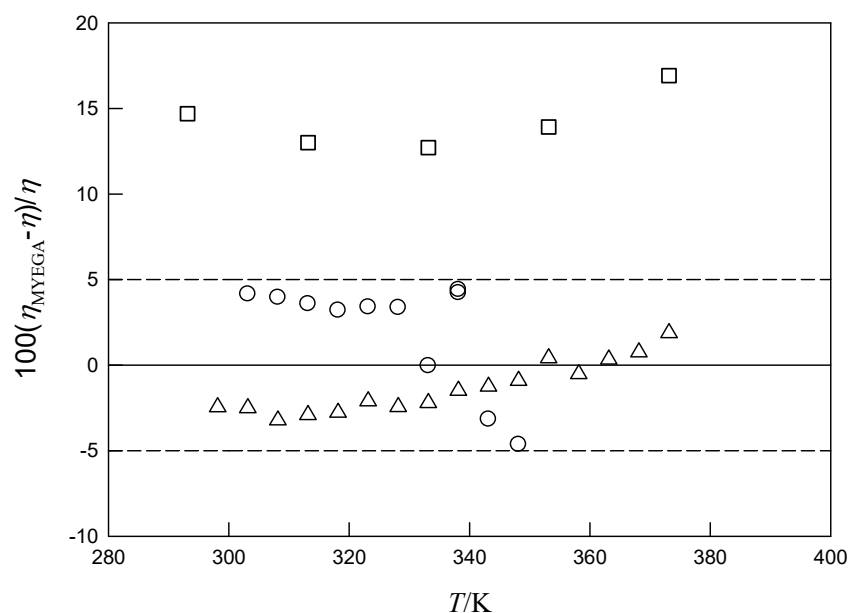


Figure 4.5. Relative deviations as function of temperature between the calculated viscosities of CSB based on MYEGA (η_{MYEGA}) and the experimental values (η). \circ , this work; Δ , Eryilmaz et al. [2]; \square , Nogueira et al. [4].

4.4.2 Prediction of CSO and CSB viscosity

The viscosity of CSO was predicted using the fragment approach given by Zong et al. [9] and the method proposed by Ceriani et al. [10]. In Figure 4.6 the *RDs* between the calculated viscosities of CSO using the fragment approach and the experimental values are displayed as a function of temperature. The calculations were made using the MTGA and STGA profiles corresponding to Figure 4.6(a) and Figure 4.6(b), respectively. The results using both profiles give almost the same results. It can be seen that the most part of experimental data are predicted with *RD* within $\pm 5\%$ at temperatures from 283 K to 340 K. Values of Rawitsch [29] can be predicted into this *RD* range up to 363 K. Negative *RDs* larger than -5% are observed at increasing temperatures from $T = 345$ K, reaching more than -15% near to 373 K. For PTGA deviations were not displayed because similar behaviour was observed.

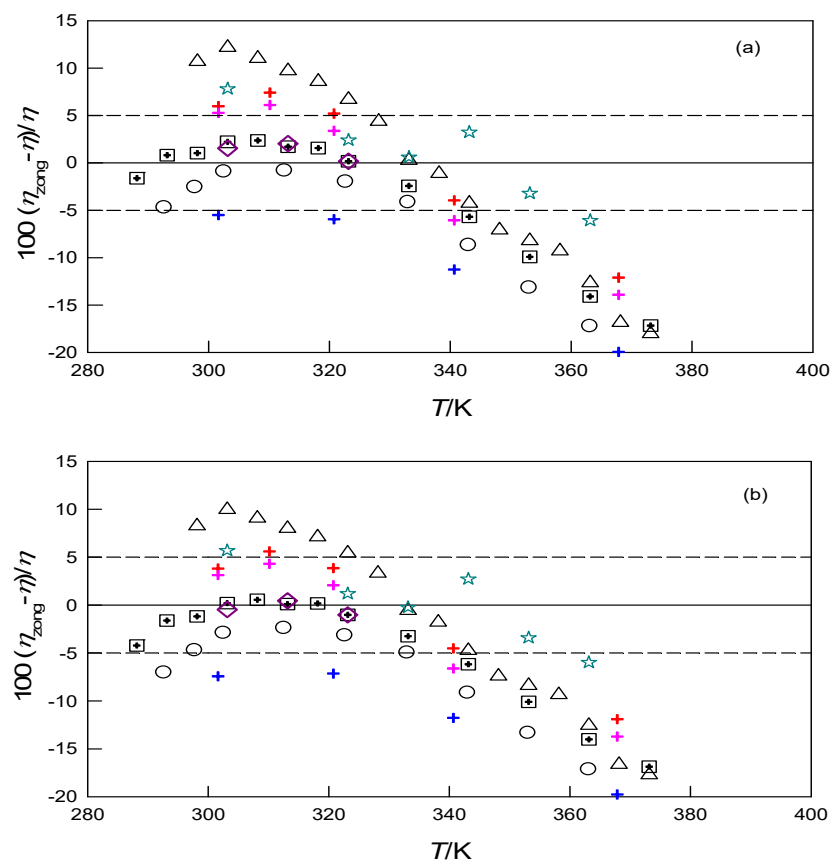


Figure 4.6. Relative deviations as function of temperature between the calculated viscosities of CSO based on Zong model (η_{Zong}) and the experimental values (η). \circ , This work; \blacksquare , Macovey [1]; Δ , Erylmaz et al. [2]; \star , Rawitsch [29]; \diamond , Boekenooogen [30]; Wakeham and Magne [3] (+, $IN=112$; +, $IN=101$; +, $IN=108$). (a) and (b) correspond to calculations with MTGA, STGA.

The predictive behaviour of Zong with MTGA model is summarized in Table 4.4, where the *AARDs* are presented for the experimental data. With the exception of data from Wakeham and Magne ($IN=101$) all the *AARDs* fall within 9% considering data up to 373 K. The overall is $OARD = 6.4\%$.

Table 4.4. Average absolute relative deviations *AARD* of viscosities for the predictive methods used in the calculation of viscosities of CSO.

Method	<i>AARD</i> (%)	
	Zong	Ceriani
This work	7.8	4.9
Macovey	4.7	2.3
Erylmaz et al	8.8	5.3
Rawitsch	3.9	4.7
Boekenoogen	1.2	0.5
Wakeham and Magne ($IN=112$)	6.9	3.3
Wakeham and Magne ($IN=108$)	6.9	3.2
Wakeham and Magne ($IN=101$)	10.7	8.0
<i>OARD</i> %	6.4	4.0

The experimental data of this work and those from the literature were compared with the viscosities predicted with Ceriani method in Figure 4.7 using MTGA, PTGA and STGA. From Figure 4.7(a), where MTGA was used it can be seen that experimental data is predicted with good accuracy. Most *RDs* values are in the range $\pm 5\%$ between 283 and 368 K. The use of STGA, corresponding to Figure 4.7(b), shifts downwards the *RDs* by 5% to 8%, comparatively to MTGA. Using PTGA, the opposite happens (see Figure 4.7(c)). *RDs* are shifted by ca. 8% upwards. The *AARD* of Ceriani's method using MTGA approach, for different sources of data, are presented in Table 4.4. It can be concluded that with the exception of data from Wakeham and Magne ($IN=101$) all the *AARDs* fall within 5% at temperatures up to 373 K. The overall is $OARD = 4\%$.

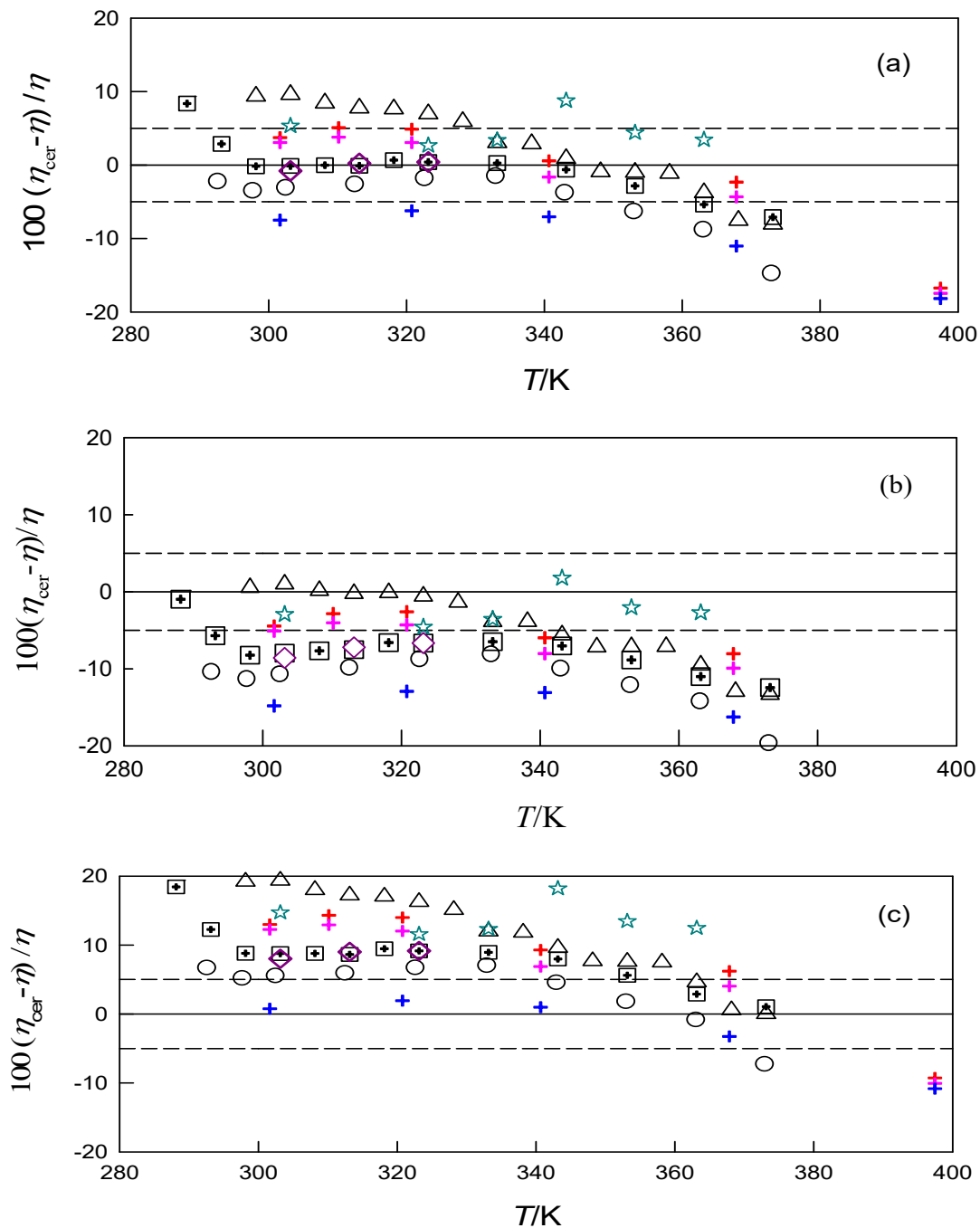


Figure 4.7. Relative deviations as function of temperature between the calculated viscosities of CSO based on CER model (η_{CER}) and the experimental values (η). \circ , This work; \boxplus , Macovey [1]; Δ , Erylmaz et al. [2]; \star , Rawitsch [29]; \diamond , Boekenoogen [30]; Wakeham and Magne [3] (+, $IN=112$; +, $IN=101$; +, $IN=108$). (a), (b) and (c) correspond to calculations with MTGA, STGA and PTGA.

The viscosity of CSB of different authors was predicted with Grunberg and Nissan model, Eq. 4-16 coupled with Ceriani and Yuan methods. For the calculations, the FAMES profile of this

work was used, since Erylmaz et al. [2] did not refer the FAMEs composition and the CSB profile reported by Nogueira et al. [4] was similar to that found in this work. The calculated viscosities using these models are compared with the experimental values in Figure 4.8, where the RDs as a function of temperature are displayed.

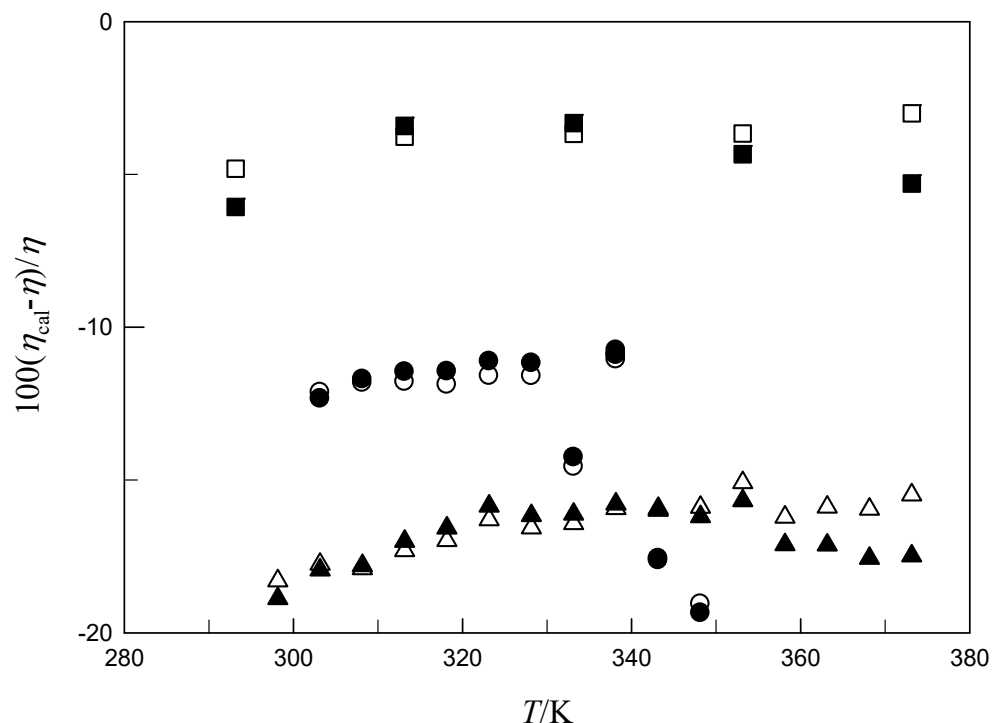


Figure 4.8. Relative deviations as function of temperature between the calculated viscosities of CSB based on predictive models (η_{cal}) and the experimental values (η). \circ , This work; Δ , Erylmaz et al. [2]; \square , Nogueira et al. [4]. Full and open symbols correspond to Ceriani et al. and Yuan models.

From Figure 4.8 it can be seen that the RDs are always negative regardless of the method used, meaning that all models underpredict the experimental viscosities. The RDs are more negative than -10% with exception of the viscosity data of Nogueira et al. [4]. In Table 4.5 the $AARD$ for the different methods are presented. From the results of Figure 4.8 and Table 4.5 it can be concluded that Ceriani and Yuan method give similar level of viscosity prediction.

Freitas et al. [11] applied the same models to a set of 24 fuels and also found high negative RDs . For CSB, Freitas et al. [11] obtained $AARDs$ 4.4% for Yuan models. The difference between $AARDs$ reported by Freitas et al. [11] and those presented in Table 4.5 are due to differences in FAME composition. For the main FAMEs of CSB (C16:0, C18:1 and C18:2),

which are the most influent in viscosity calculations, Freitas et al. reported values of 24.1%, 15.7% and 56.2% (wt %), respectively and in this work the content of those FAMES were 26.8%, 17.9% and 51.6%.

Table 4.5. Average absolute relative deviation *AARD* of viscosities for the predictive methods used in the calculation of viscosities of CSB.

Method	This work	Erylmaz et al.	Nogueira et al.	<i>OARD</i>	<i>RD</i> _{min} / <i>RD</i> _{max}
GN (without G_{ij} correction)					
Ceriani	12.9	16.8	4.5	11.4	-3.3 / -19.4
Yuan	13.1	16.5	3.8	11.1	-3.0 / -19.1
GN (with G_{ij} correction)					
Ceriani	4.2	1.8	12.7	6.2	-0.5 / 14.1
$G_{ij} = 0.523 \pm 0.102$					
Yuan	3.8	1.6	13.4	6.2	-0.5 / 14.1
$G_{ij} = 0.518 \pm 0.099$					

A criticism that can be made about the use of the Grunberg and Nissan mixing rule given by Eq. 4-16 applied to viscosity calculations is to consider the interaction parameter G_{ij} as zero with the explanation that biodiesel is a non-associated liquids formed by non-polar molecules with very similar structure interacting essentially with dispersive interaction forces between the individual molecules. A less drastic and undoubtedly more reasonable approximation would be to consider that the interaction parameters G_{ij} have all approximately the same value for interactions between pairs. According with this approximation Eq. 4-15 can be rewrite as:

$$\ln \eta_{mix} = \sum_i x_i \ln \eta_i + G_{ij} \sum_{i=1}^N \sum_{j=1}^N x_i x_j \quad \text{Eq. 4-19}$$

Since CSB viscosity data of this work are in agreement with Erylmaz et al. [2] within $\pm 5\%$, these two sets were combined and used to calculate the parameter G_{ij} from Eq. 4-19. The Ceriani and Yuan models were applied to the calculation of the viscosities η_i of individual FAMES. The resulting values of G_{ij} are presented in Table 4.5. The values are very similar for the two models. In Figure 4.9 the *RDs* between calculated viscosities from Eq. 4-19 and experimental data are represented as a function of temperature. It can be concluded that Eq. 4-19 describes the experimental data of this work and from Erylmaz et al. [2] within $\pm 5\%$.

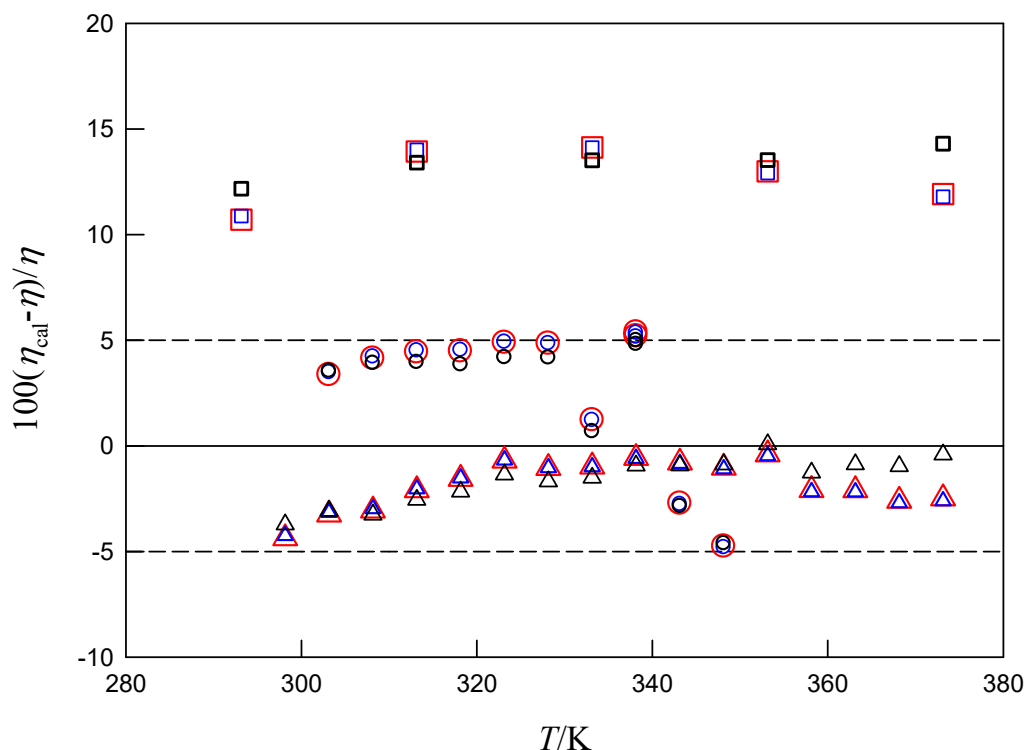


Figure 4.9. Relative deviations as function of temperature between the calculated viscosities of CSB based on predictive models (η_{cal}) with Grunberg and Nissan method with interaction term G_{ij} and the experimental values (η). \circ , This work; Δ , Erylmaz et al. [2]; \square , Nogueira et al. [4]. Red, blue and black symbols correspond to Ceriani with FA profile, Ceriani with FAMEs profile and Yuan models with FAME profile.

4.4.3 Relation between viscosity and density

The measurement of density is very simple and quick and usually requires low-cost equipment. On the other hand, the measurement of the viscosity is more complex and time consuming, requiring a more complex and expensive assessment instrumentation. Then, if a relationship between density and viscosity is known, one only needs to measure the density of the oil to calculate its viscosity. According to Rodenbush et al. [34], for vegetable oils the dependence between density and viscosity can be expressed as:

$$\rho = A + B/\eta^{1/2} \quad \text{Eq. 4-20}$$

Parameters A and B can be found from Eq. 4-20 using least-squares linear regression by choosing $\eta^{-1/2}$ as independent variable. In Figure 4.10 the density is represented as a function of $\eta^{-1/2}$ for CSO and CSB. The used data are relative to the authors that reported density and viscosity at the same temperature, namely Eryilmaz et al. [2], Macovei [1] and this work for CSO and Eryilmaz et al. [2], Nogueira et al. [4] and this work for CSB.

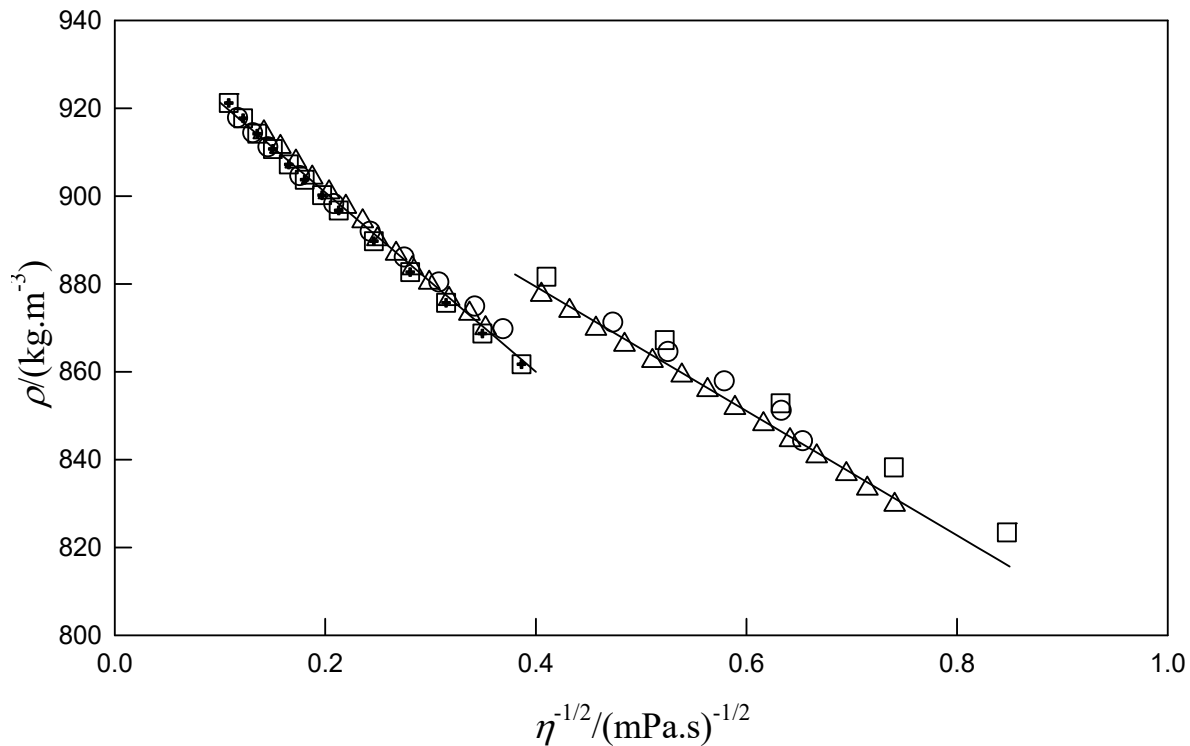


Figure 4.10. Density (ρ) as function of ($\eta^{-1/2}$) for CSO (left) and CSB (right). ○, This work; ⊕, Macovei [1]; Δ, Eryilmaz et al.[2]; □, Nogueira et al. [4]. Full lines correspond to linear correlation with Eq. 4-20.

From Figure 4.10 it can be seen that density runs almost as a linear function of $\eta^{-1/2}$ for both CSO and CSB experimental data.

For CSO, the experimental data from this work, Macovei [1] and Eryilmaz [2] were used to fit the Eq. 4-20 and for CSB data relative to this work and Eryilmaz [2] were used, due to the better intrinsic agreement compared with data from Nogueira et al. [4]. The parameters A and B of CSO and CSB are presented in Table 4.6.

Table 4.6. Parameters A and B of Eq. 4-20 and $AARD$ in density and viscosity for CSO and CSB.

	CSO	CSB
A ($\text{kg}\cdot\text{m}^{-3}$)	941.725	935.97
B ($\text{kg}\cdot\text{m}^{-3}\cdot\text{mPa}^{0.5}\cdot\text{s}^{0.5}$)	-204.352	-141.559
r^2	0.994	0.981
σ ($\text{kg}\cdot\text{m}^{-3}$)	1.3	2.0
$AARD_\rho$ (%)	0.11	0.18
$AARD_\eta$ (%)	4.7	3.9

The RDs obtained from the calculated viscosities with the adapted version of Eq. 4-20 and the experimental values, as a function of temperature, are displayed in Figure 4.11 and Figure 4.12.

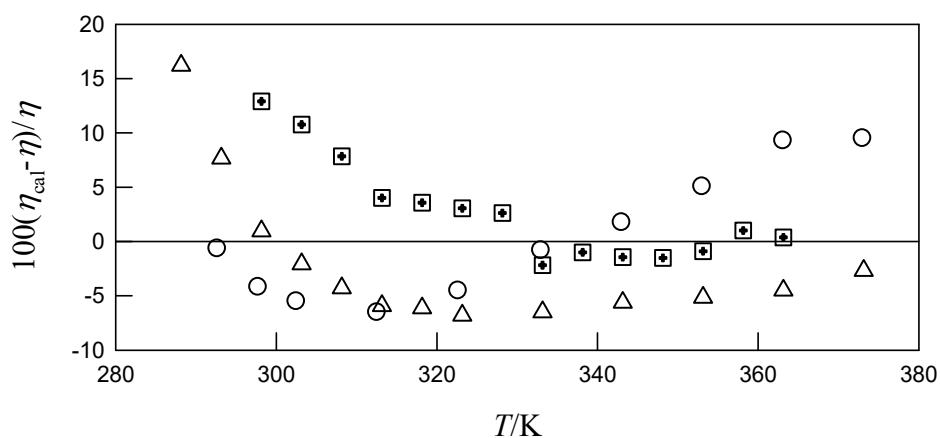


Figure 4.11. RDs between viscosities calculated from Eq. 4-20 (η_{cal}) and that from literature (η) as function of temperature, for CSO. \circ , This work; \boxplus , Macovei [1]; Δ , Eryilmaz et al. [2].

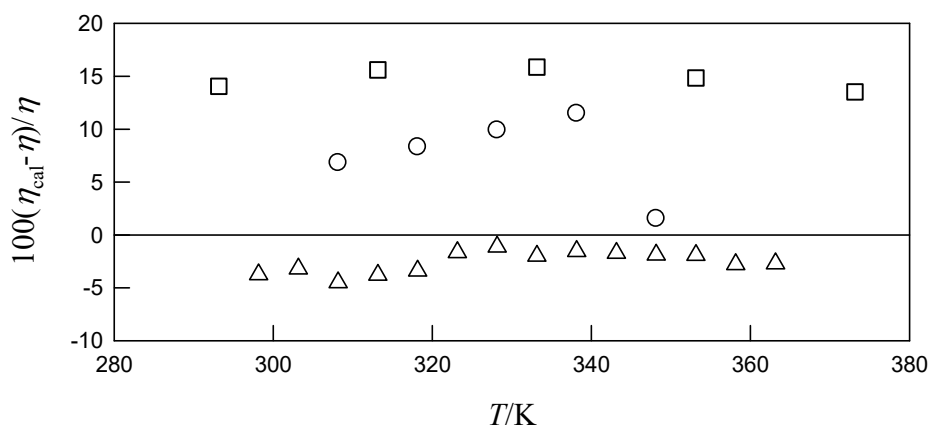


Figure 4.12. RDs between viscosities calculated from Eq. 4-20 (η_{cal}) and that from literature (η) as function of temperature, for CSB. \circ , This work; Δ , Eryilmaz et al. [2]; \square , Nogueira et al. [4].

In Figure 4.11, for CSO, 62% of the calculated values of η have RDs less than $\pm 5\%$, while for CSB (Figure 4.12), 58% of the calculated values of η have RDs less than $\pm 4\%$. This difference is due to the better agreement between the viscosities values of the authors that were used for the CSO adjustment compared to those selected for the CSB.

From Table 4.6, it can be conclude that Eq. 4-20 correlates very well density and viscosity for CSO with standard deviation of 1.3 kg.m^{-3} and $AARD_{\rho} = 0.11\%$, which is within the uncertainty of measurements. Taking into account all the sets of experimental density data, it is obtained $AARD_{\eta} = 4.7\%$ for the deviation of viscosities calculated from the densities, which can be considered very reliable. Therefore, the viscosities of CSO can be calculated from the density with accuracy not far from the expanded uncertainty for viscosity. For CSB, the two properties correlates with standard deviation 2.0 kg.m^{-3} and $AARD_{\rho} = 0.18\%$. Calculating viscosity from the densities $AARD_{\eta} = 3.9\%$ is obtained.

4.5 Conclusions

Viscosity data for CSO and CSB were measured and reported in the ranges (293 to 373) K and (303 to 348) K, respectively, at atmospheric pressure. Selected viscosities compiled from literature were used with data from this work to fit VFT and MYEGA models. Both models provide excellent correlation of dynamic viscosity with $AARD$ of about 2.6%, and good coefficient of determinations. A novelty of this work is that T_g of CSO predicted from VFT equation is not far from the few values available in literature. According to the values of fragility index, CSO and CSB have an intermediate behaviour between strong and fragile liquid.

The viscosity of the oil and biodiesel were predicted from suitable models using the information of oil fatty acid content and FAMEs composition of biodiesel. The Zong's method predicted the viscosity of CSO using the MTGA and STGA profiles with RDs within $\pm 5\%$ at temperatures from 283 K to 340 K. The Ceriani method using MTGA profile allows predicting experimental data with RDs in the range $\pm 5\%$ between 283 and 368 K. The viscosity of CSB was predicted using the model of Grunberg and Nissan with $G_{ij} = 0$, coupled with Ceriani and Yuan methods. The FAMEs profile and fatty acid profile of the oil give similar RDs , lower than -10%, for the different methods. The use of the interaction parameter G_{ij} combined with Ceriani and Yuan models allow the description of most part of CSB viscosities within $\pm 5\%$, which is close to

the experimental uncertainty of many experimental data. Therefore, it can be concluded that the usual approximation $G_{ij} = 0$ is not suitable for the prediction of viscosity of CSB.

A linear behaviour between density and the reciprocal of square root in viscosity is observed for CSO and CSB when the experimental data from different authors was used. The viscosity of CSO and CSB can be predicted from density in the temperature ranges (288 to 373) K and (298 to 363) K with *AARDs* of 4.7% and 3.9%, respectively.

4.6 References

1. Macovei VM. Culegere de caracteristici termofizice pentru biotehnologie și industria alimentară : Tabele și diagrame. Română: Alma Galați; 2000.
2. Eryılmaz T, Yeşilyurt M, Yumak H, Arslan M, Şahin S. Determination of the Fuel Properties of Cottonseed Oil Methyl Ester and Its Blends with Diesel Fuel/Pamuk Tohumu Metil Esteri Ve Dizel Yakıt İle Karışımlarının Yakıt Özelliklerinin Belirlenmesi. *International Journal of Automotive Engineering and Technologies*. 2014;3(2):79-90.
3. Wakeham H, Magne FC. Viscosities and densities of hydrogenated cottonseed oils. *Industrial & Engineering Chemistry*. 1944;36(6):568-70.
4. Nogueira Jr CA, Feitosa FX, Fernandes FA, Santiago RIS, de Sant'Ana HB. Densities and viscosities of binary mixtures of babassu biodiesel+ cotton seed or soybean biodiesel at different temperatures. *Journal of Chemical & Engineering Data*. 2010;55(11):5305-10.
5. Vogel H. The temperature dependence law of the viscosity of fluids. *Phys Z*. 1921;22:645–6.
6. Fulcher GS. Analysis of recent measurements of the viscosity of glasses. *Journal of the American Ceramic Society*. 1925;8(6):339-55.
7. Tammann G, Hesse W. Die Abhängigkeit der Viscosität von der Temperatur bei unterkühlten Flüssigkeiten. *Zeitschrift für anorganische und allgemeine Chemie*. 1926;156(1):245-57.
8. Mauro JC, Yue Y, Ellison AJ, Gupta PK, Allan DC. Viscosity of glass-forming liquids. *Proceedings of the National Academy of Sciences*. 2009;106(47):19780-4.
9. Zong L, Ramanathan S, Chen C-C. Fragment-based approach for estimating thermophysical properties of fats and vegetable oils for modeling biodiesel production processes. *Industrial & engineering chemistry research*. 2009;49(2):876-86.

10. Ceriani R, Goncalves CB, Coutinho JA. Prediction of viscosities of fatty compounds and biodiesel by group contribution. *Energy & Fuels*. 2011;25(8):3712-7.
11. Freitas SV, Pratas MJ, Ceriani R, Lima AS, Coutinho JA. Evaluation of predictive models for the viscosity of biodiesel. *Energy & Fuels*. 2010;25(1):352-8.
12. Grunberg L, Nissan AH. Mixture Law for Viscosity. *Nature*. 1949;164:799.
13. Brookfield. More solutions to sticky problems. Available from <http://www.brookfield.co.uk/support/documentation/solutions-to-sticky-problems.asp>
14. Prieto NM, Ferreira AG, Portugal AT, Moreira RJ, Santos JB. Correlation and prediction of biodiesel density for extended ranges of temperature and pressure. *Fuel*. 2015;141:23-38.
15. Kapseu C, Kayem G, Balesdent D, Schuffenecker L. The viscosity of cottonseed oil, fractionation solvents and their solutions. *Journal of the American Oil Chemists Society*. 1991;68(2):128-30.
16. Noureddini H, Teoh B, Clements LD. Viscosities of vegetable oils and fatty acids. *Journal of the American Oil Chemists Society*. 1992;69(12):1189-91.
17. Lang W, Sokhansanj S, Sosulski FW. Modelling the temperature dependence of kinematic viscosity for refined canola oil. *Journal of the American Oil Chemists' Society*. 1992;69(10):1054-5.
18. Toro-Vazquez J, Infante-Guerrero R. Regression models that describe oil absolute viscosity. *Journal of the American Oil Chemists Society*. 1993;70(11):1115-9.
19. Yilmaz N. Temperature-dependent viscosity correlations of vegetable oils and biofuel–diesel mixtures. *Biomass and Bioenergy*. 2011;35(7):2936-8.
20. Abdulkarim S, Ghazali H. Comparison of melting behaviors of edible oils using conventional and hyper differential scanning calorimetric scan rates. *ASEAN Food Journal*. 2007;14(1):25.
21. Ferreira AG, Egas AP, Fonseca IM, Costa AC, Abreu DC, Lobo LQ. The viscosity of glycerol. *The Journal of Chemical Thermodynamics*. 2017;113:162-82.
22. Schröter K, Donth E. Viscosity and shear response at the dynamic glass transition of glycerol. *The Journal of Chemical Physics*. 2000;113(20):9101-8.
23. Rössler E, Hess K-U, Novikov V. Universal representation of viscosity in glass forming liquids. *Journal of non-crystalline solids*. 1998;223(3):207-22.

24. Yuan W, Hansen A, Zhang Q. Predicting the temperature dependent viscosity of biodiesel fuels. *Fuel*. 2009;88(6):1120-6.
25. Pratas MJ, Freitas S, Oliveira MB, Monteiro SC, Lima AS, Coutinho JA. Densities and viscosities of minority fatty acid methyl and ethyl esters present in biodiesel. *Journal of Chemical & Engineering Data*. 2011;56(5):2175-80.
26. Pratas MJ, Freitas S, Oliveira MB, Monteiro SC, Lima AS, Coutinho JA. Densities and viscosities of fatty acid methyl and ethyl esters. *Journal of Chemical & Engineering Data*. 2010;55(9):3983-90.
27. Silva LES, C. A. C.; Ribeiro, J. E. S.; Souza, C. C.; Sant'Ana, A. M. S. Rheological analysis of vegetable oils used for biodiesel production in Brazil. *Thermal Engineering*. 2015;14(2):31-6.
28. Macedo TdO, Pereira RG, Pardal JM, Soares AS, Lameira VdJ. Viscosity of vegetable oils and biodiesel and energy generation. *World Academy of Science, Engineering and Technology*. 2013;77:173-8.
29. Rawitsch GB. Die Temperaturabhängigkeit der Viskosität der Fette und Fettsäuren. *Kolloid-Zeitschrift*. 1936;76(3):341-5.
30. Boekenoogen H. The viscosity of the vegetable oils and fats. *Chem Weekblad*. 1937;34:759-61.
31. Bauer ST, Markley K. Hydrogenated cottonseed oil as a substitute for palm oil in the production of tin plate and cold reduced sheet steel. *Oil & Soap*. 1943;20(1):1-11.
32. Nascimento MLF, Aparicio C. Viscosity of strong and fragile glass-forming liquids investigated by means of principal component analysis. *Journal of Physics and Chemistry of Solids*. 2007;68(1):104-10.
33. Ciesla K, Sereno WGA, Barbossa C. Differential scanning calorimetry studies of melting and glass transition processes in food. *Radiation Chemistry and Physics, Radiation Technologies*. 2000:40.
34. Rodenbush C, Hsieh F, Viswanath D. Density and viscosity of vegetable oils. *Journal of the American Oil Chemists' Society*. 1999;76(12):1415-9.

5 CHAPTER

SURFACE TENSION OF COTTONSEED OIL AND BIODIESEL

Surface tensions of CSO and CSB were measured at atmospheric pressure and temperatures in the ranges (298.3 to 353.4) K and (304.8 K to 347.5) K, respectively. Experimental data of both substances were correlated with linear surface tension dependence and with Guggenheim's equation. Different routes, including parachor methods, corresponding states and empirical correlations were used to predict the surface tensions of CSO and CSB.

5.1 Introduction

Surface tension has a great influence on fuel atomization, which is the first stage of combustion. Good mixture and complete combustion in the injection engine results from an adequate atomization, increasing the engine efficiency [1]. Higher surface tensions opposes to the formation of droplets, leading to an inefficient fuel atomization [1]. It has been found that biodiesel surface tension increases with long fatty acid hydrocarbon chains and the level of unsaturated bonds [2, 3]. Thus, more experimental knowledge and development of suitable prediction methods of surface tension for biodiesels, which composition on fatty acid esters is known, is a very important issue needed for the optimization of biodiesel production and blending processes, with the main purpose of improving the atomization performance in direct injection (DI) engines.

The drop size which is usually considered in atomization studies is given by the Sauter mean diameter (SMD) which is defined as the diameter of the drop whose ratio of volume-to-surface area is equal to that of the spray [4]. Studies on SMD were performed by Allen and Watts [5] for biodiesels at 40 °C using an experimentally determined correlation, which was a function of viscosity and surface tension only. The main conclusions of their study were that the SMDs of the biodiesels could be 5–40% higher than that for diesel fuel. Ahmed et al. [6] showed analytically that the SMD of a pure biodiesel could be reduced from 40% higher than that of diesel at 40 C to about 0.4% by blending with diesel. However, characteristic temperatures in DI are higher than 40 °C as reported by Wagner and Peterson that suggested that typical fuel temperatures in a diesel engine will be ca. 80 °C [7]. Therefore, the studies must determine the atomization properties of biodiesels and their blends near this temperature, to be useful in diesel engine or injector performance analysis

Currently, the quantitative studies of atomization in a DI engines involving variations in viscosity, density and surface tension, are made in terms of the SMD correlation of Elkotb [5] derived from dimensionless analysis, which is considered as a standard scaling method in single-phase flows. The improved atomization characteristics (related with the decrease of SMD) results to lower values on density, kinematic viscosity and surface tension. From the statistical analysis on several biodiesels and biodiesel-diesel blends, Ejim et al. [1] concluded that the contributions to the SMD variations evaluated from Elkotb correlation, due to kinematic viscosity, surface tension and density was 89.1%, 10.7% and 0.2% respectively for biodiesel with a similar trend

followed for biodiesel-diesel blends. Thus, improved atomization in DI systems is achieved first with reduction in viscosity followed by surface tension.

5.2 Experimental

Surface tension measurements of CSO and CSB were made at atmospheric pressure and temperatures from (298.3 to 353.4) K and (304.8 to 347.5) K, respectively. A Wilhelmy plate was used for the measurements with a PC controlled KSV Sigma 70 tension balance. It was thoroughly cleaned by immersion in a concentrated solution of nitric acid during several hours, then rinsed with acetone, flamed, washed again with acetone and dried. An UltraTherm P Selecta bath was used being the temperature inside the measurement vessel maintained and controlled within 0.2 K. Temperature was measured with an ERTCO-Eutechnics High Precision Digital platinum resistance thermometer certified in the ITS90 with an uncertainty of 0.01K. For each point, a set of 10 measurements of surface tension were made with maximum uncertainty (precision) of 0.1 mN m^{-1} . Prior to measurements, the balance was calibrated (checked) with N-butanol (Carlo Erba, 99.5 wt %) and water (milQ). N-Butanol was selected as calibration standard due to the availability of high accuracy surface tension data, which indicated 24.18 mN.m^{-1} at 298.15 K [8], and since this value is close to the range of surface tension of biodiesel. The mean value of $\gamma = 23.90 \pm 0.03 \text{ mN.m}^{-1}$ was obtained corresponding to a deviation of 0.28 mN.m^{-1} . Water was also used as a calibration standard. The measured surface tension at 295.85 K was $71.67 \pm 0.09 \text{ mN.m}^{-1}$ which is in good agreement with the value 72.4 mN.m^{-1} reported by Vargaftik et al. [9] corresponding to a difference of 0.73 mN.m^{-1} . Taken into account these measurements for standards, the accuracy of the measurements is near 1.0%. Taking into account the uncertainty of temperature, the predictable combined uncertainty for the domain of surface tension values of the oil and biodiesel will be $u(\gamma) = 0.3 \text{ mN.m}^{-1}$.

The surface tension measurements were made with measuring cells open to the atmosphere. The measurement of the atmospheric pressure was made using a calibrated pressure transducer (AFRISO Euro-Index, DMU03). Taking the observed values covering January to March 2017 the mean value was $p = 101.86 \pm 0.23 \text{ kPa}$.

5.3 Surface tension models

5.3.1 Correlation

Over narrow temperatures ranges, surface tension dependence on temperature can be well represented by a linear equation, as reported by Reid et al.[10]:

$$\gamma = A + BT \quad \text{Eq. 5-1}$$

where γ is the surface tension, T is the absolute temperature, A and B are parameters to be found by fitting to experimental data. Also, a van der Waals-type correlation was proposed by Guggenheim for the dependence of surface tension on temperature [11]:

$$\gamma = \gamma_0(1 - T/T_c)^n \quad \text{Eq. 5-2}$$

where T_c is the critical temperature, and γ_0 and n are parameters used to fit the equation to the experimental data.

Recently, Mullero and Cachadina suggested a correlation of ST using an extended form of Eq. 5-2 [12]:

$$\gamma = \sum_{i=1} \gamma_i (1 - T/T_c)^{n_i} \quad \text{Eq. 5-3}$$

where γ_i and n_i are coefficients obtained by fitting the available data. Eq. 5-3 is used to represent the surface tension data for 85 fluids in REFPROP (REFerence Fluid PROPERTIES), which is a program developed by the National Institute of Standards and Technology (NIST), providing tables and plots of thermodynamic and transport properties of important industrial fluids and their mixtures, with an emphasis on refrigerants and hydrocarbons, especially natural gas systems. The coefficients γ_i and n_i as well as the critical temperature were reported by Mullero and Cachadina for several FAMES [12]. Mullero et al. have been used Eq. 5-3 to correlate surface tension data of aliphatic, carboxylic, and polyfunctional organic acids including the FAs found in vegetable oils [13].

5.3.2 Prediction

Several models for the estimation of surface tension of liquids have been proposed, but model estimation for oils and biodiesel are scarce. One of the most famous correlations to estimate the surface tension was proposed in 1923 by Macleod [14] from the liquid (ρ^L) and vapor (ρ^V) molar densities at equilibrium:

$$\gamma = K(\rho_m^L - \rho_m^V)^4 \quad \text{Eq. 5-4}$$

where K is the temperature-independent but compound-dependent parameter. In 1924 the temperature-independent parameter in the Macleod's correlation was called parachor P_{ch} by Sugden [15]:

$$\gamma = [P_{ch}(\rho_m^L - \rho_m^V)]^4 \quad \text{Eq. 5-5}$$

where $P_{ch} = K^{1/4}$. The parachor was assumed to be additive with respect to chemical structures. Initially, only 11 chemical groups were assigned for the parachor values and this descriptor values were refined and expanded by Quayle [16] to over 50 chemical groups.

The surface tension obtained by Eq. 5-5 is very sensitive to the values of the parachor and density because it is correlated to the fourth power. Therefore, the error on surface tension will be amplified from errors in the P_{ch} or density. Eq. 5-5 has been shown to be good for prediction of surface tension for many organic compounds [3, 17]. Nevertheless, some shortcomings in Eq. 5-5 were pointed out [18] as for example, (i) the parachor is an empiric temperature-dependent parameter whose relationship with temperature was not known, and (ii) the absolute average relative percent deviation ($AARD\%$) in surface tension prediction increased with increasing complexity of the molecular structure of the fluid under consideration. Moreover, Guggenheim [11] pointed out that the power of Eq. 5-4 was 11/3 and not 4.

Freitas et al. used the Parachor model in the form of Eq. 5-6, in order to predict the surface tension of biodiesel [19].

$$\gamma = \left(\frac{P_{ch} \rho}{M} \right)^4 \quad \text{Eq. 5-6}$$

In this equation, γ is the surface tension in $\text{mN}\cdot\text{m}^{-1}$, ρ is the density in $\text{g}\cdot\text{cm}^{-3}$, P_{ch} is the parachor in $[(\text{mN}\cdot\text{m}^{-1})^{1/4}/(\text{cm}^3\cdot\text{mol}^{-1})]$ and M is the molar mass (in $\text{g}\cdot\text{mol}^{-1}$). Experimental densities of the biodiesel fuels reported by Pratas et al. [20] were used. For the calculation of the surface tensions of the biodiesel fuels, the parachor-based MacLeod-Sugden equation with the parachors proposed by Allen et al. [3] and Knotts et al. [17] has been used. The parachors for the biodiesel fuels (BDF) were calculated from the parachors of pure FAMES using the mixing rules [19]:

$$P_{chBDF} = \sum_i (x_i P_{ch,i}) \quad \text{Eq. 5-7}$$

where $P_{ch,i}$ represents the parachor of the FAME i . Freitas et al. tested Eq. 5-6 and 5-7 for soybean (S), rapeseed (R), palm (P), and their respective binary and ternary mixtures: soybean + rapeseed (SR), rapeseed + palm (RP), soybean + palm (SP), and soybean + rapeseed + palm (SRP), and sunflower (Sf). They used experimental densities of biodiesel instead predicted values and obtained overall *AARDs* of 7.7% and 1.3% for the parachor schemes of Allen et al. and Knotts et al., respectively.

Another method to estimate surface tension of mixtures was given by Reid et al. [10], which is based on the Macleod–Sugden correlation and negligible vapour pressure and it is represented by the equation:

$$\gamma^{1/4} = \rho \sum_{i=1}^N \frac{x_i \gamma_i^{1/4}}{\rho_{m,i}} \quad \text{Eq. 5-8}$$

where γ is the surface tension of mixture and x_i , γ_i and ρ_i are the molar fraction, surface tension and molar density of the pure component i . If the mixture can be considered as composed of similar species, with almost the same densities, Eq. 5-8 can be simplified to:

$$\gamma = \left[\sum_{i=1}^N x_i \gamma_i^{1/4} \right]^4 \quad \text{Eq. 5-9}$$

In the application of Eqs. 5-8 and 5-9 to oil and biodiesel, the surface tensions γ_i refer to the FA or FAME i , respectively, evaluated from selected standard correlations from literature [12, 13] to be presented later in the results section. For application of Eq. 5-8, densities of FAs will be calculated from the Halvorsen model due to the good predictions obtained earlier for density, while for biodiesel and the individual FAMES the GCVOL model will be used.

Verduzco et al. proposed the combination of the parachor model (Eq. 5-6) with an empirical correlation for biodiesel density giving rise to a totally predictive method, dispensing the use of the experimental data of density of individual FAMES. The predictive equation is [21, 22]:

$$\gamma_i = P_{ch,i}^4 \left(\frac{1.069 + 0.0113N_i - 7.41 \times 10^{-4}T}{M_i} + \frac{3.575}{M_i} \right)^4 \quad \text{Eq. 5-10}$$

where γ_i is the surface tension in mN/m, $P_{ch,i}$ is the parachor, M_i is the molar mass in g/mol, N_i is the number of double bonds in the fatty acid chain and T is the temperature in K. From the calculated γ_i , the biodiesel surface tension, γ , was obtained from the Dalton mass-averaged method:

$$\gamma = \sum_i^N w_i \gamma_i \quad \text{Eq. 5-11}$$

or the Kay's mixing rule

$$\gamma = \sum_i^N x_i \gamma_i \quad \text{Eq. 5-12}$$

where w_i and x_i represent the mass and molar fraction of i^{th} FAME. Eq. 5-11 was tested and validated by Allen et al. [3] and Shu et al. [2]. Kay's mixing rules are used for biodiesel because this fuel can be considered as a mixture of FAMES with small deviations from ideal behaviour. Verduzco et al. tested Eqs. 5-10 to 5-12 for 33 biodiesel samples corresponding to 88 experimental points and concluded that the mass-average method of Dalton mixing rule had an $AARD = 2.88\%$, while for the method relative to the Kay's mixing rule an $AARD = 3.04\%$ was

obtained. For individual FAMEs, the parachor model of Eq 5-10 was able to predict the surface tension with *OARD* of 4.8% and 1.3% for the parachor schemes of Allen et al. and Knotts et al. respectively [22].

Another route of predicting surface tension of oil and biodiesel using the parachor concept is the application of Eq. 5-11 with surface tension of FA or FAME *i* in the oil or biodiesel, predicted with Eq. 5-6, that could be written as:

$$\gamma_i = \left(\frac{P_{ch,i} \rho_i}{M_i} \right)^4 \quad \text{Eq. 5-13}$$

where $P_{ch,i}$, ρ_i and M_i are the parachor, the density and molar mass of the FA or FAME *i*. Eq. 5-13 was applied in this work with the parachors calculated from the contribution groups method given by Knotts et al. [17] and densities predicted by Halvorsen method [23] for FAs and GCVOL model for FAMEs (about these methods see sections 3.1.4.3.1 and 3.2.3.2).

Several corresponding states correlations (CSC) are available for surface tension prediction [24]. The critical pressure (p_c), critical temperature (T_c), and normal boiling point (T_b) are needed as inputs for estimation. A major shortcoming to the use of CSCs is the lack of reliable experimental information of these properties for FAMEs, FAs and especially for TGs and for this reason estimation methods must be used. Critical properties and normal boiling points of FAs and critical temperatures of TGs were reported by Otobrise and Monago [25] and Petcu et al. [26], while Wallek et al. [27] reviewed common group-contribution and corresponding-state models for the estimation of normal boiling points, vapour pressures, liquid densities, and dynamic viscosities in view of their application to fatty acid methyl esters, related fatty acids and triglycerides. They introduced a new group, representing the backbone structure common to all triglycerides to improve the performance of models significantly. Neto et al. [28] compared several models for fatty acid predictions and FAMEs and applied the most successful to vegetable oils and biodiesel, including CSO and CSB. Garcia et al. [29] reported values of critical properties for FAMEs and FAEs [25] and recently Evangelista et al. [30] presented a comprehensive study for the estimation of the above mentioned properties being the main outcome of their work the recommendation of the most feasible models for engineering applications. The errors associated with CSCs for surface tension of FAMEs and biodiesel are usually high [22] and for oils they were not reported.

One of the most commonly used CSC for prediction of surface tension of biodiesel related compounds is the Sastri-Rao [24, 31]:

$$\gamma = K p_c^{0.5} T_b^{-1.5} T_c^{1.85} \left(\frac{1-T_r}{1-T_{br}} \right)^{1.22} \quad \text{Eq. 5-14}$$

where $T_r (=T/T_c)$ is the reduced temperature, and T_{br} is the reduced boiling temperature and the units of temperature and pressure are kelvin and bar, respectively and $K = 0.158$. The values of P_c , T_c and T_b were calculated as follow:

$$X = \sum_{i=1}^N x_i X_i \quad \text{Eq. 5-15}$$

where X is T_c , P_c or T_b and molecular substances i can be FAs, TGs or FAMES. Eq. 5-14 has the form of Guggenheim equation, Eq. 5-2 with:

$$\gamma_0 = K p_c^{0.5} T_b^{-1.5} T_c^{1.85} \left(\frac{1}{1-T_{br}} \right)^{1.22} \quad \text{Eq. 5-16}$$

Some semi-empirical correlations are available for prediction of surface tension of biodiesel. From a free energy additivity model, Phankosol et al. derived the following equation for individual FAMES [32]:

$$\gamma = 60.211 - 0.4307z - 0.1125T + 0.00207zT + 3.676m - 0.00893mT \quad \text{Eq. 5-17}$$

where T , z and m are the temperature, the number of carbon atoms and number of double bonds of corresponding fatty acid, respectively. To apply this correlation to estimate the biodiesel surface tension, which is a mixture of FAMES, the average carbon numbers (z_{avg}) and average number of double bonds (m_{avg}) must be used. These quantities are defined as:

$$z_{avg} = \sum_{i=1}^n x_i z_i \quad \text{Eq. 5-18}$$

$$m_{avg} = \sum_{i=1}^n x_i m_i \quad \text{Eq. 5-19}$$

where x_i is the molar fraction of i^{th} FAME. For the application of Eq. 5-17 to biodiesels, the prior knowledge of surface tension of individual FAMES is not necessary. The application of Eq. 5-17 to the estimation of FAMES surface tension gave deviations ranging between 0.05% and 5.07%, at temperatures between 20°C and 100°C, corresponding to *AARD* of 1.21%. While, for biodiesel, at temperatures in the range 30°C to 80°C the deviations were in the range 0.85 to 3.93%, with *OARD* of 1.84% [32].

Another predictive method which has gained importance was proposed by Allen et al. [3]. They found that, the biodiesel surface tensions predicted from the mass-average equation as Eq. 5-11 are usually over predicted and according to their opinion this could be due to the fact that, components with lower surface tensions would produce less than 100% effect in the mixture, compared to their pure value. Allen et al. proposed that components with higher intermolecular attraction in their pure state, and thus higher surface tension, would likely have a higher intensity of attraction to each other in a mixture, thus tending to expel the components with lower surface tensions away from the surface. Thus, lower-surface tension components of a mixture will have less influence at the surface, compared with the higher-surface tension components. Based on this assumption, they assumed that the surface tension of the mixture should be obtained taking into account the effective surface tension of the individual components, given by the contribution $f_i(w_i\gamma_i)$ where f_i is the weight factor for the component i of the mixture, which is obtained by the linear function:

$$f_i = m\gamma_i + c \quad \text{Eq. 5-20}$$

where m is the slope and c the intercept. The surface tension of oil and biodiesel are predicted by:

$$\gamma = \sum_{i=1}^N f_i(w_i\gamma_i) \quad \text{Eq. 5-21}$$

The way to calculate parameters m and c have been discussed in several works [2, 3]. In the application of Eqs. 5-20 and 5-21 to oil and biodiesels, the surface tensions γ_i of individual FAs and FAME i , were evaluated from the literature [12, 13]. Thangaraja et al. [31] developed a simple and useful method using Allen's framework and reported the values of m and c for FA and FAME given in Table 5.1

Table 5.1. Correlation parameters m and c of Eq. 5-20 for FAs and FAMES [31].

Temperature / K	Fatty acid		Temperature / K	Methyl ester	
	m	c		m	c
303	0.0128	0.5523	303	0.0143	0.5523
313	0.0129	0.5567	313	0.0141	0.5764
333	0.0131	0.5696	333	0.0133	0.6207
353	0.0134	0.5827	353	0.0126	0.6595

The methods described above will be applied to CSO and CSB in the next section.

5.4 Results and discussion

5.4.1 Surface tension of CSO

The surface tension data measured with the Wilhelmy plate method for cottonseed oil is reported in Table 5.2 and they are represented in Figure 5.1.

Table 5.2. Surface tension of CSO as function of temperature.

T / K	$\gamma / \text{mN.m}^{-1}$
298.3	31.85 ± 0.10
303.0	31.32 ± 0.10
313.1	30.10 ± 0.08
323.7	28.24 ± 0.11
334.0	26.41 ± 0.12
343.1	25.45 ± 0.10
353.4	24.63 ± 0.08

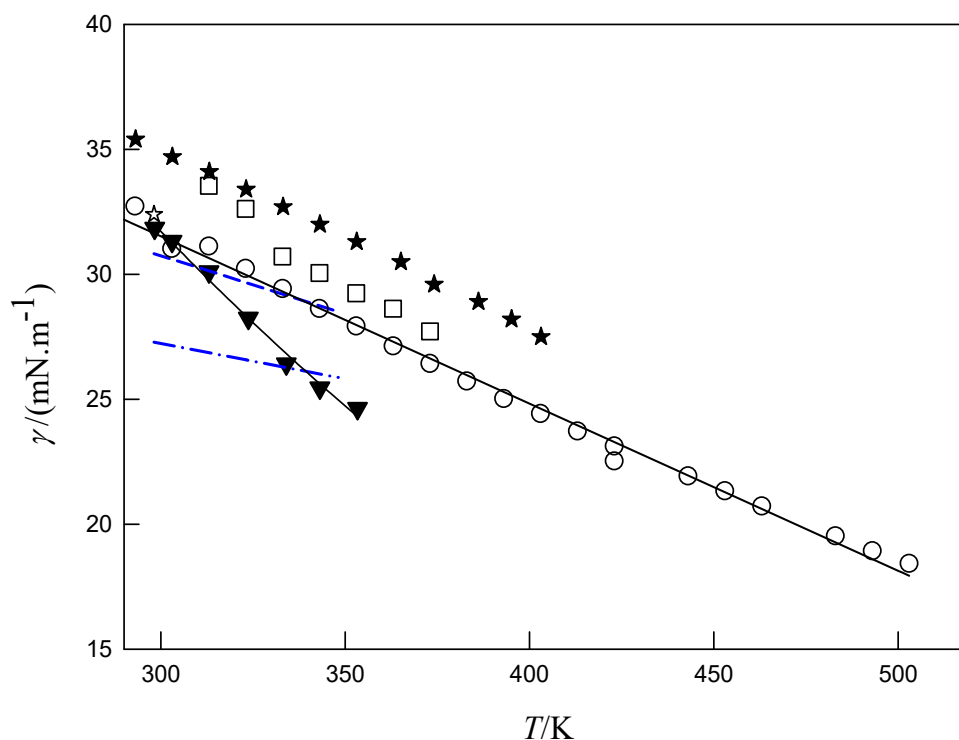


Figure 5.1. Surface tension of CSO. ▼, This work, Wilhelmy plate; ○, Menzies et al. [33]; ★, Halpern [34]; □, Dikko et al. [35]; ☆, Zeitoun et al. [36]; — · — · —, Singleton and Benerito (crude CSO) [37]; - - -, Singleton and Benerito (refined CSO) [37]. Black full lines represent correlations of values with Eq. 5-1.

From Table 5.2 and Figure 5.1 it can be concluded that the oil surface tension behaves as expected, i.e. the surface tension decreases as temperature increases.

The values of surface tension available in the literature are also represented in Figure 5.1. All the reported values in the literature are usually higher than those of this work. Menzies et al. [33] measured surface tension by capillary rise method in the range 293 to 503 K. Apparently, they are the first measurements reported in the literature for CSO. The values of Menzies et al. are in close agreement with those of this work up to 303.15 K. At 313 K the *RD* of surface tension relative to the value found in this work is 3% and it increases with the increasing of temperature, reaching about 12% at 353 K. Halpern [34] studied a commercially sample in the range 293 K to 403 K using the pendant drop weight method. From Figure 5.1 it can be concluded that Halpern data exceed largely all the data mentioned before. Singleton and Benerito [37] made measurements in the temperature range from 298.15 to 348.15 K, using the capillary rise method

for crude and purified CSO with accuracy within $\pm 0.08 \text{ mN.m}^{-1}$. Their values were reported as the linear functions:

$$\gamma = 35.728 - 0.02833 T \quad \text{Eq. 5-22}$$

and

$$\gamma = 44.588 - 0.04640 T \quad \text{Eq. 5-23}$$

for crude and refined CSO, respectively. It can be seen that, this data set shows a lower slope than for the values of this work, with good agreement at the lower and upper temperature limits for the refined and crude oils, respectively. The surface tensions of refined oil are in good agreement (in the range $\pm 3\%$) with values of this work between 298 K and 320 K, and deviations reach -12% at 348 K. For the crude oil, positive deviations from values of this work starting with 17% at 298.15 K and reaching 3% at 332 K are observed. Between 332 K and 348 K, the values of this work deviate from those of Singleton and Benerito in the range $\pm 3\%$. The surface tension values of Singleton and Benerito given for crude and refined oils deviate about 12% each other, in all the temperature range. Zeitoun et al. [36] use the de Nouy ring method and reported $\gamma = 32.4 \text{ mN.m}^{-1}$ at 298.15, which is close to the measurement obtained in this work (31.8 mN.m^{-1}). Recently, Dikko et al. [35] measured the surface tension of several vegetable oils, including CSO, by capillary rise between 313 K and 373 K. Their values for CSO show positive deviations from the values relative to this work with $RD = 11\%$ at 313 K increasing to 19% at 353 K.

Comparing surface tension data of this work with the available experimental data from literature, it can be concluded that present data shows a very marked variation with temperature, as can be observed by the sharp slope. Among the main causes that certainly explain the differences between the results obtained in the present work and those verified in the literature are the origin of crude oil feedstock and the refining treatment of cotton oil. The main purpose of chemical refining is to saponify the FA by an alkaline solution and dilute the resulting soaps in a water phase. These soaps are removed by separators. The neutral oils are subsequently bleached and deodorised. In addition to the removal of FA other undesirable non-glyceride materials are

also removed as phospholipids (gums), oxidized products, metal ions (e.g. iron, copper), colour pigments (e.g. gossypol) and insoluble impurities.

Menzies et al. [33] not gone into detail concerning to the kind of oil used in measurements, they have use an oil supplied by NBS. Dikko et al. [35] studied locally produced vegetable crude oils in Yola, Nigeria, including cottonseed oil and they were bought directly from the people that produced them with traditional and local equipments. Singleton and Benerito obtained crude CSO by conventional mechanical pressing. Next, the oil was alkali-refined, bleached and deodorized and maintained under an atmosphere of inert gas [37]. The FFA, iodine number and unsaponifiable matter of crude and refined oils used by Singleton and Benerito are shown in Table 5.3.

Table 5.3. Quality parameters of CSO crude and refined used by Singleton and Benerito [37].

Type of oil	FFA (%)	IN (g I ₂ /100g)	UM (%)
Cottonseed crude, screw-pressed	1.8	-	1.09
Cottonseed refined, screw-pressed	0.01	104.3	0.50

From Table 5.3 it can be observed that both, FFA and unsaponificable matter decrease with purification process. The most notable differences between crude and refined CSO are in the FFA content. These differences are also found in refining processes for other oils. However, it is difficult to explain the fact that the crude oil has surface tension about 12% lower than the refined one, in all the temperature range, basis on the differences between crude and refined cotton oil presented in Table 5.3.

The surface tension data of CSO measured in this work were compared with values relative to other oils, namely soy, rapeseed and palm oils in Figure 5.2. A great variability of values can be observed, even within the same type of oil, as displayed in Figure 5.1 for CSO. Esteban et al. [38] measured surface tension of used soy oil by drop weight method and Sachasrabudhe et al. [39] measured the surface tension by the pendant drop method using two different devices. Differences of more than 15% are observed for the values reported by Sahasrabudhe et al. [39] with the different methodologies. Sahasrabudhe et al. [39] explained the difference in values for the surface tension mainly because of the numerical method used by each equipment in calculating surface tension from the Young's equation. The data reported by Esteban et al. [38]

for the three oils are well above of the data measured in this work, especially at temperatures higher than 320 K.

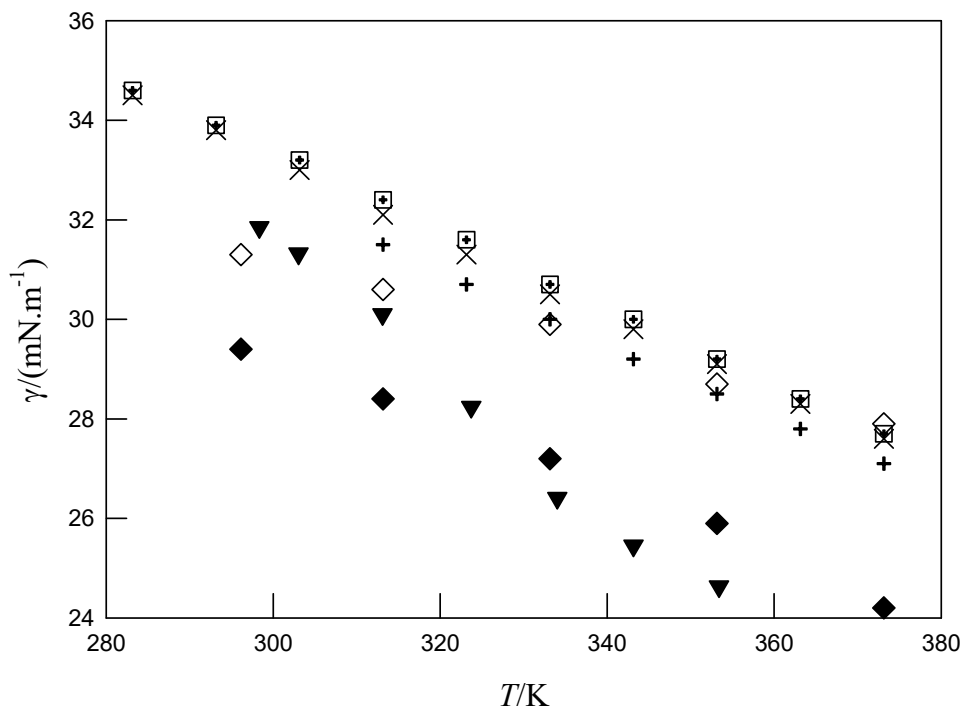


Figure 5.2. Surface tension as function of temperature of CSO compared with other oils. ▼, This work; Soy: ⊠, Esteban et al. [38]; ◆,◇ Sahasrabudhe et al. [39]; +, Esteban et al. [38] (palm); ×, Esteban et al. [38] (rapeseed).

The differences in surface tension showed for the same kind of oil (e.g. CSO) and between different types of oils, are difficult to explain and there are only few studies aiming this purpose. Xu et al. made a pioneer study in this field for corn, canola, peanut, olive and soybean oils [40]. They have shown that using pure FA the surface excess properties were not affected substantially by degree of chain unsaturation, but shorter chains reduce the surface excess energy and thus the surface tension. Cottonseed has an important amount of palmitic acid fragment in the TGs (24% wt %), which can explain in part the decrease of surface tension comparing with oils that contain lesser quantities of C16:0. However, since the triglycerides almost entirely comprise long acyl chains, different molecular compositions among these oils do not affect much surface tension. The measurement techniques and samples treatment prior to the measurement could be of fundamental importance in the differences registered.

Eqs. 5-1 and 5-2 were used to correlate surface tension data of CSO from this work and from Menzies et al. The correlation of values given by Menzies et al. is further justified by the long temperature range of the determinations and thus Eq. 5-3 was also fitted. The parameters obtained are given in Table 5.4 for the linear model and in Table 5.5 for Eqs. 5-2 and 5-3. In Figure 5.1, the correlations with Eq. 5-1 are displayed for both set of ST data. From the linear correlations with Eq. 5-1, the surface thermodynamic properties, namely, surface entropy, S^γ , and surface enthalpy, H^γ , were also determined as follow:

$$S^\gamma = - \left(\frac{\partial \gamma}{\partial T} \right)_p \quad \text{Eq. 5-24}$$

$$H^\gamma = \gamma - T \left(\frac{\partial \gamma}{\partial T} \right)_p \quad \text{Eq. 5-25}$$

Table 5.4. Correlations parameters of CSO surface tension with Eq. 5-1 and derived surface entropy and enthalpy.

Data	A	B	r^2	$\sigma/(\text{mN}\cdot\text{m}^{-1})$	$H^\gamma/(\times 10^2, \text{J}\cdot\text{m}^{-2})$	$S^\gamma/(\times 10^5, \text{J}\cdot\text{m}^{-2}\cdot\text{K}^{-1})$
This work	73.4952	-0.13949	0.9890	0.33	7.35±0.21	13.95±0.66
Menzies et al. [33]	51.586	-0.06690	0.9942	0.34	5.16±0.05	6.69±0.11

Table 5.5. Correlations parameters of CSO surface tension with Eqs. 5-2 and 5-3.

Data	T_c/K	γ_i	n	r^2	$\sigma/(\text{mN}\cdot\text{m}^{-1})$
Eq. 5-2					
This work	571.27	78.691	11/9	0.9897	0.32
Menzies et al.	851.74	53.7514	11/9	0.9957	0.29
Eq. 5-3					
Menzies et al.	780.2	4.10585	-0.514014	0.9977	0.02
		56.0751	1.53433		

The values of critical temperature predicted from fitting Eq. 5-3 to Menzies et al. data is close to that reported by Neto et al [28], $T_c = 798$ K. The value obtained from Guggenheim equation is also acceptable.

The predictive methods described above were applied to CSO and the obtained results are presented in Figure 5.3. Eqs. 5-8 and 5-9, were tested with surface tension of pure FA constituents of the oil and the coefficients needed, given by Mulero et al. [13], were used (see

Table D.1). The calculated values run very close of data from Menzies et al. [33] and the estimation given by equations Eqs. 5-8 and 5-9 were practically identical. Eq. 5-11 with Eq. 5-13 were tested with the parachors of pure fatty acids presented in Table 5.6. Those for the corresponding FAMES of CSB are given as well. Results are plotted in Figure 5.3. The predicted surface tension give higher values than the data from this work, with *RDs* starting with 3% at 298 K and increasing with temperature. The predictions are in excellent agreement with ST values reported by Menzies et al. [33].

Table 5.6. Composition of CSO and CSB and Knotts' parachors, $P_{ch,i}$ [17].

Component	CSO			CSB		
	w_i (wt %)	x_i	$P_{ch,i}$	w_i (wt %)	x_i	$P_{ch,i}$
Myristic C14:0	1.45	0.0174	611.04	0.93±0.28	0.0110	657
Palmitic C16:0	24.15	0.2579	691.26	26.76±1.56	0.2845	737
Stearic C18:0	2.90	0.0279	771.48	2.81±0.29	0.0271	817
Oleic acid C18:1	19.32	0.1873	760.48	17.89±1.71	0.1735	806
Linoleic acid C18:2	50.72	0.4952	749.48	51.61±2.99	0.5039	795
Linolenic acid C18:3	1.45	0.0143	736.40	0	0	782

The values resulting for surface tension calculated with Allen method (Eqs. 5-20 and 5-21) were plotted in Figure 5.3. Predictions at 303 K and 313 K are in good agreement with the measurements of this work, with *RDs* less than 2% and those at 333 K and 353 K differ from measured values about 7%. In general the predictions are reasonable. The CSC of Sastri and Rao given by Eq. 5-14 gives variable results. The calculations reproduce well data of Menzies et al [33] using the critical parameters reported by Otobrise and Mnago [25]. The parameters reported by Neto et al. [28] for CSO gives similar results as Allen method.

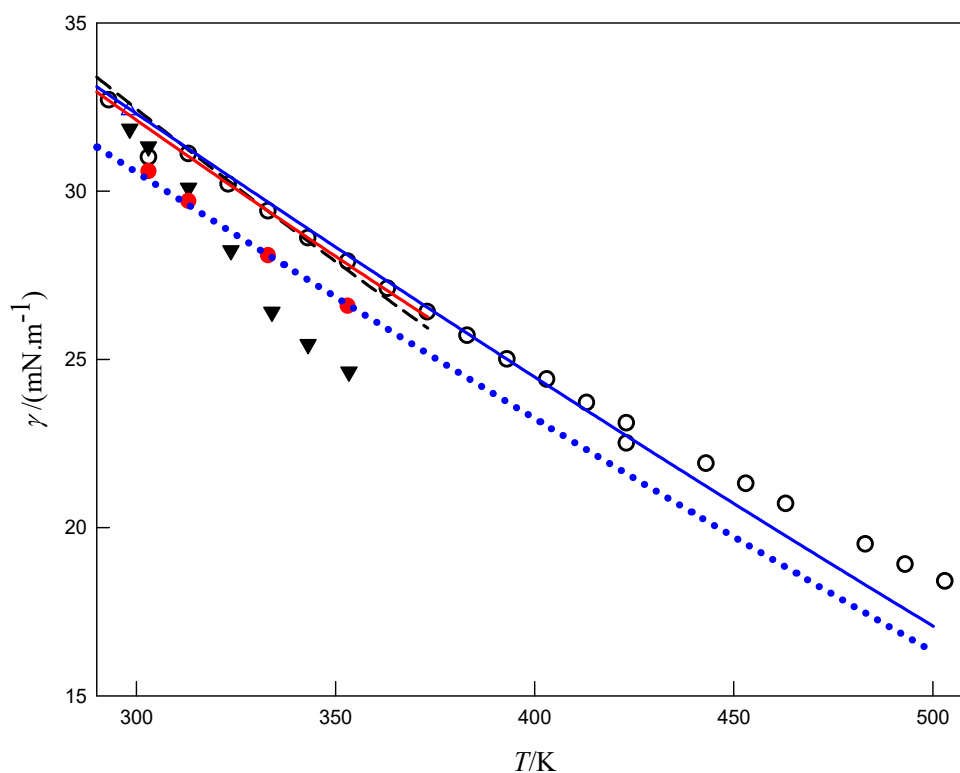


Figure 5.3. Prediction of surface tension of CSO. Experimental: \blacktriangledown , This work, Wilhelmy plate; \circ , Menzies et al. [33]. Prediction: --- , Reid et al. [10], Eq. 5-8; - - - , Eqs. 5-11 and 5-13 using FA profile of the oil; \bullet , Allen et al. method; — , Sastri-Rao, $K = 0.158$ with critical parameters from Otoberise and Monago [25]; \cdots , Sastri-Rao, $K = 0.158$ with CSO critical parameters calculated by Neto et al. [28].

5.4.2 Surface tension of CSB

Two series of surface tension data were measured for cottonseed biodiesel some days apart and for the same sample after being dried in a rotatory evaporator. Data and standard deviation from the mean value, for each measurement, are reported in Table 5.7 and are represented in Figure 5.4.

Table 5.7. Surface tension of CSB as a function of temperature.

T/K	$\gamma/mN.m^{-1}$	T/K	$\gamma/mN.m^{-1}$
1 st series		2 nd series	
304.75	28.60±0.09		
311.35	27.65±0.10	308.85	26.97±0.07
319.13	26.77±0.09	316.20	26.55±0.09
327.90	25.88±0.10	324.60	25.64±0.09
338.38	25.51±0.14	334.81	24.87±0.06
347.49	24.96±0.11		

From Table 5.7 and Figure 5.5 it can be concluded that the surface tension decreases as temperature increases, as expected.

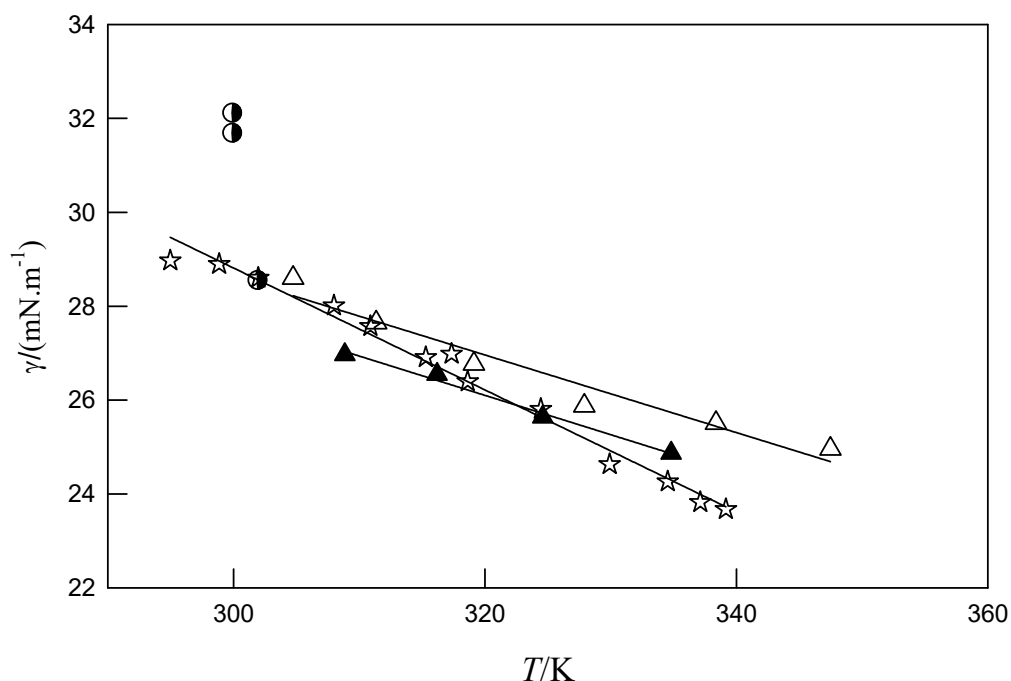


Figure 5.4. Experimental surface tension of CSB as function of temperature: Δ , This work, 1st series; \blacktriangle , This work, 2nd series; \bullet , Al-Iwayzi et al. [41]; \star , Wimala and Brown [42]. The lines represent the correlation of values with linear Eq. 5-1.

The values of surface tension available in the literature for CSB are very scarce and were represented in Figure 5.4 Al-Iwayzi et al. [41] measured the surface tension with Du Nouy ring at 300 K and 302 K. At 302 K the obtained value is consistent with data of this work. The same

measurement technique was employed by Wimala and Brown [42] for CSB and their values follow a very close path to that observed for the determinations of this work.

In Figure 5.5, the surface tension of other biodiesels, namely soybean and rapeseed, are displayed for comparison with CSB data. The values reported by Freitas et al. [19] for soy and rapeseed are similar throughout the temperature range, mainly at the higher temperatures. They deviate by more than 10% from the values measured in this work. From the same figure it can be observed that surface tension of soy biodiesels, measured by different authors, differ significantly, which could be explained by the composition of oils and measurement technique. As far as the methodology is concerned, the measures for the same feedstock can have large uncertainties as for example the surface tensions reported by Watts and Tate [43] for commercial biodiesel samples of soy oil. They measured the surface tension at temperatures up to 333 °C using a pendant drop tensiometer. Significant errors result from operational factors as misplacement of the origin, tilted drop profiles, and aspect ratio. Some of these results obtained for soy biodiesel are shown in Figure 5.5. Surface tension of biodiesels seems to be sensible to composition, to the preparation of samples prior to measurement and measurement technique itself.

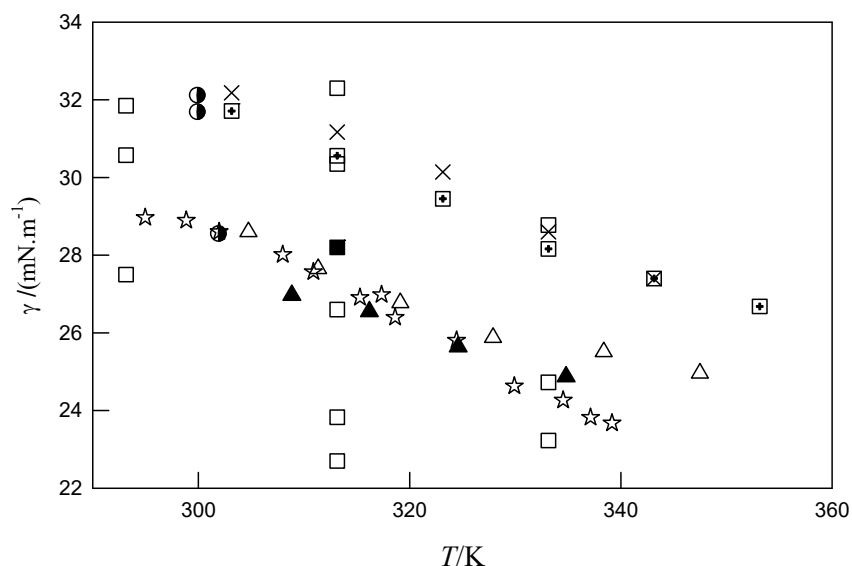


Figure 5.5. Experimental surface tension of CSB compared with biodiesel from other oils. Experimental (CSB): Δ , This work, 1st series; \blacktriangle , This work, 2nd serie; \circ , Al-Iwayzi et al. [41]; \star , Wimala and Brown [42]; Experimental (other biodiesels): \boxplus , Soy, Freitas et al. [19]; \times , Rapeseed, Freitas et al. [19]; \square , Soy, Watts and Tate [47]; \blacksquare , Soy, Allen et al. [3].

As for CSO, Eqs. 5-1 and 5-2 were used to correlate data of CSB. Both sets of surface tension data measured in this work and those from Wimala and Brown (WB) [42] were correlated separately for comparison purposes. The parameters obtained are given in Table 5.8 for linear model and in Table 5.9 for Eq. 5-2. From Eq. 5-1, the surface entropy and surface enthalpy were determined from Eqs. 5-24 and 5-25. These properties and their corresponding uncertainties are also presented in Table 5.8.

Table 5.8. Parameters for the correlations of surface tension of CSB with Eq. 5-1.

Data	A	B	r^2	$\sigma/(\text{mN}\cdot\text{m}^{-1})$	$H^{\sigma}/(\times 10^2, \text{J}\cdot\text{m}^{-2})$	$S^{\sigma}/(\times 10^5, \text{J}\cdot\text{m}^{-2}\cdot\text{K}^{-1})$
1 st serie ^a	52.8870	-0.08371	0.999	0.12	5.29±0.19	8.37±0.60
2 nd serie ^a	53.4100	-0.08265	0.950	0.34	5.34±0.31	8.27±0.95
WB	67.7647	-0.1298	0.958	0.25	6.77±0.16	12.98±0.49

Table 5.9. Parameters for the correlations of surface tension of CSB with Eqs. 5-2.

Data	T_c / K	γ_0	n	r^2	$\sigma/(\text{mN}\cdot\text{m}^{-1})$
1 st series	716.6459	55.5480	11/9	0.9394	0.3395
2 nd series	700.6628	55.0133	11/9	0.9897	0.1171
WB	567.3975	72.2764	11/9	0.9837	0.2560

From Table 5.8 it is depicted that the surface properties resulting from the two series of measurements, present similar values, which makes sense because they belong to the same sample. The surface enthalpy relative to the CSB studied in this work differs 28% from the value of Wimala and Brown and the surface entropy differs by 56%. This result are explained by the high dependency of surface entropy upon the slope of (γ, T) curve.

The surface tensions of CSB were predicted using the methods described in section 5.3.2 and the results are presented in Figure 5.6. The Reid equations (Eqs. 5-8 and 5-9) provide reasonable estimation of the surface tensions of the present work, with $AARD = 2.9\%$ and $AARD = 6.4\%$ for the 1st and 2nd series, respectively. For the Eqs. 5-7, 5-10 and 5-13, the parachors of FAMES needed are given in Table 5.6. The methods based in the Parachor (Eqs. 5-11/5-13 and 5-10/5-12) give prediction of surface tensions differing by more than 5% in the studied temperature range. The Phankosol method (5-17 and 5-19) gives almost the same results. The Sastri and Rao predictive method gives variable results that are dependent of the p_c , T_c and T_b set used. These parameters reported by Neto et al. [28] for CSB and those calculated from Eq. 5-15 using

experimental values reported by Evangelista et al. [30], give predictions of surface tension encompassing the available experimental data. The experimental values of surface tension of this work were predicted with Eq. 5-15 using parameters calculated with Constantinou and Gani group contribution method (CG) [44], obtaining $AARD = 5.9\%$ for the 1st series and $AARD = 1.0\%$ for 2nd ones. The Allan method requires the surface tension of pure FAMEs. Thus, the coefficients of Eq. 5-3 given by Mulero et al. [12] were used for the calculation of surface tensions in the range 303 to 353 K of C16:0, C18:0, C18:1 and C18:2 (see Table D.2). For C14:0 the least squares constants reported by Jasper [45] were used for calculation of surface tension, giving:

$$\gamma/(\text{mN}\cdot\text{m}^{-1}) = 52.825 - 0.0800 T/(\text{K}) \quad \text{Eq. 5-26}$$

The surface tensions predicted from Allen's method are in good agreement with those of the 1st series of this work, with RDs within $\pm 2\%$ ($ARRD = 1.5\%$) and for the 2nd series the RDs are the range $\pm 4\%$ ($ARRD = 4.2\%$).

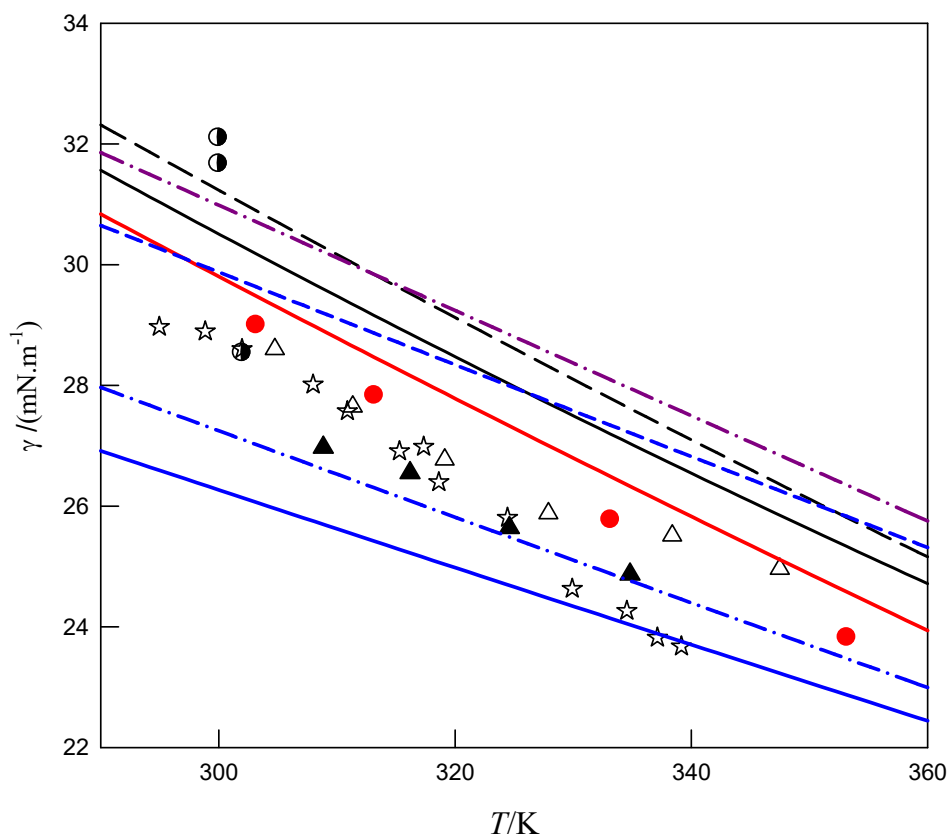


Figure 5.6. Prediction of surface tension of CSB. Experimental: Δ , This work, 1st series; \blacktriangle , This work, 2nd series; \bullet , Al-Iwayzi et al. [41]; \star , Wimala and Brown [42]; Prediction: --- , Reid et al.; --- , Eqs. 5-11 and 5-13; — , Eqs. 5-10 and 5-12; $\text{—}\cdot\text{—}$, Eqs. 5-17 to 5-19; — , Sastri-Rao, $K = 0.158$ and model parameters given by Neto et al. [28]; --- , Sastri-Rao, $K = 0.158$ with FAME parameters given by Evangelista et al. [30]; $\text{—}\cdot\text{—}$, Sastri-Rao, $K = 0.158$ with FAME parameters from predictive Constantinou and Gani [44]. \bullet , Allen et al. method [3].

As can be seen in Figure 5.6, the surface tension determined by Wimala and Brown are consistent with data from this work. Therefore, this data was also evaluated with Sastri and Rao using CG and Allen methods, which provided the most reliable predictions for data of this work. In the Table 5.10 the *AARDs* resulting from the method applied to the surface tension data of this work and those of Wimala and Brown are compared. The *OARDs* are also presented. Data of Wimala and Brown are reasonable predicted with *AARDs* of 3.6% corresponding to about $1 \text{ mN}\cdot\text{m}^{-1}$.

Table 5.10. Average absolute relative deviations, % *AARD* and % *OARD* for selected predictive methods applied to CSB.

Method	Data			
	1 st series	2 nd series	UW	<i>OARD</i> %
Allen	1.51	4.18	3.59	3.09
Reid	2.88	6.40	5.87	5.05
Sastri-Rao	5.90	0.95	3.41	3.42

In Figure 5.7 and Figure 5.8, the *RDs* are plotted as function of temperature and parity plot are also presented for the data sets and selected method.

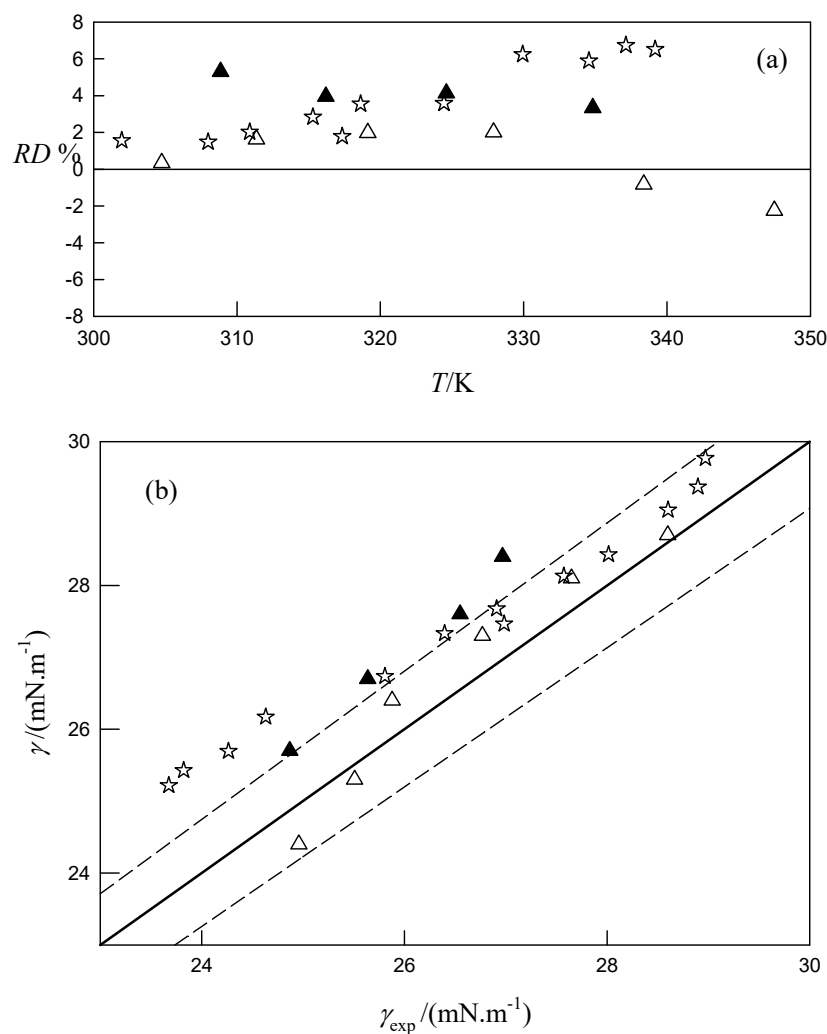


Figure 5.7. Predicted surface tension of CSB with Allen method. (a) Relative percent deviations between predicted and measured surface tension as function of temperature. (b) Parity plots for predicted and measured surface tension. Δ , 1st serie; \blacktriangle , 2nd serie; \star , Wimala and Brown [42]. Dashed line corresponds to *RDs* $\pm 3\%$.

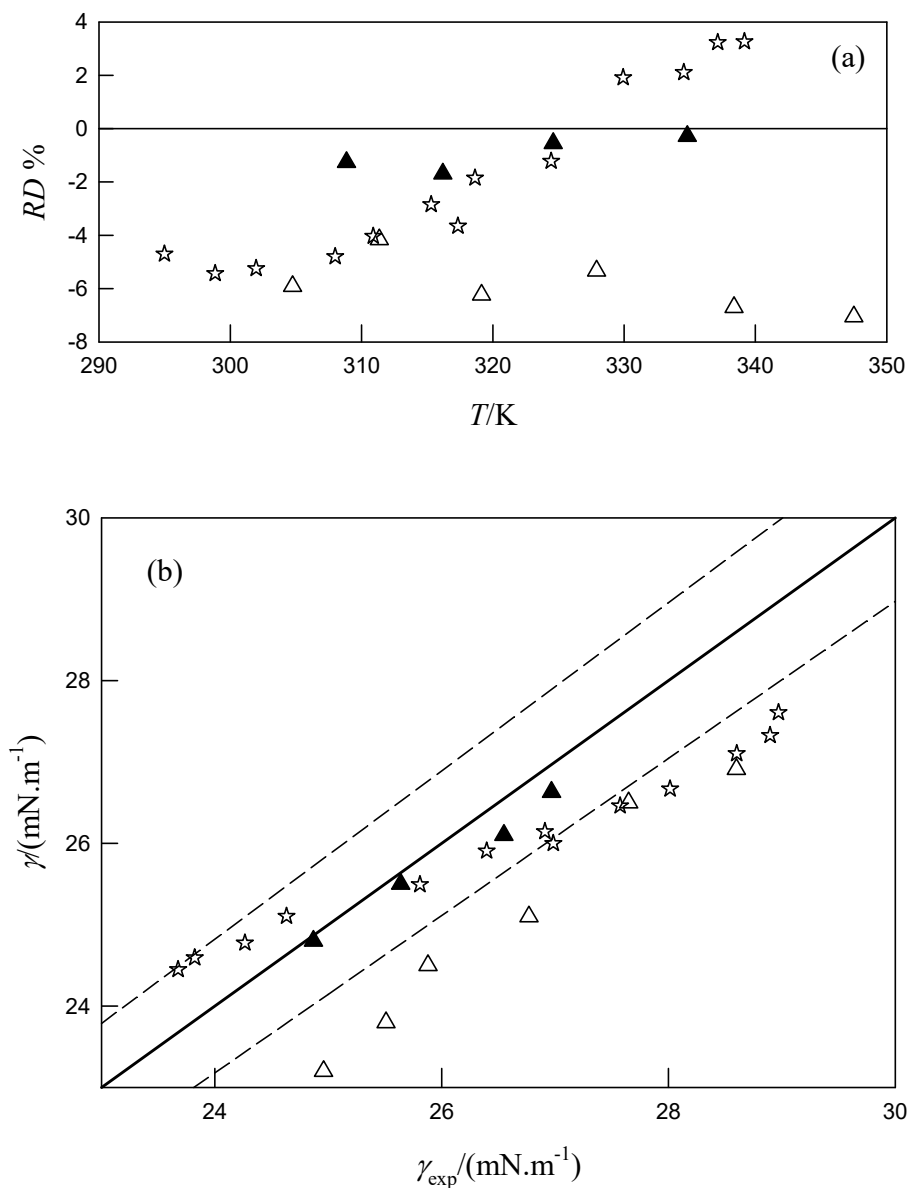


Figure 5.8. Predicted surface tension of CSB with Sastri and Rao method with CG properties. (a) Relative percent deviations between predicted and measured surface tension as function of temperature. (b) Parity plots for predicted and measured surface tension. Δ , 1st serie; \blacktriangle , 2nd serie; \star , Wimala and Brown [42]. Dashed line corresponds to $RDs \pm 3\%$.

From the Figure 5.7 and Figure 5.8 it can be conclude that the Allen method is the most suitable for prediction of CSB surface tension. Furthermore, Figure 5.7(b) allows to say that the absolute deviation in surface tension are usually less than $1 \text{ mN}\cdot\text{m}^{-1}$.

5.4.3 Viscosity - Surface tension correlations

Surface tension and viscosity are two properties of fluids which are different in nature but whose values need to be known for industrial and practical applications in biodiesel processing. At the microscopic point of view, both properties are related to the molecular information of the fluid, such as the interaction potential function. In general, viscosity is easily measured with accurately compare with surface tension. As both properties are related to the microscopic structure and the intermolecular potential energy, one might expect there some theoretical correlation between them should exist, although no such link has yet been established. Furthermore, such a relationship could also be used to check the validity of the measured data, since any deviations due to experimental errors can be detected. Some empirical correlations has been proposed by Pelofsky [46], Zheng et al. [47], Ghatee et al. [48] and Tian and Mulero [49]. The later author derived the equation:

$$\ln \gamma = A + \frac{B}{\eta^{m+C}} \quad \text{Eq. 5-27}$$

where A , B , C , and m are adjustable coefficients which have to be determined by using an adequate sets of data of surface tension and the viscosity, available over the same range of temperatures. Eq. 5-27 was applied to CSO and CSB taking data on viscosity reported in chapter 4. As the sets of temperature of measurements for the two properties differ, a procedure described next was developed to build consistent data for processing. For each (T, γ) pair, the corresponding value of viscosity was calculated. The nearest four (T, η) pairs of values, in the vicinity of that value of temperature, were used to fit MYEGA equation (Eq. 4-4) and the resulting value of viscosity from this equation was considered very close to the experimental value that would exist at the test temperature (pseudo experimental value). For CSB the first series of measurements was selected for fitting the Eq. 5-27.

In Figure 5.10 the natural logarithm of surface tension is represented as a function of viscosity for CSO and CSB. The different occupied areas of the graph by each of substances are justified by fact that viscosity values are very different for each one. The coefficients of Eq. 5-27 resulting from the fittings to the data are recorded in Table 5.11, where the *AARDs* for calculated surface tension are also provided. Eq. 5-27 allows good correlations of data for both CSO and CSB, as it can be seen by the excellent coefficient of determinations, r^2 , and *AARDs*. For the second set of

surface tension of CSB the $AARD = 2.7\%$ is obtained, which means only about 0.7 mN.m^{-1} in average for predicted values from Eq. 5-27. Relative deviations between calculated values from Eq. 5-27 and experimental data are presented in Figure 5.11. RDs for CSO and CSB (first series) are low and of the same level. RDs for CSB relative to second series of experiments are higher but still of reasonable level of prediction.

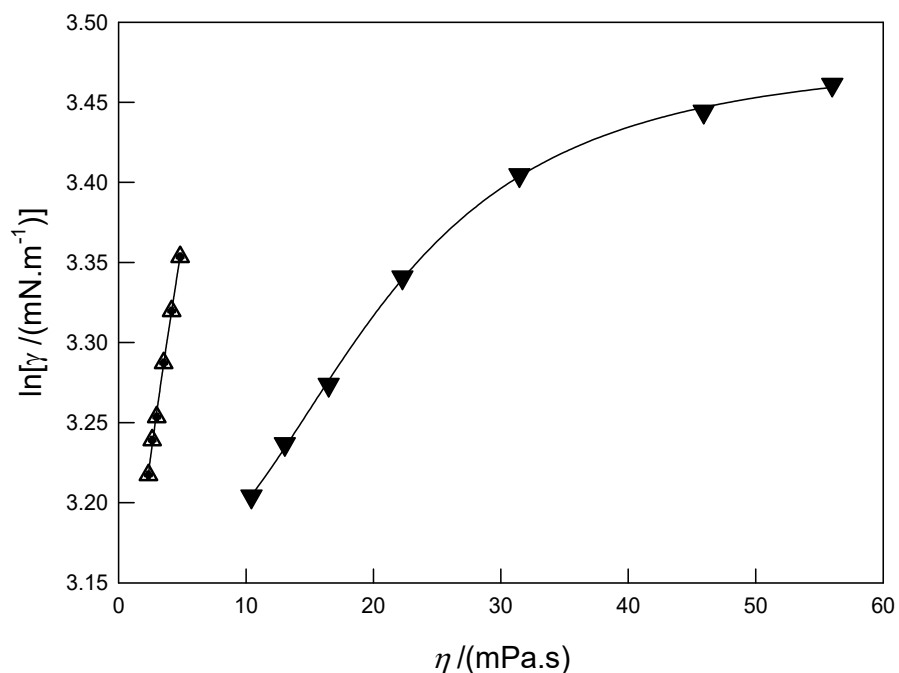


Figure 5.10. Log plots of surface tension vs. viscosity for ▼, CSO and ▲, CSB.

Table 5.11. Parameters of Eq. 5-27 for CSO and CSB.

Data	A	B	C	m	r^2	$\sigma_{\ln\gamma}$	$AARD_\gamma$
CSO	3.4795	-916.3156	2837.3436	2.6468	0.9998	0.0028	0.17
CSB	2.7819	0.0475	-0.8597	-0.0374	0.9990	0.0031	0.13

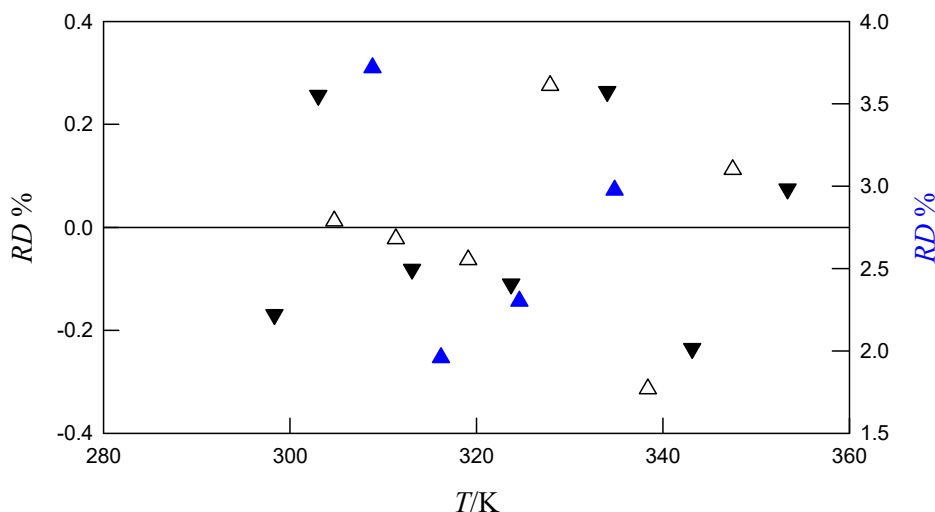


Figure 5.11. Relative deviations between calculated values from Eq. 5-27 and experimental data of this work: ▼, CSO; CSB, ▲, first series, △, second series.

5.5 Conclusions

Surface tensions of cottonseed oil were measured at temperatures from 298.3 to 353.4 K and at atmospheric pressure and those for cottonseed biodiesel in the range 304.8 K to 347.5 K.

Comparing the surface tension values of CSO obtained in this work with those available in the literature, in the studied temperature ranges, it can be concluded that some values from literature overlap with those of this work and other are higher, with deviations ranging from 3% to 9% at 298.15 K and 12% to 24% at 353.15K. For CSB, the values of the literature are very consistent with those of this work in the temperature range of measurements.

Experimental data of both substances were correlated with linear and Guggenheim equations with reasonable accuracy, with standard deviations near $0.3 \text{ mN}\cdot\text{m}^{-1}$.

Different routes including parachor methods, corresponding states and empirical correlations were used to predict the surface tensions of CSO and CSB. For CSO, the values resulting for surface tension, calculated with empiric method of Allen are of reasonable accuracy being deviations in the range 2% to 7% at lower and higher temperatures, respectively. Using the Knotts' parachors for FAs, the FA profile of oil and predicted densities, the surface tensions can be calculated with *RDs* between 3% and 12%. The same deviations were obtained using Reid et al. methods. The corresponding states method of Sastri and Rao gives variable results but it was possible to obtain accurate predictions similar to those for the Allen method. For the CSB the

values of the surface tension of this study are well predicted by the method of Allen et al. The deviations are in the range 2% for 1st series and 4% for the second. Once more Sastri and Rao gives variable results dependent on the set of critical properties which are used but it is possible to encompass all the available experimental data with this method. The experimental data of this work can be predicted with reliable accuracy for the 1st series of measurements ($AARD = 6\%$) and with good accuracy for 2nd series ($AARD = 1.0\%$). Sastri and Rao method achieves much better results than methods based on the parachors. The results from the prediction section clearly show that, provided that cottonseed oil FA and biodiesel FAME compositions are known, the predictive method of Allen et al. can be very useful either for the oil or biodiesel.

The surface tensions of CSO can be calculated from measured viscosity with $AARD$ of 0.17% while those for CSB can be calculated within 0.13% or 2.7% from the measured viscosities.

5.6 References

1. Ejim CE, Fleck BA, Amirfazli A. Analytical study for atomization of biodiesels and their blends in a typical injector: Surface tension and viscosity effects. *Fuel*. 2007;86(10):1534-44.
2. Shu Q, Wang J, Peng B, Wang D, Wang G. Predicting the surface tension of biodiesel fuels by a mixture topological index method, at 313K. *Fuel*. 2008;87(17):3586-90.
3. Allen CA, Watts KC, Ackman RG. Predicting the surface tension of biodiesel fuels from their fatty acid composition. *Journal of the American Oil Chemists' Society*. 1999;76(3):317-23.
4. Lefebvre A. *Atomization and sprays* hemisphere publishing corporation. New York. 1989.
5. Allen C, Watts K. Comparative analysis of the atomization characteristics of fifteen biodiesel fuel types. *Transactions of the ASAE*. 2000;43(2):207.
6. Ahmed M, Ejim C, Fleck B, Amirfazli A. Effect of biodiesel fuel properties and its blends on atomization. *SAE Technical Paper*, 2006 0148-7191.
7. Wagner G, Peterson C. Performance of winter rape (*Brassica napus*) based fuel mixtures in diesel engines. *Performance of winter rape (Brassica napus) based fuel mixtures in diesel engines*. 1982(4-82):329-36.
8. Benson GC, Lam VT. Surface tensions of binary liquid systems. II. Mixtures of alcohols. *Journal of Colloid and Interface Science*. 1972;38(2):294-301.

9. Vargaftik N, Volkov B, Voljak L. International tables of the surface tension of water. *Journal of Physical and Chemical Reference Data*. 1983;12(3):817-20.
10. Reid RC, Prausnitz JM, Poling BE. *The properties of gases and liquids* 1987. 14 p.
11. Guggenheim EA. The principle of corresponding states. *The Journal of Chemical Physics*. 1945;13(7):253-61.
12. Mulero A, Cachadiña I. Recommended correlations for the surface tension of several fluids included in the REFPROP program. *Journal of Physical and Chemical Reference Data*. 2014;43(2):023104.
13. Mulero A, Cachadiña I, Sanjuán E. Recommended correlations for the surface tension of aliphatic, carboxylic, and polyfunctional organic acids. *Journal of Physical and Chemical Reference Data*. 2016;45(3):033105.
14. Macleod D. On a relation between surface tension and density. *Transactions of the Faraday Society*. 1923;19(July):38-41.
15. Sugden S. VI.—The variation of surface tension with temperature and some related functions. *Journal of the Chemical Society, Transactions*. 1924;125:32-41.
16. Quayle OR. *The Parachors of Organic Compounds. An Interpretation and Catalogue*. *Chemical Reviews*. 1953;53(3):439-589.
17. Knotts TA, Wilding WV, Oscarson JL, Rowley RL. Use of the DIPPR database for development of QSPR correlations: Surface tension. *Journal of Chemical & Engineering Data*. 2001;46(5):1007-12.
18. Escobedo J, Mansoori GA. Surface tension prediction for pure fluids. *AIChE Journal*. 1996;42(5):1425-33.
19. Freitas SV, Oliveira MB, Queimada AJ, Pratas MJ, Lima ÁS, Coutinho JA. Measurement and prediction of biodiesel surface tensions. *Energy & Fuels*. 2011;25(10):4811-7.
20. Pratas MJ, Freitas SV, Oliveira MB, Monteiro SC, Lima ÁS, Coutinho JA. Biodiesel density: Experimental measurements and prediction models. *Energy & Fuels*. 2011;25(5):2333-40.
21. Verduzco LFR. Density and viscosity of biodiesel as a function of temperature: empirical models. *Renewable and Sustainable Energy Reviews*. 2013;19:652-65.
22. Ramírez-Verduzco LF. Models for predicting the surface tension of biodiesel and methyl esters. *Renewable and Sustainable Energy Reviews*. 2015;41:202-16.

23. Halvorsen J, Mammel W, Clements L. Density estimation for fatty acids and vegetable oils based on their fatty acid composition. *Journal of the American Oil Chemists' Society*. 1993;70(9):875-80.
24. Poling BE, Prausnitz JM, John Paul OC, Reid RC. *The properties of gases and liquids*: McGraw-hill New York; 2001.
25. Otoberise C, Monago K. Group contribution method for estimating the critical pressures of C₁ C₂₀ n-alkanes. *Scientia Africana*. 2015;14(1).
26. Petcu AC, Plesu V, Berbente C. Estimation methods for thermophysical properties of *Camelina sativa* crude oil. *University Politehnica of Bucharest Scientific Bulletin, Series B*. 2016;78:59-70.
27. Wallek T, Rarey Jr, Metzger JrO, Gmehling Jr. Estimation of pure-component properties of biodiesel-related components: fatty acid methyl esters, fatty acids, and triglycerides. *Industrial & engineering chemistry research*. 2013;52(47):16966-78.
28. Neto EL, Silva G, Silva G. Evaluation of group-contribution methods to estimate vegetable oils and biodiesel properties. *International Journal of Engineering and Technology*. 2012;2(9).
29. García M, Alba J-J, Gonzalo A, Sánchez JL, Arauzo J. Comparison of methods for estimating critical properties of alkyl esters and its mixtures. *Journal of Chemical & Engineering Data*. 2011;57(1):208-18.
30. Evangelista NS, do Carmo FR, de Sant Ana HB. Estimation of Physical Constants of Biodiesel-Related Fatty Acid Alkyl Esters: Normal Boiling Point, Critical Temperature, Critical Pressure, and Acentric Factor. *Industrial & Engineering Chemistry Research*. 2018.
31. Thangaraja J, Anand K, Mehta PS. Predicting surface tension for vegetable oil and biodiesel fuels. *RSC Advances*. 2016;6(88):84645-57.
32. Phankosol S, Sudaprasert K, Lilitchan S, Aryusuk K, Krisnangkura K. Estimation of surface tension of fatty acid methyl ester and biodiesel at different temperatures. *Fuel*. 2014;126:162-8.
33. Menzies AWCK, W. G.; Bingham, e. C. *Cutting fluids*1922;193:247-9.
34. Halpern A. The Surface Tension of Oils. *The Journal of Physical and Colloid Chemistry*. 1949;53(6):895-7.

35. Dikko AB, Oriolowo NZ, Edwin S. The effect of temperature change on the surface tension of some locally produced vegetable oils in Yola, Nigeria. *International Journal of Multidisciplinary Research and Development*. 2015;2(1):118-21.
36. Zeitoun M, Harris W, Harris W. Refining crude cottonseed oil dissolved in hexane. *Journal of the American Oil Chemists Society*. 1962;39(6):286-9.
37. Singleton W, Benerito RR. Surface phenomena of fats for parenteral nutrition. *Journal of the American Oil Chemists' Society*. 1955;32(1):23-5.
38. Esteban B, Riba J-R, Baquero G, Puig R, Rius A. Characterization of the surface tension of vegetable oils to be used as fuel in diesel engines. *Fuel*. 2012;102:231-8.
39. Sahasrabudhe SN, Rodriguez-Martinez V, O'Meara M, Farkas BE. Density, viscosity, and surface tension of five vegetable oils at elevated temperatures: Measurement and modeling. *International Journal of Food Properties*. 2017;20(sup2):1965-81.
40. Xu T, Rodriguez-Martinez V, Sahasrabudhe SN, Farkas BE, Dungan SR. Effects of Temperature, Time and Composition on Food Oil Surface Tension. *Food Biophysics*. 2017;12(1):88-96.
41. Al-lwayzy SH, Yusaf T, Al-Juboori RA. Biofuels from the fresh water microalgae *Chlorella vulgaris* (FWM-CV) for diesel engines. *Energies*. 2014;7(3):1829-51.
42. Brown FWaR. Influence of temperature control on surface tension and density of biodiesel2013 2018. Available from: <http://www.lib.ui.ac.id/naskahringkas/2015-08/S44774-fadil%20wimala>.
43. Tate RE, Watts K. Experimental Determination of the Density, Viscosity and Surface Tension of Three Commercial Biodiesel Fuels up to 300 o C. *Journal of the Canadian Society of Engineering in Agricultural, Food and Biological Systems*. 2005:5-383.
44. Constantinou L, Gani R. New group contribution method for estimating properties of pure compounds. *AIChE Journal*. 1994;40(10):1697-710.
45. Jasper JJ. The surface tension of pure liquid compounds. *Journal of physical and chemical reference data*. 1972;1(4):841-1010.
46. Pelofsky AH. Surface Tension-Viscosity Relation for Liquids. *Journal of Chemical and Engineering Data*. 1966;11(3):394-7.
47. Zheng M, Tian J, Mulero Á. New correlations between viscosity and surface tension for saturated normal fluids. *Fluid Phase Equilibria*. 2013;360:298-304.

48. Ghatee MH, Zare M, Zolghadr AR, Moosavi F. Temperature dependence of viscosity and relation with the surface tension of ionic liquids. *Fluid Phase Equilibria*. 2010;291(2):188-94.
49. Tian J, Mulero An. Improved correlation for viscosity from surface tension data for saturated normal fluids. *Industrial & Engineering Chemistry Research*. 2014;53(22):9499-505.

6 CHAPTER

SPEED OF SOUND OF COTTONSEED OIL AND BIODIESEL

In this section the speed of sound of biodiesel samples and cottonseed oil were measured using a non-intrusive ultrasonic methodology. The measurements were made at atmospheric pressure and $T = (298.15 \text{ to } 353.21) \text{ K}$ for biodiesels and $T = (298.15 \text{ to } 343.15) \text{ K}$ for CSO. The speed of sound data combined with available density data from literature was used to calculate the isentropic compressibility and the molar compressibility for the FAMEs and the biodiesel samples. Prediction methods for speed of sound for both kinds of substances were established.

In this chapter, the speed of sound data regarding to biodiesel, is based on the article already been published in Fuel 116 (2014) 242–254.

The sound velocity measurements of CSO were carried out in the CIEPQPF chemistry laboratory by Joao MG Baptista, as part of the integrated master dissertation work "Monitoring of the transesterification reaction of vegetable oils by ultrasound". The treatment of these data was done in section 6.2.

6.1 SPEED OF SOUND OF COTTONSEED BIODIESEL

6.1.1 Introduction

The property changes associated with the differences in chemical composition of biodiesel may change the fuel injection timing which in turn causes different exhaust emissions and performance of engines. All injection process is strongly influenced by the thermophysical fuel properties. In this process an appropriate quantity of fuel is feed to the engine cylinder forming a spray of tiny fuel droplets to optimize the combustion and reduce the fuel consumption and emissions. The properties of major influence in the injection time are the surface tension [1], the viscosity, and the isentropic bulk modulus [2], which is determined by the sound speed. Therefore, for the suitable design and maintenance of injection systems, the accurate knowledge of the sound speed of the fuel plays an important role. Biodiesel speed of sound information is very scarce in the literature, although several authors have measured this property for pure methyl and ethyl esters (FAEs). Some previous literature reports on speed of sound of pure FAMES and biodiesel are summarized in Table 6.1, calculated for different temperature and pressure ranges, techniques and uncertainties of the measurements.

Table 6.1. Previous report of speed of sound data relative to FAMES and biodiesel studied in this section.

Authors	Year	N_p	T/K	p / MPa	(u) and $\sigma_u / (\text{m}\cdot\text{s}^{-1})^a$	Method ^b	Purity/wt %
Methyl laurate (MeC12:0)							
Gouw and Vlugtert [3]	1964	2	293 - 313	0.1	(1278, 1351) (0.08%)	Interf	>99.7
Tat and Van Gerpen [4] ^c	2003	-	293 - 373	0.1 - 32.5	(1086 - 1502) (0.1 - 0.7%)	PE	d
Tat and Van Gerpen, NREL[2]	2003	30	293 - 373	0.1 - 34.5	(1080 - 1498) (0.1 - 0.7%)	PE	d
Freitas et. al. [5]	2013	12	288 - 343	0.1	(1171 - 1370) (0.01)	PE	97
Methyl myristate (MeC14:0)							
Gouw and Vlugtert [3]	1964	2	293, 313	0.1	(1299, 1372) (0.08%)	Interf	>99.7
Freitas et. al. [5]	2013	10	298 - 343	0.1	(1194 - 1353) (0.01)	PE	98
Daridon et. al. [6]	2013	8	303 - 373	0.1	(1098 - 1335) (<0.1%)	PE	99
Ndiaye et al. [7]	2013	53	303 - 393	0.1 - 80	(1036 - 1614) (0.2%)	PE	99
Methyl palmitate (MeC16:0)							
Gouw and Vlugtert [3]	1964	1	313	0.1	(1318) (0.08%)	Interf	>99.7
Tat and Van Gerpen [4] ^c	2003	-	293 - 373	0.1 - 32.5	(1123 - 1537) (0.1 - 0.7%)	PE	>99
Tat and Van Gerpen, NREL [2]	2003	24	313 - 373	0.1 - 34.5	(1019 - 1463) (0.1 - 0.7%)	PE	e
Ott et al. [8]	2008	7	308 - 338	0.1	(1233 - 1338) (0.1%)	PE	>99.0
Daridon et. al. [6]	2013	7	313 - 373	0.1	(1171 - 1370) (< 0.1%)	PE	99
Ndiaye et al. [7]	2013	35	303 - 393	0.1 - 50	(1057 - 1507) (0.2%)	PE	99
Freitas et al. [9]	2013	8	308 - 343	0.1	(1216 - 1337) (0.02)	DSA5000	99
Methyl Stearate (MeC18:0)							
Gouw and Vlugtert [3]	1964	1	313	0.1	(1333) (0.08 %)	Interf	>99.7
Tat and Van Gerpen [4] ^c	2003	-	293 - 373	0.1 - 32.5	(1141 - 1541) (0.1 - 0.7%)	PE	>99
Ott et al. [8]	2008	5	318- 338	0.1	(1248 - 1317) (0.1%)	PE	>99.0
Freitas et al. [9]	2013	7	313 - 343	0.1	(1231 - 1333) (0.02)	DSA5000	99
Methyl oleate (MeC18:1)							
Gouw and Vlugtert [3]	1964	2	293, 313	0.1	(1338 - 1408) (0.08%)	Interf	>99.7

Ott et al. [8]	2008	7	278 - 338	0.1	(1250 - 1462) (0.1%)	PE	>99.0
Freitas et. al. [5]	2013	12	288 - 343	0.1	(1238 - 1427) (0.01)	PE	99
Daridon et. al. [6]	2013	10	283 - 373		(1139 - 1446) (< 0.1%)	PE	99
Methyl linoleate (MeC18:2)							
Gouw and Vlugtert [3]	1964	2	293, 313	0.1	(1348 - 1419) (0.08%)	Interf	>99.7
Tat and Van Gerpen [4] ^c	2003	-	293 - 373	0.1 - 32.5	(1156 - 1554) (0.1 – 0.7%)	PE	f
Tat and Van Gerpen, NREL[2]	2003	30	293 - 373	0.1 - 34.5	(1151 - 1550) (0.1 – 0.7%)	PE	f
Ott et al. [8]	2008	7	278 - 338	0.1	(1260 - 1472) (0.1%)	PE	>99.0
Daridon et. al. [6]	2013	10	283 - 373	0.1	(1149 - 1456) (< 0.1%)	PE	99
Freitas et al. [9]	2013	11	288 - 343	0.1	(1246 - 1418) (0.02)	DSA5000	99
Biodiesel							
Tat and Van Gerpen [2, 4]	2003	384	293 - 373	0.1 - 34.5	(1053 - 1551) (0.1 – 0.7%)	PE	-
Huber et al. [10]	2009	14	278 - 333	0.08	(1255 - 1467) (0.03 – 1.00)	PE	g
Payri et al. [11] ^c	2011	-	298 - 343	15 - 180	(1213 - 1848) (≈0.3%)	TOF	h
Nicolic et al. [12] ^c	2012	17	293	0.1 - 160	(1404 - 1893) (0.05)	PE	i
Freitas et al. [5]	2013	120	288 - 343	0.1	(1230 - 1432) (0.01)	DSA5000	j

^a The uncertainty in speed of sound (σ_u) is given in $\text{m}\cdot\text{s}^{-1}$ or percentage.

^b Interf: interferometer; PE: pulse-echo; TOF: time of flight.

^c Data is given in expression(s) form(s).

^d Sample: MeC12:0 (99.2), MeC18:1 (0.6), MeC18:2 (0.2).

^e Sample: MeC12:0 (0.2), MeC14:0 (4.6), MeC16:0 (88.2); MeC17:0 (0.4), MeC18:0 (6.3).

^f Sample: MeC16:0 (1.4); MeC18:0 (0.7), MeC18:1 (5.2); MeC18:2 (86.5); MeC18:3 (6.2).

^g Two commercial samples from rapeseed oil were used.

^h Rape methyl ester used in Spain.

ⁱ Rape methyl ester used in Serbia.

^j Samples synthesized at laboratory: soybean (S), rapeseed (R), palm (P), soybean+rapeseed (SR), palm+rapeseed (PR), soybean+palm (SP), soybean+rapeseed+palm (SRP), sunflower (SF); from portuguese biodiesel producers: soybean+rapeseed (GP) and SoyA.

This sections aims to evaluate the speed of sound of pure liquid FAMES, most frequently found in biodiesels, and also the biodiesel speed of sound. This property has been measured for MeC12:0, MeC14:0, MeC16:0, MeC18:0, MeC18:1, MeC18:2 at atmospheric pressure and temperatures ranging from 288.15 to 353.15 K. Additionally, five synthetic biodiesel samples composed by different FAMES were prepared, and a cottonseed biodiesel sample was produced by transesterification of the cottonseed oil. Next, the respective speed of sound was measured at $T = (298.15 \text{ to } 353.15) \text{ K}$ and atmospheric pressure. The speed of sound was combined with density to calculate the isentropic and molar compressibilities for the FAMES and biodiesel studied in this work. Additional information of speed of sound for FAMES and biodiesel obtaining from literature was also used, in order to extend and complete the knowledge of the molar compressibility. From the information collected, predictive models of molar compressibility and speed of sound for FAMES and biodiesel were formulated.

6.1.2 Experimental

6.1.2.1 Calibration liquids and fuels

Water (mili-Q), toluene obtained from ACROS (Cas No: 142–82-5) with a mass fraction purity of 99.9 wt %, and 2-butanediol from Carlo Erba (Cas No. 64–17-5) with a stated mass fraction of 99.9 wt % have been used as speed of sound calibrant liquids in the cell. The liquids were previously degassed ultrasonically.

The methyl esters (MeC12:0, purityP97%, wt %), (MeC14:0, purityP98%), (MeC16:0, purityP97%), (MeC18:0, purityP96%), (MeC18:1, purityP99%, GC grade), were purchased from Sigma Aldrich and (MeC18:2, purityP99%, GC) from Acros Organics. All the FAMES were used without further purification. Five synthetic biodiesel samples were prepared from known masses of FAMES (MeC14:0, MeC16:0, MeC18:0 MeC18:1 and MeC18:2). Also, one biodiesel sample was produced by transesterification of cottonseed oil, which was supplied by Acros Organic. The detailed specifications of all materials are summarized in Table 6.2.

Table 6.2. Sample material purities of the calibration standards and FAMES.

Material	Supplier	CAS No	Sample purity (wt %)	Structure / properties
Water			mili-Q	
Toluene	Acros Organics	142-82-5	99.9	
2-Butanediol	Carlo Erba	64-17-5	99.9	
methyl laurate	Sigma Aldrich	111-82-0	> 97	
methyl myristate	Sigma Aldrich	124-10-7	> 98	
methyl palmitate	Sigma Aldrich	112-39-0	> 97	
methyl stearate	Sigma Aldrich	112-61-8	>96	
methyl oleate	Sigma Aldrich	112-62-9	>99 GC	
Methyl linoleate	Acros Organics	112-63-0	>99 GC	
Cotton seed oil	Acros Organics	17711	Fatty acid composition:	$AV \leq 0.5 \text{ mg KOH}\cdot\text{g}^{-1}$
			MeC14:0 and lower: ca	$SV = 185 - 198 \text{ mg KOH}\cdot\text{g}^{-1}$;
			1.5%; MeC16:0 ca	$IN = 95 \text{ to } 115 \text{ g I}/100\text{g}$,
			25%; MeC18:0 ca 3%;	$UM < 1.5\%$;
			MeC18:1, 16 to 24%;	$n = 1.4720 \text{ to } 1.4730 (20^\circ\text{C}, 589$
			MeC18:2, 50 to 55%;	$\text{nm})$
			MeC18:3 and higher	
			< 1.5%.	

AV = acid value; SV = Saponification value; IN = Iodine number; UM = unsaponifiable matter; n = refractive index.

6.1.2.2 Synthetic samples and cottonseed biodiesel preparation

The composition choice for the synthetic samples was based on the availability of their experimental cetane number and covering wide range, since it was intended to study this important parameter in a future work. Methyl esters were mixed in appropriate mass proportions to simulate the target biodiesel samples. The biodiesel samples were prepared as follows: the synthetic cottonseed (SCS) biodiesel was based on the compositions reported by Wadumesthrige et al. [13]; the synthetic beef tallow (SBT) was from the composition given by Ramirez-Verduzco et al. [14]; synthetic biodiesel poultry fat (SPF) was obtained from composition reported by Wadumesthrige et al. [13]; two synthetic samples from yellow grease (SYG1 and SYG2), obtained from cooking oil used in fast food, were prepared from the composition reported by Kinast [15] and Canacki and Gerpen [16], respectively. The composition of synthetic biodiesel samples are presented in Table 6.3. The transesterification of cottonseed oil was described in Section 3.1.2.2.

Table 6.3. Biodiesel compositions (wt %) of this study.

Biodiesel	SCS ^a	SBT ^b	SPF ^c	SYG1 ^d	SYG2 ^d	CSB ^e
FAME						
MeC14:0	0.93	0.50	0.94	0.00	2.83	0.93
MeC16:0	24.98	17.00	25.56	11.90	28.57	26.76
MeC18:0	2.66	9.41	7.83	14.43	13.07	2.81
MeC18:1	18.48	31.24	36.34	72.46	46.60	17.89
MeC18:2	52.94	41.85	29.32	1.21	8.92	51.60

^a SCS : synthetic cotton seed oil; ^b SBT : synthetic beef tallow; ^c SPF: synthetic biodiesel poultry fat;

^d SYG1 and SYG2: synthetic samples from yellow grease; ^e CSB: Produced cottonseed biodiesel.

6.1.2.3 Analytical methods

The biodiesel produced from cottonseed oil supplied by Acros Organic, was analyzed by gas chromatography as described in Section 3.1.2.3. The composition is presented in Table 6.3.

6.1.2.4 Sound speed measurement

In order to measure the ultrasound propagation velocity in the esters and biodiesel fuels, a stainless steel cell was used. A schematic of the cell inserted in the measurement system is shown in Figure 6.1(a), and its construction details can be observed in Figure 6.1(b). The cylindrical cell contains a hollow having diameter and length of 12 mm and 15.5 mm, respectively, where the testing liquids are accommodate. Two 5 MHz ultrasonic transducer were mounted in cavities drilled on the cell plane surfaces, one acting as a transmitter and the other as a receiver. To minimize reflections, the transducers were in contact with the stainless steel walls of the cavities and silicone oil was used to enhance the wave transmission.

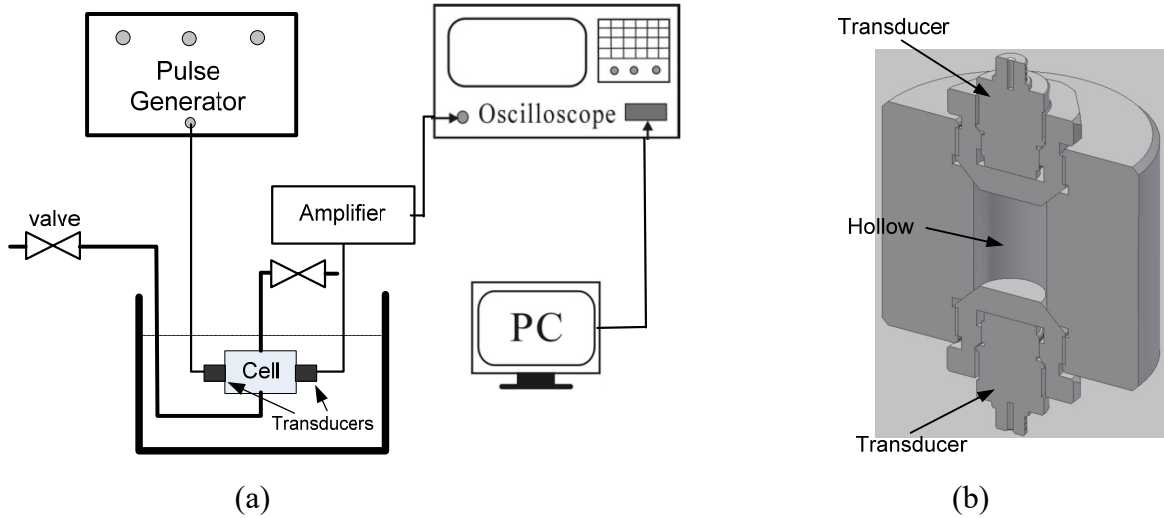


Figure 6.1. Scheme of speed of sound measurement system. (a) Ultrasound cell and peripheral equipment. (b) Ultrasound cell details

A wide band pulse generator is used to excite the transmitter transducer. The acoustical wave propagates through the testing liquid and is collected by the receiver. Then, the signal is amplified and displayed in the oscilloscope, and transferred to the computer for processing (see Figure 6.1(a)). An A-scan representation of a signal corresponding to the propagation over the media between the transmitter and the receiver is shown in Figure 6.2. The time of flight $\Delta\tau$ in the testing sample is obtained from the difference between the emitter-receiver propagation time and the propagation time in the steel walls (see Figure 6.2). The cell was calibrated by measuring $\Delta\tau$ in water, toluene and 2-butanediol at atmospheric pressure, over the full range of temperatures $T = (298.15\text{--}343.15)$ K and $u = (1117\text{--}1602)$ m·s⁻¹ using a total of 22 (T, u) data points for these liquids (water [17], toluene [18], and 2-butanediol [19]). The literature $u(T)$ data were fitted using the following equation:

$$\frac{1}{u} = (c_1 + c_2T) + (c_3 + c_4T)\Delta\tau \quad \text{Eq. 6-1}$$

where $c_1 = (-1.84069 \cdot 10^{-4} \pm 3.1489 \cdot 10^{-5})$ m⁻¹·s, $c_2 = (3.45446 \cdot 10^{-7} \pm 9.8981 \cdot 10^{-8})$ m⁻¹·s·K⁻¹, $c_3 = (64.0477 \pm 2.0235)$ m⁻¹ and $c_4 = (-3.17784 \cdot 10^{-2} \pm 6.3000 \cdot 10^{-3})$ m⁻¹·K⁻¹. The obtained correlation coefficients and standard deviation were $r = 1.000$ and $\sigma = 6.30 \cdot 10^{-7}$ m⁻¹·s, respectively. In terms of speed of sound, the standard deviation $\sigma_u = 1.2$ m·s⁻¹ and $AARD = 0.07\%$ were obtained.

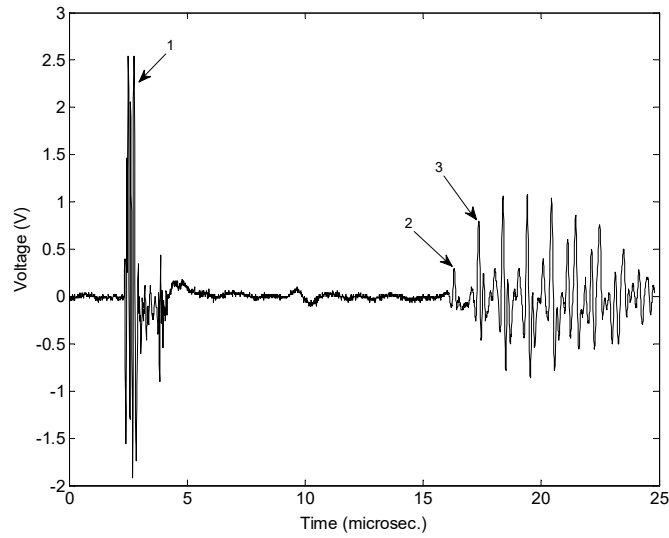


Figure 6.2. A-scan signal: 1-Emission signal; 2-Receiving signal; 3-Steel wall reflected signal.

6.1.3 Results and discussion

6.1.3.1 Speed of sound correlation

The speed of sound measured at extended ranges of temperature for the FAMEs and biodiesel studied here are given in Table 6.4. The following polynomial expression,

$$u = \sum_{i=0}^2 u_i T^i \quad \text{Eq. 6-2}$$

was fitted to the experimental (T, u) data and the obtained coefficients u_i are shown in Table 6.5. The coefficient of correlation, the low standard deviation and *AARD* values reveal the good quality of measured data. The second degree polynomial accounts for the slight curvature sometimes observed in (T, u) data. This behaviour is particularly seen for water used here as calibration fluid.

Table 6.4. Experimental speed of sound (u) for FAMES, synthetic and produced biodiesels at atmospheric pressure.

T/K	$u / (\text{m}\cdot\text{s}^{-1})$	T/K	$u / (\text{m}\cdot\text{s}^{-1})$	T/K	$u / (\text{m}\cdot\text{s}^{-1})$	T/K	$u / (\text{m}\cdot\text{s}^{-1})$	T/K	$u / (\text{m}\cdot\text{s}^{-1})$	T/K	$u / (\text{m}\cdot\text{s}^{-1})$
MeC12:0		MeC14:0		MeC16:0		MeC18:0		MeC18:1		MeC18:2	
										288.41	1434.5
										293.33	1414.5
298.25	1332.3	298.15	1350.9					298.28	1389.9	298.15	1398.3
303.17	1313.5	303.15	1331.5					303.79	1365.3	303.20	1378.5
308.26	1293.5	308.17	1312.8					308.15	1353.3	308.20	1360.3
313.15	1277.8	313.15	1296.6	313.42	1317.0			313.28	1336.0	313.15	1343.7
318.15	1258.2	318.15	1276.4	318.15	1297.0			318.15	1318.2	318.15	1327.6
323.17	1243.6	323.15	1255.3	323.17	1282.1	323.15	1297.3	323.15	1301.0	323.15	1308.3
328.17	1224.5	328.15	1243.2	328.15	1263.4	328.15	1281.7	328.15	1282.6	328.34	1288.8
333.15	1207.6	333.15	1228.2	333.15	1247.1	333.15	1263.1	333.15	1266.5	333.15	1272.5
338.15	1187.5	338.15	1212.1	338.15	1231.2	338.15	1248.4	338.15	1249.2	338.15	1255.9
343.15	1171.2	343.16	1192.7	343.15	1211.9	343.15	1230.1	343.15	1233.4	343.15	1239.0
348.17	1156.1	348.15	1178.4	348.15	1193.3	348.15	1215.6	348.15	1215.6	348.15	1225.1
353.15	1138.0	353.15	1162.4	353.15	1179.1	353.24	1200.1	353.15	1200.0		
SCS		SBT		SPF		SYG1		SYG2		CSB	
										298.15	1394.1
303.15	1369.2	303.15	1371.3	303.15	1371.3	303.38	1369.3	303.17	1365.2	303.23	1376.4
308.15	1353.3	308.17	1351.3	308.19	1351.4	308.17	1352.3	308.18	1345.4	308.21	1358.3
313.15	1335.9	313.15	1334.0	313.15	1332.1	313.28	1328.3	313.17	1326.4	313.15	1338.8
318.19	1314.4	318.15	1317.2	318.15	1314.4	318.17	1316.3	318.15	1309.8	318.15	1322.9
323.16	1298.2	323.45	1304.7	323.15	1297.3	323.22	1292.8	323.15	1292.8	323.15	1305.5
328.16	1283.4	328.17	1283.4	328.16	1278.2	328.16	1279.9	328.19	1275.5	328.18	1286.1
333.15	1264.8	333.17	1263.9	333.10	1263.1	333.17	1261.4	333.17	1258.0	333.15	1271.6
338.15	1250.1	338.16	1250.9	338.18	1247.6	338.18	1250.1	338.20	1242.6	338.20	1253.4
343.15	1230.1	343.15	1235.0	343.15	1231.0	343.16	1230.1	343.17	1225.3	343.15	1237.4
348.18	1216.4	348.15	1214.8	348.24	1215.7	348.16	1213.3	348.18	1211.7	348.18	1221.1
353.15	1203.1	353.15	1200.8	353.21	1200.8	353.17	1204.6	353.16	1194.7	353.17	1206.2

The uncertainty in u is less than $1.2 \text{ m}\cdot\text{s}^{-1}$.

Table 6.5. Parameters of equation 6-2 fitted to the (u , T) data of this study.

Coefficient	MeC12:0	MeC14:0	MeC16:0	MeC18:0	MeC18:1	MeC18:2
$u_0 / \text{m.s}^{-1}$	2686.63	3161.21	2618.54	3176.01	2735.85	2891.28
	± 149.84	± 229.98	± 397.50	± 519.87	± 156.48	± 107.69
$u_1 / \text{m.s}^{-1} \cdot \text{K}^{-1}$	-5.4044	-8.3242	-4.7717	-8.1501	-5.4332	-6.3177
	± 0.9220	± 1.4152	± 2.3882	± 3.0764	± 0.9625	± 0.6784
$u_2 / \text{m.s}^{-1} \cdot \text{K}^{-2}$	2.887×10^{-3}	7.550×10^{-3}	1.963×10^{-3}	7.235×10^{-3}	3.068×10^{-3}	4.387×10^{-3}
	$\pm 1.4 \times 10^{-3}$	$\pm 2.2 \times 10^{-3}$	$\pm 3.6 \times 10^{-3}$	$\pm 4.5 \times 10^{-3}$	$\pm 1.5 \times 10^{-3}$	$\pm 1.1 \times 10^{-3}$
N_p	12	12	9	7	12	13
r	1.000	1.000	1.000	1.000	1.000	1.000
$\sigma / \text{m.s}^{-1}$	1.3	2.0	1.55	1.05	1.33	1.18
AARD %	0.08	0.1	0.09	0.06	0.06	0.07
	SCS	SBT	SPF	SYGI	SYG2	CSB
$u_0 / \text{m.s}^{-1}$	3132.04	2591.71	3542.03	3732.82	3201.08	2989.51
	± 253.21	± 348.09	± 100.62	± 405.15	± 123.33	± 100.45
$u_1 / \text{m.s}^{-1} \cdot \text{K}^{-1}$	- 7. 8994	- 4.5707	- 10.3988	- 11.6045	- 8.3564	- 6.9645
	± 1.5457	± 2.1251	± 0.6142	± 2.4727	± 0.7529	± 0.6181
$u_2 / \text{m.s}^{-1} \cdot \text{K}^{-2}$	6.890×10^{-3}	1.784×10^{-3}	10.678×10^{-3}	12.573×10^{-3}	7.581×10^{-3}	5.418×10^{-3}
	$\pm 2.4 \times 10^{-3}$	$\pm 3.2 \times 10^{-3}$	$\pm 9.0 \times 10^{-4}$	$\pm 3.8 \times 10^{-3}$	$\pm 1.1 \times 10^{-3}$	$\pm 9.0 \times 10^{-4}$
N_p	11	11	11	11	11	12
r	1.000	0.999	1.000	0.999	1.000	1.000
$\sigma / \text{m.s}^{-1}$	1.7	2.4	0.7	2.7	0.9	0.9
AARD %	0.105	0.127	0.036	0.162	0.380	0.05

The experimental speeds of sound for the studied samples, calculated from the A-Scan data (see Figure 6.2) versus temperature are illustrated in Figure 6.3. The melting points of the FAMES given by Knothe and Dunn [20] are also shown. It can be seen that the speed of sound decreases with the increase of temperature as expected, with almost the same slopes. It can also be seen that, the saturated and unsaturated MeC18 show similar values of speed of sound, where the differences are less than 10 m.s^{-1} . This is important because most of biodiesel systems are formed mainly by MeC18 FAMES of several degrees of saturation. The speed values for biodiesel at a given temperature are similar to those of MeC18 FAMES, as illustrated in Table 6.4

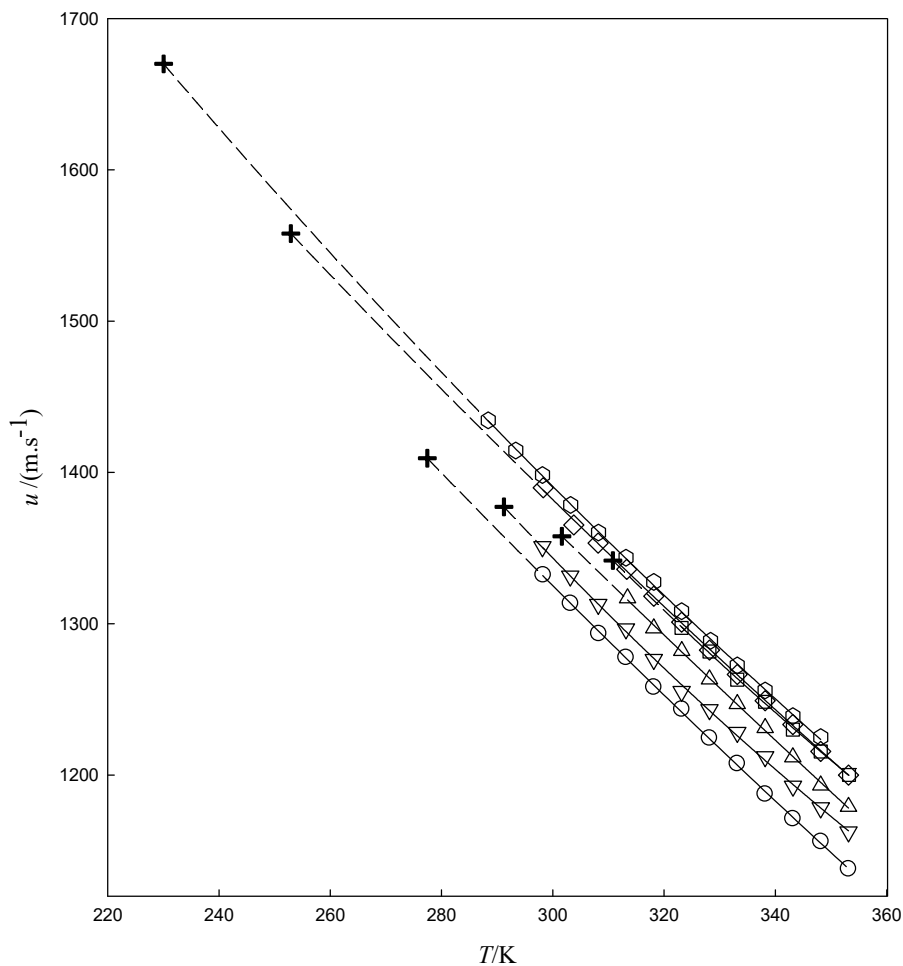


Figure 6.3. Speed of sound (u) of methyl esters measured in this work as function of the temperature. \circ , MeC12:0; ∇ , MeC14:0; Δ , MeC16:0; \square , MeC18:0; \diamond , MeC18:1; \hexagon , MeC18:2; +, melting points [20].

The experimental speeds of sound values of FAMEs were compared with those from the literature in Figure 6.4 to Figure 6.6. It can be concluded that the speed of sound values obtained in this work are in agreement with the ones provided by the literature, presenting RD s less than 0.3%, which corresponds ca. to $4 \text{ m}\cdot\text{s}^{-1}$, except for the results obtained by Tat and Van Gerpen [2].

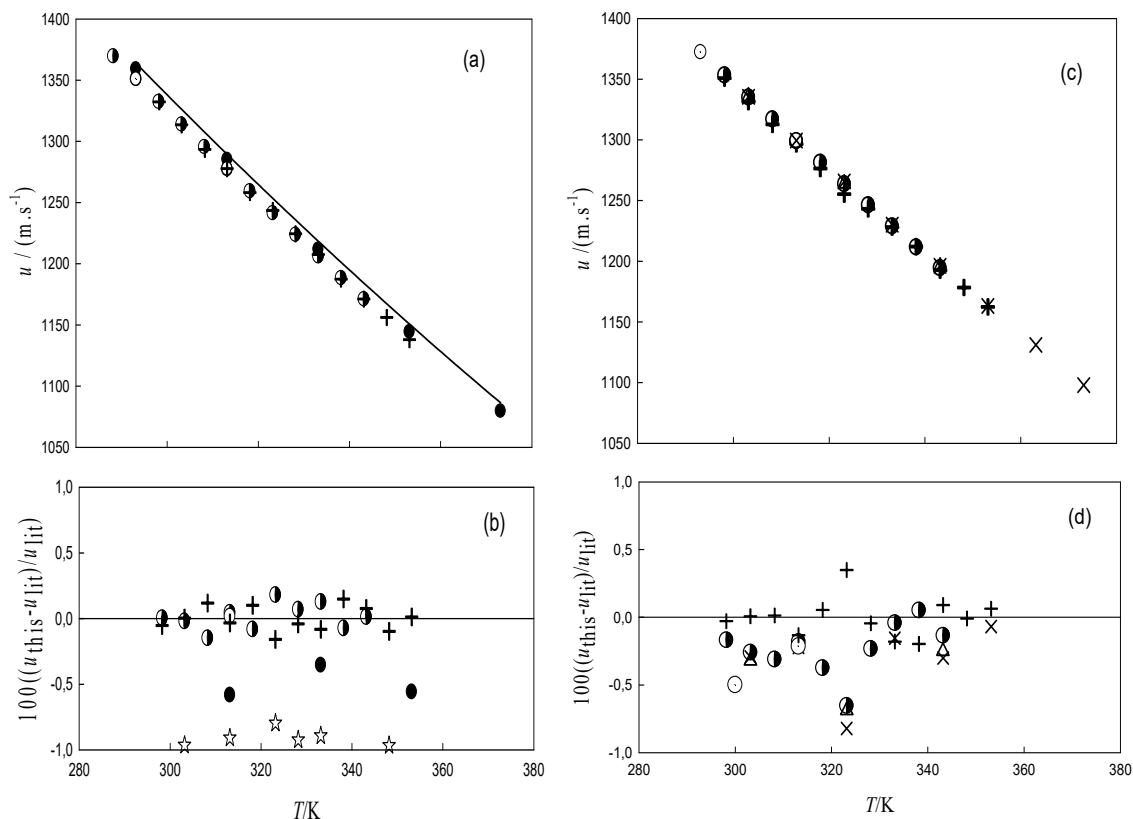


Figure 6.4. Speed of sound (u) as a function of the temperature and comparison of experimental data of this work with the previous literature data. Legend: (a) values for MeC12:0; (b) relative deviations for MeC12:0; (c) values for MeC14:0; (d) relative deviations for MeC14:0. In the relative deviations (u_{this}) represent this work's experimental data and (u_{lit}) the values from the literature. +, this work; ●, Tat and van Gerpen, NREL [2]; ⊗, Gouw and Vlugter [3]; ◐, Freitas et al. [5]; (—), Tat and van Gerpen [4]; ×, Daridon et al. [6]; Δ, Ndiaye et al. [7]. In (b, d) the symbol + represents the relative deviations between the fitted values with Eq. 6-2 and experimental data of this work.

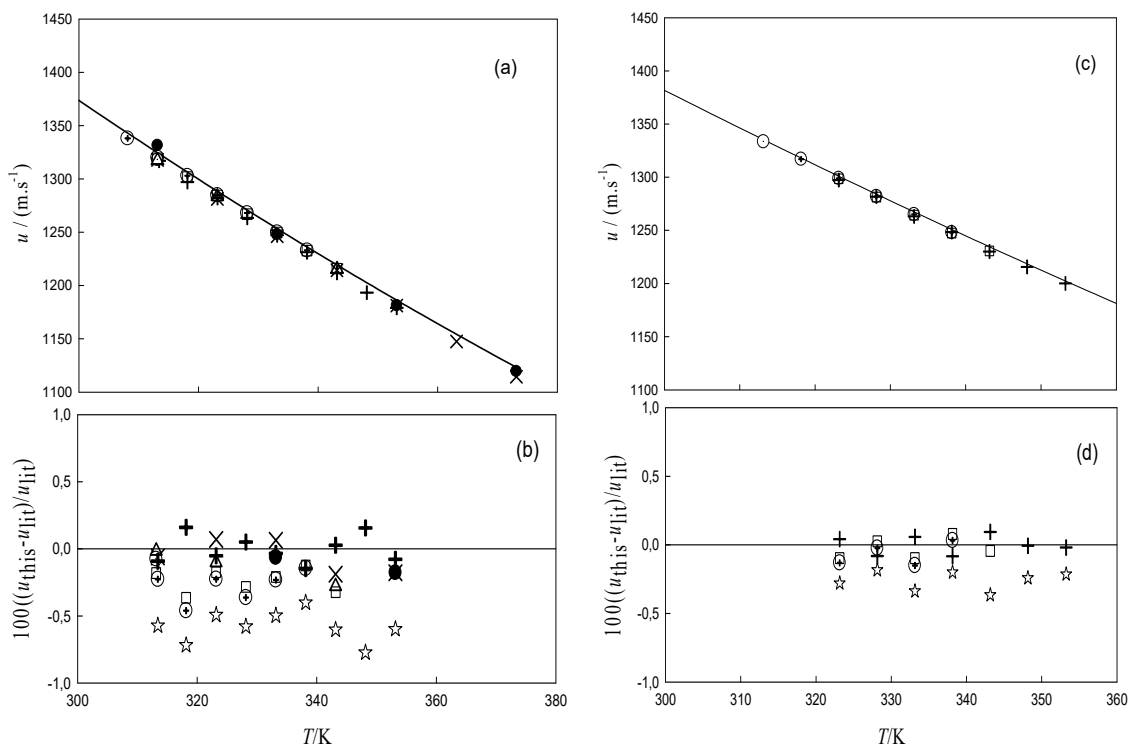


Figure 6.5. Speed of sound (u) as a function of the temperature (T) and comparison of experimental data of this work with the previous literature data. Legend: (a) values for MeC16:0; (b) relative deviations for MeC16:0; (c) values for MeC18:0; (d) relative deviations for MeC18:0. In the relative deviations (u_{this}) represent this work's experimental data and (u_{lit}) the values from the literature. +, this work; ●, Tat and van Gerpen, NREL [2]; ⊗, Gouw and Vlughter [3]; (—), Tat and van Gerpen [4]; ☆, Tat and van Gerpen [4]; ×, Daridon et al. [6]; Δ, Ndiaye et al. [7]; ⊕, Ott et al. [8]; □, Freitas et al. [9]. In (b, d) the symbol + represents the relative deviations between the fitted values with Eq. 6-2 and experimental data of this work.

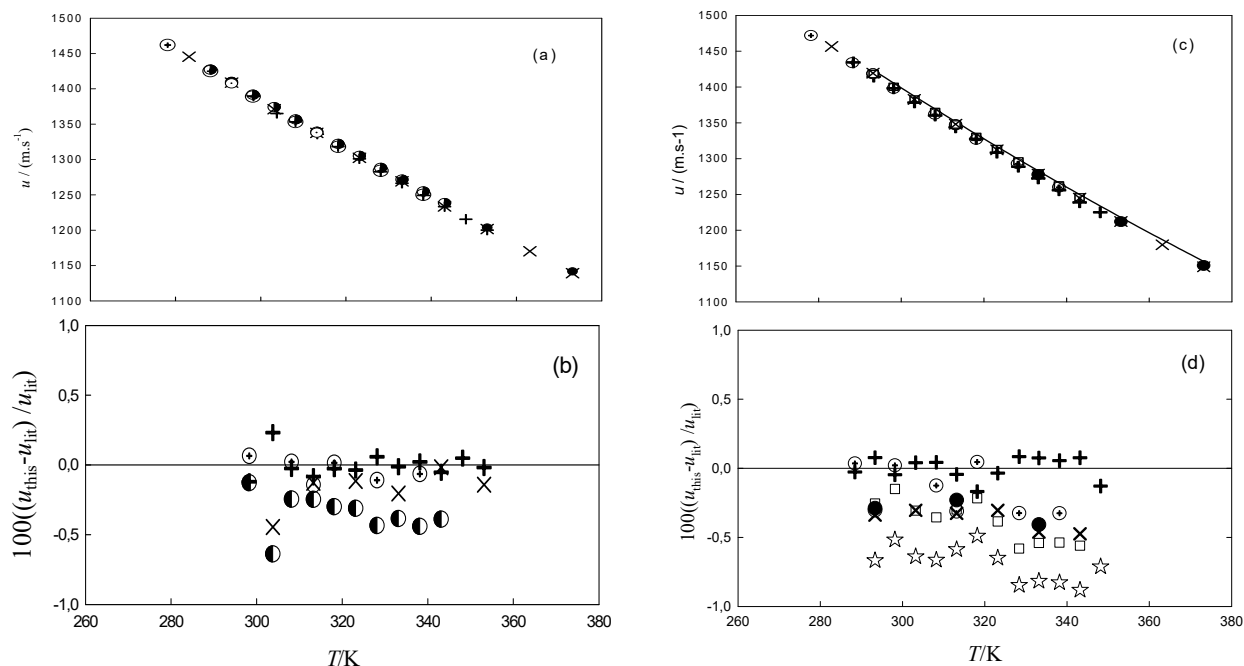


Figure 6.6. Speed of sound (u) as a function of the temperature (T) and comparison of experimental data of this work with the previous literature data. Legend: (a) values for MeC18:1; (b) relative deviations for MeC18:1; (c) values for MeC18:2; (d) relative deviations for MeC18:2. In the relative deviations (u_{this}) represent this work's experimental data and (u_{lit}) the values from the literature. +, this work; ●, Tat and van Gerpen, NREL [2]; ⊙, Gouw and Vlugter [3]; ◐, Freitas et al. [5]; (—), Tat and van Gerpen [4]; ×, Daridon et al. [6]; ☆, Tat and van Gerpen [4]; Δ, Ndiaye et al. [7]; ⊕, Ott et al. [8]; □, Freitas et al. [9]. In (b, d) the symbol + represents the relative deviations between the fitted values with Eq. 6-2 and experimental data of this work.

The experimental speeds of sound in synthetic samples and in the produced cottonseed biodiesel are shown in Figure 6.7. It can be observed that they fall in a narrow range of ca. $11 \text{ m}\cdot\text{s}^{-1}$ and this range is almost independent of the temperature. The experimental values of Freitas et al. [5] for soy and palm methylic biodiesel, as well as the speed of sound of conventional diesel given in expression form by Payri et al. [11] were included for comparison purpose. Other biodiesel samples studied by Freitas et al. have (T, u) values into the mentioned speed of sound range.

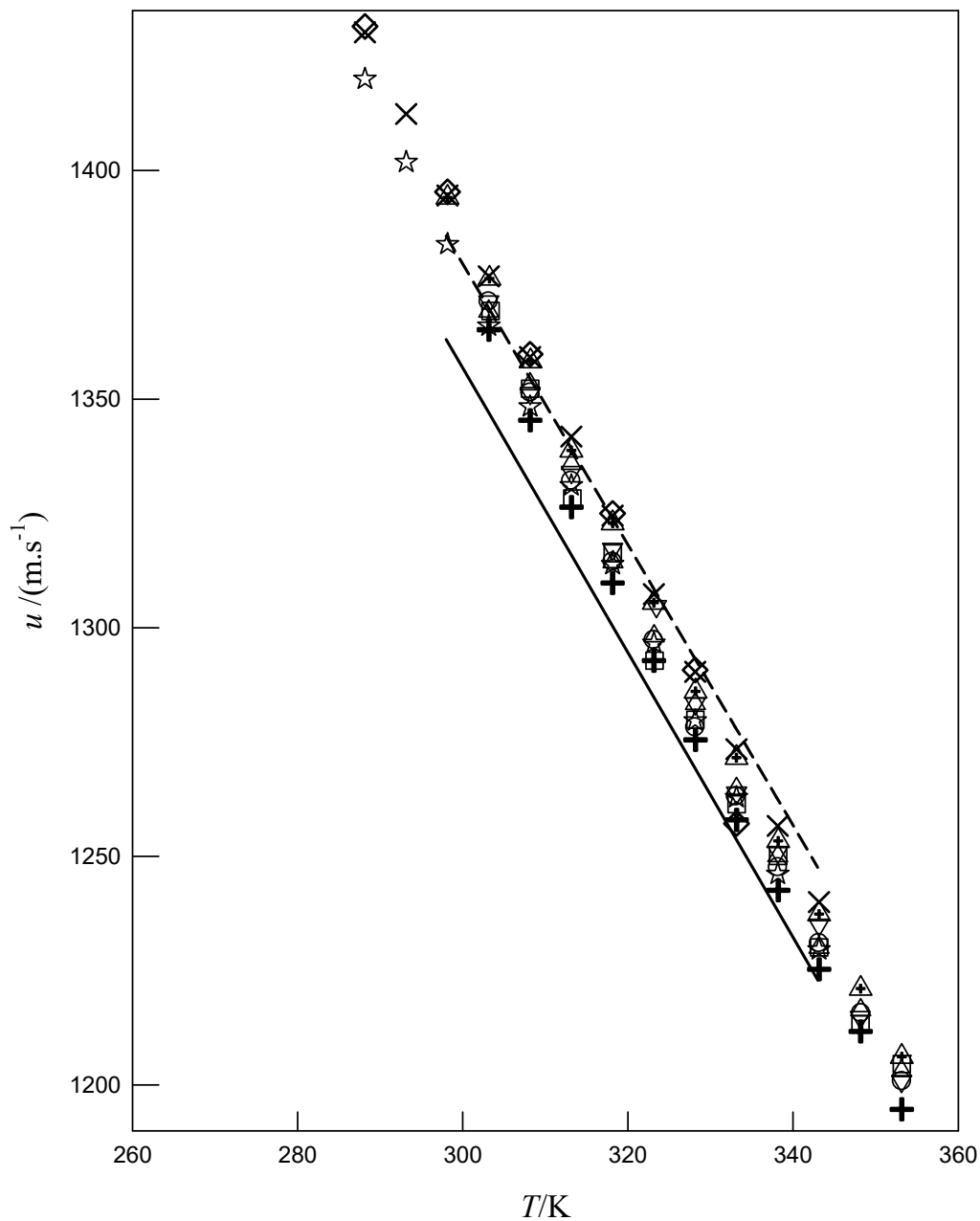


Figure 6.7. Speed of sound of biodiesel (u) as function of temperature. Legend: Δ , SCS; ∇ , SBT ; \circ , SPF; \square , SYGI; $+$, SYGII; \blacktriangle , CSB; \times , Soy (S), Freitas et al. [5]; \star , Palm (P), Freitas et al. [5]; (—) conventional diesel, Payri et al. [11]; (----), Rapeseed biodiesel, Payri et al. [11]; \diamond , Huber et al.[10].

6.1.3.2 Molar compressibility

An important parameter in the study of liquid state is the molar compressibility also called Wada's constant [21] defined by:

$$k_m = \frac{M}{\rho} k_s^{-1/7} \quad \text{Eq. 6-3}$$

where M is the molar mass, k_s the isentropic compressibility and ρ the density. The isentropic compressibility k_s is calculated from the Laplace equation,

$$k_s = \left[\frac{1}{\rho} \left(\frac{\partial \rho}{\partial p} \right)_S \right] = \frac{1}{\rho u^2} \quad \text{Eq. 6-4}$$

where S is the entropy, and p the pressure.

The molar compressibility is assumed to be independent of the temperature in liquids and it is obtained from integration of the differential relationship [22],

$$\left(\frac{\partial \ln k_s}{\partial T} \right)_p = -7\alpha_p \quad \text{Eq. 6-5}$$

where $\alpha_p = -(1/\rho)(\partial\rho/\partial T)_p$ is the isobaric expansibility.

For the saturated FAMES MeC10:0, MeC14:0, and MeC16:0, Daridon et al. [6] found an almost constant temperature dependence of k_m and they developed a group contribution method to predict the molar compressibility and speed of sound for methyl and ethyl esters with an uncertainty of ca. 0.1%. In this chapter, the experimental density data of Pratas et al. [23] were used to calculate the isentropic and molar compressibility of the pure FAMES. The results for molar compressibility are presented in Table 6.6 and depicted in Figure 6.8(a) versus temperature. It is clearly observed that k_m is an almost constant function of temperature, tending to be lightly decreasing. Table 6.7 shows the coefficients k_1 and k_2 of the linear representation $k_m = k_1 + k_2 T$ as well as the standard deviations of the fitting. As the molar compressibility is only slightly temperature dependent, the average values $\langle k_m \rangle = (1/N_p) \sum_i^{N_p} (k_m)_i$ was calculated for future applications and these values for the FAMES are also presented in Table 6.6, as well as the standard deviation from the mean value of molar compressibility, σ_{k_m} , and the *AARD*, from the mean value of molar compressibility, which are usually lower than 5×10^{-3} and 0.05%, respectively.

Table 6.6. Molar compressibility (k_m) for FAMES, synthetic and produced biodiesels.^a

T/K	$k_m \cdot 10^3$	T/K	$k_m \cdot 10^3$	T/K	$k_m \cdot 10^3$	T/K	$k_m \cdot 10^3$	T/K	$k_m \cdot 10^3$	T/K	$k_m \cdot 10^3$
MeC12:0		MeC14:0		MeC16:0		MeC18:0		MeC18:1		MeC18:2	
										288.41	6.967
										293.33	6.964
298.25	5.082	298.15	5.783					298.28	7.084	298.15	6.964
303.17	5.082	303.15	5.781					303.79	7.076	303.20	6.961
308.26	5.080	308.17	5.780					308.15	7.080	308.20	6.959
313.15	5.082	313.15	5.781	313.42	6.490			313.28	7.080	313.15	6.960
318.15	5.080	318.15	5.778	318.15	6.484			318.15	7.078	318.15	6.961
323.17	5.083	323.15	5.772	323.17	6.488	323.15	7.190	323.15	7.077	323.15	6.957
328.17	5.081	328.15	5.779	328.15	6.485	328.15	7.192	328.15	7.074	328.34	6.953
333.15	5.081	333.15	5.781	333.15	6.485	333.15	7.188	333.15	7.074	333.15	6.952
338.15	5.078	338.15	5.782	338.15	6.486	338.15	7.191	338.15	7.073	338.15	6.951
343.15	5.078	343.16	5.778	343.15	6.482	343.15	7.187	343.15	7.073	343.15	6.950
348.17	5.080	348.15	5.781	348.15	6.478	348.15	7.190	348.15	7.070	348.15	6.953
353.15	5.078	353.15	5.781	353.15	6.481	353.24	7.191	353.15	7.070		
$\langle k_m \rangle$	5.081		5.780		6.484		7.190		7.076		6.958
σ_{k_m}	$1.70 \cdot 10^{-3}$		$2.72 \cdot 10^{-3}$		$3.24 \cdot 10^{-3}$		$1.47 \cdot 10^{-3}$		$4.07 \cdot 10^{-3}$		$5.36 \cdot 10^{-3}$
AARD %	0.03		0.04		0.04		0.02		0.05		0.07

Continued

<i>T</i> /K	$k_m \cdot 10^3$	<i>T</i> /K	$k_m \cdot 10^3$	<i>T</i> /K	$k_m \cdot 10^3$	<i>T</i> /K	$k_m \cdot 10^3$	<i>T</i> /K	$k_m \cdot 10^3$	<i>T</i> /K	$k_m \cdot 10^3$
SCS		SBT		SPF		SYG1		SYG2		CSB	
										298.15	6.863
303.15	6.850	303.15	6.927	303.15	6.885	303.38	7.022	303.17	6.863	303.23	6.864
308.15	6.852	308.17	6.923	308.19	6.881	308.17	7.021	308.18	6.859	308.21	6.862
313.15	6.851	313.15	6.923	313.15	6.878	313.28	7.011	313.17	6.857	313.15	6.859
318.19	6.845	318.15	6.923	318.15	6.877	318.17	7.018	318.15	6.857	318.15	6.860
323.16	6.846	323.45	6.931	323.15	6.876	323.22	7.008	323.15	6.857	323.15	6.859
328.16	6.848	328.17	6.922	328.16	6.872	328.16	7.013	328.19	6.856	328.18	6.855
333.15	6.845	333.17	6.918	333.10	6.874	333.17	7.010	333.17	6.854	333.15	6.858
338.15	6.847	338.16	6.923	338.18	6.876	338.18	7.018	338.20	6.856	338.20	6.856
343.15	6.841	343.15	6.923	343.15	6.875	343.16	7.011	343.17	6.854	343.15	6.856
348.18	6.845	348.15	6.916	348.24	6.877	348.16	7.010	348.18	6.858	348.18	6.856
353.15	6.849	353.15	6.919	353.21	6.878	353.17	7.022	353.16	6.856	353.17	6.857
$\langle k_m \rangle$	6.847		6.923		6.877		7.015		6.857		6.859
σ_{k_m}	$3.09 \cdot 10^{-3}$		$3.95 \cdot 10^{-3}$		$3.28 \cdot 10^{-3}$		$5.10 \cdot 10^{-3}$		$2.48 \cdot 10^{-3}$		$2.92 \cdot 10^{-3}$
AARD %	0.04		0.04		0.04		0.07		0.03		0.04

^a $\text{m}^3 \cdot \text{mol}^{-1} \cdot \text{Pa}^{1/7}$ **Table 6.7.** Fitting parameters and standard deviation (σ) of linear of equation fitted to the (k_m , T) data.

Coefficients	MeC10:0	MeC12:0	MeC14:0	MeC16:0	MeC18:0	MeC18:1	MeC18:2	MeC18:3
$k_1/\text{m}^3 \cdot \text{mol}^{-1} \cdot \text{Pa}^{1/7}$	4.4151	5.1007	5.7805	6.5523	7.1962	7.1455	7.0448	6.8400
	± 0.0031	± 0.0081	± 0.0163	± 0.0187	± 0.0219	± 0.0104	± 0.0086	
$k_2 \cdot 10^5/\text{m}^3 \cdot \text{mol}^{-1} \cdot \text{Pa}^{1/7} \cdot \text{K}^{-1}$	-10.8571	-6.2091	-0.2170	-20.3650	-1.8152	-21.4394	-27.300	-3.9300
	± 0.9939	± 2.4734	± 4.9955	$\pm 5-6001$	± 6.4877	± 3.1809	± 2.7127	
$\sigma/\text{m}^3 \cdot \text{mol}^{-1} \cdot \text{Pa}^{1/7}$	0.001	0.002	0.003	0.002	0.002	0.002	0.002	0

The molar compressibility for the biodiesel samples processed in this work and those studied by Freitas et al. [5] and Huber et al. [10] were also calculated. For the samples of Freitas et al., the calculated k_m values, using Eq. 6-3, were obtained from the speed of sound and density of biodiesel presented by Freitas et al. [5] and Pratas et al. [23], respectively, and from Huber's sample, the same data was determined by Huber et al. [10]. For the processed synthetic samples and produced cottonseed biodiesel, the density was calculated by using the Kay mixing rule:

$$\rho_{biod} = \sum_i^{FAMES} x_i \rho_i \quad \text{Eq. 6-6}$$

where ρ_i and x_i represent the density and molar fraction of FAME i in the mixture, respectively. Pratas et al. [23] have been shown that using molar fractions in Kay rule is preferable than the use of other concentration unit, being the *AARD* between calculated and experimental density values of ca. 0.33%. The molar compressibility of biodiesels are presented in Table 6.6 and illustrated in Figure 6.8(b). A statistical analysis of the biodiesel data was also performed calculating the standard deviation and the average absolute relative deviation from the mean value of the molar compressibility. The results are also shown in Table 6.6. The analysis of Figure 6.8(b) allows concluding that, for biodiesel, k_m is also slightly dependent of temperature and this behaviour is related to the nature of biodiesel sample (biodiesel composition). The standard deviation and the average absolute relative deviation from the mean value of k_m , are usually lower than 5×10^{-3} and 0.05%, respectively, as verified for FAMES.

Daridon et al. [6] have been observed a linear increase of the molar compressibility with the molecular weight for FAMES and FAEEs. This behaviour is displayed in Figure 6.9, where the molar compressibility of saturated FAMES (MeC8:0, MeC10:0, MeC12:0, MeC14:0, MeC16:0, MeC18:0) are represented as a function of molecular weight. The linear behaviour can be described by the expression,

$$\langle k_m \rangle = -(0.2825 \pm 0.0049) + (0.02502 \pm 2.12 \times 10^{-5})M \quad \text{Eq. 6-7}$$

which correlation coefficient, standard deviation and *AARD* are $r = 1.000$, $\sigma = \pm 0.0025$, and 0.03%, respectively. The unsaturated FAMES MeC18:1, MeC18:2 and MeC18:3 have lower values of molar compressibility than MeC18:0. Daridon et al. [6] have been observed similar and

coincident straight lines for saturated FAMES and FAEEs, which were parallel to the corresponding line for paraffins. This means that, the molar compressibility is not only function of molecular weight, but also depends on the molecular structure of molecules. The parallelism observed between paraffins and FAEs is due to the constant contribution of the ester group for k_m , which is independent of the fatty acid ester considered [6]. Based on these results, Daridon et al. developed a group contribution method for the prediction of k_m of FAEs, with *AARD* usually less than 0.05%.

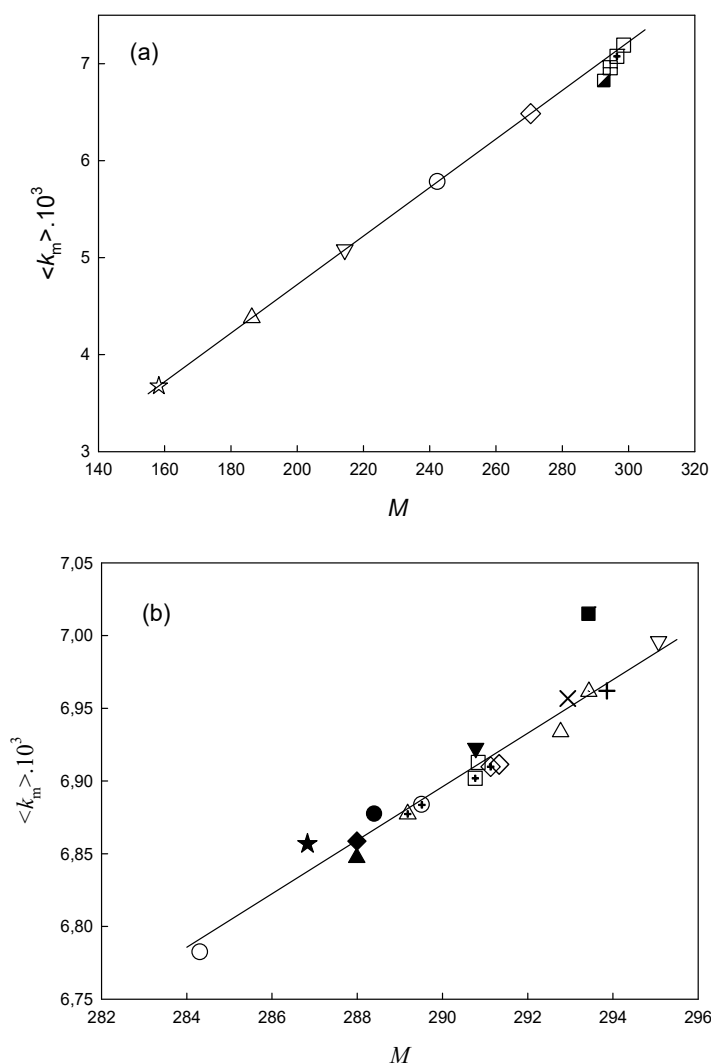


Figure 6.9. Relation between molar compressibility (k_m) and molar mass (M). (a) FAMES: ☆, MeC8:0; △, MeC10:0; ▽ MeC12:0; ○, MeC14:0; ◇, MeC16; □, MeC18:0; ⊠, MeC18:1; ⊡, MeC18:2; ■, MeC18:3. (b) Biodiesel: △, S [5]; ▽, R [5]; ○, P [5]; △, SR [5]; ⊕, PR [5]; ⊠, SP [5]; □, SRP [5]; +, Sf [5]; ×, GP [5]; ⊡, SoyA [5]; ◇, Sample A and ⊠, Sample B [10]; ▲, SCS; ▼, SBT; ●, SPF; ■, SYG1; ☆, SYG2; ◆, CSB.

For the methyl biodiesel samples studied in this chapter, the existence of such relationship between k_m and M it was also checked. In Figure 6.9(b), the mean molar compressibility averaged to the temperature ranges of data, is represented as a function of the mean molar mass of biodiesel, given by

$$M = \sum_i^{FAMES} x_i M_i \quad \text{Eq. 6-8}$$

As before, a linear behaviour between $\langle k_m \rangle$ and M was observed and considering the $(\langle k_m \rangle, M)$ pairs for Freitas et al., Huber et al. and the ones for this work (with the exception of SYG1, since $\langle k_m \rangle$ is outside of the observed range), the equation,

$$\langle k_m \rangle = -(1.5630 \pm 0.2475) + (0.01839 \pm 0.0009)M \quad \text{Eq. 6-9}$$

was obtained. The correlation coefficient, standard deviation and *AARD* of Eq. 6-9 are $r = 0.984$, $\sigma = 0.0095$ and 0.11%, respectively. It is important to emphasize that this equation results from wide temperature and composition ranges of fuels. At the extreme molar mass are the values corresponding to the palm and rapeseed biodiesel samples studied by Freitas et al. [5], presenting significant differences in composition: the palm sample (P) has composition (wt %) MeC16:0 = 42.45%, MeC18:1 = 41.92% and MeC18:2 = 9.80%, while for rapeseed sample (R), MeC16:0 = 5.22%, MeC18:1 = 62.11% and MeC18:2 = 21.07%. From the data existent in the literature, it can be said that a narrow range is observed for the variation of molar mass ($M_{\min} = 284.317$ corresponding to palm biodiesel to $M_{\max} = 295.072$ for rapeseed fuel). Considering the molar compressibility and mean molar mass of biodiesels from Freitas et al., Huber et al. and the ones from this work, the following equation was obtained by fitting the data by least squares,

$$k_m = 6.8178 - 1.127 \cdot 10^{-4}T + F(M, T)(0.2351 - 6.8 \times 10^{-5}T) \quad \text{Eq. 6-10}$$

with statistical parameters $r = 1.000$, $\sigma = 0.0102$ and *AARD* = 0.1%. In Eq. 6-10,

$$F(M, T) = -4.284 \cdot 10^{-7}(M - 295.07)(M - 284.32)T + 0.09298 (M - 284.32) \quad \text{Eq. 6-11}$$

This equation provides accurate data of molar compressibility at molar mass M_{\min} and M_{\max} mentioned before, therefore giving bounded values of k_m . The *AARD* values from Eq. 6-10, related to the biodiesel fuels are given in Table 6.8. The error analysis is made considering the subsets (Freitas et al., Huber et al. and this work), justified by the different variation range of speed of sound versus temperature (see Figure 6.7) and the different composition of fuels for the subsets. The results of Eq. 6-10 can be compared with those obtaining by assuming the ideal mixing rule defined as,

$$k_m = \sum_i^{FAMES} x_i k_{m,i} \quad \text{Eq. 6-12}$$

where $k_{m,i}$ is the molar compressibility of the FAMES i . Due to the lack of experimental data of the speed of sound for some minority FAMES, a pseudo-component concept, similar to that applied by Freitas et al [5], was adopted in this chapter: it was assumed that the molar compressibility of C16:1 as that of MeC16:0, that of MeC20:0, MeC22:0 and MeC24:0 as that of MeC18:0 and for MeC20:1 and MeC22:1 as that for C18:3. For methyl caprate (MeC10:0), the speed of sound provided by Daridon et al. [6] for temperatures ranging from 283.15 K to 343.15 K and density measured by Pratas et al. [24] were used to obtain the relation $k_m = 4.4151 - 1.0857 \cdot 10^{-4} T$. For methyl linolenate (MeC18:3) the speed of sound measured by Gouw and Vlugter [3] at temperatures of 293.15 K and 313.15 K and the density measured by Pratas et al. [25] provided a similar relation $k_m = 6.8400 - 3.9300 \cdot 10^{-5} T$.

From Table 6.8, it can be concluded that the predictions for the molar compressibility with the simple mixing rule given by Eq. 6-12 provide good estimates of that parameter. For the subsets of Freitas et al. and this work, the *AARD* is lower than 0.1%. The prediction with Eq. 6-10 is also possible with deviations lower than 0.1%, particularly for Freitas et al. subset. The predictive capacity of both methods was evaluated in term of overall average deviation, being the *OARD* of 0.17% and 0.19% for Eqs. 6-10 and 6-12, respectively.

Table 6.8. Error analysis of predictions molar compressibility and speed of sound, by different methods.

Biodiesel	<i>AARD%</i> (k_m)		<i>AARD%</i> (u)							
	Eq. 6-10	Eq. 6-12	ID	VD	NMT	CT	MC1	MC2	JJ	IMP
S	0.24	0.04	0.23	0.31	0.22	0.22	0.23	0.40	0.24	0.22
R	0.00	0.02	0.27	0.34	0.27	0.26	1.86	0.99	0.28	0.26
P	0.01	0.12	0.31	0.51	0.28	0.33	0.62	0.70	0.30	0.31
SR	0.03	0.06	0.34	0.42	0.34	0.34	1.01	0.25	0.35	0.33
PR	0.04	0.14	0.29	0.45	0.27	0.30	1.24	0.12	0.29	0.29
SP	0.04	0.11	0.23	0.40	0.21	0.24	0.59	0.39	0.23	0.22
SRP	0.01	0.11	0.31	0.46	0.29	0.31	1.02	0.08	0.31	0.30
SF	0.14	0.02	0.32	0.37	0.31	0.31	0.69	0.07	0.32	0.31
GP	0.04	0.13	0.23	0.31	0.22	0.22	0.82	0.08	0.24	0.22
SoyA	0.14	0.18	0.33	0.42	0.32	0.34	0.54	0.36	0.34	0.33
<i>AARD</i> ^a	0.07	0.09	0.28	0.40	0.27	0.29	0.86	0.34	0.26	0.22
HA	0.18	0.31	0.40	0.45	0.39	0.40	0.74	0.08	0.41	0.39
HB	0.14	0.52	0.37	0.43	0.37	0.37	1.12	0.32	0.38	0.37
<i>AARD</i> ^b	0.16	0.42	0.39	0.44	0.38	0.39	0.93	0.06	0.40	0.38
SCS	0.10	0.05	0.15	0.24	0.14	0.15	0.58	1.49	0.15	0.14
SBT	0.19	0.04	0.14	0.20	0.14	0.14	0.63	0.34	0.14	0.14
SPF	0.21	0.05	0.16	0.29	0.14	0.17	0.58	0.50	0.15	0.15
SYG1	0.76	0.06	0.20	0.22	0.20	0.20	2.78	1.55	0.20	0.20
SYG2	0.37	0.03	0.10	0.18	0.11	0.10	0.95	0.30	0.10	0.10
CSB	0.06	0.15	0.52	0.64	0.49	0.54	0.14	0.96	0.52	0.51
<i>AARD</i> ^c	0.28	0.06	0.21	0.30	0.20	0.21	0.94	0.86	0.21	0.21
<i>OARD</i> % ^d	0.17	0.19	0.29	0.38	0.28	0.30	0.91	0.42	0.29	0.27

^a Total *AARD* for the biodiesels from Freitas et al. [5].

^b Total *AARD* for the biodiesels from Hubbet et al. [10].

^c Total *AARD* for the biodiesels fuels of this work. ID: ideal mixture; VD: van Dael; CT: Collision theory; MC1: Eq. 6-14 with density by Eq. 6-6; MC2: Eq. 6-14 with density of FAMES by GCVOL method.

^d $N_s = 3$ (subsets number).

6.1.3.3 Prediction of speed of sound

From Eq. 6-4, the sound speed is obtained by,

$$u = \rho^3 \left(\frac{k_m}{M} \right)^{7/2} \quad \text{Eq. 6-13}$$

Therefore the speed of sound can be calculated from the molar compressibility, density and molar mass. As the molar compressibility can be considered as constant in wide ranges of temperatures, $\langle k_m \rangle$ can be used in Eq. 6-13, giving

$$u = \rho^3 \left(\frac{\langle k_m \rangle}{M} \right)^{7/2} \quad \text{Eq. 6-14}$$

The density of FAMES can be accurately calculated [24, 25] or predicted, while Kay mixing rule, given by Eq. 6-6, can be used for biodiesel samples. Thus, Eq. 6-14 can be used to predict the speed of sound in FAMES and biodiesel. The comparison between the speeds of sound calculated by Eq. 6-14 using Eq. 6-7 for $\langle k_m \rangle$ and the experimental ones, for saturated FAMES are given in Figure 6.10. The individual *AARD* values were usually less than 0.20% (ca. 3 m·s⁻¹), which is not far from the experimental error found in the measurements. For the saturated FAMES (MeC6:0 to MeC18:0), the *OARD* is 0.15% (ca. 2 m·s⁻¹), while for FAMES not included in the fitting of Eq. 6-7 (MeCn:0, with n = 7, 9, 11, 13, 15, 17), the *OARD* in the speed of sound is 0.26% (ca. 3 m·s⁻¹).

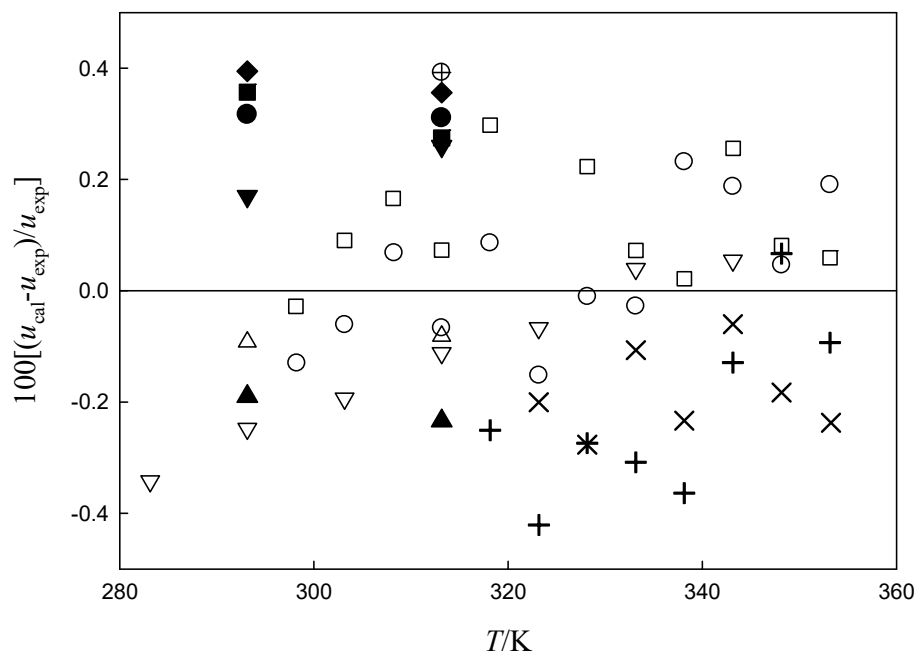


Figure 6.10. Deviation between the calculated speeds of sound from Eq. 6-14 applied to FAMES (u_{cal}) and experimental (u_{exp}). \blacktriangle , MeC7:0; \triangle MeC8:0; \blacktriangledown , MeC9:0; \triangledown , MeC10:0; \bullet , MeC11:0; \circ , MeC12:0; \square , MeC13:0; \blacksquare , MeC14:0; \blacklozenge , MeC15:0; $+$, MeC16:0; \oplus , MeC17:0; \times , MeC18:0.

Eq. 6-14 was also applied to biodiesel fuels considering the (u, T) subsets of Freitas et al. [5], Huber et al. [10] and the six biodiesel fuels of this work. The correlation 6-9 was used for the $\langle k_m \rangle$ calculation and for the density of biodiesel two methods were applied. In a first one (MC1) the density of biodiesel was calculated by Eq. 6-6, using the density linear equations found by Pratas et al. [24, 25] for the saturated and unsaturated FAMES. In the second method, labelled as (MC2), the following relationship has been used,

$$\rho_{biod} = \left(\frac{\sum_i^{FAMES} x_i M_i}{\sum_i^{FAMES} x_i V_{m,i}} \right) \quad \text{Eq. 6-15}$$

where the molar volume $V_{m,i}$ of the FAME i is calculated by GCVOL group contribution method revised by Pratas et al. [23].

Some predictive models usually used in the literature were also applied to calculate the speed of sound for biodiesels. As biodiesel is a mixture of FAMES of similar molar mass, it could be use the mixing rule, assuming an “ideal” mixture behaviour,

$$u_{biod} = \sum_i^{FAMES} x_i u_i \quad \text{Eq. 6-16}$$

In Eq. 6-16 the sound speed of FAME *i* was calculated for MeC12:0, MeC14:0, MeC16:0, MeC18:0, MeC18:1 and MeC18:2 using Eq. 6-2. For methyl caprate (MeC10:0) and methyl linolenate (MeC18:3) the (*T*, *u*) data of Daridon et al. [6] and Gouw and Vlugter [3] were considered, respectively. For MeC10:0, the data gave $u = 2802.4 - 6.2236T + 4.0357 \cdot 10^{-3}T^2$ with standard deviation, $\sigma = 0.24 \text{ m}\cdot\text{s}^{-1}$ and for MeC18:3, $u = 2454.3 - 3.5050T$ it was found. The calculation of u_{biod} by Eq. 6-16 was made using again the pseudo-component concept. Other models are the equation of Van Dael [26], given as

$$u_{biod} = \left[\left(\sum_i^{FAMES} \frac{x_i}{M_i u_i^2} \right) \left(\sum_i^{FAMES} x_i M_i \right) \right]^{-1/2} \quad \text{Eq. 6-17}$$

the Nomoto relation [27], written as

$$u_{biod} = \left(\sum_i^{FAMES} x_i R_i / \sum_i^{FAMES} x_i V_{m,i} \right) \quad \text{Eq. 6-18}$$

where R_i and $V_{m,i}$ are the molar speed of sound and the molar volume of FAME *i*, respectively. The molar sound speed is defined as $R = u^{1/3} V_m$ [28]. Another model is the Schaaff's collision factor theory (CFT) [29-31], giving by,

$$u_{biod} = u_\infty \left(\left(\sum_i^{FAMES} x_i S_i \right) \left(\sum_i^{FAMES} x_i B_i \right) / V_{mix} \right) \quad \text{Eq. 6-19}$$

where $u_\infty = 1600 \text{ m}\cdot\text{s}^{-1}$ and $S = (u V_m) / (u_\infty B)$ is the collision factor for the *i*th pure FAME in the biodiesel mixture. The molar volume of the mixture V_{mix} can be evaluated as $V_{mix} = \left(\sum_i^{FAMES} x_i M_i / \rho_{mix} \right)$ and ρ_{mix} is evaluated using Eq. 6-6. B_i is the actual volume of a molecule per mole of FAME *i* in the biodiesel mixture which is evaluated as $B = 4/3\pi r^3 N_A$, where N_A is the Avogadro's number and r is the molecular radius of the pure FAME, calculated as $r = (3b/(16\pi N_A))^{1/3}$, where

$$b = \left(\frac{M}{\rho}\right) - \left(\frac{RT}{\rho u^2}\right) \left[\left(1 + \frac{Mu^2}{3RT}\right)^{1/2} - 1 \right] \quad \text{Eq. 6-20}$$

The Junjie relation [32]

$$u_{biod} = \left(\sum_i^{FAMES} x_i V_{m,i}\right) / \left[\left(\sum_i^{FAMES} (x_i M_i)^{1/2}\right) \left(\sum_i^{FAMES} (x_i V_{m,i} / \rho_i u_i^2)\right)^{1/2} \right] \quad \text{Eq. 6-21}$$

was also used to predict the speed of sound in biodiesel. Finally the speed of sound in biodiesel was also calculated based on the acoustical impedance ($Z = u\rho$),

$$u_{biod} = \left(\sum_i^{FAMES} x_i Z_i / \sum_i^{FAMES} x_i \rho_i\right) \quad \text{Eq. 6-22}$$

The values of *AARD* corresponding to the various methods described before are given in Table 6.8. The values of the *AARD*, for the different subsets of biodiesels, and the overall average relative deviation are also presented. The ideal mixture model which is the simplest to use, gives the same results compared with more sophisticated methods. It allows the representation of speed of sound data with *OARD* = 0.29%, being particularly good for the subsets of this work and for Freitas et al. The ideal mixture method has equivalent predicting capacity as Nomoto, collision theory, Junjie and impedance methods. The ideal mixture works better in the subset of this work, being the individual values of *AARD* of each biodiesel sample lower compared with the subsets of Freitas et al. and Hubber et al. This could be because of the largest variation range of speed of sound for the samples of this work (see Figure 6.7). The ideal mixture method was applied by Freitas et al. [5] to biodiesel fuels produced from different feedstock, obtaining *OARD* of 0.36%. In this work the value 0.28% was obtained and the difference is explained by the different range of temperature tested by Freitas et al. These same authors tried another prediction method based in a modified Auerbach model [5], but the results obtained were poor, being the deviations around 1.5%. It is interesting to see that Eq. 6-14 provides different *AARD* values when different density calculation methods are used. The MC2 method which uses GCVOL group contribution gives usually lower deviations compared with MC1, which uses Eq. 6-6. For the subset of this work, the deviations for CSB are higher than for SCS, although both fuels have the same composition (see Table 6.3). This is due to the higher speed of sound measured in CSB (see Table

6.4) and because it is possible that CSB contains residual chemical species other than the detected FAMEs. The relative deviations between calculated and experimental speed of sound with the MC2 method is presented in Figure 6.11. This method gives very good predictions of speed of sound particularly in Freitas et al. subset.

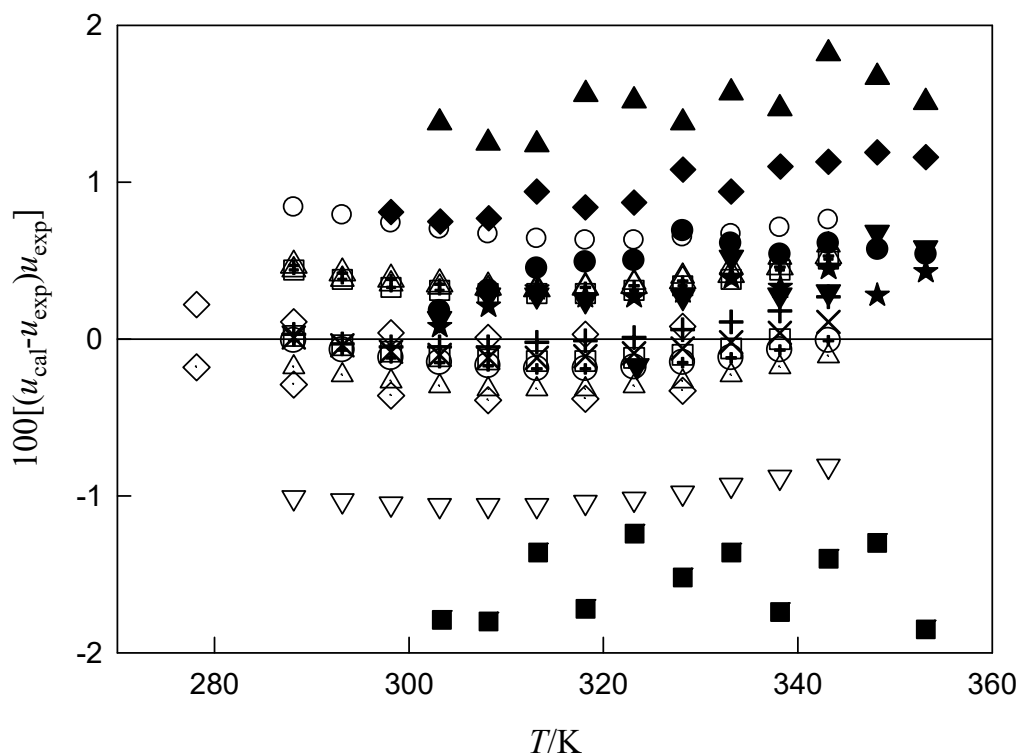


Figure 6.11. Deviation between calculated speed of sound from Eq. 6-14 applied to biodiesel fuels (u_{cal}) and experimental (u_{exp}). Δ , S [5]; ∇ , R [5]; \circ , P [5]; \triangle , SR [5]; \oplus , PR [5]; \triangleleft , SP [5]; \square , SRP [5]; $+$, Sf [5]; \times , GP [5]; \blacksquare , SoyA[5]; \diamond , Sample A and \blacklozenge , sample B [10]; \blacktriangle , SCS; \blacktriangledown , SBT; \bullet , SPF; \blacksquare , SYG1; \star , SYG2; \blacklozenge , CSB.

6.1.4 Conclusions

The speed of sound for six fatty acid methyl ester and six biodiesel fuels were measured at atmospheric pressure and temperatures ranging from 288 to 353 K using a new non-intrusive method. For the six biodiesel samples five were prepared by weight from the pure FAMEs and one was produced from transesterification of cottonseed oil, being characterized by gas chromatography. The speed of sound of FAMEs and biodiesel is very well described by polynomial quadratic equations in temperature. An extensive compilation of speed of sound data from the literature was used for the purpose of comparison. The results produced in this work are

in close agreement with the literature ones. A particular and interesting aspect is that the biodiesel samples of this work show a large variation range of speed of sound at a given temperature compared with the narrow range relative to the samples measured by Freitas et al. [5]. Taking the values of the density for FAMES and speed of sound data, the molar compressibilities were calculated. This property is a very weak function of temperature, either for FAMES or biodiesel and can be considered as a constant, dependent on the substance, over wide temperature ranges. Deviations from mean value are usually less than 0.05%. Linear correlations were developed for mean molar compressibility as a function of molar mass for FAMES and biodiesel with *AARD* of 0.03% and 0.11%, respectively. A new correlation for the molar compressibility of biodiesel as function of mean molar mass and temperature was developed with *OARD* of 0.17%, taking into account subsets of data from the literature and of this work. The deviation was less than 0.1% for several biodiesel fuels. For all biodiesels the ideal mixture model, which is the simplest to use, has equivalent predictive capability of speed of sound in biodiesel to more sophisticated methods. The new method developed in this section, based on mean molar compressibility and the GCVOL group contribution for density calculation of FAMES, gives good estimates of speed of sound. More accurate relationships for $\langle k_m \rangle$ and k_m could be developed, and used with GCVOL method to give even more accurate estimates of speed of sound in biodiesel fuels. It is expected that the prediction methods here developed for molar compressibility and speed of sound could produce useful correlations for other biodiesel properties as the cetane number and other exhaust emission related issues.

6.2 SPEED OF SOUND OF COTTONSEED OIL

6.2.1 Experimental part

6.2.1.1 Measurements

A new stainless steel cell designed for liquid speed of sound measurements was used. A schematic representation of the system used is shown in Figure 6.12. A 2.25 MHz transducer (Panametrics V305) was mounted in the top of a cell built of solid steel. This cell has a hole, with planar surfaces and following the central vertical axis, where liquid penetrates. The variation in the temperature of the sample liquid contained in the double wall glass vessel was made by using a liquid circulator system (Grant Type VFP) connected to the vessel using silicone tubes. The temperature of the bath system was controlled and stabilized inside the vessel, at the desired values by means of a thermocouple type K, inserted into the vessel. The thermocouple (Labfacility KMI / 3x500 (IEC)) was connected to an operational amplifier (Analog Devices AD595 and coupled to a temperature acquisition board (National Instruments NI USB-6008). This device enables simple basic data acquisition functions for data logging and communicates with Labview interface. In order to obtain uniform temperature distribution into the liquid, a magnetic stirring system, J.P. Selecta Multimatic - 5N was used, as well as a small stirrer inside the vessel. Prior to temperature measurement the thermocouple was inserted in Milli-Q water and calibrated against a certified digital thermometer (ITS90) with precision of 0.001K (Isotech TTI-10). The temperature was measured within $u(T) = 0.01\text{K}$. The ultrasound wave, corresponding to the path followed by the going and returning of the first echo, to the transmitter was collected by a NI-PCI data acquisition board (PCIe-9852) and recorded by means of the developed *Labview* program, which provides and saves the wave propagation time in the liquid. In summary, the thermocouple and the transducer are connected to the *Labview* interface in order to obtain the data on the acoustic propagation velocity in the liquid present in the vessel. Temperature, time of flight, $\Delta\tau$, and resulting speed of sound, u , are recorded and saved continuously.

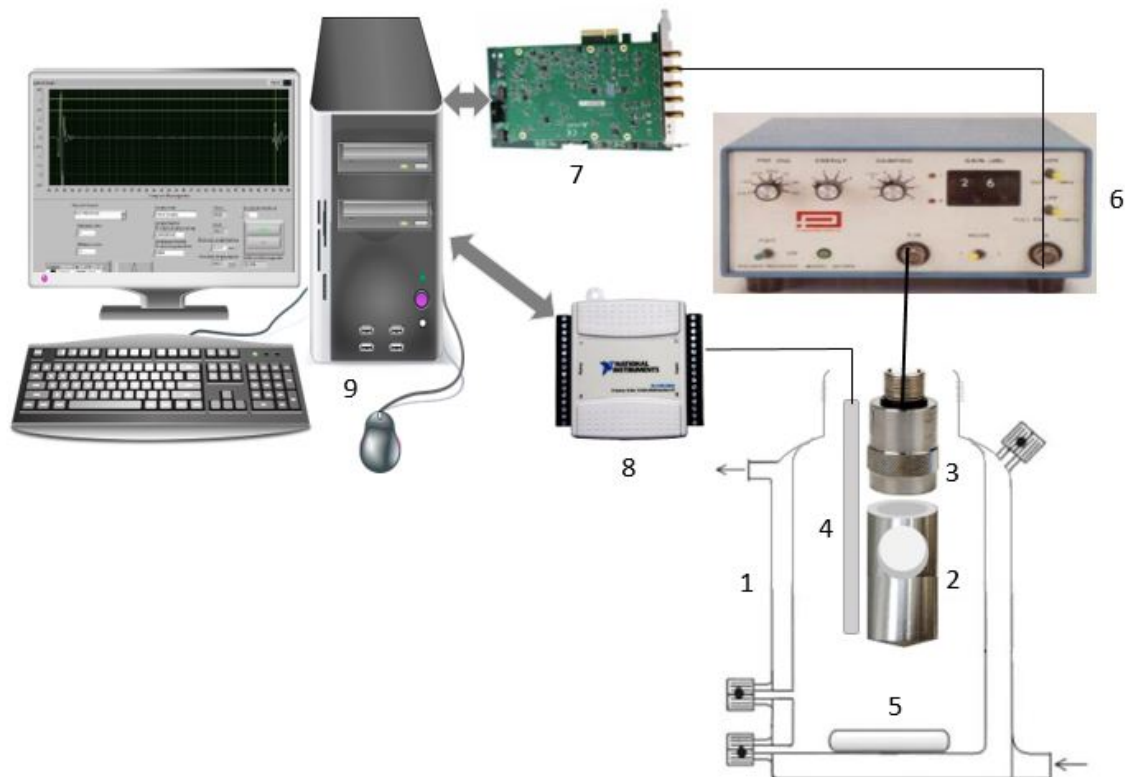


Figure 6.12. Schematic apparatus. 1-Double walled thermostated vessel; 2-Ultrasound cell; 3-Transducer Panametrics V305, 2.25 MHz; 4-Thermometer (Type K); 5-Magnetic stirrer; 6-Pulser-receiver Panametrics (5072PR); 7-PCI data acquisition board (PCIe-9852), Addlink; 8-Data acquisition board (NI USB-6008); 9-PC.

The speed of sound, ignoring diffraction corrections, is obtained from the measured time of flight, $\Delta\tau$, and the distance between the transducer and the reflecting surface (L), from the following expression:

$$u = \frac{2L}{\Delta\tau} \quad \text{Eq. 6-23}$$

In order to be able to use Eq. 6-23 it is necessary to know, with great precision, the distance (L). The geometry of the reflecting surface, as well as its constitution, prevents the measurement of the distance between the probe and that surface with the required degree of accuracy. Therefore, this task was done using water as calibrating standard. The reference speed of sound values were taken from NIST [17] with claimed uncertainties of 0.1% (about $1.5 \text{ m}\cdot\text{s}^{-1}$). The experimental propagation times of the acoustic waves in water were obtained and from standard

SOS values, at temperatures in the range 298.15 K to 343.15 K, the use of Eq. 6-23 gives the distance L at each temperature. The mean value is $L = (21.010 \pm 0.012)$ mm. The uncertainty for the flight of time is estimated to be $\sigma_{\Delta\tau} = 0.022 \mu\text{s}$.

From the propagation error law, an upper limit $u(L)$ of error for the flight distance can be obtained by:

$$\sigma_{(L)} = \sqrt{\left(\frac{\Delta\tau}{2}\right)^2 \sigma_u^2 + \left(\frac{u}{2}\right)^2 \sigma_{\Delta\tau}^2} \quad \text{Eq. 6-24}$$

Replacing the values of u and $\Delta\tau$ for the given temperature range and taking into account that $\sigma_u = 0.001u$ and $\sigma_{\Delta\tau} = 0.022 \mu\text{s}$, the maximum error for the path is $\sigma_L = 0.027$ mm is obtained, which is about twice the standard error from the mean. In the same way, the maximum expected uncertainty for the SOS, σ_u can be obtained from the propagation error law:

$$\sigma_u = \sqrt{\left(\frac{2}{\Delta\tau}\right)^2 \sigma_L^2 + \left(\frac{2L}{\Delta\tau^2}\right)^2 \sigma_{\Delta\tau}^2} \quad \text{Eq. 6-25}$$

with the values of $L = 21.010$ mm, $\sigma_L = 0.027$ mm and $\sigma_{\Delta\tau} = 0.022 \mu\text{s}$, the value $\sigma_u = 2.3 \text{ m}\cdot\text{s}^{-1}$ is calculated for the range 298.15 K to 343.15 K as the maximum uncertainty. The uncertainty in the speed of sound due to temperature uncertainty can be evaluated from the variation du/dT . From the selected data from NIST [17] in the range of temperature 298.15 K to 343.15 K:

$$u = -1711.63 + 19.0063T - 0.027652T^2 \quad \text{Eq. 6-26}$$

with $r^2 = 0.9998$ and $\sigma = 0.31 \text{ m}\cdot\text{s}^{-1}$. From the propagation error law, the uncertainty σ_u due to the temperature is:

$$\sigma_u = \sqrt{\left(\frac{du}{dT}\right)^2 \sigma_T^2} \quad \text{Eq. 6-27}$$

and taking into account that $\sigma_T = 0.01\text{K}$, the uncertainty in the speed of sound due to temperature fluctuation is less than $0.03 \text{ m}\cdot\text{s}^{-1}$. Thus, it is expected that the combined uncertainty in speed of sound, $u_c(u)$ would be between $1.5 \text{ m}\cdot\text{s}^{-1}$ and $2.3 \text{ m}\cdot\text{s}^{-1}$.

One way of avoiding errors in the propagation path of the acoustic wave, for example because of its change by temperature variation of the liquid which in turn implies the change of the thermal expansibility of the steel, is to use the relative method. In this method the sound velocities of water and oil and the respective time of flight, are simultaneously compared. From Eq. 6-23,

$$u_{oil} = u_{H2O} \frac{\Delta\tau_{H2O}}{\Delta\tau_{oil}} \quad \text{Eq. 6-28}$$

For this method, the maximum expected uncertainty for the SOS, σ_u , can be predicted from the equation:

$$\sigma_u = \sqrt{\left(\frac{\Delta\tau_{H2O}}{\Delta\tau_{oil}}\right)^2 \sigma_{u_{H2O}}^2 + \left(\frac{u_{H2O}}{\Delta\tau_{oil}}\right)^2 \sigma_{\Delta\tau_{H2O}}^2 + \left(\frac{u_{H2O}\Delta\tau_{H2O}}{\Delta\tau_{oil}^2}\right)^2 \sigma_{\Delta\tau_{oil}}^2} \quad \text{Eq. 6-29}$$

Taking the uncertainties as before in the speed of sound of water and in the time of flight, the maximum level of combined uncertainty $u_c(u) = 2.04 \text{ m}\cdot\text{s}^{-1}$ is obtained for 2nd method.

6.2.2 Speed of sound models

6.2.2.1 Correlation

The variation of the speed of sound in liquids with changes in temperature has been studied by various researchers. For most liquids studied, with the exception of water, the speed of sound decreases with increasing temperature. Over short ranges of temperature the speed of sound-

temperature curves appear essentially linear. The SOS dependence on temperature in liquids can be well represented by Eq. 6-2.

Rao [33] proposed the relation:

$$u = u_0 \left(1 - \frac{T}{T_c}\right)^{0.9} \quad \text{Eq. 6-30}$$

where u_0 is the speed of sound at absolute zero and T_c is the critical temperature in K. This relation is similar to that proposed by Guggenheim [34] for the dependence of surface tension on temperature and used in section 5.3.1.

6.2.2.2 Prediction

Several equations have been proposed for prediction of SOS in vegetable oils. The simplest approximation is the “ideal” mixture used for biodiesel, Eq. 6-16 here applied to triglycerides as components of oil:

$$u_{oil} = \sum_i^{TG} \phi_i u_i \quad \text{Eq. 6-31}$$

where u_i and ϕ are the speed of sound and volume fraction or mass fraction, respectively, of i^{th} component of triglyceride. A more complex relation has been proposed by Wood [35] and has been applied in several studies [36]. Wood equation relates the SOS of oil with the velocities and densities of the constituent triglycerides:

$$u_{oil} = \left[\left(\sum_{i=1}^{TG} \frac{\phi_i}{u_i^2 \rho_i} \right) \left(\sum_{i=1}^{TG} \phi_i \rho_i \right) \right]^{-1/2} \quad \text{Eq. 6-32}$$

where u is the SOS in the oil, ρ and ϕ are the density and the volume fraction or mass fraction, respectively and TG is the number of triglyceride components. For many oils, the densities of different triglycerides are almost the same and thus the velocity of mixed triglyceride can be simplified to the following form [36]:

$$u_{oil} = \left[\sum_{i=1}^{TG} \frac{\phi_i}{u_i^2} \right]^{-1/2} \quad \text{Eq. 6-33}$$

which depends on velocity of TGs only. According to Clements and Povey [36], the difference between the velocities calculated using Eq. 6-32 and Eq. 6-33, was always less than 0.2 m/s, even when the triglyceride mass fraction were used instead of the volume fraction. The prediction of SOS in oils using Eqs. 6-31 and 6-33 needs the u_i values of TGs. The way in which the fatty acids are distributed among the triglycerides in the oil is difficult to know, although liquid chromatography provides a method of achieving this. The experimental determinations of SOS available in literature for the relevant triglycerides are scarce and can be summarized to the values reported by Gouw and Vlugter [37], those by Clements and Povey [36] given in Table 6.9 and data given by Hustad et al. [38] reported in graphical form, which were accessed through the use of data capture software WebPlotDigitizer (3.8).

Table 6.9. Experimental speed of sound of triglycerides.

TAG	T/K	n	m	$u/(m.s^{-1})$	TAG	T/K	n	m	$u/(m.s^{-1})$
Tributyrin	293.15	12	0	1339.1	2-Oleodipalmitin	313.15	50	1	1389.4
Tricaproin	293.15	18	0	1356.7	1-Palmito-2-oleostearin	313.15	52	1	1392.4
Tricaprylin	293.15	24	0	1381.1	1-Palmito-2-stearoolein	313.15	52	1	1393.1
Tricaprin	293.15	30	0	1402.7	1-Oleo-2-Palmitostearin	313.15	52	1	1393.9
Triolein	293.15	54	3	1462.5	Trilaurin	343.15	36	0	1262.7
Trilinolein	293.15	54	6	1473.8	Tripalmitin	343.15	48	0	1290.2
Tributyrin	313.15	12	0	1269.9	1-Palmitin-2-stearopalmitin	343.15	50	0	1292.3
Tricaproin	313.15	18	0	1288.9	Tristearin	343.15	54	0	1301.0
Tricaprylin	313.15	24	0	1315.0	2-Oleodipalmitin	343.15	50	1	1293.4
Tricaprin	313.15	30	0	1339.4	1-Oleodipalmitin	343.15	50	1	1294.8
Trilaurin	313.15	36	0	1357.0	1-Palmito-2-Oleostearin	343.15	52	1	1297.3
Triolein	313.15	54	3	1397.2	2-Palmitodistearin	343.15	54	1	1301.5
Trilinolein	313.15	54	6	1407.7	Triolein	343.15	54	3	1303.5
1-Oleodipalmitin	313.15	50	1	1389.7					

Values at 293.15 K and 313.15 K are from Gouw and Vlugter [37] and at 343.15 K from McClements and Povey [36].

Javanaud and Rahalkar have suggested an empirical equation, applicable at 293 K, that relates ultrasonic speed to molecular formula of TG:

$$u_{TG} = u_0 + nu_1 + mu_2 \quad \text{Eq. 6-34}$$

where u_0 , u_1 and u_2 are parameters, being u_1 the increase in SOS due to additional carbon and u_2 corresponds to the increase per additional double bond, n is the number of carbon atoms (not counting the glycerol skull) and m is the total number of double bonds in the triglyceride. Eq. 6-34 assumes that the SOS of triglyceride isomers is the same. Although isomers do generally have different ultrasonic speed, differences are usually small, as can be seen in Table 6.9. Clements and Povey [36] reviewed Eq. 6-34 assuming that the addition of an unsaturated bond to an unsaturated fatty acid chain leads to a greater increase in velocity than the addition of an unsaturated bond to a saturated fatty acid chain. They proposed:

$$u_{TG} = u_0 + nu_1 + mu_2 + ou_3 \quad \text{Eq. 6-35}$$

where u_2 is the increase in SOS due to the addition of an unsaturated bond to a saturated fatty acid chain, u_3 is the increase in velocity due to the addition of an unsaturated bond to an unsaturated fatty acid chain, m is the number of unsaturated fatty acid chains per triglyceride molecule and o is the total number of unsaturated bonds in the triglyceride, excluding the first on each unsaturated fatty acid chain. Clements and Povey found the parameters values $u_0 = 1187.1 \pm 3 \text{ m}\cdot\text{s}^{-1}$, $u_1 = 2.12 \pm 0.07 \text{ m}\cdot\text{s}^{-1}$, $u_2 = 0.7 \pm 0.4 \text{ m}\cdot\text{s}^{-1}$ and $u_3 = 3.5 \text{ m}\cdot\text{s}^{-1}$, to be used at $T = 343 \text{ K}$.

From the values reported in Table 6.9, a general equation for prediction of triglyceride speed of sound at any temperature in the range 293K to 343 K was developed. The new correlation takes into account a linear dependence of the temperature in each term contributing to SOS in the form:

$$U_{TG} = U_{main} + U_{doub} \quad \text{Eq. 6-36}$$

where U_{main} and U_{doub} are the contributions relative to main structure due to carbon skull, excluding the glycerol part, and to the double bonding arrangement in TG fragments, respectively. They are calculated by:

$$U_{\text{main}} = (u_{m0} + u_{m1}T) + (u_{m2} + u_{m3}T)n + (u_{m4} + u_{m5}T)n^2 \quad \text{Eq. 6-37}$$

$$U_{\text{doub}} = (u_{d0} + u_{d1}T) + (u_{d2} + u_{d3}T)n_1 + (u_{d4} + u_{d5}T)n_2(u_{d6} + u_{d7}T)n_3 \quad \text{Eq. 6-38}$$

where n_1 , n_2 and n_3 are the number of double bonds in fragment sn-1, sn-2 and sn-3 of triglyceride. The position of double bonds has importance in the value of the SOS between isomers (e.g. OPP and POP in Table 6.9). The quadratic dependence in the number of carbon atoms, n , in U_{main} is necessary to represent the curvature observed when u is plotted vs. n , at fixed T (see Figure 6.13).

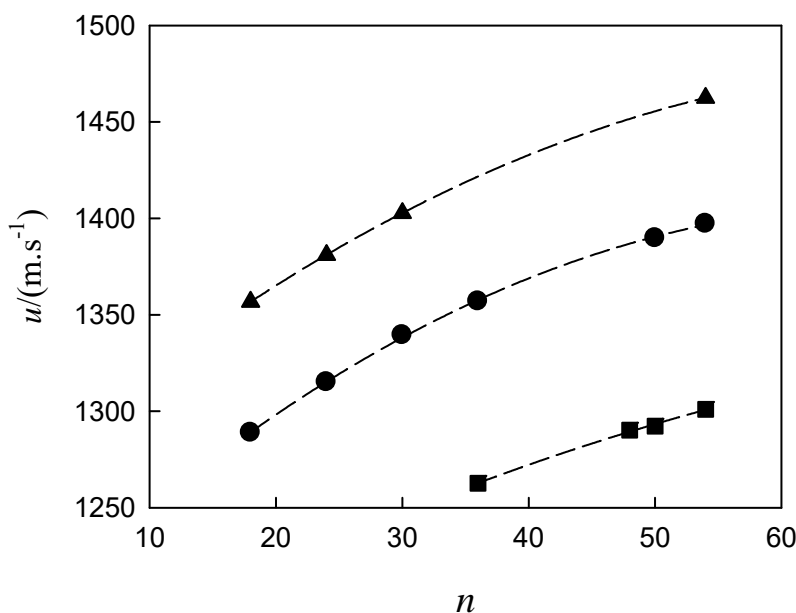


Figure 6.13. Speed of sound of TGs as function of n , at 293.15 K (▲), 313.15 K (●) and 343.15 K (■).

The parameters u_{mi} and u_{di} were obtained by fitting Eq. 6-37 and 6-38 to the data reported by Gouw and Vlугter [37] and by Clements and Povey [36], presented in Table 6.9. Data reported by Hustad et al. [38] were used as validation. Values of parameters u_{mi} and u_{di} , their uncertainties and other relevant statistical data are provided in Table 6.10, where it can be seen that *AARD* is

very low (0.06%) as well as the standard deviation of the fitting ($1.5 \text{ m}\cdot\text{s}^{-1}$), which is of the order of the experimental uncertainty. In Figure 6.14 and Figure 6.15 comparisons of experimental and calculated SOS data as function of temperature are made.

Table 6.10. Coefficients of Eqs. 6-37 and 6-38.

	U_{main}		U_{doub}
u_{m0}	2313.36	u_{d0}	-32.3795
u_{m1}	-3.59132	u_{d1}	0.10152
u_{m2}	1.4754	u_{d2}	42.933
u_{m3}	0.0160344	u_{d3}	-0.130212
u_{m4}	-9.53797×10^{-3}	u_{d4}	53.645
u_{m5}	-1.30487×10^{-4}	u_{d5}	-0.164015
		u_{d6}	-33.3901
		u_{d7}	0.115713
σ	$1.5 \text{ m}\cdot\text{s}^{-1}$		
<i>AARD</i>	0.06 %		

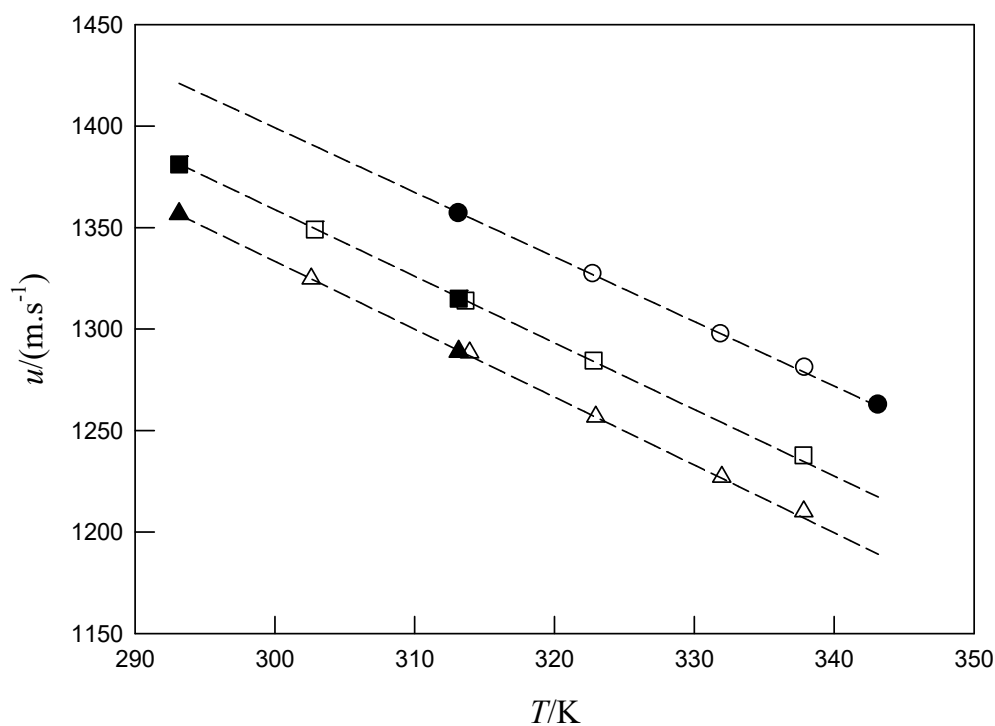


Figure 6.14. Speed of sound of TGs as function of temperature. Symbols represent experimental data and lines calculated values from Eq. 6-37. Experimental data from Table 6.9: \blacktriangle tricaproin; \blacksquare , tricaprylin and \bullet , trilaurin; data from Hustad et al. [38]: Δ , tricaproin; \square , tricaprylin; \circ , trilaurin.

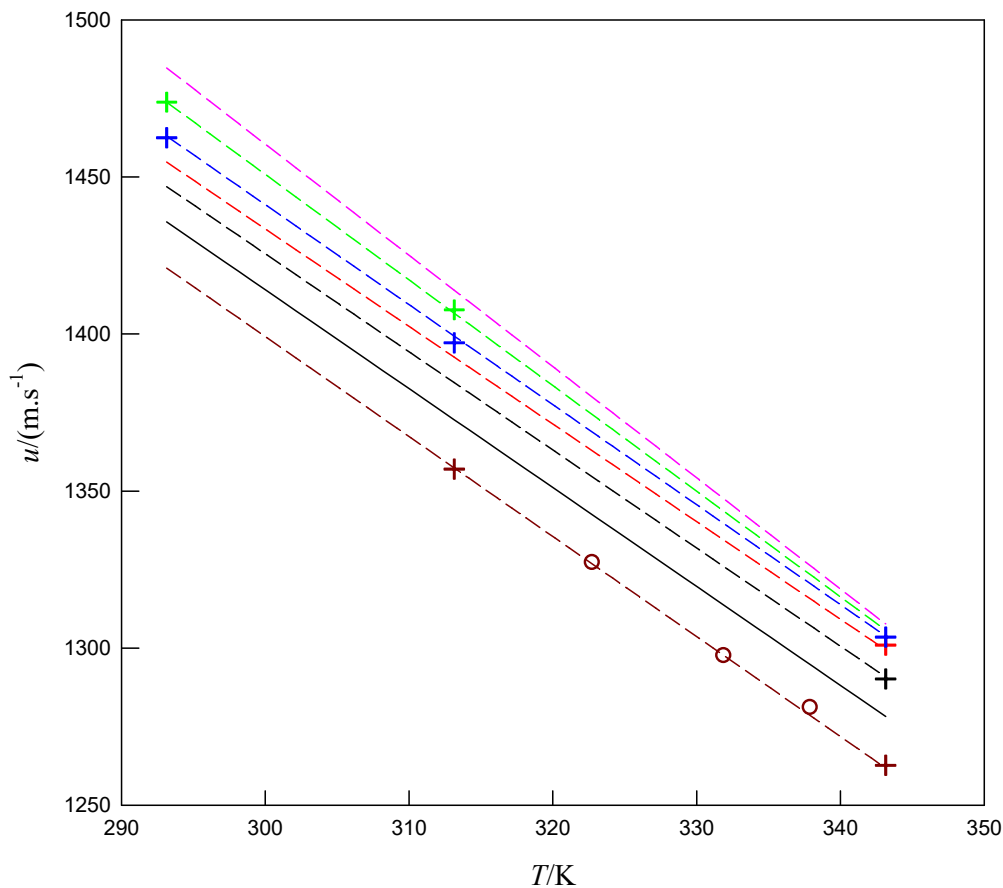


Figure 6.15. Speed of sound of representative TGs in oils as function of temperature. Symbols represent experimental data and lines calculated one from Eq. 6-37 and 6-38. Brown, black, red, blue, green and pink dashed lines correspond to trilaurin, tripalmitin, tristearin, triolein, trilinolein and trilinolenin, respectively. Black solid line corresponds to trimyristin. Experimental data: +, data from Table 6.9; o, Hustad et al. [38].

In Figure 6.16 and Figure 6.17, the excellent accuracy of the model to represent the selected data can be observed. In this figures, the experimental data reported by Gouw and Vlugter [37], McClements and Povey [36] and Hustad et al. [38] follow closely the data calculated from Eqs. 6-37 and 6-38, with relative deviations usually in the range $\pm 0.1\%$, corresponding to absolute deviations of $\pm 1.5 \text{ m}\cdot\text{s}^{-1}$.

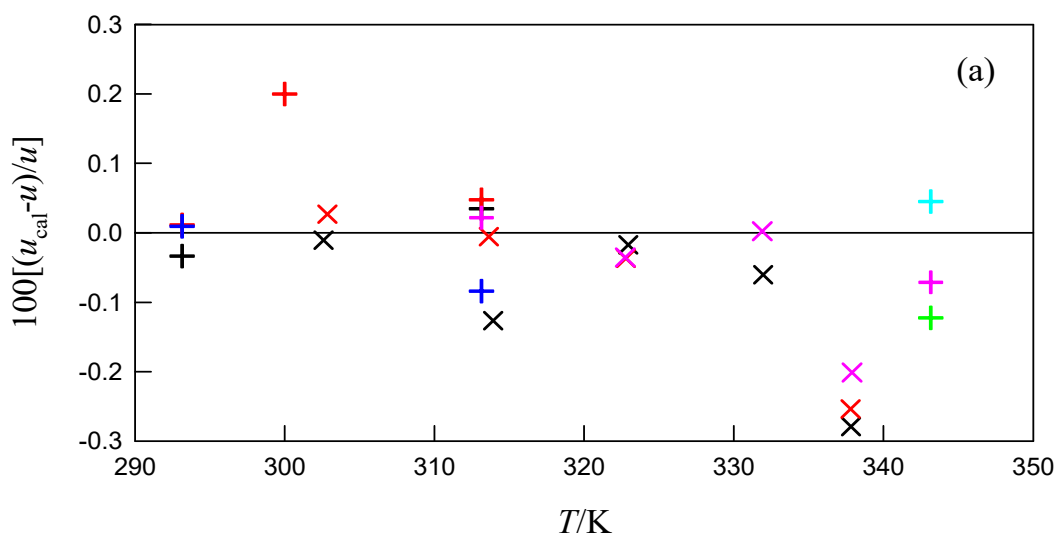


Figure 6.16. Relative deviations between calculated and experimental SOS in saturated TGs as function of temperature. Symbols (+) and (x) correspond to comparison with data from Table 6.9 and Hustad et al., respectively. Colours black, red, blue, pink, cyan and green correspond to tricaproin, tricaprylin, tricaprin, trilaurin, tripalmitin and tristearin, respectively.

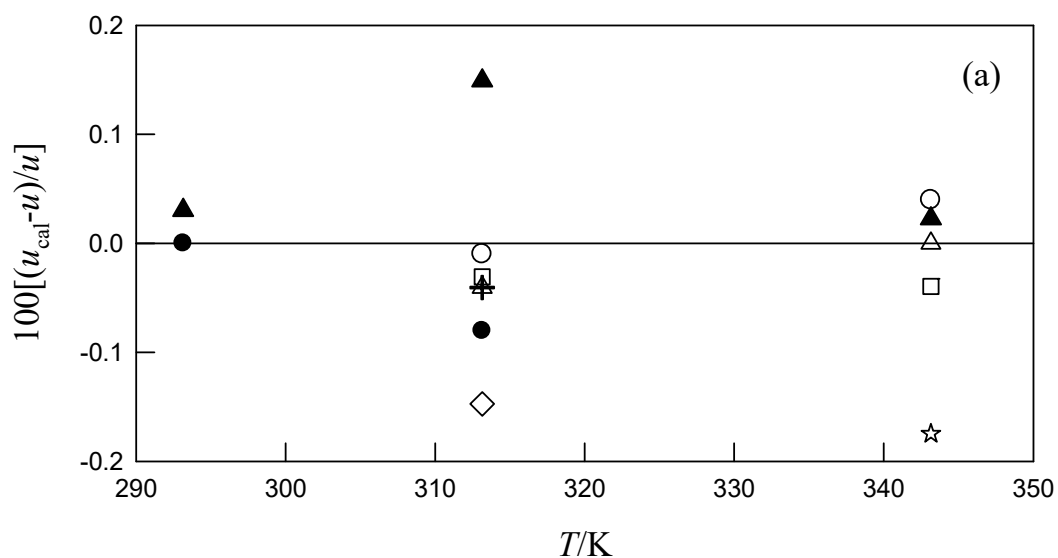


Figure 6.17. Relative deviations between calculated and experimental SOS in unsaturated TGs as function of temperature. The symbols correspond to comparison with data from Table 6.9: Δ , 1OPP; \circ , 2OPP; \square , 1POS; $+$, 1PSO; \diamond , 1OPS; \star , SOS; \blacktriangle , OOO; \bullet , LiLiLi.

6.2.3 Results and discussion

The speed of sound data measured with the methodology 1 and 2, described in experimental section are reported in Table 6.11 and Table 6.12, respectively.

Table 6.11. Speed of sound of CSO as function of temperature using method 1.

T/K	$u / (\text{m.s}^{-1})^a$	$u / (\text{m.s}^{-1})^b$	$u / (\text{m.s}^{-1})^c$	$u / (\text{m.s}^{-1})^d$	$\sigma_u / (\text{m.s}^{-1})^e$
298.15	1454.18	1455.63	1456.06	1455.29	0.99
303.15	1438.54	1439.19	1439.31	1439.01	0.42
308.15	1422.19	1422.14	1422.54	1422.29	0.22
313.15	1406.26	1406.44	1406.67	1406.46	0.20
318.15	1390.09	1390.76	1390.87	1390.57	0.42
323.15	1374.61	1374.34	1374.98	1374.64	0.33
328.15	1359.09	1359.04	1359.78	1359.30	0.41
333.15	1343.82	1343.84	1344.15	1343.94	0.19
338.15	1328.63	1328.80	1328.95	1328.79	0.16
343.15	1313.39	1314.06	1314.19	1313.88	0.43

^a, ^b, ^c are the different acquisitions. ^d, mean value of acquisitions. ^e, Standard deviation from mean of the acquisitions. Uncertainties: $u(T) = 0.01 \text{ K}$; $u_c(u)$ less than 2.3 m.s^{-1} .

Table 6.12. Speed of sound of CSO as function of temperature using method 2.

T/K	$u / (\text{m.s}^{-1})^a$	$u / (\text{m.s}^{-1})^b$	$u / (\text{m.s}^{-1})^c$	$u / (\text{m.s}^{-1})^d$	$\sigma_u / (\text{m.s}^{-1})^e$
298.15	1455.29	1456.75	1457.17	1456.40	0.99
303.15	1439.18	1439.83	1439.95	1439.65	0.42
308.15	1422.82	1422.77	1423.17	1422.92	0.22
313.15	1406.92	1407.09	1407.32	1407.11	0.20
318.15	1389.63	1390.30	1390.41	1390.11	0.42
323.15	1373.24	1372.97	1373.62	1373.27	0.33
328.15	1358.66	1358.61	1359.35	1358.87	0.41
333.15	1342.84	1342.87	1343.18	1342.96	0.19
338.15	1328.94	1329.11	1329.26	1329.10	0.16
343.15	1313.43	1314.11	1314.23	1313.92	0.43

^a, ^b, ^c are the different acquisitions. ^d, mean value of acquisitions. ^e, Standard deviation from mean of the acquisitions. Uncertainties: $u(T) = 0.01 \text{ K}$; $u_c(u)$ less than 2.0 m.s^{-1} .

From Table 6.11 and Table 6.12, the high precision of SOS data can be concluded. Low standard deviations from the mean calculated at each temperature for the three acquisitions are

obtained. The standard deviations, at each temperature, are practically the same for both methods, with differences only detectable at large decimals. The results obtained with the two methods are compared in Figure 6.18. In this figure it can be observed that the differences in the SOS are small, falling in the range $\pm 1 \text{ m}\cdot\text{s}^{-1}$ (or $\pm 0.08\%$). Therefore, the methods are consistent.

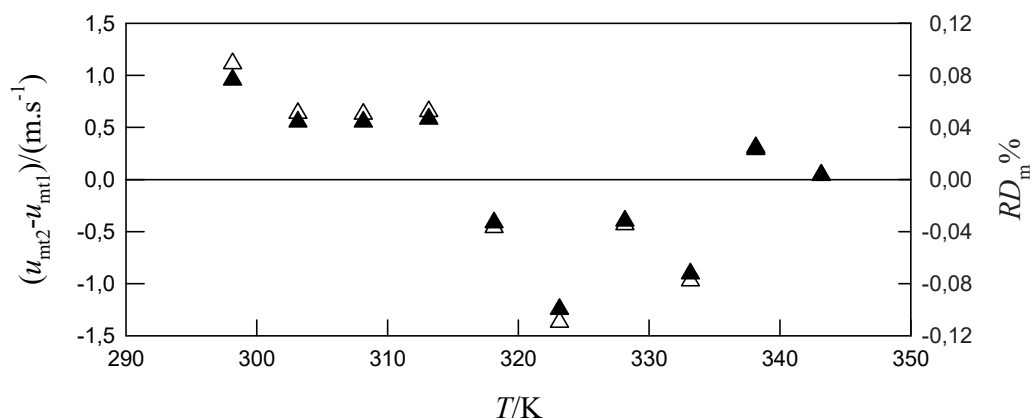


Figure 6.18. Differences between determinations of speeds of sound with methods 1 ($u_{\text{mtd}1}$) and 2 ($u_{\text{mtd}2}$). Open and full symbols correspond to absolute deviation and relative deviation, respectively.

In Figure 6.19, the experimental values obtained with method 1 are plotted as function of temperature. For method 2 data overlap with those from method 1. From Table 6.11 and Table 6.12 and from Figure 6.19, it can be concluded that the oil SOS decreases as temperature increases, which is expected for the majority of liquids.

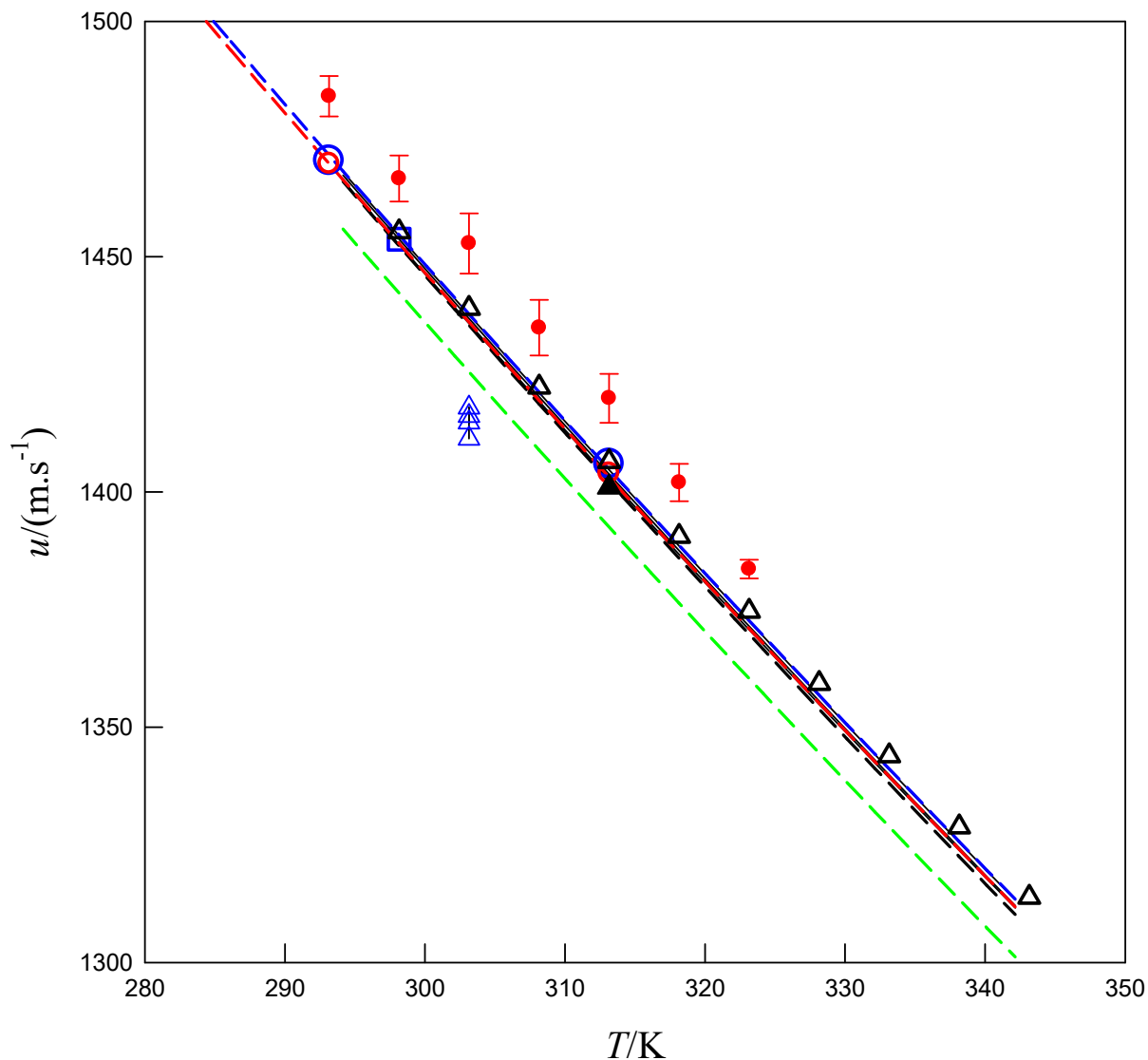


Figure 6.19. Speed of sound of CSO and other oils. CSO: Δ , This work; \blacktriangle , Gouw and Vlugter [37]; \triangle , Ali and Ali [39]. Other oils: (sunflower) \square , González et al. [40]; \circ , Javanaud and Rahalkar [41]; - - -, McClements and Povey [36]; (Soy) \bullet , Oliveira et al. [42]; \circ , Javanaud and Rahalkar [41]; - - -, McClements and Povey [36]; (Rapeseed) — , McClements and Povey [36]; (Palm) - - -, McClements and Povey [36];

The few values of speed of sound available in the literature for CSO are represented in Figure 6.19. The value reported by Gouw and Vlugter [37] at 313.15 K deviates only $5 \text{ m}\cdot\text{s}^{-1}$ (or -0.4%) of the value found in this work. Data reported by Ali and Ali measured at 303.15 K, under different frequencies, present deviations of about -2% (maximum deviation of $-28 \text{ m}\cdot\text{s}^{-1}$) relative to the corresponding value of this work. In Figure 6.19, the SOS for other vegetable oils are also

presented. The data reported by McClements and Povey [36] for sunflower, soybean, rapeseed and palm are represented. With the exception of palm oil, all other have speed of sound close to the values of this work, in the studied range of temperature. The values reported by Javanaou and Rahalkar [41], for sunflower and soy, shown the same behaviour. The values reported by Oliveira et al. [42] for soy, deviate about 1% from those given by McClements and Povey for the same kind of oil, which close match the values of Javanaou and Rahalkar.

Eqs. 6-2 and 6-30 were used to correlate the measured speed of sound data in the temperature range $T = (298.15 \text{ to } 343.15) \text{ K}$. The fitting parameters, the coefficient of determination, r^2 , standard deviation, σ , and the *AARD* are given in Table 6.13.

Table 6.13. Correlation parameter of speed of sound data, for CSO.

Polynomial equation					
$u_0 / \text{m}\cdot\text{s}^{-1}$	$u_1 / \text{m}\cdot\text{s}^{-1}\cdot\text{K}^{-1}$	$u_2 / \text{m}\cdot\text{s}^{-1}\cdot\text{K}^{-2}$	r^2	$\sigma / \text{m}\cdot\text{s}^{-1}$	<i>AARD</i>
2799.75±23.1235	-5.6957±0.1444	3.9798×10 ⁻³ ±0.0002	1.000	0.13	0.01
Rao equation					
n	$u_0 / \text{m}\cdot\text{s}^{-1}$	T_c / K	r^2	$\sigma / \text{m}\cdot\text{s}^{-1}$	<i>AARD</i>
0.9	2359.21±5.98	716.793±2.490	0.9996	0.90	0.05
11/9	2449.83±5.39	858.330±2.590	0.9998	0.69	0.04

From this table it can be seen that polynomial equation describes very well the measured (u , T) data, with coefficient of determination $r^2 = 1.000$ and low standard deviation $\sigma = 0.13$ (*AARD* = 0.01). This correlation is compared with experimental data in Figure 6.20. For the fitting of SOS with Rao equation, similar results were obtained, overlapping those of quadratic equation. The critical temperature predicted from fitting Eq. 6-30, taking n as 11/9, is comparable with the value obtained from the Guggenheim equation applied to Menzies et al. [43] surface tension data (see Table 5.5).

Equation 6-32 and the simplified form 6-33 were used to predict the speed of sound, in the studied temperature range, for CSO. In these equations, mass and volumetric fractions of triglycerides were considered for ϕ_i and the speed of sound were calculated from Eqs. 6-37 and 6-38. The densities needed in Eq. 6-32 were calculated from Zong's model [44]. It was found that both Eqs. 6-32 and 6-33 gives similar results, either using volumetric or mass fractions. The predicted ultrasonic speeds obtaining differ by no more than 0.3 $\text{m}\cdot\text{s}^{-1}$. Predictions using Eq. 6-

31, with speed of sound for TGs calculated by Eqs. 6-37 and 6-38 were also performed, giving almost the same results as Eq. 6-33. The predicted results are compared with the experimental values in Figure 6.20, corresponding to negative deviations between 0.5 and 1%, with $AARD = 0.7\%$.

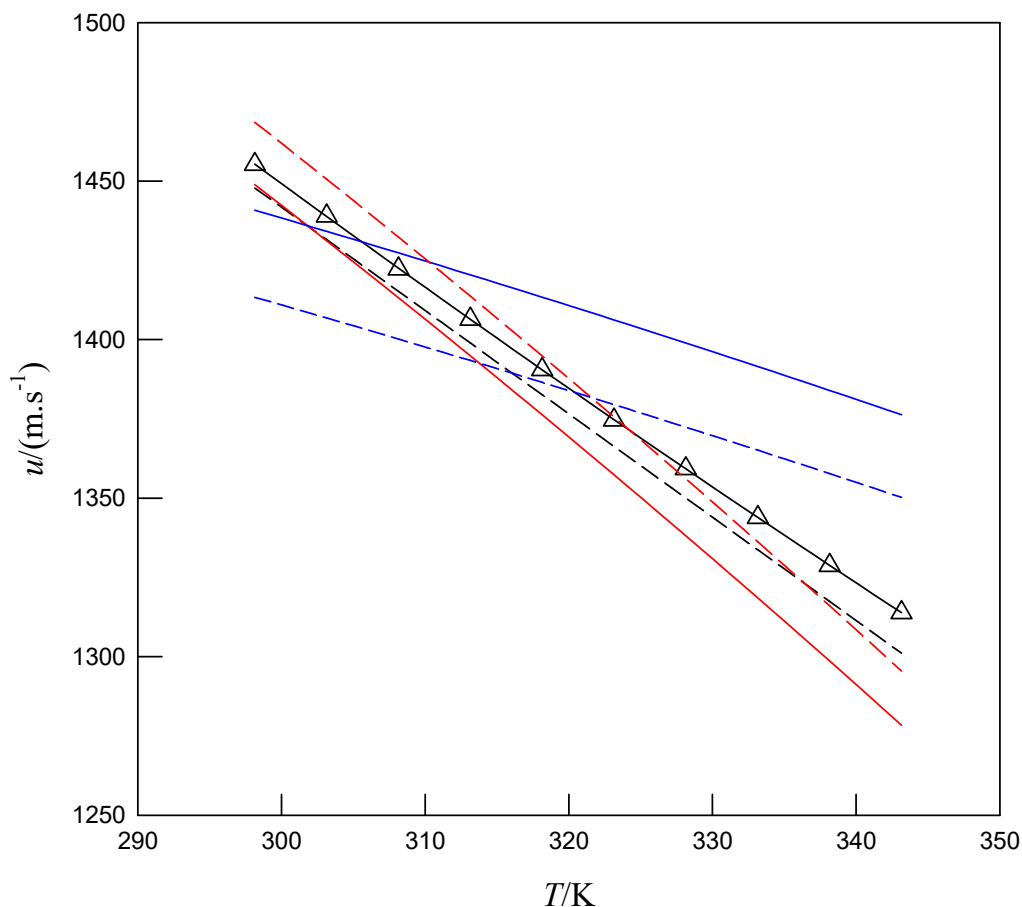


Figure 6.20. Speed of sound as function of temperature. Symbols correspond to experimental data of this work. Black full line is the correlation with quadratic equation, Eq. 6-2. Black dashed line corresponds to prediction with ideal mixture, Eq. 6-31. Prediction with Auerbach relation: —, with surface tension of this work; —, surface tension of Menzies et al. [43]. Prediction with Auerbach relation with adjusted exponent: - - -, with surface tension of this work; - - -, with surface tension of Menzies et al. [43].

6.2.3.1 Auerbach relation

The experimental values of the CSO relative to density and surface tension were presented in chapters 3 and 5, respectively. These properties and the speed of sound are related to each other by Auerbach's relation [45]:

$$u = \left(\frac{\gamma}{6.33 \times 10^{-10} \rho} \right)^c \quad \text{Eq. 6-39}$$

where u is the speed of sound in $\text{m}\cdot\text{s}^{-1}$, γ is the surface tension in $\text{N}\cdot\text{m}^{-1}$ and ρ is the density in $\text{kg}\cdot\text{m}^{-3}$ and $c = 0.6667$. Therefore, the knowledge of densities and surface tensions allows the calculation of speed of sound. For this purpose, the linear correlations of experimental surface tension data of this work and those of Menzies et al. [43] reported in Table 6.12 were used. To correlate densities, the quadratic equation:

$$\rho = 1210.00 - 1.31268T + 1.07211 \times 10^{-3}T^2 \quad \text{Eq. 6-40}$$

was obtained by fitting the experimental data of CSO, given in the Table 3.10, at $p = 0.1$ MPa. The statistical indicators for the fitting $r^2 = 1.000$ and $\sigma = 0.03 \text{ kg}\cdot\text{m}^{-3}$ gives the excellence of the correlation. In Figure 6.20, the predicted values were compared with the experimental ones and in Table 6.15 the main statistical indicators are provided. From Figure 6.20, it can be seen that using the surface tension data of this work, Auerbach's relation gives almost the same results as the ideal mixture up to ca. 305 K, but predictions diverge after this point. The obtained $AARD = 1.3\%$ and $AAD = 17.9 \text{ m}\cdot\text{s}^{-1}$ over all the range of temperature are very high. Using surface tension data of Menzies et al. [43], Auerbach's relation crosses the experimental SOS data near 305 K, but after this point diverges and abnormally high RDs are obtained, causing an $AARD = 2.2\%$ and AAD near $30 \text{ m}\cdot\text{s}^{-1}$. In order to obtain SOS values in better agreement with the experimental ones, the adjustment of exponent c was done. The values $c = 0.6679$ and $c = 0.6649$ were obtained for the surface tension of this work and for that of Menzies et al., respectively. With the adjusted exponent, the Auerbach's model with surface tension of this work crosses the SOS data at 323.15 K and RDs are in the range $\pm 1\%$, corresponding to $AARD = 0.7\%$ and $AAD = 9 \text{ m}\cdot\text{s}^{-1}$, which could be considered as reasonable predictions. However, using the surface tension data of Menzies et al., the crossing occurs at 320 K, resulting $AARD = 1.6\%$ and $AAD = 22 \text{ m}\cdot\text{s}^{-1}$, which are indicators of unsatisfactory predictions. The main conclusion that can be obtained from the use of Auerbach's relation for prediction the speed of sound of CSO is that it fails to provide a good description of the experimental data, either in its original form or by fitting the exponent. This is due to the deficient temperature dependency of the model, with strong dependency of the surface

tension slope in the temperature. This problem was already mentioned and discussed by Freitas et al. [5].

6.2.3.2 Molar compressibility

Molar compressibility, k_m , defined by Eq. 6-3, is an important parameter in the study of liquid state. In this section, the molar compressibility of CSO, calculated from densities obtained by Eq. 6-40 and experimental speed of sound was determined in the range $T = (298.15 \text{ to } 343.15) \text{ K}$ and $p = 0.1 \text{ MPa}$. The values of k_m as a function of T are presented in Table 6.14. As can be seen, k_m presents a very small temperature dependency, thus the mean value $\langle k_m \rangle$ was determined over the range of temperature variation. The mean value is $\langle k_m \rangle = (19.932 \pm 0.017) \times 10^{-3} / (\text{m}^3 \cdot \text{mol}^{-1} \cdot \text{Pa}^{1/7})$, which is about three times the value obtained for the CSB previously studied in chapter.

Table 6.14. Molar compressibility (k_m) of CSO as function of temperature. The mean molar compressibility ($\langle k_m \rangle$) taken over temperature range and corresponding standard deviation are presented.

T/K	$k_m \times 10^3 / \text{m}^3 \cdot \text{mol}^{-1} \cdot \text{Pa}^{1/7}$
298.15	19.951
303.15	19.950
308.15	19.945
313.15	19.942
318.15	19.938
323.15	19.931
328.15	19.926
333.15	19.919
338.15	19.911
343.15	19.903
$\langle k_m \rangle \times 10^3 / \text{m}^3 \cdot \text{mol}^{-1} \cdot \text{Pa}^{1/7}$	19.932 ± 0.017

Assuming that $k_m = \langle k_m \rangle$, the speed of sound can be estimated using Eq. 6-14, at the desired temperature. Using density calculated from Eq. 6-40 the speed of sound can be predicted with $AARD = 0.2\%$ and $AAD = 3.3 \text{ m} \cdot \text{s}^{-1}$. If instead of $k_m = \langle k_m \rangle$, the molar compressibility at 298.15 K, $k_{m,298} = 19.951 \times 10^{-3} \text{ m}^3 \cdot \text{mol}^{-1} \cdot \text{Pa}^{1/7}$ is used, the SOS in the entire range of temperature are predicted with $ARRD = 0.3\%$ and $AAD = 4.6 \text{ m} \cdot \text{s}^{-1}$. The statistical indicators for both situations correspond to good representations of experimental data, as can be seen in Figure 6.21. The

prediction of speed of sound, with density calculated by Zong/STGA method and considering Kay rule, $k_m = \sum_i^{TG} x_i k_{m,i}$ was also attempted. The individual molar compressibility of TGs were calculated using Eq. 6-3, with SOS of TGs predicted with correlation developed in this work (see Eqs. 6-37 and 6-38). The SOS calculated for CSO in the range $T = (298.15 \text{ to } 343.15) \text{ K}$ are also represented in Figure 6.21 and only differ 0.06% from those corresponding to the ideal mixture approach. As can be seen from Table 6.15, very close values of *AARD* and *AAD* are obtained for the two predictive methods.

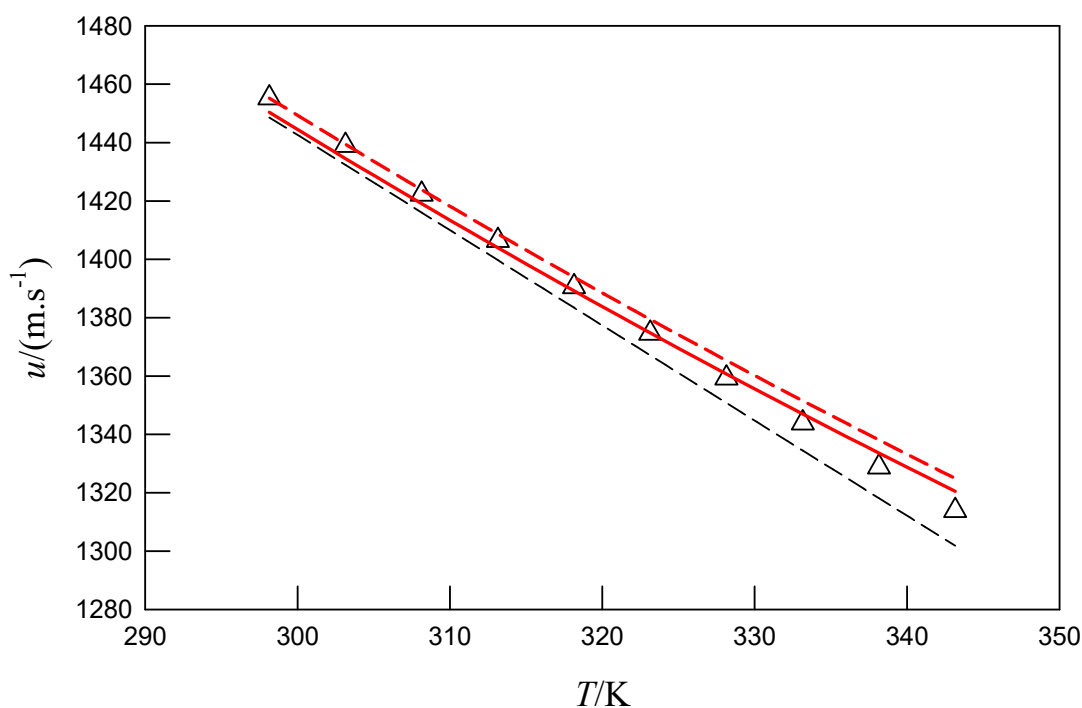


Figure 6.21. Speed of sound as function of temperature. Symbols correspond to experimental data of this work. . - - -, Zong/STGA and SOS of TGs with Eqs. 6-37 and 6-38; —, Pseudo-experimental density and $\langle k_m \rangle$; - - -, pseudo-experimental density and k_m at 298 K.

Table 6.15. Summary of results obtained with the prediction methods applied to SOS of CSO.

Method	AARD %	AAD / m.s ⁻¹	AD _{min} / m.s ⁻¹	AD _{max} / m.s ⁻¹	Comments about the method.
Wood	0.7	9.1	-7.6	-12.9	$u_{oil} = \left[\left(\sum_{i=1}^{TG} \frac{\phi_i}{u_i^2 \rho_i} \right) \left(\sum_{i=1}^{TG} \phi_i \rho_i \right) \right]^{-1/2}$ u_i calculated from Eq. 6-36 and density from Zong model.
Wood	0.7	8.9	-7.4	-12.7	$u_{oil} = \left[\sum_{i=1}^{TG} \frac{\phi_i}{u_i^2} \right]^{-1/2}$ u_i calculated from Eq. 6-36.
Kay rule	0.7	9.0	-7.1	-12.8	$u_{oil} = \sum_i^{TG} x_i u_i$; with u_i calculated from Eq. 6-36.
Ideal mix			at 308 K	at 343 K	
Auerbach	1.3	17.9	-6.4	-35.5	$u = \left(\frac{\gamma}{6.33 \times 10^{-10} \rho} \right)^c$ (Eq. 6-39) $c = 0.6667$; surface tension of this work and density from Eq. 6-40.
Auerbach	2.2	29.8	-4.9	62.4	Eq. 6-39, $c = 0.6667$; surface tension of Menzies et al. and density from Eq. 6-40.
Auerbach	0.7	9.0	1.0	-18.5	Eq. 6-39, $c = 0.6679$; surface tension of this work and density from Eq. 6-40.
Auerbach	1.6	21.8	-4.1	36.3000	Eq. 6-39, $c = 0.6649$; surface tension of Menzies et al. and density from Eq. 6-40.
$\langle k_m \rangle$	0.2	3.3	0.1	6.6	$u = \left(\frac{\langle k_m \rangle}{M} \right)^{7/2} \rho^3$ Density calculated from Eq. 6-40.
$k_{m,298}$	0.3	4.6	-0.1	11.1	$u = \left(\frac{k_{m,298}}{M} \right)^{7/2} \rho^3$ Density calculated from Eq. 6-40.
k_m / Kay	0.6	8.2	-6.7	-12.1	$u = \left(\frac{k_m}{M} \right)^{7/2} \rho^3$ and $k_m = \sum_i^{TG} x_i k_{m,i}$; In $k_{m,i}$ density of TGs calculated from STGA/Zong and u_i from Eq. 6-36.

6.2.4 Conclusion

Speed of sound of cottonseed oil was measured at atmospheric pressure and temperatures range between 298.15 and 343.15 K. The experimental data were well represented by a polynomial quadratic equation, obtaining coefficient of determination $r^2 = 1.000$ and low standard deviation $\sigma = 0.1294$ ($AARD = 0.006\%$). Given the scarcity of experimental data for SOS of individual TG, a general equation for prediction of speed of sound in the temperature range of 293K to 343 K, for any triglyceride, including isomers, was developed. The obtained RDs are usually in the range of $\pm 0.1\%$, corresponding to absolute deviations of $\pm 1.5 \text{ m}\cdot\text{s}^{-1}$, which is almost the value of the experimental uncertainty. This new correlation was used to estimate the speed of sound of CSO from the ideal mixture and from Wood equation. The predicted SOS with both methods, using densities calculated from Zong/STGA model, give similar results, being the $AARD = 0.7\%$ (RDs between 0.5 and 1%). The molar compressibility at 298.15 K was used to predict SOS, in the entire range of temperature, allowing obtaining good results, corresponding to $AARD = 0.3\%$. Regarding Auerbach's prediction method, reasonable results were only obtained when adjusted exponent is used and with the surface tension data of this work.

6.3 References

1. Pogorevc P, Kegl B, Skerget L. Diesel and biodiesel fuel spray simulations. *Energy & Fuels*. 2008;22(2):1266-74.
2. Tat ME, Van Gerpen JH. Measurement of biodiesel speed of sound and its impact on injection timing: Citeseer; 2003.
3. Gouw T, Vlugter J. Physical properties of fatty acid methyl esters. IV. Ultrasonic sound velocity. *Journal of the American Oil Chemists' Society*. 1964;41(8):524.
4. Tat ME, Van Gerpen JH. Speed of sound and isentropic bulk modulus of alkyl monoesters at elevated temperatures and pressures. *Journal of the American Oil Chemists' Society*. 2003;80(12):1249-56.
5. Freitas SV, Paredes ML, Daridon J-L, Lima ÁS, Coutinho JA. Measurement and prediction of the speed of sound of biodiesel fuels. *Fuel*. 2013;103:1018-22.

6. Daridon J-L, Coutinho JA, Paredes ML. Novel data and a group contribution method for the prediction of the speed of sound and isentropic compressibility of pure fatty acids methyl and ethyl esters. *Fuel*. 2013;105:466-70.
7. Ndiaye EHI, Habrioux M, Coutinho JAP, Paredes MLL, Daridon JL. Speed of Sound, Density, and Derivative Properties of Ethyl Myristate, Methyl Myristate, and Methyl Palmitate under High Pressure. *Journal of Chemical & Engineering Data*. 2013;58(5):1371-7.
8. Ott LS, Huber ML, Bruno TJ. Density and speed of sound measurements on five fatty acid methyl esters at 83 kPa and temperatures from (278.15 to 338.15) K. *Journal of Chemical & Engineering Data*. 2008;53(10):2412-6.
9. Freitas SV, Cunha DL, Reis RA, Lima ALS, Daridon J-L, Coutinho JoA, et al. Application of Wada's group contribution method to the prediction of the speed of sound of biodiesel. *Energy & Fuels*. 2013;27(3):1365-70.
10. Huber ML, Lemmon EW, Kazakov A, Ott LS, Bruno TJ. Model for the thermodynamic properties of a biodiesel fuel. *Energy & Fuels*. 2009;23(7):3790-7.
11. Payri R, Salvador F, Gimeno J, Bracho G. The effect of temperature and pressure on thermodynamic properties of diesel and biodiesel fuels. *Fuel*. 2011;90(3):1172-80.
12. Nikolić BD, Kegl B, Marković SD, Mitrović MS. Determining the speed of sound, density and bulk modulus of rapeseed oil, biodiesel and diesel fuel. *Thermal Science*. 2012;16(suppl. 2):505-14.
13. Wadumesthrige K, Smith JC, Wilson JR, Salley SO, Ng KS. Investigation of the parameters affecting the cetane number of biodiesel. *Journal of the American Oil Chemists' Society*. 2008;85(11):1073-81.
14. Ramírez-Verduzco LF, Rodríguez-Rodríguez JE, del Rayo Jaramillo-Jacob A. Predicting cetane number, kinematic viscosity, density and higher heating value of biodiesel from its fatty acid methyl ester composition. *Fuel*. 2012;91(1):102-11.
15. Kinast JA. Production of biodiesels from multiple feedstocks and properties of biodiesels and biodiesel/diesel blends: National Renewable Energy Laboratory USA; 2003.
16. Canakci M, Van Gerpen JH. Comparison of engine performance and emissions for petroleum diesel fuel, yellow grease biodiesel, and soybean oil biodiesel. *Transactions of the ASAE*. 2003;46(4):937.

17. NIST. Thermophysical properties of fluids. Accessed in May 2013. Available from: <http://webbook.nist.gov/chemistry/fluid/>.
18. Fortin TJ, Laesecke A, Freund M, Outcalt S. Advanced calibration, adjustment, and operation of a density and sound speed analyzer. *The Journal of Chemical Thermodynamics*. 2013;57:276-85.
19. Zorębski E, Dzida M. The effect of temperature and pressure on acoustic and thermodynamic properties of 1, 4-butanediol. The comparison with 1, 2-, and 1, 3-butanediols. *The Journal of Chemical Thermodynamics*. 2012;54:100-7.
20. Knothe G, Dunn RO. A comprehensive evaluation of the melting points of fatty acids and esters determined by differential scanning calorimetry. *Journal of the American Oil Chemists' Society*. 2009;86(9):843-56.
21. Wada Y. On the relation between compressibility and molal volume of organic liquids. *Journal of the Physical Society of Japan*. 1949;4(4-6):280-3.
22. Mathur S, Gupta P, Sinha S. Theoretical derivation of Wada's and Rao's relations. *Journal of Physics A: General Physics*. 1971;4(3):434.
23. Pratas MJ, Freitas SV, Oliveira MB, Monteiro SC, Lima AS, Coutinho JA. Biodiesel density: Experimental measurements and prediction models. *Energy & Fuels*. 2011;25(5):2333-40.
24. Pratas MJ, Freitas S, Oliveira MB, Monteiro SC, Lima AS, Coutinho JA. Densities and viscosities of fatty acid methyl and ethyl esters. *Journal of Chemical & Engineering Data*. 2010;55(9):3983-90.
25. Pratas MJ, Freitas S, Oliveira MB, Monteiro SC, Lima AS, Coutinho JA. Densities and viscosities of minority fatty acid methyl and ethyl esters present in biodiesel. *Journal of Chemical & Engineering Data*. 2011;56(5):2175-80.
26. Van Dael W, Vangeel E. *Proceedings of the first international conference on calorimetry and Thermodynamics*. Warsaw; 1969.
27. Nomoto O. Empirical formula for sound velocity in liquid mixtures. *Journal of the Physical Society of Japan*. 1958;13(12):1528-32.
28. Rao MR. The adiabatic compressibility of liquids. *The Journal of Chemical Physics*. 1946;14(11):699-.

29. Jacobson B. Ultrasonic velocity in liquids and liquid mixtures. *The Journal of Chemical Physics*. 1952;20(5):927-8.
30. Schaaffs W. *Molekularakustik*. . 1st ed. Verlag, Berlin: Springer; 1963. 852- p.
31. Nutsch-Kuhnkie R. Sound characteristics in binary mixtures and solutions. *Acustica*. 1965;15(1):383.
32. Junjie Z. *J China Univ Sci Tech* 1984(14):298-300.
33. Rao MR. Velocity of sound in liquids and chemical constitution. *The Journal of Chemical Physics*. 1941;9(9):682-5.
34. Guggenheim EA. The principle of corresponding states. *The Journal of Chemical Physics*. 1945;13(7):253-61.
35. Wood AB. *A textbook of sound: being an account of the physics of vibrations with special reference to recent theoretical and technical developments*: G. Bell; 1955.
36. McClements D, Povey M. Ultrasonic velocity measurements in some liquid triglycerides and vegetable oils. *Journal of the American Oil Chemists' Society*. 1988;65(11):1787-90.
37. Gouw I, Vlugter I. Physical properties of triglycerides III: ultrasonic sound velocity. *Fette, Seifen, Anstrichmittel*. 1967;69(3):159-64.
38. Hustad G, Richardson T, Winder W, Dean M. Acoustic properties of some lipids. *Chemistry and Physics of Lipids*. 1971;7(1-2):61-74.
39. Ali SM, Ali B. Velocity of ultrasoudn in commonly used vegetable oils at low frequencies. *International Journal of Science, Enviroment and Technology*. 2014;3(5):1803-09.
40. González C, Resa JM, Lanz J, Fanega MA. Speed of sound and isentropic compressibility of organic solvents+ sunflower oil mixtures at 298.15 K. *Journal of the American Oil Chemists' Society*. 2002;79(6):543-8.
41. Javanaud C, Rahalkar R. Velocity of sound in vegetable oils. *European Journal of Lipid Science and Technlogy*. 1988;90(2):73-5.
42. Oliveira PA, Silva RdMB, Morais GCd, Alvarenga AV, Costa-Félix R, editors. *Speed of sound as a function of temperature for ultrasonic propagation in soybean oil*. *Journal of Physics: Conference Series*; 2016: IOP Publishing.
43. Menzies AWCK, W. G.; Bingham, e. C. *Cutting fluids*1922;193;247-9.

44. Zong L, Ramanathan S, Chen C-C. Fragment-based approach for estimating thermophysical properties of fats and vegetable oils for modeling biodiesel production processes. *Industrial & engineering chemistry research*. 2009;49(2):876-86.
45. Auerbach N. *Experientia*. 1948;12(4):473-4.

7 CHAPTER

MONITORING OF THE TRANSESTERIFICATION REACTION

In this chapter, the transesterification of cottonseed oil at 323.15 K and 343.15 K, with methanol/oil molar ratios of 4.5, 6.0 and 7.5 were carried out and the oil conversion as a function of reaction time was evaluated by ^1H NMR. The density of the reaction mixture, at these experimental conditions, was measured as a function of the reaction time by an off-line methodology. From the density-time and FAMES conversion-time profiles an operative relationship between conversions, densities, alcohol to oil ratio and temperature was established.

7.1 Introduction

Biodiesel is a biofuel used in compression ignition engines that can be produced from different types of oilseeds, animal fats or waste oils. The success of introducing biodiesel into the market is mainly due to the efficient standardization as consequence of the wide variety of raw materials that can be used in production. The continuously monitoring of transesterification reaction in industrial production is of high relevance in order to avoid operational problems, eliminate batch sampling and analysis delay and guarantee the quality of the final product through a process control system. Also it is essential for kinetic studies. An appreciable number of analytical procedures have been developed to assess the quality of biodiesel in terms of the specified standards. However, due to the rapid conversion of methanolysis reaction, most of the analytical techniques are not suitable for on-line monitoring of the process. For this purpose, analytical methods based on easily measurable physical properties such as the refractive index, viscosity, density and speed of sound are preferred.

Regarding to the analytical procedures for the quality control of biodiesel, chromatographic techniques (GC and HPLC) were and still are the most used methods, due to their high sensitivity and ability to detect low levels of possible contaminants. Gas chromatography (GC) is the established method in most standards, and protocols are available for the characterization of individual FAMES, FFAs, glycerides (mono-, di- and tri-) as well as free glycerol in biodiesels obtained through transesterification processes with methanol. However, this method has the disadvantages that it requires sample preparation and derivatization, calibrations and long time analysis. HPLC is less employed than GC, in spite of analysis time is shorter and sample derivatization is not needed. Also, inexpensive methods based on thin layer chromatography (TLC) have been used to determine the main categories of compounds present in the reaction [1]. However, these methods show lower accuracy and are sensitive to humidity, so that the analysis is only qualitative [1, 2]. An exception is the method developed by Chattopadhyay et al. which allows the accurate quantification of FAMES, MG, DG and TG, as well as free fatty acids using high performance thin layer chromatography (HPTLC) [3]. Additionally, gel permeation chromatography (GPC) and size exclusion chromatography (SEC) have been developed, allowing the simultaneous analysis of FAMES, total glycerides and glycerol, but do not the individual characterization of compounds within each category [4-6]. All these chromatographic techniques

require sampling of the reaction mixture and then off-line sample analysis, so that suffer from the defect of not allowing convenient monitoring of the transesterification process in real time.

Other fast-growing techniques used for both, the monitoring of the transesterification reaction and the evaluation of biodiesel quality are ^1H -proton nuclear magnetic resonance (^1H NMR) and infrared (IR) spectroscopy. ^1H NMR was used first by Gelbard et al. for monitoring the yield of transesterification reaction with methanol [7]. Also, Neto et al. used the same technique to monitor the ethanolysis of soybean, as well as to quantify the content of ethyl ester in mixtures of soybean oil and its biodiesel [8]. Different authors have been used the ^1H NMR technique for the amount of methyl esters, free fatty acids, free glycerine, glycerides and the average degree of fatty acid unsaturation [9-12]. Also, for on-line monitoring the transesterification reaction, a fast, portable and inexpensive unilateral NMR technique have been developed by Cabeça et al. [13] and more recently, a compact ^1H NMR spectroscopy was used by Killner [14]. Nuclear magnetic resonance (NMR) spectroscopy is an excellent technique, quicker and simpler than GC and HPLC. Moreover, a small amount of sample is required and it could be analyzed without a pre-purification process [8], but the instrumentation and maintenance costs are relatively high.

The NIR method could be used to monitor the transesterification reaction as well as to ensure the biodiesel quality when employed with other analytical techniques. The reasons underlying this interest are the operational ease, quickly, accuracy and reliability of measurements, as well as the possibility of easy adaptation of online monitoring techniques (e.g. using fiber-optic probes) This has been done by Knothe, who developed a fiber-optic near infrared (NIR) method to monitor the methanolysis of soybean oil, based on the differences in the NIR spectra at 6005 and 4425-4430 cm^{-1} , where FAs display peaks and TGs exhibit shoulders, and the results were correlated with ^1H NMR spectroscopy [15]. Also, Richard et al. used NIR spectroscopy and a multivariate approach to monitor the ethanolysis of sunflower oil, through sequential scans of the reaction medium with a probe in a batch reactor without collecting and preparing samples. To calibrate the NIR analytical method, gas chromatography-flame ionization detection was used as a reference method [16]. Another work [17] reports a near infrared calibration models to predict FAMES yield, MG, DG, TG, free and total glycerol during biodiesel production. In addition, NIR and visible spectroscopy allow to determine traces of alcohol and glycerol in the biodiesel produced [18]. FT-IR and FT-Raman can also be used to monitor and quantify the transesterification reaction [19-21].

All these analytical procedures although of high accuracy, are impractical, time-consuming and requiring instrumentation not available in all standard laboratories. For this reason, alternative reaction monitoring techniques readily adaptable to the industrial production have been studied.

As mentioned before, most of these analytical methods are not applicable to consecutive determinations in small time intervals due to inherent limitations of the technique, which means that the monitoring of the transesterification process is not carried out in real time. In other cases, the difficulty for the industrial implementation is that expensive equipment and qualified personnel to acquire data and interpret the results are required.

Some physical properties, such as the refractive index, viscosity, density and speed of sound, vary significantly for the main components of biodiesel (TG, Me, FAME and Gly) and considerable changes of these properties take place during the transesterification reaction due to the concentration of species variation. This situation makes it possible to monitor the reaction, as evidenced by the growing number of studies in this field. Previous studies refer the use of viscosity [22], refractive index [23, 24], acoustic techniques [23], pH [25] and impedance measurements [26] used for real-time monitoring. Also, a methodology using calibration curves for density, refractive index and viscosity of biodiesel was used to determine the composition in TGs and FAMEs [27]. Recently, an off-line monitoring of transesterification reaction was made through density variations measured by using an electronic analytical balance [28].

The main goal of this chapter is to study a simple, cheap and easy monitoring methodology based on the measurements of the density variations of the reaction medium during the course of the transesterification reaction, with emphasis on real-time applications.

7.2 Experimental part

7.2.1 Materials

The detailed specifications of all materials used in the transesterification reaction were summarized in Table 3.1. Also, deuterated chloroform 99.8% D, containing 1% (v/v) of TMS, from sigma-Aldrich was used in the sample preparation for ^1H NMR analysis.

7.2.2 *Transesterification reaction*

The transesterification of cottonseed oil was carried out in a 50 ml three-necked double wall jacketed reactor. A reflux condenser was placed in the central neck of the reactor to avoid methanol losses, one of the side necks was equipped with a stopper to feed reagents and for sampling and the other was provided with a digital thermometer (ERTCO-EUTECHNICS Model 4400 Digital thermometer certified in the ITS 90 with accuracy of 0.01K) and tubes for circulation of the reaction mixture through the densimeter. The tubes were isolated thermally by using isolating foam and a peristaltic pump was used. The reaction vessel was initially charged with a known amount of CSO and heated to the desired temperature. Solution of 0.5% *wt* (based on oil) of sodium methoxide in methanol was prepared and fed to the reactor for transesterification of the previously heated oil. After that, the reactor was air tight closed and the temperature maintained constant by circulating hot water through the vessel jacket. For this purpose a thermostatic bath Grant Y14 was used. After 90 minutes of reaction, the heating and stirring were stopped and the products transferred to a sedimentation funnel. The ester layer containing mainly FAMEs and the glycerol layer containing mainly glycerol and methanol were separated. The biodiesel was washed and dried as specified in Section 3.1.2.2.

7.2.3 *Density monitoring*

The biodiesel production was monitored using an Anton Parr DMA 60 vibrating tube densimeter with a DMA measurement cell 512P. The assembly for the monitoring process is presented in Figure 7.1.

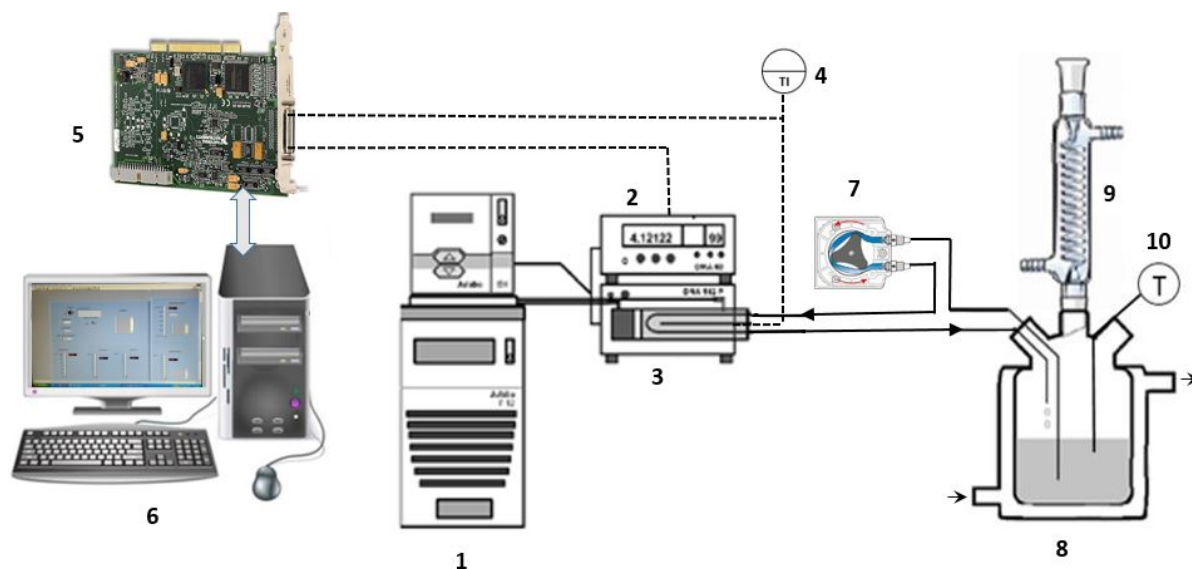


Figure 7.1. Assembly for the monitoring of the transesterification reaction by the density variation. 1-Julabo F12-ED thermostatic bath; 2-DMA 60 (Anton Paar) device for measuring the period of oscillation; 3-Measuring cell DMA 512P (Anton Paar); 4-PT probe; 5-NI PCI-6220 data acquisition board; 6-PC; 7-Peristaltic pump; 8-Reaction vessel; 9-Condenser; 10-Digital thermometer (EUTHECNICS 4400).

The reaction mixture is circulated through the 512 P cell so that the density is measured continuously and in real time under the same pressure and temperature conditions at which the reaction occurs. The transesterification reaction was carried out at atmospheric pressure, two temperatures (323.15 and 343.15) K and three methanol/oil molar ratios (4.5: 1, 6: 1 and 7.5: 1). For each reaction condition a minimum of three replicates were performed.

The temperature in the vibrating tube cell was measured with a platinum resistance probe (PT100). A Julabo F12-ED thermostatic bath with ethylene glycol was used as circulating fluid in the thermostat circuit of the measuring cell and the temperature was held constant to 0.01 K. The measuring setup and the calibration of the vibrating tube densimeter were described in Section 3.1.2.4.

7.2.4 ^1H NMR analysis

Reaction conversions were determined by ^1H NMR at different times, during the course of the reaction. From the reaction mixture, a sample of 15mg were collected and dissolved in 600 μl of deuterated chloroform (CDCl_3). To ensure that the reaction did not continue, the vials containing the sample were placed in an ice bath. Tetramethylsilane was used as an internal chemical shift

standard. The ^1H NMR spectra data were recorded using on a Bruker Avance III, operating at 400 MHz at 298.2 K. The spectrum was acquired by using (4, 8 or 16) data point (number of scans), spectral width 8417.5, acquisition time 9s, relaxation delay 1s. Data were processed using MestReNova software (10.0.0).

7.3 Results and discussion

7.3.1 Determination of cottonseed oil conversion to biodiesel

Understanding the resonance shift in the ^1H NMR spectra of reagents and products is crucial for quantification of the reaction progress. The assignments of chemical shifts of protons for glycerides and for methyl esters are summarized in Figure 7.2.

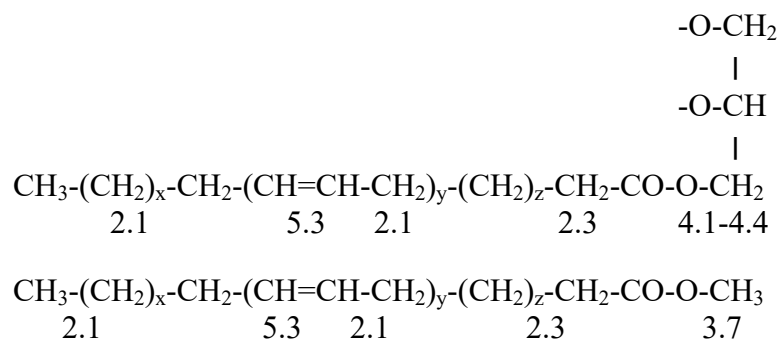


Figure 7.2. Chemical shifts of protons for glycerides and for methyl esters.

Different methods have been developed for quantification of methyl and ethyl esters from transesterification of oils. Gelbard et al. [7] developed a method that allows the direct quantification of the methyl esters present in the mixture reaction, with an error of 2% using the integration values of the signal corresponding to the methoxy groups in the methyl ester (singlet at approximately 3.67 ppm) and the signal corresponding to the α -carbonyl methylene groups (triplet at approximately 2.3 ppm) present in all fatty acid derivatives. The yield for transesterification was obtained by,

$$\%C_{ME} = \frac{2A_{ME}}{3A_{\alpha-CH_2}} 100 \quad \text{Eq. 7-1}$$

where $\%C_{ME}$ is the conversion of oil to FAME, A_{ME} is the area of the ester signal at 3.67ppm and $A_{\alpha-CH_2}$ is the area of the α -carbonyl hydrogens, at 2.33ppm. The coefficients used in the equation correspond to the number of hydrogen atoms present in the ester molecule, i.e., two α -carbonyl hydrogens and three methoxylic hydrogens.

Another NMR signal-based approach, developed by Knothe, involves the use of the integration values of the glyceride protons of the oil (4.10 - 4.35 ppm) and the methoxylic group signal at 3.67 ppm. The conversion of the vegetable oil in biodiesel is calculated from the following equation [15],

$$\%C_{ME} = \frac{5A_{ME}}{5A_{ME}+9A_{TG}} 100 \quad \text{Eq. 7-2}$$

where A_{TG} is the integration value of the signal at (4.10 - 4.35 ppm). Factors 5 and 9 in Eq. 7.2 result from the fact that the glycerol moiety of a triglyceride has 5 protons and the three methyl ester molecules produced from a triglyceride molecule have 9 protons. However, only protons sn-1 and sn-3 of the glyceride moiety (see Figure 2.3) have signals in the region (4.10 - 4.35 ppm), since the sn-2 proton appears at a lower field, approximately at 5.2 ppm. Because of this, Morgenstern et al. [12] have proposed to correct the equation by using a factor of 4, instead of 5. This equation was used by Cabeça et al. [13] in the form,

$$\%C_{ME} = \frac{2A_{ME}}{2A_{ME}+9A_{TG}} * 100 \quad \text{Eq. 7-3}$$

were the factor 2 corresponds to the hydrogen atoms of the signal between 4.25 and 4.35 (two glyceridic protons) and the factor 9 correspond to the methoxylic hydrogens of three molecules of ester produced from an oil molecule.

The NMR spectra obtained from CSO and a sample took from the reaction mixture are shown in Figure 7.3(a) and Figure 7.3(b). Figure 7.3(a) shows the presence of peaks associated with triglyceride hydrogen atoms between 4.10 and 4.35 ppm and the subsequent disappearance

(Figure 7.3(b)) with the consequent increase of the 3.67 peak corresponding to the hydrogen of the methyl group of fatty acid esters formed.

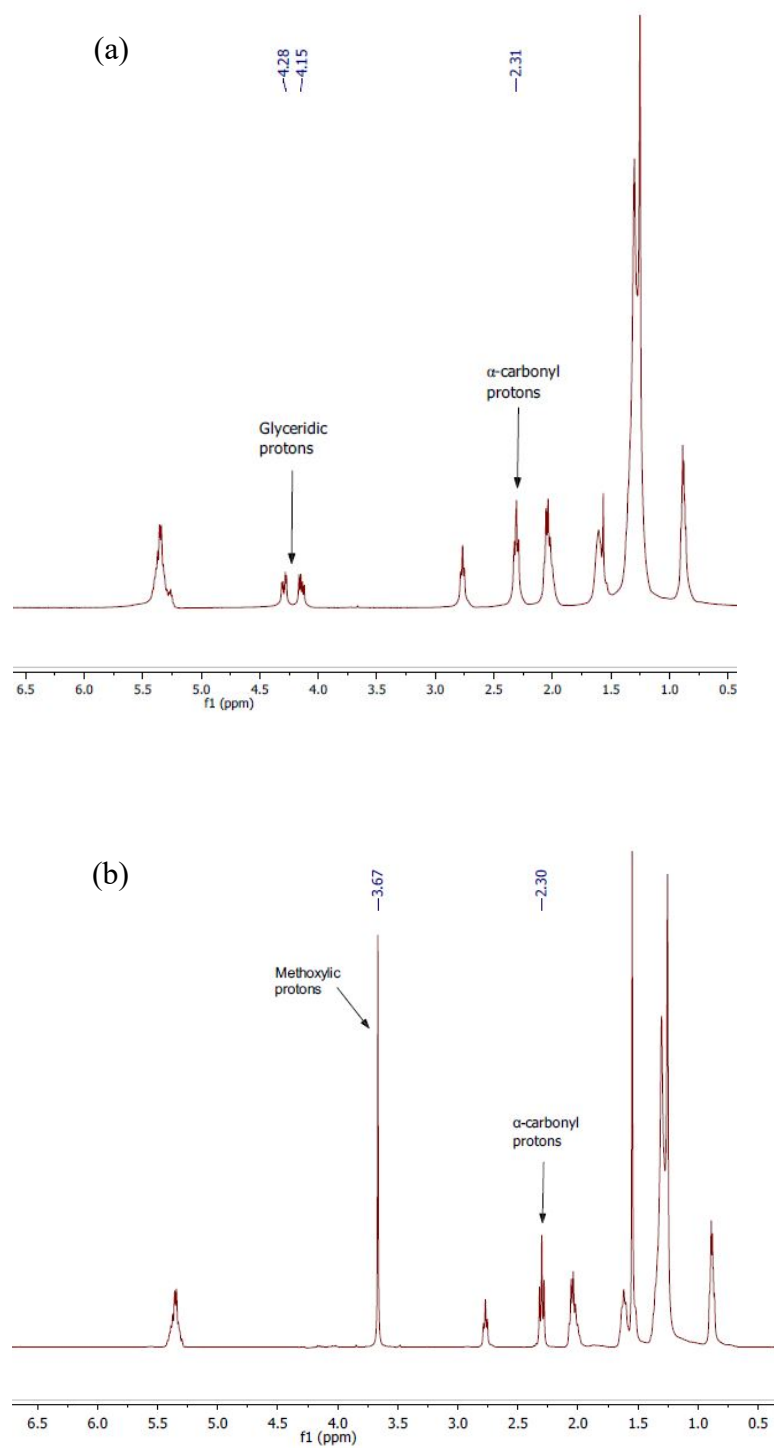


Figure 7.3. ^1H NMR spectra of CSO (a) and sample removed from the mixture of transesterification reaction (b).

The progress of a transesterification reaction is depicted in the Figure 7.4. As can be seen, the spectra of samples collecting at different time clearly show the decrease of the oil signal at 4.05 - 4.35 ppm and the increase of the ester signal at 3.67 ppm. The signal at 2.33 corresponding to the α -carbonyl group remains constant.

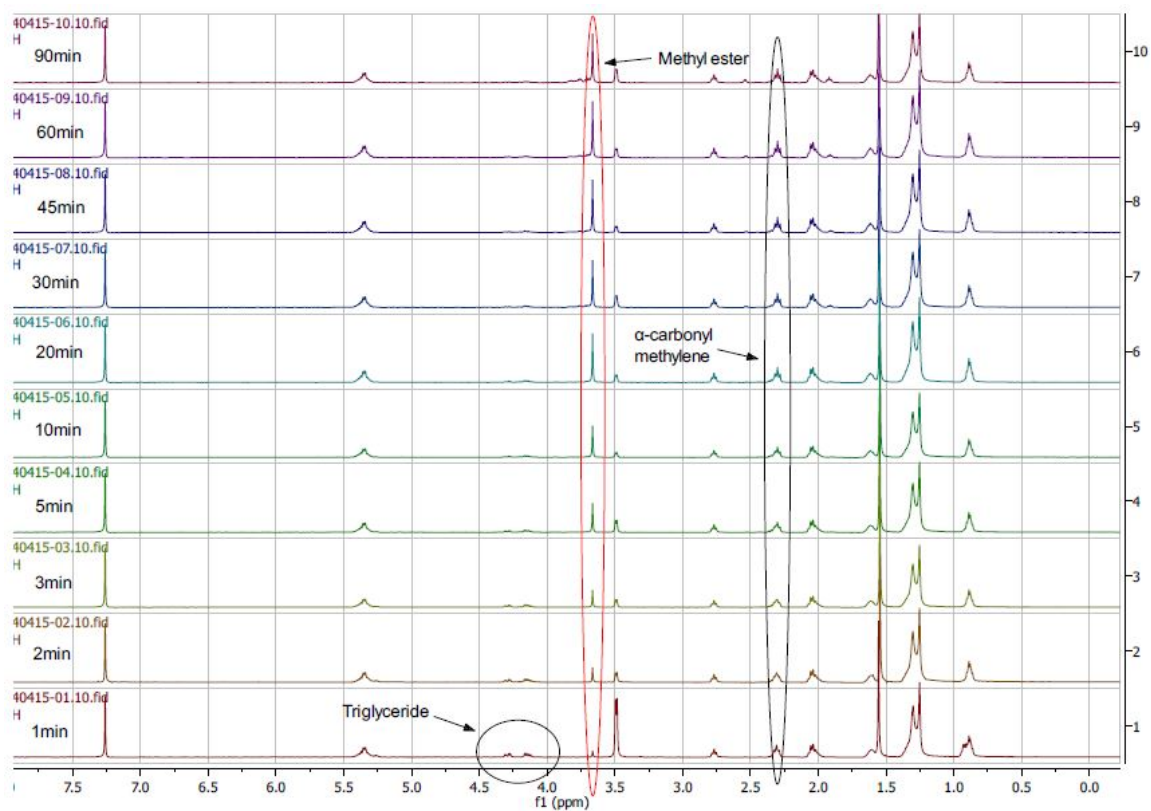


Figure 7.4. ¹H NMR spectra of samples removed from the transesterification reaction at different times. Reaction conditions: $r = 4.5$ and $T = 323.15$ K.

The Gelbard method was chosen to calculate the FAME conversion from the oil, due to the deficiency discussed before, presented by the other methods. The integration of signal at 4.10-4.35 ppm became somewhat uncertain with the progress of the reaction and progressively more difficult to access (see Figure 7.4). The conversions of oil to FAMEs, obtained by Eq. 7-1 are presented in Table 7.1 for all the experiences.

Table 7.1. Conversions of CSO to FAMES (%C) calculated by Gelbard et al. method [7], for all the experiences.

323.15 K												
r = 4.5				r = 6.0				r = 7.5				
t/min	%C ₁	%C ₂	%C ₃	t/min	%C ₁	%C ₂	t/min	%C ₁	t/min	%C ₂	t/min	%C ₃
0.0	0.0	0.0	0.0	0.0	0.0	0.0	0.0	0.0	0.0	0.0	0.0	0.0
1.0	9.3	3.8	9.3	1.0	5.7	3.2	1.0	3.4	1.0	-	1.0	7.1
2.0	22.9	12.9	34.3	2.0	16.8	10.7	2.0	6.8	2.0	18.6	2.0	11.8
3.0	30.1	25.7	54.2	3.0	36.9	22.1	3.0	13.2	3.0	21.6	3.0	30.8
5.0	44.8	40.9	63.6	5.0	60.7	36.9	5.0	23.4	5.0	44.4	5.0	49.3
10.0	63.1	61.2	77.1	10.0	69.4	56.8	10.0	55.1	11.0	73.9	10.0	71.2
20.0	70.1	70.6	82.4	20.0	78.8	66.4	20.0	73.1	20.0	82.8	20.0	79.8
30.0	73.6	67.8	86.9	30.0	82.6	72.7	30.0	72.6	30.0	90.6	30.0	85.0
45.0	79.7	72.4	87.4	45.0	92.6	73.3	45.0	84.0	45.0	90.8	45.0	90.8
60.0	83.0	80.7	84.2	60.0	89.0	80.3	60.0	85.4	60.0	92.8	60.0	89.9
90.0	84.7	85.7	90.2	90.0	93.8	82.0	90.0	87.3	90.0	91.3	90.0	90.2
343.15 K												
r = 4.5			r = 6.0			r = 7.5						
t/min	%C ₁	%C ₂	t/min	%C ₁	%C ₂	t/min	%C ₁	%C ₂	%C ₃			
0.0	0.0	0.0	0.0	0.0	0.0	0.0	0.0	0.0	0.0			
1.0	33.2	32.9	1.0	21.2	30.4	1.0	8.1	34.3	18.3			
2.0	60.8	63.0	2.0	62.1	61.6	2.0	34.4	64.6	62.8			
3.0	60.0	67.6	3.0	61.8	71.8	3.0	60.6	75.1	83.9			
5.0	63.0	68.9	5.0	67.4	74.4	5.0	73.8	89.6	87.9			
10.0	67.9	107.6	10.0	72.0	83.4	10.0	84.6	94.7	92.3			
20.0	68.6	-	20.0	87.3	90.1	20.0	91.8	95.9	90.7			
30.0	77.4	94.8	30.0	82.2	91.0	30.0	93.6	91.3	96.2			
45.0	79.3	100.2	45.0	91.2	91.2	45.0	90.0	92.6	95.7			
60.0	82.2	91.8	60.0	90.3	92.1	60.0	-	94.9	95.3			
90.0	-	91.0	90.0	93.4	93.7	90.0	90.3	94.9	94.9			

As was previously mentioned, the methanolysis is an equilibrium reaction in which an excess of alcohol is required for successful completion of reaction. In this work, molar ratios of methanol-to-oil $r = 4.5:1$, $6:1$ and $7.5:1$ were used. After a carefully selection of data made for future applications, the yield of methyl esters vs. time at the different r and T are shown in Figure 7.5. Conversions, %C, were correlated as a function of time through the following exponential equation:

$$\%C = c_1(1 - e^{-c_2t}) + c_3(1 - e^{-c_4t}) \quad \text{Eq. 7-4}$$

where c_1 to c_4 are the fitting parameters given in Table 7.2. In this table determination coefficient and standard deviation are also given. From the Figure 7.5, it can be observed that the increase in the methanol/oil ratio from 6:1 to 7.5:1 showed a lesser increase effect on esters yield, than the step from 4.5 to 6:1. Rashid et al. [29], studied the effect of methanol/oil molar ratio (3:1–15:1), catalyst concentration (0.25–1.50%), temperature (25–65°C), and stirring intensity (180–600 rpm) in the transesterification of CSO founding that beyond the molar ratio of 6:1, further methanol addition had no considerable effect on ester formation; rather it complicated ester recovery and raised process cost. They reported that to produce 96.9% yield of methyl esters from CSO, the optimum methanol/oil ratio was 6:1 in 90 minutes. In this work 94% yields are obtained with $r = 6:1$ at 323.15 K and 343.15 K. In the figure, the influence of reaction temperature on the transesterification of CSO is also observed. Raising temperature to 343.15 K a high conversion is observed significantly early relative to 323.15 K. Figure 7.5 displays that all curves have an asymptotic bent with time, and increasing the methanol/oil molar ratio the conversion does not change much after 40 minutes. At 343.15 K there are little changes after 20 minutes for 6:1 and 7.5:1 methanol/oil molar ratios.

Table 7.2. Fitting parameters of Eq. 7-4. Coefficient of determination and standard deviation are also indicated.

$T = 323.15 \text{ K}$			
	$r = 4.5$	$r = 6.0$	$r = 7.5$
c_1	65.116	78.749	63.063
c_2	0.2050	0.1987	0.1240
c_3	25.940	18437.7	29.122
c_4	0.0169	8.9457×10^{-6}	0.1240
r^2	0.997	0.976	0.992
σ	2.1	6.8	3.9
$T = 343.15 \text{ K}$			
	$r = 4.5$	$r = 6.0$	$r = 7.5$
c_1	59.594	76.956	94.908
c_2	0.7777	0.6290	0.4776
c_3	24.060	16.074	0.7649
c_4	0.04278	0.0640	0.4776
r^2	1.000	0.999	0.963
σ	1.6	3.7	6.9

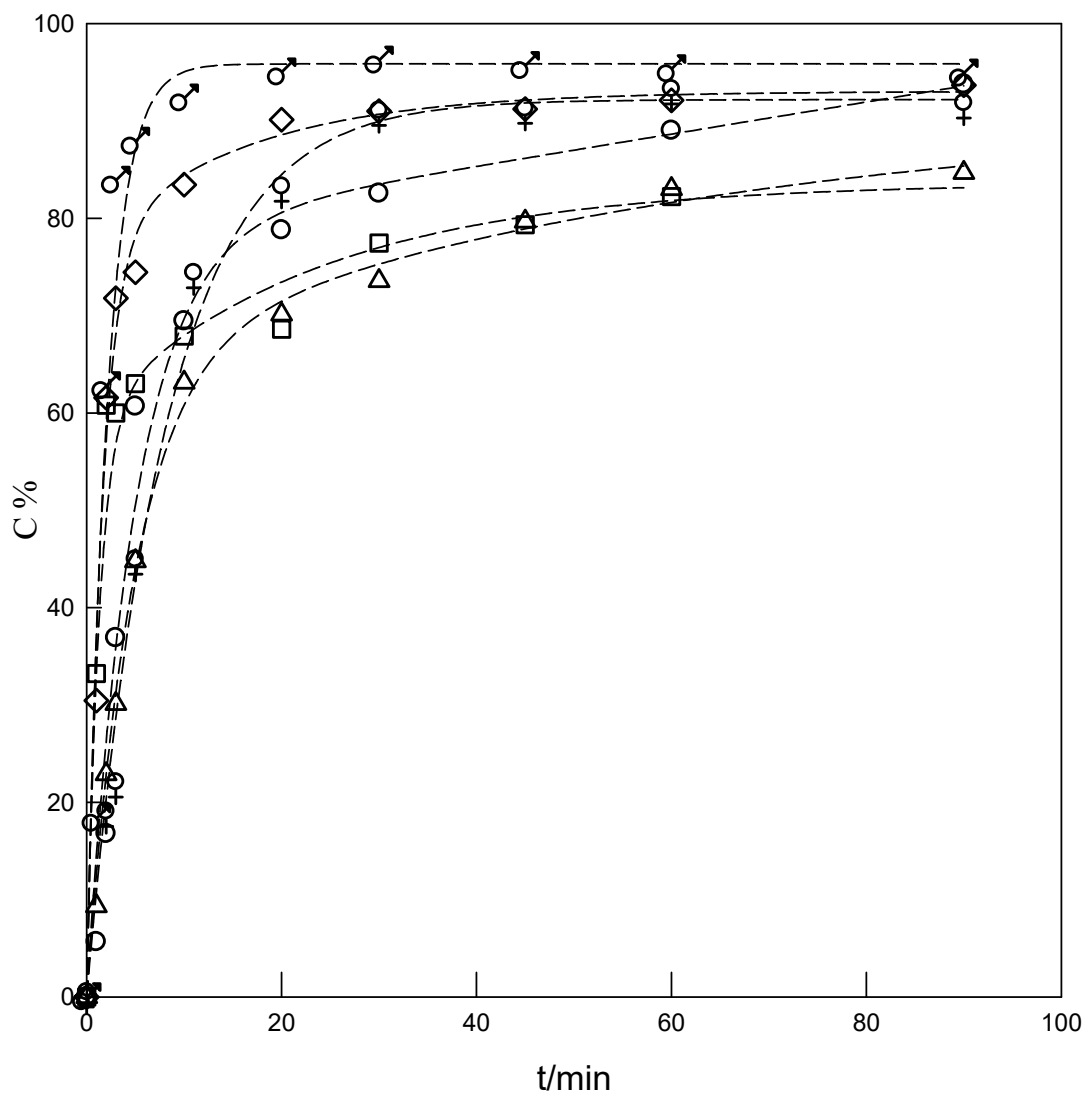


Figure 7.5. Conversion of CSO (%C) as function of reaction time (t) from NMR analysis for different alcohol to oil ratios. At $T = 323.15$: Δ , $r = 4.5$; \circ , $r = 6.0$; \square , $r = 7.5$. At $T = 343.15$ K: \diamond , $r = 4.5$; \blacktriangledown , $r = 6.0$; $\♂$, $r = 7.5$.

7.3.2. Monitoring the methanolysis reaction of CSO by density measurements

The changes in phase behaviour during the transesterification reaction are a very important subject for an appropriate understanding and discussion of changes in properties with time during the monitoring. Therefore, it makes sense to discuss the physical phase changes that take place during reaction. The TGs and FAMES form the non-polar continuous phase (OIL), whereas MeOH and Gly, which are highly polar, constitute the dispersed alcoholic phase (AL). FAMES and methanol are poorly soluble in the AL and OIL phases, respectively. The FFAs (and TGs) and glycerol are mutually immiscible, whereas DGs and MGs distribute between both phases

although they have tendency to stay in the OIL phase. In the course of reaction the remaining TGs and FAMES are completely miscible and they stay in the OIL phase.

At low oil conversions, the upper layer is the (AL) because it is mainly constituted by methanol whose density is much lower than that of the oil. However, during the course of the reaction the FAMES and glycerol concentrations increase, in the OIL and AL phases, respectively. The result of these changes in the mixture is that as oil conversion increases, the density of the OIL phase decreases and that of the AL phase significantly increases. Close to the end of reaction, the OIL phase (mainly biodiesel) becomes the upper layer. According to this, there will be an oil conversion for a given methanol-to-oil molar ratio, at which the change in densities would lead to a change of the relative position of the OL and AL phases in the reactor.

The change on density of the mixture during the reaction is due to the variation of composition of the media and the spent and production of the species that have very different densities, as can be seen in Table 7.3.

Table 7.3. Density of main compounds existing in the reaction mixture at $T = 323.15$ K and 343.15 K, and atmospheric pressure.

	$\rho / (\text{kg.m}^{-3})$ at $T = 323.15$ K	$\rho / (\text{kg.m}^{-3})$ at $T = 343.15$ K
Cottonseed oil ^a	897.76	885.80
Methanol ^b	762.58	742.83
Cottonseed biodiesel ^c	861.08	847.53
Glycerol ^d	1243.17	1231.84

^a Obtained from experimental data (see Eq. 6-40).

^b At L/G saturation (vapour pressure of 0.125 MPa) [30].

^c Obtained from $\rho = 1040.30 - 0.4392T - 3.5714 \times 10^{-4}T^2$ found with experimental data (see Table 3.3).

^d Obtained from $\rho = 1450,57 - 0,6741T + 0,0001T^2$ found with experimental data [31].

Figure 7.6 shows the evolution of measured density with reaction time for the methanolysis at 343.15 K and for alcohol to oil molar ratio $r = 6$. As methanol is not soluble in the oil, the first minutes, corresponding to stages (1+2), are spent to the dispersion / diffusion of catalyst and methanol in the oil. In stage 1 the density of the system is mainly that of oil and after few seconds the mixing process takes places and reaction occurs, as can be seen in the Figure 7.3(a), where the signal of methyl ester at 3.67 ppm is clearly observable. Due to this process, the density of mixture will be lowered abruptly to a minimum density value, ρ_m , which corresponds to the

reaction time t_m at stage (3). This almost vertical profile of density was described by Tubino et al. [28] in their monitoring study using mass variation techniques, which can be considered as derived from the density monitoring. After sequence (1+2+3), a fast reaction stage is observed (4). According to kinetic data of several oils, this region is characterized by a strong decrease in the concentration of triglycerides and a marked increase in the concentration of FAMES and glycerol. It is interesting to see that the shape of density profile in this region is quite similar to the one observed from kinetic studies [32] corresponding to the increasing concentration of FAMES as a function of time. After 10 to 15 minutes the chemical equilibrium is reached and density increases slowly with time (stage 5), corresponding to the slowdown of the formation of FAMES and glycerol over time. Also at this stage the concentrations of glycerides decrease very slowly stabilizing to values practically independent with time.

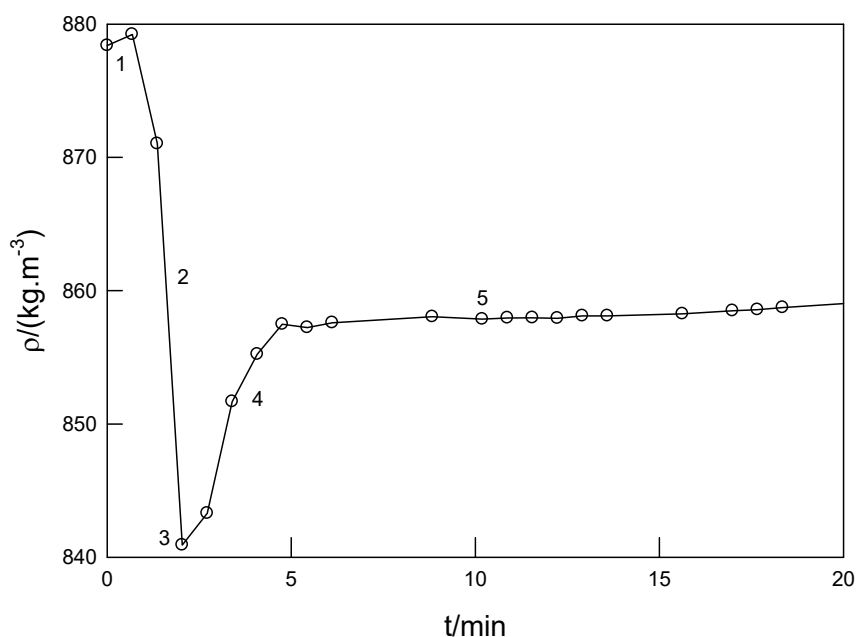


Figure 7.6. Evolution of density with reaction time, at 343.15 K and $r = 6.0$. Stages: (1+2) oil+MeOH mixture, dispersion of oil and slow rate; (3) minimum density; (4) fast reaction; (5) chemical equilibrium.

As mentioned before, replicates of density and oil conversion as a function of time were performed for each temperature and alcohol to oil ratio (Figures E.1 to E.4). Due to inconsistencies for some sets of experimental data, a careful selection of values has to be done. The strategy used for selection of density and oil conversion data sets are presented with detail in Table E.1. According to this strategy, Figure 7.7 shows the evolution of the density during the

reaction time for series of reactions performed at temperatures of 323.15 K and 343.25 K and methanol to oil molar ratios of 4.5 6 and 7.5. In the same figure the time evolution curves of the conversion, for all conditions, obtained from the Eq. 7-4 are also shown.

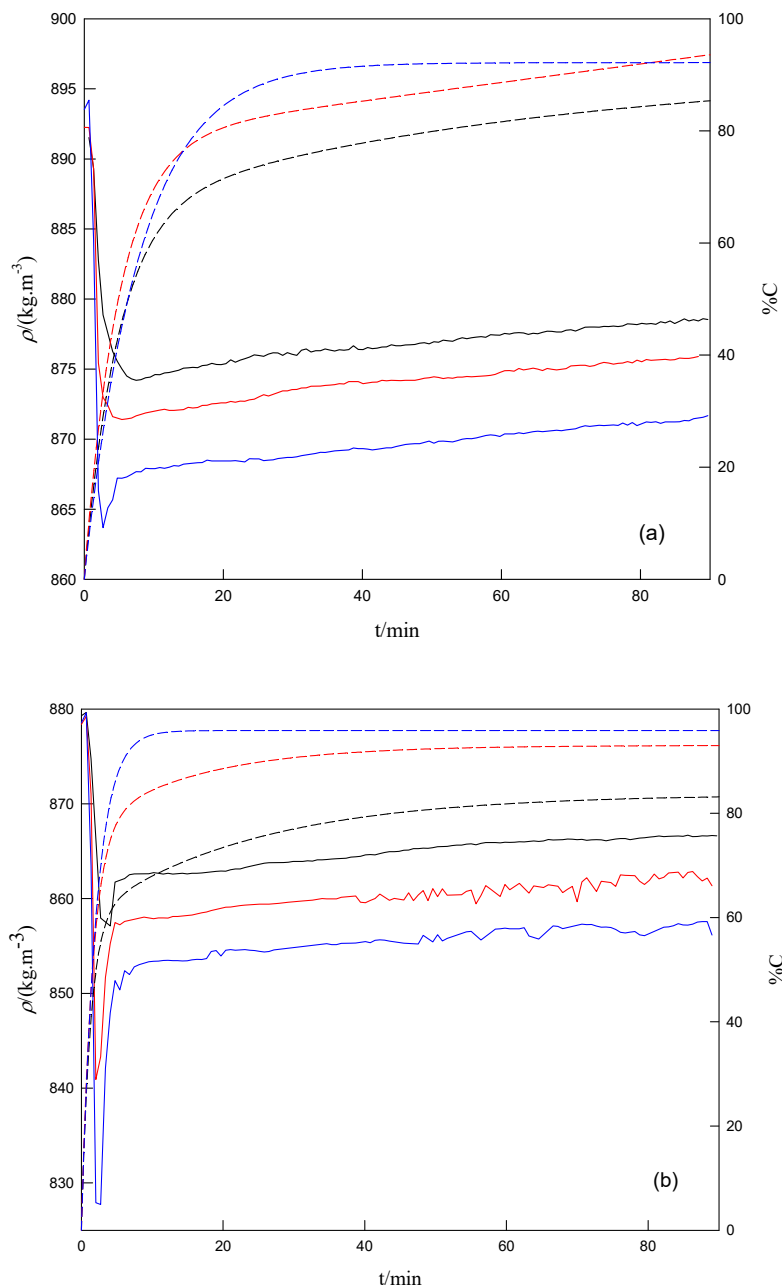


Figure 7.7. Evolution of density, ρ , and oil conversion %C with reaction time, t , measured for two series of methanolysis reactions with catalyst concentration of 0.5 wt %: (a) 323.15 K; (b) 343.15 K. Full lines correspond to density variation and dashed lines correspond to oil conversion. Black, red and blue refer to $r = 4.5$, 6.0 and 7.5 respectively.

From Figure 7.7, it can be observed that for each temperature, the increase of r by 1.5 causes the displacement of the monitoring curves to successively lower values of density and the displacement of the minimum of the density observed at t_m toward lower values of time. These behaviours are due to the dilution effect resulting from increasing r and with the fact that FAMES and glycerol are produced earlier in the reaction, at high rates. This is related to what is observed in the $(\%C, t)$ curves at small reaction times. Comparing these curves for ratios of 4.5 and 6 at 323.15 K and 343.15 K it can be observed that a small shift of these steep curves toward lower times. The minimum value ρ_m at t_m is increasingly deeper relative to the density for t values higher than t_m , particularly meaningful for $r = 7.5$. As result, the density drop, $\Delta\rho$, observed between $t = 0$ and t_m increases as r rise (see Table 7.4). This behaviour is more pronounced at 343.15 K. In Figure 7.7, when t is greater than t_m , the concentration profiles for the different ratios of r , at each temperature, run almost parallel one to each other with density differences of approximately 5 kg.m^{-3} (this is particularly valid at 343.15 K). In Table 7.4 the parameters discussed before for the monitoring curves are presented.

Table 7.4. Characteristic parameters of density monitoring curves.

$t / ;K$	r	t_m / min	$\rho_{(t=0)} / (\text{kg.m}^{-3})$	$\rho_m / (\text{kg.m}^{-3})$	$\Delta\rho / (\text{kg.m}^{-3})$
323.15	4.5	7.47	892.7	874.2	17.8
	6.0	5.44	892.3	871.4	20.9
	7.5	2.72	893.5	863.7	29.9
343.15	4.5	4.08	879.3	857.1	22.2
	6.0	2.04	878.4	840.9	37.5
	7.5	2.72	878.6	827.7	50.8

In Figure 7.8, a 3D plot is given, where it can be seen that a virtual horizontal plane, corresponding to $\rho = 865 \text{ kg.m}^{-3}$, separates the monitoring curves at 323.15 K from those relative to 343.15 K. Thus the differences discussed before at the different (time, temperature, density) domains are clearly observed in a more global perspective.

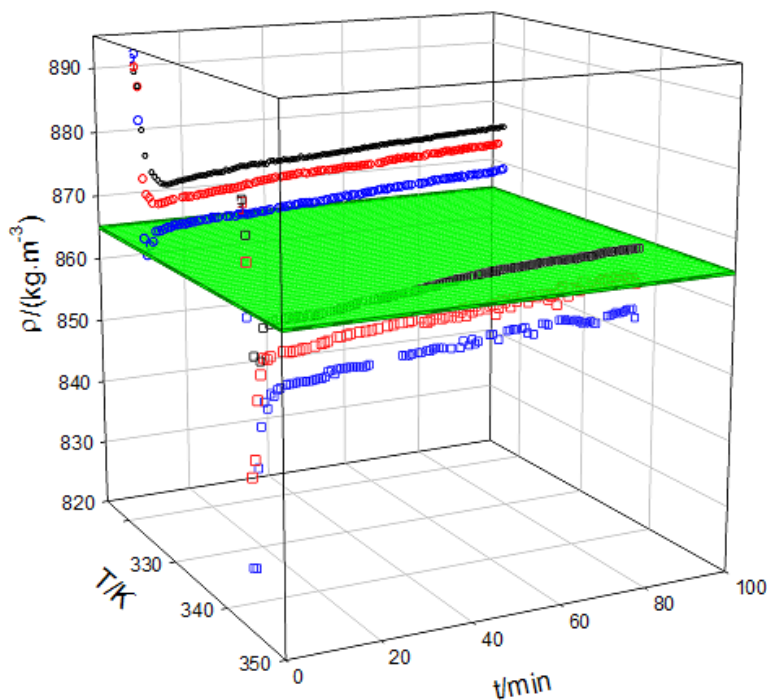


Figure 7.8. Evolution of density, ρ , with reaction time, t , and temperature T measured for two series of methanolysis reactions with catalyst concentration of 0.5 wt %: at 323.15 K and 343.15 K. Black, red and blue symbols refer to $r = 4.5, 6.0$ and 7.5 respectively.

7.3.3. Correlation

To develop a practical correlation, NMR and density data, at the same reaction time should be used. For this purpose, at each time for which the conversion was experimentally accessed, the density was calculated by interpolation between neighbour values. With this method, the expected uncertainty for calculated value will be less than the experimental uncertainty in density. For the calculation for $t < t_m$, the uncertainty can be higher. The results are given in Table 7.5 and they were plotted in Figure 7.9.

Table 7.5. Selected values for the conversion of CSO (% C) and densities of the reaction mixture as function of time (t), temperature (T) and methanol to oil ratio (r).

$T = 343.15 \text{ K}$								
r = 4.5			r = 6.0			r = 7.5		
t/min	%C	$\rho/\text{kg.m}^{-3}$	t/min	%C	$\rho/\text{kg.m}^{-3}$	t/min	%C	$\rho/\text{kg.m}^{-3}$
1.0	9.3	890.5	1.0	5.7	890.8	1.0	-	889.2
2.0	22.9	883.1	2.0	16.8	876.2	2.0	18.6	867.3
3.0	30.1	878.3	3.0	36.9	872.8	3.0	21.6	864.3
5.0	44.8	875.4	5.0	60.7	871.8	5.0	44.4	867.2
10.0	63.1	874.6	10.0	69.4	872.0	10.0	73.9	867.9
20.0	70.1	875.4	20.0	78.8	872.6	20.0	82.8	868.4
30.0	73.6	876.1	30.0	82.6	873.5	30.0	90.6	868.7
45.0	79.7	876.7	45.0	92.6	874.2	45.0	90.8	868.0
60.0	83.0	877.5	60.0	89.0	874.8	60.0	92.8	870.3
90.0	84.7	878.5	90.0	93.8	876.1	90.0	91.3	871.7
$T = 343.15 \text{ K}$								
r = 4.5			r = 6.0			r = 7.5		
t/min	%C	$\rho/\text{kg.m}^{-3}$	t/min	%C	$\rho/\text{kg.m}^{-3}$	t/min	%C	$\rho/\text{kg.m}^{-3}$
1.0	33.2	877.3	1.0	30.4	875.4	1.0	18.3	872.0
2.0	60.8 ^a	867.5	2.0	61.6	842.6	2.0	62.8	829.9
3.0	60.0 ^a	857.8	3.0	71.8	846.8	3.0	83.9	833.7
5.0	63.0	861.8	5.0	74.4	857.4	5.0	87.9	851.0
10.0	67.9	862.7	10.0	83.4	857.9	10.0	92.3	853.4
20.0	68.6	862.9	20.0	90.1	859.0	20.0	95.0	854.2
30.0	77.4	863.9	30.0	91.0	859.7	30.0	96.2	854.8
45.0	79.3	865.0	45.0	91.2	859.9	45.0	95.7	855.4
60.0	82.2	865.9	60.0	92.1	861.3	60.0	95.3	856.9
90.0	-	866.6	90.0	93.7	860.2	90.0	94.9	854.1

^a Valued not considered for the fitting with Eq. 7.4.

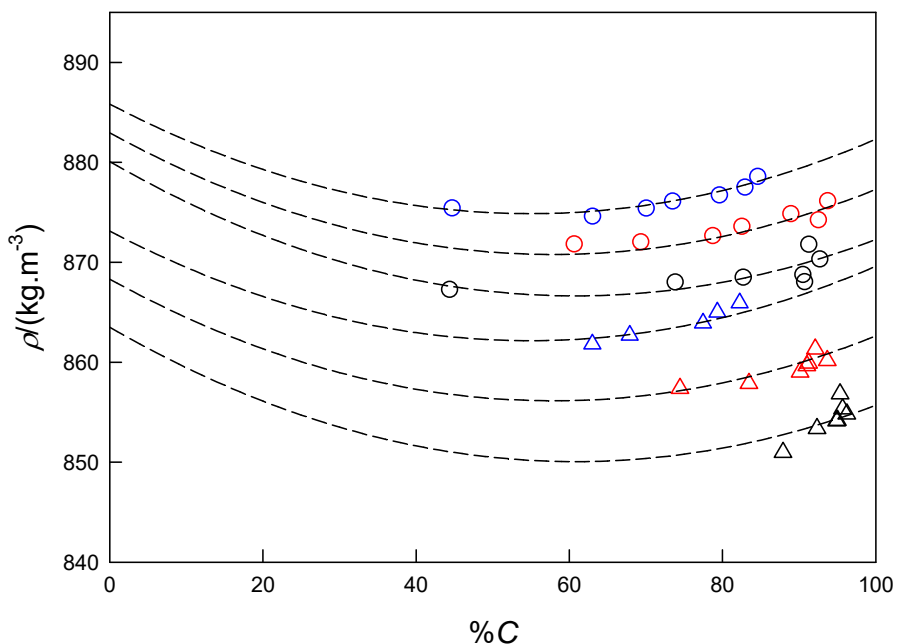


Figure 7.9. Density of the reaction mixture as function of oil conversion (%C). Symbols correspond to experimental data at time greater than $t = 5$ min. Circles and triangles correspond to $T = 323.15$ and $T = 343.15$ K, respectively and colours blue, red and black are relative to alcohol to oil ratios $r = 4.5$, 6.0 and 7.5 , respectively. Dashed lines represent calculated data from the correlation with Eq. 7-6.

From Figure 7.9, it can be seen that (density, %C) data for reaction times above 5 minutes are consistent, following well-defined paths according to the values of alcohol to oil ratio and temperature. For times below that limit (ρ , %C) data diverge from the tendency observed for $t > 5$ min.

The following relationship between the density and the CSO conversion was found from the analysis of the experimental results,

$$\rho = A_0 + A_1 \cdot T + A_2 \cdot r + A_3 \cdot (\%C) + A_4 \cdot r \cdot T + A_5 \cdot r \cdot (\%C) + A_6 \cdot (\%C)^2 \quad \text{Eq. 7-5}$$

where A_i are parameters obtained from the fitting of (density, %C) data, resulting in coefficient of determination $r^2 = 0.989$ and standard deviation $\sigma = 0.91 \text{ kg}\cdot\text{m}^{-3}$, a value which is close to the combined uncertainty on density measurement. Parameters A_i and the statistical information of fitting are provided in Table 7.6.

Table 7.6. Fitting parameters of Eq. 7-5, with 95% confidence limits. The determination coefficient (r^2) and standard deviation in density (σ_ρ) are given.

Parameter	Value
A_0^a	1006.14
A_1^b	-0.3457
A_2^c	18.8955
A_3^d	-0.3354
A_4^e	-0.0644
A_5^f	-0.0143
A_6^g	0.0036
σ_ρ^h	0.91
r^2	0.989

^a $A_0/(\text{kg}\cdot\text{m}^{-3})$; ^b $A_1/(\text{kg}\cdot\text{m}^{-3}\cdot\text{K}^{-1})$; ^c $A_2/(\text{kg}\cdot\text{m}^{-3})$; ^d $A_3/(\text{kg}\cdot\text{m}^{-3})$; ^e $A_4/(\text{kg}\cdot\text{m}^{-3}\cdot\text{K}^{-1})$; ^f $A_5/(\text{kg}\cdot\text{m}^{-3})$; ^g $A_6/(\text{kg}\cdot\text{m}^{-3})$; ^h $\sigma_\rho/(\text{kg}\cdot\text{m}^{-3})$.

The oil conversion can be calculated from the density by solving Equation 7-5 for %C as:

$$\%C = \frac{-C_1 \pm (C_1^2 - 4C_2)^{1/2}}{2} \quad \text{Eq. 7-6}$$

where the signs + and – apply for the time conditions ($t > t_{\min}$) and ($t < t_{\min}$), respectively and

$$C_1 = \frac{(A_3 + A_5 \cdot r)}{A_6} \quad \text{Eq. 7-7}$$

$$C_2 = \frac{(A_0 + A_1 \cdot T + A_2 \cdot r + A_4 \cdot r \cdot T) - \rho}{A_6} \quad \text{Eq. 7-8}$$

The monitoring of methanolysis reactions through off-line density measurements and NRM are displayed in Figure 7.10 and Figure 7.11 for 323.15 K and 343.15 K, respectively. In these figures, the oil conversion values were calculated from the density-time profiles using Eq. 7-6 and they were compared with the values from NMR analysis. It can be seen that the agreement between both techniques is good. At $T = 323.15$ K, in spite of the Eq. 7-5 obtained from fitting of (ρ , %C) data for $t \geq 5$ minutes, the agreement starts early usually at less than 5 minutes (see Figure 7.10). In both figures, and in particularly in Figure 7.11, at alcohol to oil ratios of 6 and 7.5, some pronounced noise is observed at higher reaction times. This is due to the noise observed for measured densities at those conditions. By changing the operating variables

(temperature and initial methanol/oil molar ratio) very different reaction rates and oil conversion evolutions with reaction time are achieved. The measurement of the density allows describing accurately the evolution of the processes.

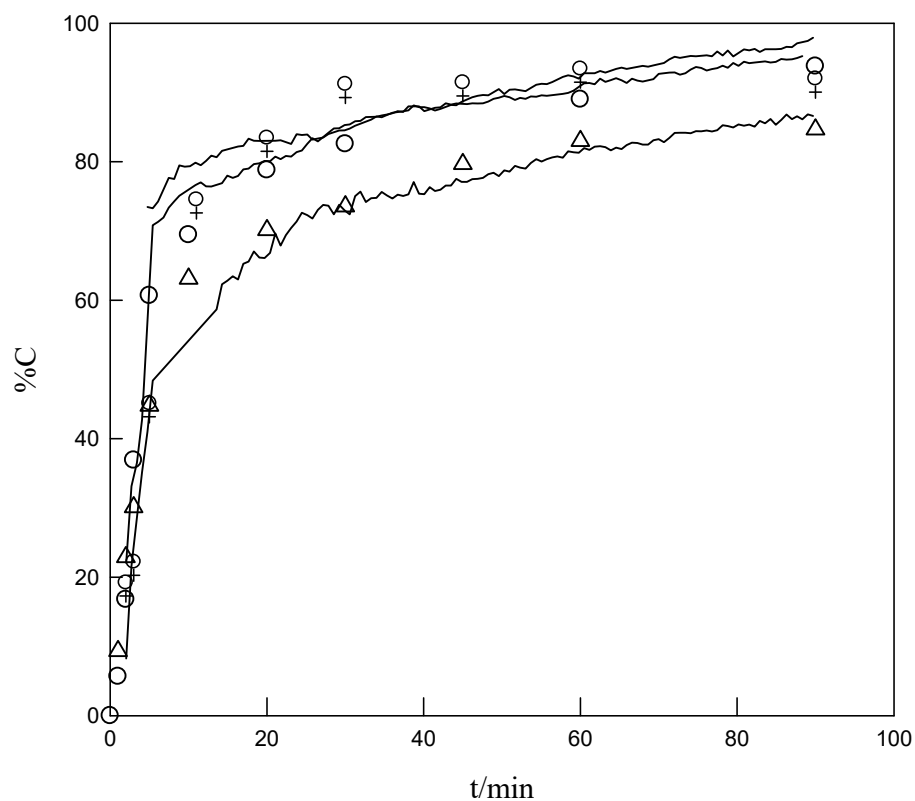


Figure 7.10. Conversion of CSO (%C) as function of time, at $T = 323.15$ K. Δ , $r = 4.5$; \circ , $r = 6.0$; \square , $r = 7.5$. Lines represent %C calculated with density from Eq. 7-6.

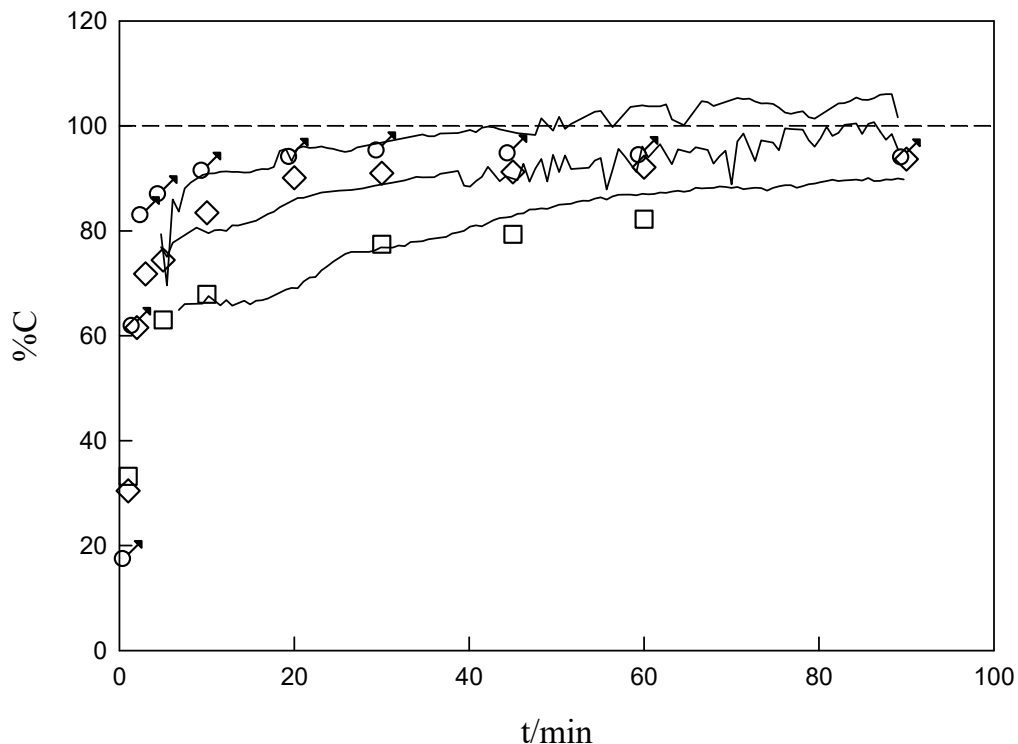


Figure 7.11. Conversion of CSO (%C) as function of time, at $T = 343.15$ K. \square , $r = 4.5$; \diamond , $r = 6.0$; \circ , $r = 7.55$. Lines represent %C calculated data from correlation with Eq. 7-6.

The conversions of oil to FAMES calculated from Eq. 7-6 are compared with the data from NMR in Figure 7.12. In this figure the *RDs* between the sets of values, at 323.15 K and 343.15 K, are displayed as function of reaction time and in Figure 7.13, the parity plot is presented. The *RDs* fall usually within the range $\pm 5\%$ (84% of all data for the two temperatures). The *AARDs* for 323.15 K and 343.15 K are 3.0% and 2.9%, respectively and the corresponding standard deviations are 3.3% and 3.6%.

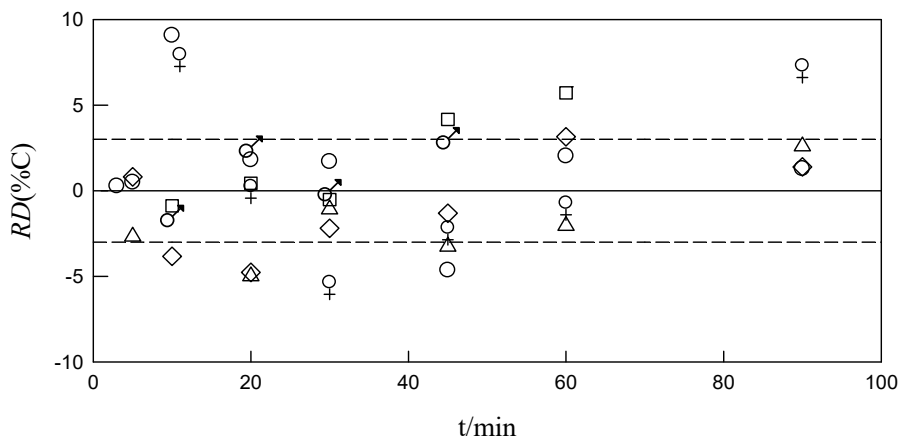


Figure 7.12. Relative deviations of %C as function of reaction time. At $T = 323.15$: Δ , $r = 4.5$; \circ , $r = 6.0$; ∇ , $r = 7.5$. At $T = 343.15$ K: \square , $r = 4.5$; \diamond , $r = 6.0$; \odot , $r = 7.5$. The limits at $\pm 3\%$, corresponding to the *OARD*, are displayed.

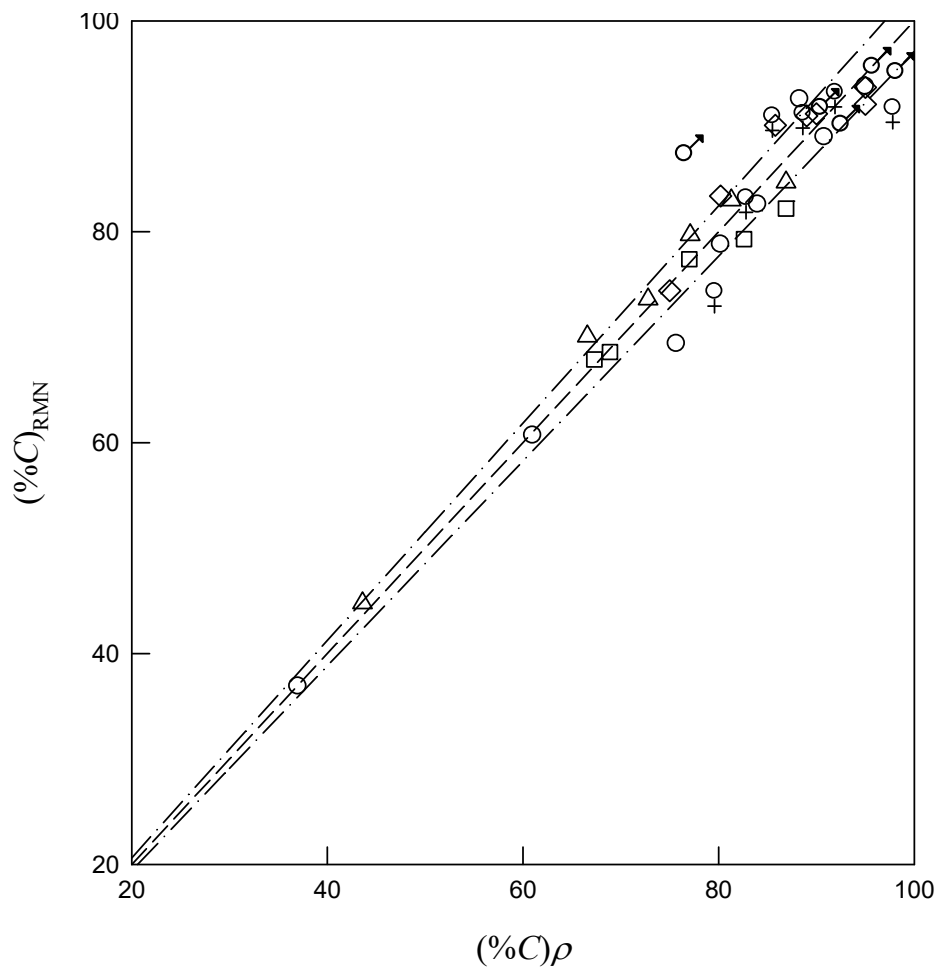


Figure 7.13. Parity plot for the conversion obtained from NMR analysis $(\%C)_{\text{NMR}}$ and from Eq. 7-6, taking density at time for which samples were taken for NMR analysis $(\%C)_{\rho}$. At $T=323.15$: Δ , $r = 4.5$; \circ , $r = 6.0$; $+$, $r = 7.5$. At $T=343.15$ K: \square , $r = 4.5$; \diamond , $r = 6.0$; \times , $r = 7.5$. The limits at $\pm 3\%$, corresponding to the *OARD*, are displayed.

7.4 Conclusions

The transesterification of CSO, at 323.15 and 343.15 K and alcohol to oil ratios of 4.5, 6 and 7.5 were studied. The density of the reaction medium was measured off-line using a vibrating tube densimeter. Samples were taken from the reactor, at convenient times, for the determination of oil conversion by ^1H NMR. The NMR and density time profiles were established from the measurements and a useful correlation for reaction monitoring, that relates the oil conversion with the density of the reaction medium was found. This correlation can be applied with uncertainty less than 5% in the conversion for reaction times higher than 5 minutes. It was found that about 84% of conversion data, calculated from the densities at 323.15 K and 343.15 K for alcohol to oil ratios of 4.0, 6.0 and 7.5 show *RDs* in the range $\pm 5\%$, relative to the determinations by NMR. This correlation will be of the interest for the industrial biodiesel production if reaction times higher than 5 minutes are considered.

7.5 References

1. Cvangros J, Cvangrosova Z, Hoka C. Conversion of acyl glycerols to methyl esters by TLC method. *Petroleum and Coal*. 2002;44(1/2):67-71.
2. Pinto AC, Guarieiro LL, Rezende MJ, Ribeiro NM, Torres EA, Lopes WA, et al. Biodiesel: an overview. *Journal of the Brazilian Chemical Society*. 2005;16(6):1313-30.
3. Chattopadhyay S, Das S, Sen R. Rapid and precise estimation of biodiesel by high performance thin layer chromatography. *Applied energy*. 2011;88(12):5188-92.
4. Dubé MA, Zheng S, McLean DD, Kates M. A comparison of attenuated total reflectance-FTIR spectroscopy and GPC for monitoring biodiesel production. *Journal of the American Oil Chemists' Society*. 2004;81(6):599-603.
5. Arzamendi G, Arguiñarena E, Campo I, Gandía L. Monitoring of biodiesel production: Simultaneous analysis of the transesterification products using size-exclusion chromatography. *Chemical Engineering Journal*. 2006;122(1-2):31-40.
6. Pinzi S, Gandía L, Arzamendi G, Ruiz J, Dorado M. Influence of vegetable oils fatty acid composition on reaction temperature and glycerides conversion to biodiesel during transesterification. *Bioresource technology*. 2011;102(2):1044-50.

7. Gelbard G, Bres O, Vargas R, Vielfaure F, Schuchardt U. ^1H nuclear magnetic resonance determination of the yield of the transesterification of rapeseed oil with methanol. *Journal of the American Oil Chemists' Society*. 1995;72(10):1239-41.
8. Neto PRC, Caro MSB, Mazzuco LM, da Graça Nascimento M. Quantification of soybean oil ethanolysis with ^1H NMR. *Journal of the American Oil Chemists' Society*. 2004;81(12):1111-4.
9. Satyarthi JK, Srinivas D, Ratnasamy P. Estimation of free fatty acid content in oils, fats, and biodiesel by ^1H NMR spectroscopy. *Energy & Fuels*. 2009;23(4):2273-7.
10. Coral N, Rodrigues E, Rumjanek V, Zamian JR, Rocha Filho GN, Costa CEF. Soybean biodiesel methyl esters, free glycerin and acid number quantification by ^1H nuclear magnetic resonance spectroscopy. *Magnetic Resonance in Chemistry*. 2013;51(2):69-71.
11. Jin F, Kawasaki K, Kishida H, Tohji K, Moriya T, Enomoto H. NMR spectroscopic study on methanolysis reaction of vegetable oil. *Fuel*. 2007;86(7-8):1201-7.
12. Morgenstern M, Cline J, Meyer S, Cataldo S. Determination of the kinetics of biodiesel production using proton nuclear magnetic resonance spectroscopy (^1H NMR). *Energy & Fuels*. 2006;20(4):1350-3.
13. Cabeça LF, Marconcini LiV, Mambrini GP, Azeredo RB, Colnago LA. Monitoring the transesterification reaction used in biodiesel production, with a low cost unilateral nuclear magnetic resonance sensor. *Energy & Fuels*. 2011;25(6):2696-701.
14. Killner M, Linck YG, Danieli E, Rohwedder J, Blümich B. Compact NMR spectroscopy for real-time monitoring of a biodiesel production. *Fuel*. 2015;139:240-7.
15. Knothe G. Monitoring a progressing transesterification reaction by fiber-optic near infrared spectroscopy with correlation to ^1H nuclear magnetic resonance spectroscopy. *Journal of the American Oil Chemists' Society*. 2000;77(5):489-93.
16. Richard R, Li Y, Dubreuil B, Thiebaud-Roux S, Prat L. On-line monitoring of the transesterification reaction between triglycerides and ethanol using near infrared spectroscopy combined with gas chromatography. *Bioresource Technology*. 2011;102(12):6702-9.
17. Pinzi S, Alonso F, Olmo JG, Dorado MP. Near infrared reflectance spectroscopy and multivariate analysis to monitor reaction products during biodiesel production. *Fuel*. 2012;92(1):354-9.

18. Dorado MP, Pinzi S, De Haro A, Font R, Garcia-Olmo J. Visible and NIR Spectroscopy to assess biodiesel quality: Determination of alcohol and glycerol traces. *Fuel*. 2011;90(6):2321-5.
19. Siatis N, Kimbaris A, Pappas C, Tarantilis P, Polissiou M. Improvement of biodiesel production based on the application of ultrasound: monitoring of the procedure by FTIR spectroscopy. *Journal of the American Oil Chemists' Society*. 2006;83(1):53-7.
20. Zhang F, Adachi D, Tamalampudi S, Kondo A, Tominaga K. Real-time monitoring of the transesterification of soybean oil and methanol by Fourier-transform infrared spectroscopy. *Energy & Fuels*. 2013;27(10):5957-61.
21. Ghesti GF, de Macedo JL, Resck IS, Dias JA, Dias SCL. FT-Raman spectroscopy quantification of biodiesel in a progressive soybean oil transesterification reaction and its correlation with ¹H NMR spectroscopy methods. *Energy & Fuels*. 2007;21(5):2475-80.
22. Ellis N, Guan F, Chen T, Poon C. Monitoring biodiesel production (transesterification) using in situ viscometer. *Chemical Engineering Journal*. 2008;138(1-3):200-6.
23. Zabala S, Arzamendi G, Reyero I, Gandía L. Monitoring of the methanolysis reaction for biodiesel production by off-line and on-line refractive index and speed of sound measurements. *Fuel*. 2014;121:157-64.
24. Tubino M, Junior JGR, Bauerfeldt GF. Biodiesel synthesis with alkaline catalysts: a new refractometric monitoring and kinetic study. *Fuel*. 2014;125:164-72.
25. Clark WM, Medeiros NJ, Boyd DJ, Snell JR. Biodiesel transesterification kinetics monitored by pH measurement. *Bioresource technology*. 2013;136:771-4.
26. Rachmanto T, Allanson D, Matthews C, Jenkinson I. Monitoring of biodiesel transesterification process using impedance measurement: Liverpool John Moores University; 2014.
27. Kanda LR, Yamamoto CI, Lopes AR, Voll FA, Corazza ML, Wypych F. Density, refractive index and viscosity as content monitoring tool of acylglycerols and fatty acid methyl esters in the transesterification of soybean oil. *Analytical Methods*. 2016;8(28):5619-27.
28. Tubino M, Oliveira Júnior AG, Salomão AA. Continuous Monitoring of a Transesterification Reaction Using an Analytical Balance. *Journal of the Brazilian Chemical Society*. 2018;29(1):200-4.

29. Rashid U, Anwar F, Knothe G. Evaluation of biodiesel obtained from cottonseed oil. *Fuel Processing Technology*. 2009;90(9):1157-63.
30. NIST. Thermophysical properties of fluids [June]. Available from: <http://webbook.nist.gov/chemistry/fluid/>.
31. Prieto NM, Souza TA, Egas AP, Ferreira AG, Lobo LQ, Portugal AT. Liquid glycerol: Experimental densities at pressures of up to 25MPa, and some derived thermodynamic properties. *The Journal of Chemical Thermodynamics*. 2016;101:64-77.
32. Nouredini H, Zhu D. Kinetics of transesterification of soybean oil. *Journal of the American Oil Chemists' Society*. 1997;74(11):1457-63.

8 CHAPTER

CONCLUSIONS

8.1 General Conclusions

After a careful analytical developed work, the main conclusions of this thesis are highlighted.

Taking into account the scarce data on the thermodynamic properties of biodiesel and its raw materials, in particular for cottonseed oil whose use for production of biodiesel is not so widespread, it can be affirmed that this thesis fulfilled its objective of providing new experimental data of important thermodynamic properties, necessary for an adequate development of the process and design of equipment and facilities for the production of biodiesel. Experimental density, viscosity, surface tension and speed of sound of cottonseed oil and its methyl derivatives are reported. In addition several models for the prediction of these properties were evaluated and the most suitable models are recommended.

Relative to density, the measurements were made as a function of temperature and the influence of pressure was study for the first time. The experimental data were correlated by the Goharshadi–Morsali–Abbaspour equation of state, obtaining $AARD = 0.018\%$ for oil and $AARD = 0.007\%$ for biodiesel, which are less than the uncertainty of measurements ($u_{(\rho)} = 0.81 \text{ kg}\cdot\text{m}^{-3}$). In order to be able to predict densities over wide ranges of T and p , two methods were developed for CSB, obtaining better or similar results than many other complex methods. One of them, the DU method allow to predict densities from the fatty acid profile with deviation of 0.42% (about $\approx 3 \text{ kg}\cdot\text{m}^{-3}$) while for the 4PGMA, the maximum deviation was 0.25% ($\approx 2 \text{ kg}\cdot\text{m}^{-3}$). For CSO, the group contribution method GCVOL, combined with Halvorsen model, was the most suitable for density prediction, with $AARDs$ of 0.16% , Also, a simple method to predict biodiesel densities from the oil density, with very low deviations ($AARD = 0.08\%$), was developed.

Regarding to viscosity, experimental data at atmospheric pressure, were obtained for CSO and CSB and the dynamic viscosities of each of them were very well described by Vogel-Fulcher-Tamman and MYEGA equations ($AARD$ about 2.6%). The Ceriani method, using MTGA profile, was found to be the most suitable for prediction of oil viscosity, presenting RDs in the range $\pm 5\%$. The Zong's model allowed prediction with the same deviation in more restricted range of temperature. For CSB, the Grunberg and Nissan equation combined with Ceriani and Yuan models enable to obtain viscosities with deviation within $\pm 5\%$, which is close to the experimental uncertainty of many experimental data reported in literature. It was found that the interaction parameter G_{ij} cannot be neglected.

Surface tensions of cottonseed oil and cottonseed biodiesel were measured at atmospheric pressure and each set of data were correlated with reasonable accuracy by linear and Guggenheim equations (standard deviations near $0.3 \text{ mN}\cdot\text{m}^{-1}$ in all cases). Several methods to predict the surface tensions were evaluated. The empiric Allen's method was found to be the most suitable for both substances, with deviation in the range 2 - 7% for CSO and 2 - 4% for CSB.

Finally, the speed of sound of six fatty acid esters, five synthetic biodiesel, cottonseed oil and the produced cottonseed biodiesel were measured at atmospheric pressure. The experimental data very well described by a quadratic equation in temperature ($AARD = 0.01\%$ for CSO, while for biodiesel $AARD = 0.05\%$). A new general equation for TG speed of sound prediction was developed obtaining good results. This equation describes experimental data with RDs usually in the range of $\pm 0.1\%$, in the temperature range of 293K to 343 K. Also a new correlation for the molar compressibility of biodiesel as function of mean molar mass and temperature was developed with $OARD$ of 0.17%, taking into account data from the literature and the one of this work. The prediction of speed of sound by using the molar compressibility at 298.15 K is the recommended method for both CSO ($AARD = 0.3\%$) and mean molar compressibility was used for CSB ($AARD = 0.14\%$). For biodiesel the ideal mixture could also be used obtaining estimations with the similar accuracy.

In order to relate the studied properties, some relationships between them were tested and evaluated. A simple method for prediction of viscosity of CSO and CSB from experimental density was attempted, obtaining $AARDs$ of 4.7% and 3.9%, respectively. For surface tensions, this property could be calculated from measured viscosity with $AARD$ of 0.17% for the CSO and 0.13% for CSB. Regarding to the speed of sound, the Auerbach's prediction method, which relate this property with density and surface tension, gave only reasonable results with the surface tension data of this work and adjusted exponent.

With regards to the second goal of the thesis, it can be concluded that the monitoring of the transesterification reaction through density off-line measurements was successful. From the relationship observed between NMR and density time profiles, for cottonseed oil transesterification at 323.15 and 343.15 K and alcohol to oil ratios of 4.5, 6 and 7.5, a useful correlation between density and oil conversion was developed. The correlation takes into account the operative variables temperature and alcohol to oil ratios, and it can be applied for reaction times higher than 5 minutes with uncertainty in oil conversion less than 5%. This relationship

will let to follow the course of the reaction through simple and easy determinations of the density, allowing stopping the reaction when the desired conversion is reached. Moreover, it would enable to detect possible drawbacks in early stages, during the industrial production.

8.2 Future works

The thermophysical properties studied in this work were measured at atmospheric pressure and density data was also measured at high pressure. The speed of sound and viscosity of oils and biodiesels should be extended for high pressure domain to account for important industrial applications as supercritical process. Currently, we have developed and tested acoustical cells for speed of sound measurements up to 30MPa.

The measurements of the mentioned properties in extended temperature and pressure ranges will produce new data correlation. The existent predictive methods will be improved and new one will be developed.

The monitoring of transesterification reaction using thermodynamic properties is a very important issue. Thus, related research will be intensified in order to extended experiments in situ processes and other properties such as viscosity and speed of sound will be used as monitoring target. Some preliminary results obtained in our laboratories are promising. The use of portable density and viscosity meters commercially available and cheap will be also used with monitoring purpose.

It is important to make kinetic studies on transesterification to understand the relation between the production of esters and triglycerides depletion with the evolution of thermodynamic properties as the reaction evolves

APPENDIX

A Data for chapter 2

Table A.1. Fatty acid methyl esters (FAME) for diesel engines - Requirements and test methods. CEN EN 14214: 2008+A1:2009 [39].

Properties	Units	Limits		Test method ^a
		Min.	Max.	
FAME content ^a	% (m/m)	96.5 ^b		EN 14103
Density at 15°C ^c	Kg/m ³	860	900	EN ISO 3675
Viscosity at 40°C ^d	mm ² /s	3.5	5.0	EN ISO 3104
Flash point	°C	101		EN ISO 2719 ^e / EN ISO 3679 ^f
Sulphur content	mg/Kg	-	10	EN ISO 20846 / EN ISO 20884
Carbon residue (on 10% distillation residue) ^g	% (m/m)	-	0.30	EN ISO 10370
Cetane number ^h		51	-	EN ISO 5165
Sulphur ash content	% (m/m)	-	0.02	ISO 3987
Water content	mg/kg	-	500	EN ISO 12937
Total contamination	mg/kg	-	24	EN 12662 ⁱ
Copper strip corrosion (3hr at 50°C)	rating		class 1	EN ISO 2160
Oxidation stability (at 110°C)	hours	6.0	-	EN 15751 ^j / EN 14112
Acid value	mg KOH/g	-	0.5	EN 14104
Iodine value	g iodine/100g	-	120	EN 14111 / EN 16300
Linolenic acid methyl ester	% (m/m)	-	12.0	EN 14103
Polyunsaturated methyl ester (≥4 double bonds)	% (m/m)	-	1.00	EN 14103
Methanol content	% (m/m)	-	0.2	EN 14110
Monoglycerides content	% (m/m)	-	0.8	EN 14105
Diglycerides content	% (m/m)	-	0.2	EN 14105
Triglycerides content	% (m/m)	-	0.2	EN 14105
Free glycerine	% (m/m)	-	0.02	EN 14105 ^j / EN 14106
Total glycerol	% (m/m)	-	0.25	EN 14105
Group I metals (Na ⁺ , K ⁺) ^e	mg/Kg	-	5.0	EN 14108 ^k / EN 14109 / EN 14538
Group II metals (Ca ⁺⁺ , Mg ⁺⁺)	mg/Kg	-	5.0	EN 14538
Phosphorus content	mg/Kg	-	4	EN 14107

Notes:

^a See 5.6.1.

^b The addition of non-FAME components other than additives is not allowed, see 5.2. When C17-methyl esters naturally appear in FAME this can result in a lower measured fatty acid methyl ester content. In this situation

reference should be made for verification to a modified determination procedure [3], until a modified method is established within CEN.

^e Density may be measured over a range from temperature of 20°C to 60°C. Temperature correction shall be made according to the formula given in Annex C. See also 5.6.3.

^d If CFPP is 20 or lower, the viscosity shall be measured at 20°C. The measured value shall not exceed 48 mm²/s. In this case, EN ISO 3104 is applicable without the precision data owing to non-Newtonian behaviour in a two phase system,

^e Procedure A shall be applied. Only a flash point test apparatus equipped with a suitable detection device (thermal or ionisation detection) shall be used.

^f A 2 ml sample and apparatus equipped with a thermal detection device shall be used.

^g ASTM D 1160 shall be used to obtain the 10% distillation residue. See also 5.4.4.

^h See 5.6.3.

ⁱ The test method developed for diesel fuel may show analytical problems when applied to FAME. A test method more suitable for arbitration in disputes is under development by CEN.

^j See 5.6.2.

^k See 5.6.2. See Annex A for precision data for sum of Na + K.

B Data for chapter 3**Table B.1.** Values of the mechanical coefficients α_p , k_T , γ_V and p_i at regular temperature and pressure intervals calculated from GMA EoS for CSB.

p/MPa	$\alpha_p \times 10^4 / (\text{K}^{-1})$ at T/K							
	288.15	298.15	308.15	318.15	328.15	338.15	348.15	358.15
0.1	7.200	7.380	7.550	7.710	7.870	8.030	8.170	8.310
1.0	7.170	7.350	7.510	7.680	7.830	7.990	8.130	8.260
2.0	7.140	7.310	7.470	7.640	7.790	7.940	8.080	8.210
3.0	7.110	7.270	7.440	7.590	7.750	7.890	8.030	8.160
4.0	7.070	7.240	7.400	7.550	7.700	7.850	7.980	8.110
5.0	7.040	7.200	7.360	7.520	7.660	7.800	7.940	8.060
6.0	7.010	7.170	7.320	7.480	7.620	7.760	7.890	8.010
7.0	6.970	7.130	7.290	7.440	7.580	7.720	7.850	8.010
8.0	6.940	7.100	7.250	7.400	7.540	7.670	7.800	7.970
9.0	6.910	7.070	7.220	7.360	7.500	7.630	7.760	7.920
10.0	6.880	7.030	7.180	7.330	7.460	7.590	7.710	7.870
15.0	6.730	6.870	7.010	7.150	7.270	7.390	7.500	7.610
20.0	6.580	6.720	6.850	6.980	7.100	7.210	7.310	7.400
25.0	6.440	6.580	6.700	6.820	6.930	7.030	7.130	7.210
30.0	6.310	6.440	6.560	6.670	6.770	6.870	6.960	7.040

p/MPa	k_T / GPa^{-1} at T/K							
	288.15	298.15	308.15	318.15	328.15	338.15	348.15	358.15
0.1	0.6350	0.6707	0.7086	0.7489	0.7918	0.8373	0.8856	0.9369
1.0	0.6317	0.6670	0.7046	0.7444	0.7867	0.8317	0.8793	0.9298
2.0	0.6281	0.6630	0.7001	0.7395	0.7812	0.8255	0.8724	0.9221
3.0	0.6246	0.6591	0.6957	0.7346	0.7757	0.8194	0.8656	0.9145
4.0	0.6211	0.6552	0.6914	0.7297	0.7704	0.8134	0.8589	0.9070
5.0	0.6177	0.6514	0.6871	0.7250	0.7651	0.8075	0.8523	0.8997
6.0	0.6143	0.6476	0.6829	0.7203	0.7599	0.8017	0.8459	0.8925
7.0	0.6109	0.6439	0.6788	0.7157	0.7547	0.7960	0.8395	0.8925
8.0	0.6076	0.6402	0.6747	0.7112	0.7497	0.7904	0.8333	0.8855
9.0	0.6043	0.6366	0.6707	0.7067	0.7447	0.7849	0.8272	0.8785
10.0	0.6011	0.6330	0.6667	0.7023	0.7398	0.7794	0.8211	0.8717
15.0	0.5854	0.6157	0.6475	0.6811	0.7163	0.7534	0.7924	0.8332
20.0	0.5707	0.5994	0.6296	0.6613	0.6945	0.7293	0.7657	0.8038
25.0	0.5568	0.5841	0.6127	0.6427	0.6741	0.7068	0.7411	0.7767
30.0	0.5436	0.5696	0.5968	0.6252	0.6549	0.6859	0.7181	0.7515

Continued

p/Mpa	$\gamma_V / \text{MPa}\cdot\text{K}^{-1}$ at T/K							
	288.15	298.15	308.15	318.15	328.15	338.15	348.15	358.15
0.1	1.135	1.100	1.065	1.030	0.994	0.959	0.923	0.887
1.0	1.136	1.101	1.066	1.031	0.996	0.960	0.924	0.889
2.0	1.137	1.102	1.068	1.033	0.997	0.962	0.926	0.891
3.0	1.138	1.103	1.069	1.034	0.999	0.963	0.928	0.892
4.0	1.139	1.105	1.070	1.035	1.000	0.965	0.930	0.894
5.0	1.140	1.106	1.071	1.037	1.002	0.966	0.931	0.896
6.0	1.140	1.107	1.073	1.038	1.003	0.968	0.933	0.898
7.0	1.141	1.108	1.074	1.039	1.004	0.970	0.934	0.898
8.0	1.142	1.109	1.075	1.041	1.006	0.971	0.936	0.900
9.0	1.143	1.110	1.076	1.042	1.007	0.973	0.938	0.901
10.0	1.144	1.111	1.077	1.043	1.009	0.974	0.939	0.903
15.0	1.149	1.116	1.083	1.049	1.015	0.981	0.947	0.913
20.0	1.153	1.121	1.088	1.055	1.022	0.988	0.955	0.921
25.0	1.157	1.126	1.094	1.061	1.028	0.995	0.962	0.929
30.0	1.161	1.130	1.099	1.067	1.034	1.002	0.969	0.936

p/MPa	p_i / MPa at T/K							
	288.15	298.15	308.15	318.15	328.15	338.15	348.15	358.15
0.1	326.1	327.1	327.3	326.6	325.2	323.0	320.0	316.4
1.0	325.5	326.5	326.7	326.1	324.7	322.5	319.6	316.1
2.0	324.7	325.8	326.1	325.6	324.2	322.1	319.3	315.7
3.0	324.0	325.2	325.5	325.0	323.7	321.6	318.8	315.4
4.0	323.3	324.5	324.9	324.4	323.2	321.2	318.4	315.0
5.0	322.6	323.8	324.3	323.8	322.6	320.7	318.0	314.7
6.0	321.9	323.2	323.6	323.3	322.1	320.2	317.6	314.3
7.0	321.2	322.5	323.0	322.7	321.6	319.8	317.2	314.3
8.0	320.5	321.8	322.4	322.1	321.1	319.3	316.8	313.9
9.0	319.7	321.1	321.7	321.5	320.5	318.8	316.3	313.6
10.0	319.0	320.5	321.1	320.9	320.0	318.3	315.9	313.2
15.0	315.3	317.0	317.9	317.9	317.2	315.8	313.6	310.8
20.0	311.6	313.5	314.6	314.9	314.4	313.2	311.3	308.7
35.0	307.8	309.9	311.2	311.7	311.5	310.5	308.8	306.5
30.0	304.0	306.3	307.8	308.5	308.5	307.8	306.3	304.2

Table B.2. Minimum and maximum values of mechanical coefficients for the biodiesels of database.

Biodiesel	$\alpha_{p,\min} \times 10^4 / \text{K}^{-1}$	$\alpha_{p,\max} \times 10^4 / \text{K}^{-1}$	$k_{T,\min} / \text{GPa}^{-1}$	$k_{T,\max} / \text{GPa}^{-1}$	$p_{i,\min} / \text{MPa}$	$p_{i,\max} / \text{MPa}$
R	6.7160	8.8590	0.5072	0.9742	334	364
P	6.9340	8.5970	0.5114	0.9997	308	372
S	7.0900	10.7890	0.5084	1.0726	342	374
SR	7.0320	10.8720	0.5106	1.0910	336	371
RP	7.1740	9.9640	0.5124	1.0635	324	375
SP	7.0340	8.7530	0.5119	1.0229	311	370
SRP	7.1740	9.9640	0.5124	1.0635	331	375
N5	6.9560	9.1950	0.5269	1.0644	308	351
N6	6.7700	8.4070	0.5209	1.0387	290	355
N7	6.8550	8.7070	0.5109	1.0260	297	388
N8	6.7540	8.5700	0.5174	1.0781	280	363
N9	6.5400	8.5090	0.4986	1.0450	277	371
N17	6.1960	9.4780	0.5217	1.0739	258	427
N19	6.7030	8.5420	0.5233	1.0545	283	365
N20	6.9560	9.1950	0.5269	1.0645	308	351
N21	6.5150	8.5340	0.5152	1.0446	295	348
N23	6.7790	8.5960	0.5323	1.0873	279	361
CSB	6.0100	8.5040	0.5076	1.0197	295	327
SCHB	7.0400	8.9250	0.5062	0.9974	324	371

Table B.3. Rackett parameters for fatty acids of CSO.

Fatty Acid	$M/\text{g}\cdot\text{mol}^{-1}$	T_c/K^a	p_c/MPa^a	Z_{RA}^a
C14:0	228.37	779.07	1.635	0.2326
C16:0	256.42	799.89	1.408	0.2267
C18:0	284.48	819.00	1.225	0.2205
C18:1	282.46	819.41	1.276	0.2230
C18:2	280.45	819.82	1.331	0.2255
C18:3	278.43	820.23	1.389	0.2284

^a From Halvorsen et al. [82].

Table B.4. Names and symbols for common fatty acids.

Fatty acid	Symbol	Fatty acid	Symbol
Caprylic (C8:0)	Cy	Oleic (C18:1)	O
Capric (C10:0)	C	Linoleic (C18:2)	Li
Lauric (C12:0)	L	Linolenic (C18:3)	Ln
Myristic (C14:0)	M	Arachidic (C20:0)	A
Palmitic (C16:0)	P	Behenic (C22:0)	B
Palmitoleic (C16:1)	Po	Eurici (C22:1)	E
Stearic (C18:0)	S		

Table B.5. Mechanical coefficients of CSO calculated from GMA EoS.

T/K	p/MPa	$\rho_{\text{exp}}/\text{kg}\cdot\text{m}^{-3}$	GMA $\rho/\text{kg}\cdot\text{m}^{-3}$	$RD\%$	α_p/K^{-1}	k_T/GPa^{-1}
278.15	0.1	927.80	927.45	-0.0379	0.000762	0.509146
278.15	1.0	928.20	927.87	-0.0352	0.000760	0.507054
278.15	2.0	928.70	928.34	-0.0385	0.000757	0.504752
278.15	3.0	929.10	928.81	-0.0311	0.000755	0.502474
278.15	4.0	929.60	929.28	-0.0348	0.000752	0.500219
278.15	5.0	930.10	929.74	-0.0386	0.000750	0.497986
278.15	6.0	930.50	930.20	-0.0319	0.000747	0.495775
278.15	7.0	931.00	930.66	-0.0361	0.000745	0.493587
278.15	8.0	931.30	931.12	-0.0190	0.000742	0.491420
278.15	9.0	931.80	931.58	-0.0236	0.000740	0.489274
278.15	10.0	932.30	932.03	-0.0284	0.000737	0.487149
278.15	15.0	934.40	934.28	-0.0123	0.000726	0.476827
278.15	20.0	936.40	936.49	0.0099	0.000714	0.466982
278.15	25.0	938.50	938.66	0.0172	0.000703	0.457581
278.15	30.0	940.60	940.79	0.0203	0.000693	0.448592
283.15	0.1	924.00	923.95	-0.0052	0.000749	0.522534
283.15	1.0	924.50	924.39	-0.0124	0.000747	0.520331
283.15	2.0	924.80	924.87	0.0071	0.000744	0.517908
283.15	3.0	925.40	925.34	-0.0060	0.000741	0.515509
283.15	4.0	925.80	925.82	0.0022	0.000739	0.513136
283.15	5.0	926.40	926.29	-0.0113	0.000736	0.510787
283.15	6.0	926.70	926.77	0.0073	0.000733	0.508462
283.15	7.0	927.50	927.24	-0.0282	0.000731	0.506160
283.15	8.0	927.60	927.71	0.0115	0.000728	0.503882
283.15	9.0	928.10	928.17	0.0079	0.000726	0.501627
283.15	10.0	928.50	928.64	0.0149	0.000723	0.499394
283.15	15.0	930.80	930.94	0.0146	0.000711	0.488556
283.15	20.0	933.00	933.19	0.0204	0.000699	0.478230
283.15	25.0	935.10	935.40	0.0323	0.000688	0.468380
283.15	30.0	937.20	937.57	0.0400	0.000677	0.458972
288.15	0.1	920.40	920.53	0.0137	0.000737	0.536422
288.15	1.0	920.90	920.97	0.0076	0.000734	0.534101
288.15	2.0	921.10	921.46	0.0392	0.000731	0.531548
288.15	3.0	921.80	921.95	0.0163	0.000729	0.529022
288.15	4.0	922.20	922.44	0.0258	0.000726	0.526523

Continued

T/K	p/MPa	$\rho_{\text{exp}}/\text{kg}\cdot\text{m}^{-3}$	GMA $\rho/\text{kg}\cdot\text{m}^{-3}$	$RD\%$	α_p/K^{-1}	k_T/GPa^{-1}
288.15	5.0	922.80	922.92	0.0133	0.000723	0.524050
288.15	6.0	923.20	923.41	0.0223	0.000721	0.521603
288.15	7.0	923.90	923.89	-0.0015	0.000718	0.519182
288.15	8.0	924.10	924.37	0.0287	0.000715	0.516786
288.15	9.0	924.70	924.84	0.0154	0.000713	0.514414
288.15	10.0	925.00	925.32	0.0343	0.000710	0.512067
288.15	15.0	927.40	927.66	0.0285	0.000697	0.500681
288.15	20.0	929.70	929.97	0.0286	0.000685	0.489847
288.15	25.0	931.90	932.22	0.0347	0.000674	0.479523
288.15	30.0	934.10	934.44	0.0364	0.000663	0.469673
293.15	0.1	917.00	917.17	0.0182	0.000726	0.550849
293.15	1.0	917.30	917.62	0.0350	0.000723	0.548401
293.15	2.0	917.80	918.12	0.0353	0.000720	0.545710
293.15	3.0	918.30	918.62	0.0353	0.000717	0.543048
293.15	4.0	918.90	919.12	0.0242	0.000715	0.540415
293.15	5.0	919.30	919.62	0.0346	0.000712	0.537811
293.15	6.0	919.90	920.11	0.0230	0.000709	0.535235
293.15	7.0	920.30	920.60	0.0330	0.000706	0.532686
293.15	8.0	920.90	921.09	0.0210	0.000703	0.530164
293.15	9.0	921.30	921.58	0.0305	0.000701	0.527669
293.15	10.0	921.80	922.07	0.0289	0.000698	0.525200
293.15	15.0	924.30	924.46	0.0178	0.000685	0.513233
293.15	20.0	926.70	926.82	0.0124	0.000672	0.501860
293.15	25.0	928.90	929.12	0.0237	0.000660	0.491036
293.15	30.0	931.20	931.38	0.0195	0.000649	0.480719
298.15	0.1	913.95	913.87	-0.0089	0.000716	0.565857
298.15	1.0	914.33	914.33	0.0007	0.000713	0.563274
298.15	2.0	914.83	914.85	0.0022	0.000710	0.560435
298.15	3.0	915.39	915.36	-0.0033	0.000707	0.557629
298.15	4.0	915.94	915.87	-0.0077	0.000704	0.554853
298.15	5.0	916.49	916.38	-0.0121	0.000701	0.552108
298.15	6.0	917.00	916.88	-0.0128	0.000698	0.549394
298.15	7.0	917.53	917.38	-0.0159	0.000695	0.546709
298.15	8.0	918.01	917.88	-0.0137	0.000693	0.544054
298.15	9.0	918.42	918.38	-0.0040	0.000690	0.541427

Appendix

Continued

T/K	p/MPa	$\rho_{\text{exp}}/\text{kg}\cdot\text{m}^{-3}$	GMA $\rho/\text{kg}\cdot\text{m}^{-3}$	$RD\%$	α_p/K^{-1}	k_T/GPa^{-1}
298.15	10.0	919.05	918.88	-0.0184	0.000687	0.538829
298.15	15.0	921.66	921.33	-0.0352	0.000673	0.526245
298.15	20.0	924.10	923.73	-0.0399	0.000660	0.514300
298.15	25.0	926.54	926.09	-0.0492	0.000648	0.502944
298.15	30.0	928.86	928.39	-0.0500	0.000636	0.492134
308.15	0.1	907.33	907.43	0.0107	0.000700	0.597806
308.15	1.0	907.88	907.91	0.0039	0.000697	0.594924
308.15	2.0	908.36	908.45	0.0104	0.000693	0.591758
308.15	3.0	909.03	908.99	-0.0040	0.000690	0.588630
308.15	4.0	909.58	909.52	-0.0067	0.000687	0.585539
308.15	5.0	910.16	910.06	-0.0111	0.000684	0.582484
308.15	6.0	910.75	910.58	-0.0186	0.000680	0.579464
308.15	7.0	911.25	911.11	-0.0156	0.000677	0.576479
308.15	8.0	911.78	911.64	-0.0157	0.000674	0.573529
308.15	9.0	912.41	912.16	-0.0274	0.000671	0.570612
308.15	10.0	912.85	912.68	-0.0189	0.000668	0.567728
308.15	15.0	915.51	915.24	-0.0296	0.000653	0.553785
308.15	20.0	918.08	917.75	-0.0359	0.000639	0.540585
308.15	25.0	920.59	920.21	-0.0417	0.000626	0.528069
308.15	30.0	923.01	922.61	-0.0426	0.000613	0.516182
318.15	0.1	900.92	901.16	0.0261	0.000687	0.632694
318.15	1.0	901.58	901.67	0.0102	0.000684	0.629467
318.15	2.0	902.06	902.24	0.0191	0.000681	0.625924
318.15	3.0	902.80	902.80	0.0003	0.000677	0.622425
318.15	4.0	903.37	903.36	-0.0013	0.000674	0.618970
318.15	5.0	903.97	903.92	-0.0058	0.000670	0.615558
318.15	6.0	904.62	904.48	-0.0165	0.000667	0.612188
318.15	7.0	905.12	905.03	-0.0097	0.000663	0.608859
318.15	8.0	905.68	905.58	-0.0115	0.000660	0.605570
318.15	9.0	906.40	906.13	-0.0306	0.000656	0.602321
318.15	10.0	906.79	906.67	-0.0133	0.000653	0.599110
318.15	15.0	909.53	909.36	-0.0184	0.000637	0.583616
318.15	20.0	912.21	911.98	-0.0251	0.000622	0.568990
318.15	25.0	914.80	914.55	-0.0276	0.000608	0.555159
318.15	30.0	917.32	917.07	-0.0274	0.000594	0.542056

Continued

T/K	p/MPa	$\rho_{\text{exp}}/\text{kg}\cdot\text{m}^{-3}$	GMA $\rho/\text{kg}\cdot\text{m}^{-3}$	$RD\%$	α_p/K^{-1}	k_T/GPa^{-1}
328.15	0.1	894.73	895.02	0.0329	0.000680	0.671032
328.15	1.0	895.43	895.56	0.0151	0.000676	0.667403
328.15	2.0	895.94	896.16	0.0239	0.000672	0.663421
328.15	3.0	896.70	896.75	0.0052	0.000668	0.659492
328.15	4.0	897.30	897.34	0.0042	0.000665	0.655616
328.15	5.0	897.93	897.93	-0.0004	0.000661	0.651790
328.15	6.0	898.61	898.51	-0.0106	0.000657	0.648014
328.15	7.0	899.12	899.09	-0.0024	0.000653	0.644286
328.15	8.0	899.72	899.67	-0.0053	0.000649	0.640606
328.15	9.0	900.40	900.25	-0.0173	0.000646	0.636973
328.15	10.0	900.87	900.82	-0.0057	0.000642	0.633386
328.15	15.0	903.69	903.64	-0.0054	0.000625	0.616108
328.15	20.0	906.50	906.39	-0.0114	0.000608	0.599849
328.15	25.0	909.18	909.08	-0.0106	0.000592	0.584519
328.15	30.0	911.78	911.71	-0.0077	0.000577	0.570036
338.15	0.1	888.74	888.97	0.0263	0.000677	0.713442
338.15	1.0	889.42	889.54	0.0141	0.000673	0.709340
338.15	2.0	889.99	890.17	0.0203	0.000669	0.704844
338.15	3.0	890.74	890.80	0.0063	0.000664	0.700412
338.15	4.0	891.37	891.42	0.0055	0.000660	0.696042
338.15	5.0	892.03	892.04	0.0007	0.000656	0.691732
338.15	6.0	892.70	892.66	-0.0052	0.000652	0.687482
338.15	7.0	893.25	893.27	0.0022	0.000647	0.683290
338.15	8.0	893.89	893.88	-0.0012	0.000643	0.679155
338.15	9.0	894.41	894.48	0.0085	0.000639	0.675076
338.15	10.0	895.09	895.09	-0.0002	0.000635	0.671051
338.15	15.0	898.01	898.06	0.0055	0.000616	0.651705
338.15	20.0	900.93	900.95	0.0018	0.000598	0.633564
338.15	25.0	903.72	903.77	0.0059	0.000581	0.616513
338.15	30.0	906.41	906.53	0.0132	0.000564	0.600452
348.15	0.1	882.96	882.97	0.0013	0.000679	0.760692
348.15	1.0	883.55	883.57	0.0024	0.000675	0.756030
348.15	2.0	884.21	884.24	0.0035	0.000670	0.750925
348.15	3.0	884.91	884.90	-0.0010	0.000665	0.745897
348.15	4.0	885.58	885.56	-0.0022	0.000660	0.740944

Appendix

Continued

T/K	p/MPa	$\rho_{\text{exp}}/\text{kg}\cdot\text{m}^{-3}$	GMA $\rho/\text{kg}\cdot\text{m}^{-3}$	$RD\%$	α_p/K^{-1}	k_T/GPa^{-1}
348.15	5.0	886.28	886.22	-0.0069	0.000655	0.736064
348.15	6.0	886.91	886.87	-0.0047	0.000651	0.731255
348.15	7.0	887.52	887.51	-0.0004	0.000646	0.726517
348.15	8.0	888.19	888.16	-0.0034	0.000641	0.721846
348.15	9.0	888.42	888.80	0.0428	0.000637	0.717243
348.15	10.0	889.44	889.43	-0.0010	0.000633	0.712705
348.15	15.0	892.47	892.56	0.0104	0.000611	0.690943
348.15	20.0	895.51	895.61	0.0108	0.000591	0.670613
348.15	25.0	898.41	898.58	0.0185	0.000572	0.651572
348.15	30.0	901.18	901.47	0.0320	0.000554	0.633696
358.15	0.1	877.38	876.97	-0.0475	0.000687	0.813739
358.15	1.0	877.83	877.61	-0.0253	0.000682	0.808407
358.15	2.0	878.59	878.31	-0.0316	0.000676	0.802573
358.15	3.0	879.21	879.02	-0.0219	0.000671	0.796833
358.15	4.0	879.93	879.72	-0.0237	0.000665	0.791184
358.15	5.0	880.66	880.41	-0.0282	0.000660	0.785624
358.15	6.0	881.22	881.10	-0.0138	0.000655	0.780151
358.15	7.0	881.92	881.79	-0.0148	0.000649	0.774763
358.15	8.0	882.62	882.47	-0.0167	0.000644	0.769458
358.15	9.0	882.43	883.15	0.0811	0.000639	0.764233
358.15	10.0	883.93	883.82	-0.0125	0.000634	0.759087
358.15	15.0	887.08	887.13	0.0052	0.000611	0.734477
358.15	20.0	890.24	890.35	0.0117	0.000588	0.711582
358.15	25.0	893.26	893.48	0.0237	0.000567	0.690220
358.15	30.0	896.11	896.52	0.0456	0.000548	0.670237

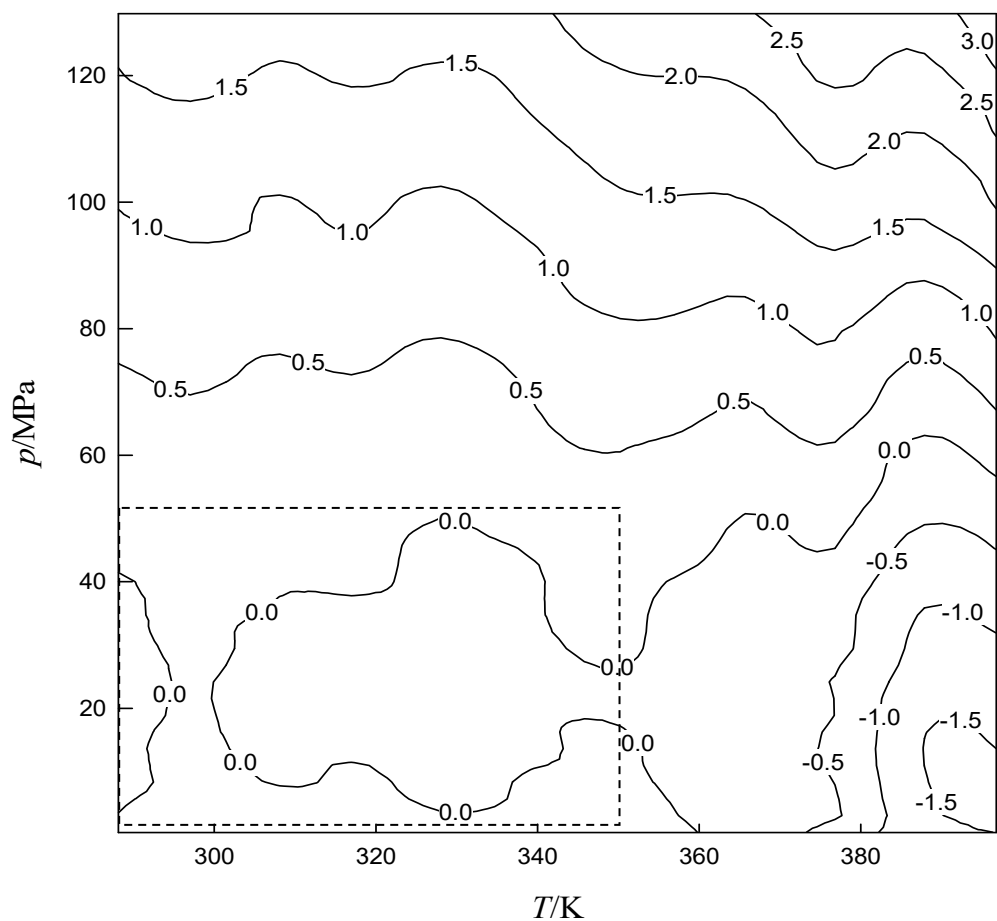


Figure B.1. Difference in density isolines ($\text{kg}\cdot\text{m}^{-3}$) obtained from GMA EoS as a function of the temperature and pressure for the SCHB biodiesel. The isolines were calculated from the fitting of GMA EoS to pVT data in the restricted ranges (288 to 357) K and (0.4 to 50) MPa (dotted square).

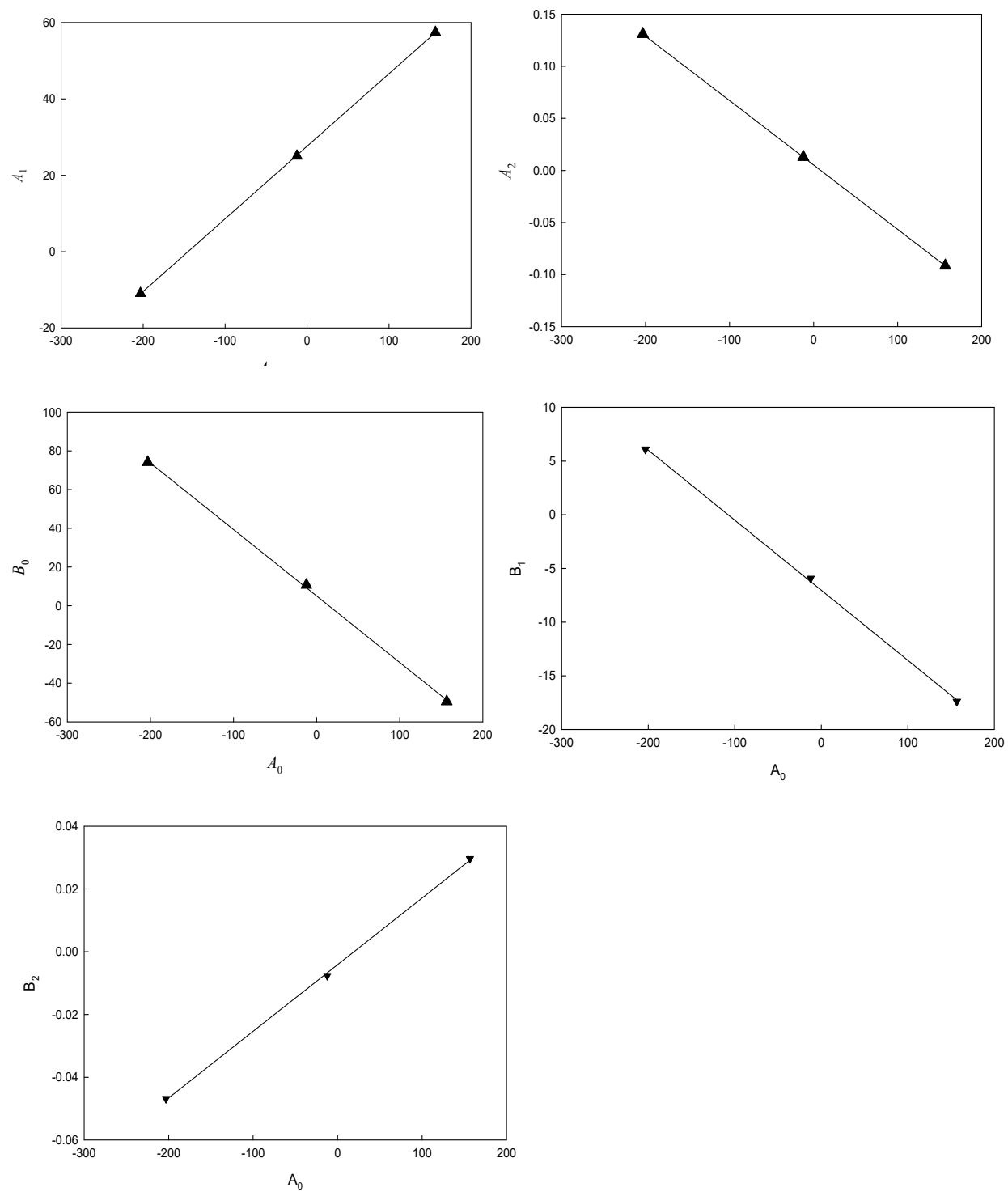


Figure B.2. Correlation between coefficients A_1 , A_2 , B_0 , B_1 and B_2 of the GMA EoS vs. A_0 for biofuels R, SR, N20 (path1).

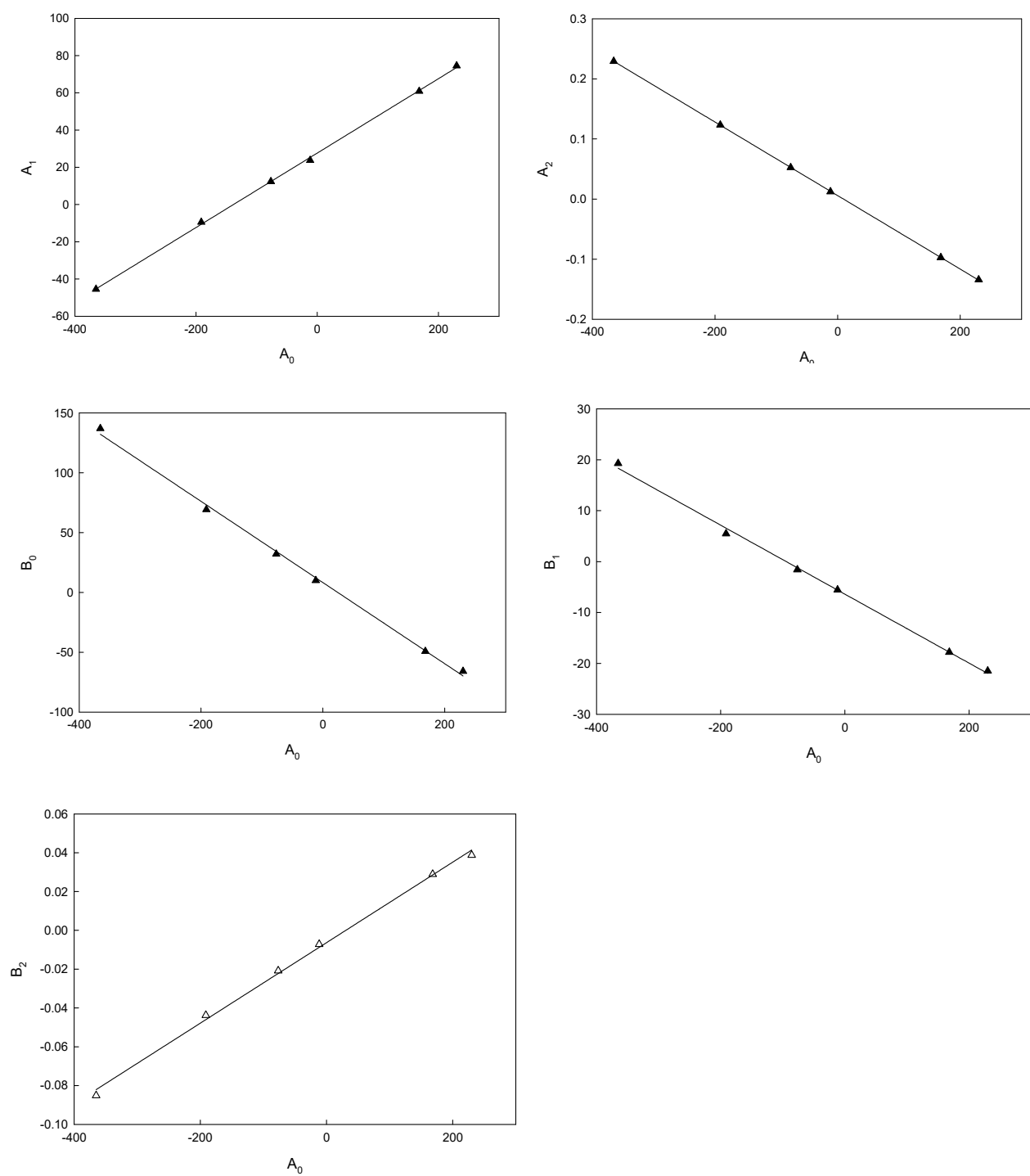


Figure B.3. Correlation between coefficients A_1 , A_2 , B_0 , B_1 and B_2 of the GMA EoS vs. A_0 for biofuels S, SRP, N5, N9, N17, N21 (path2).

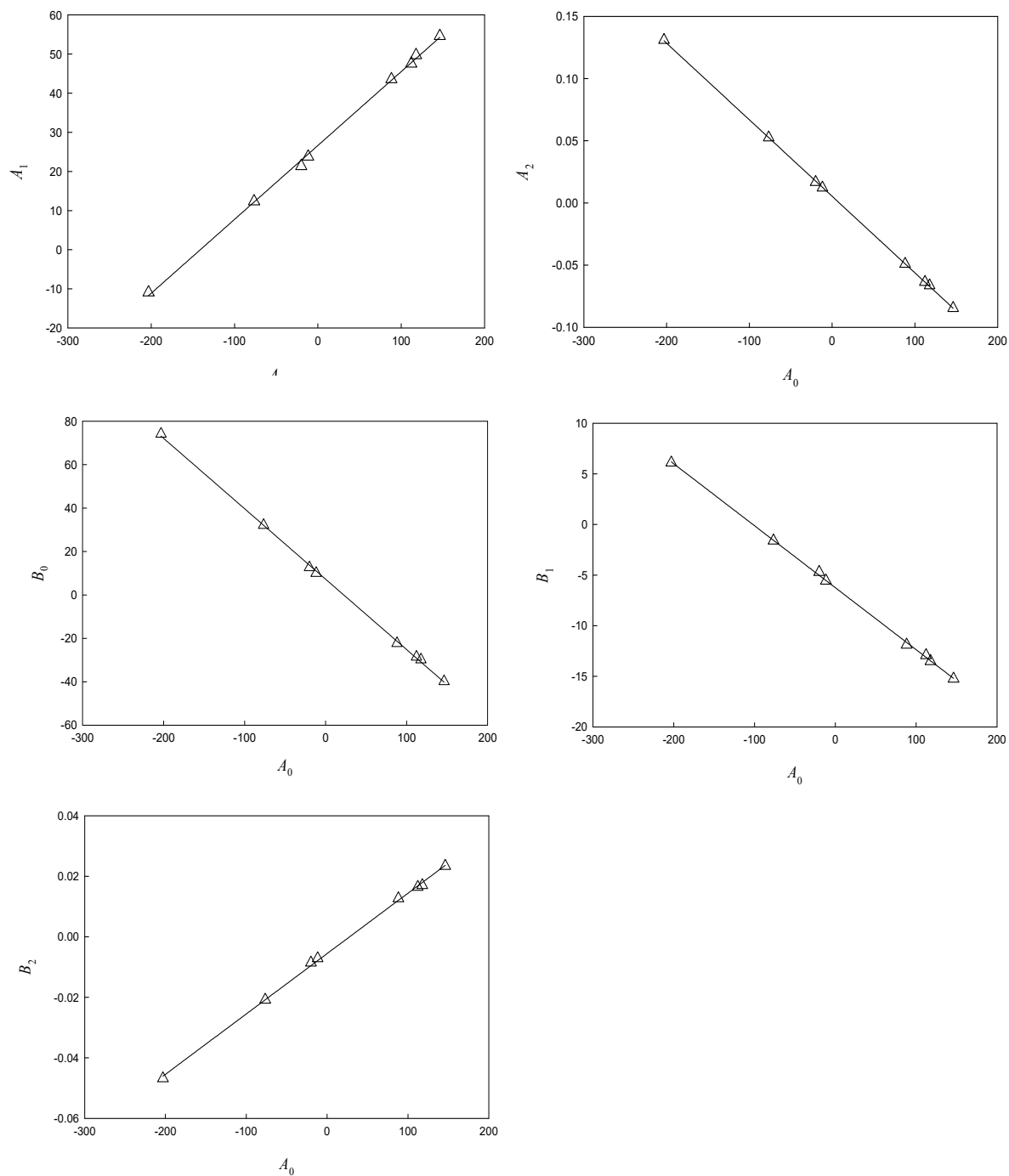


Figure B.4. Correlation between coefficients A_1 , A_2 , B_0 , B_1 and B_2 of the GMA EoS vs. A_0 for biofuels SR, SP, RP, SRP, N5, N8 N19, N23 (path3).

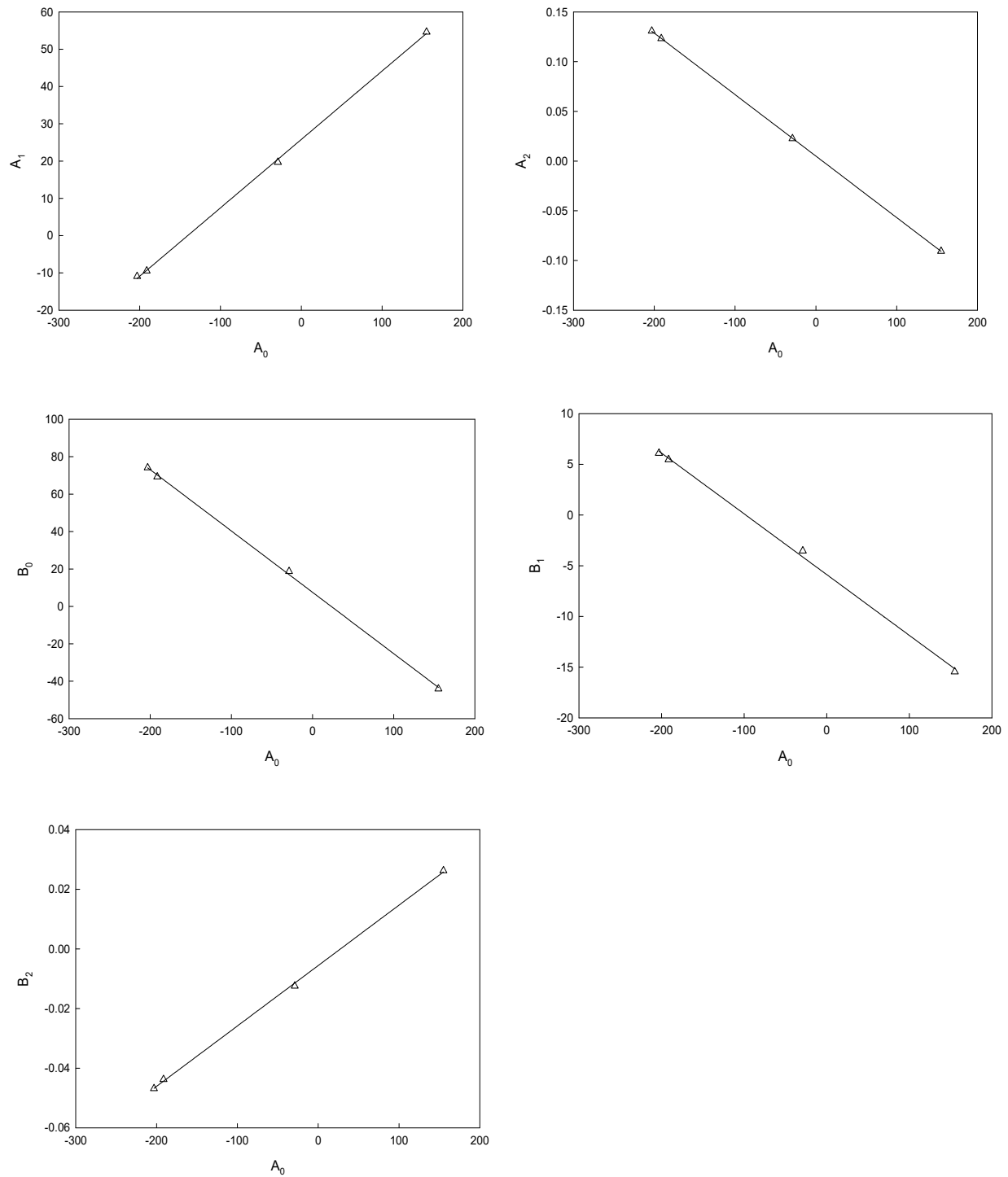


Figure B.5. Correlation between coefficients A_1 , A_2 , B_0 , B_1 and B_2 of the GMA EoS vs. A_0 for biofuels P, S, SR, N7 (path4).

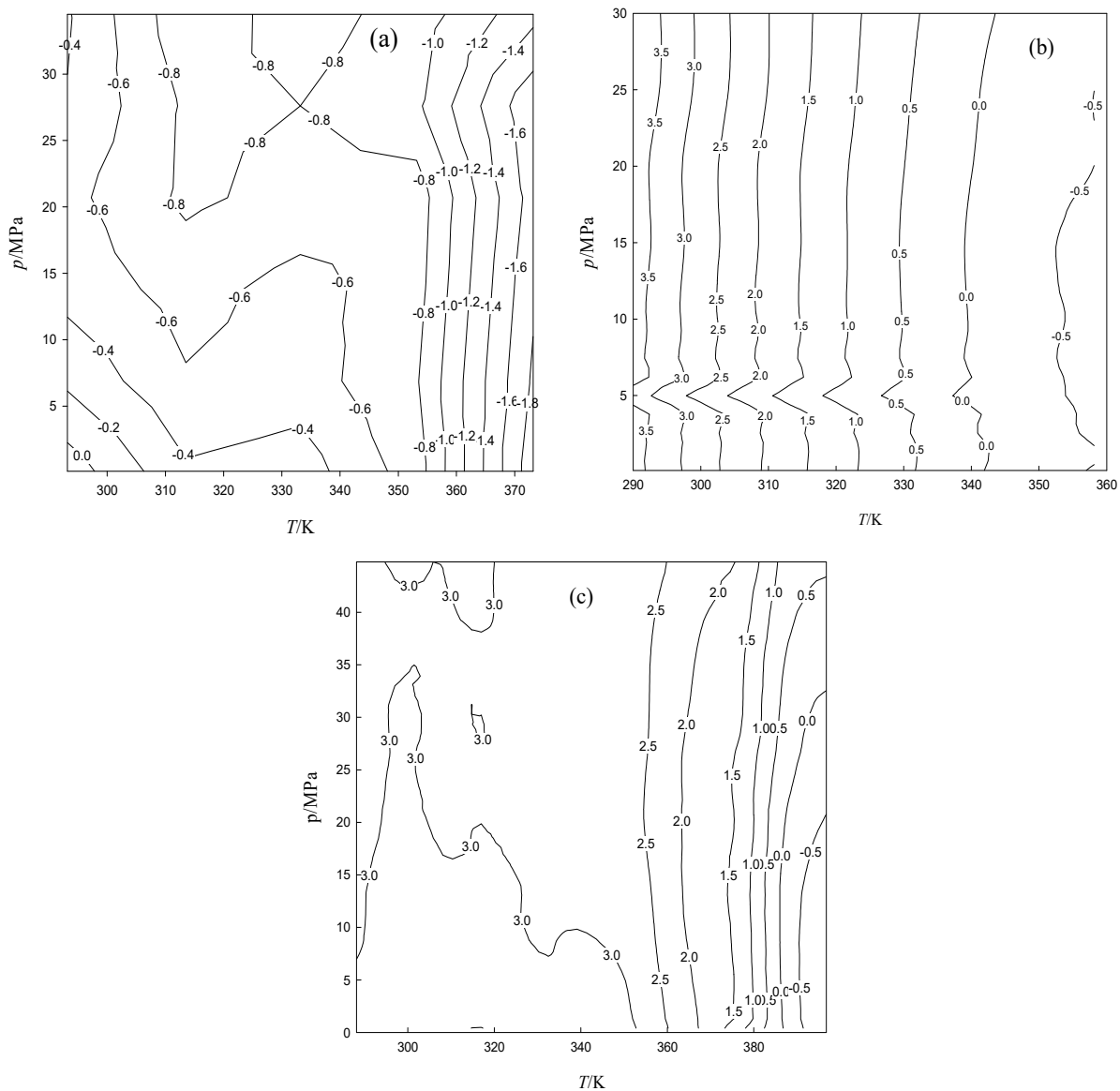


Figure B.6. Difference of density isolines ($\text{kg}\cdot\text{m}^{-3}$) obtained from predictive 4PGMA EoS as function of the temperature and pressure. (a) N6; (b) CSB; (c) SCHB.

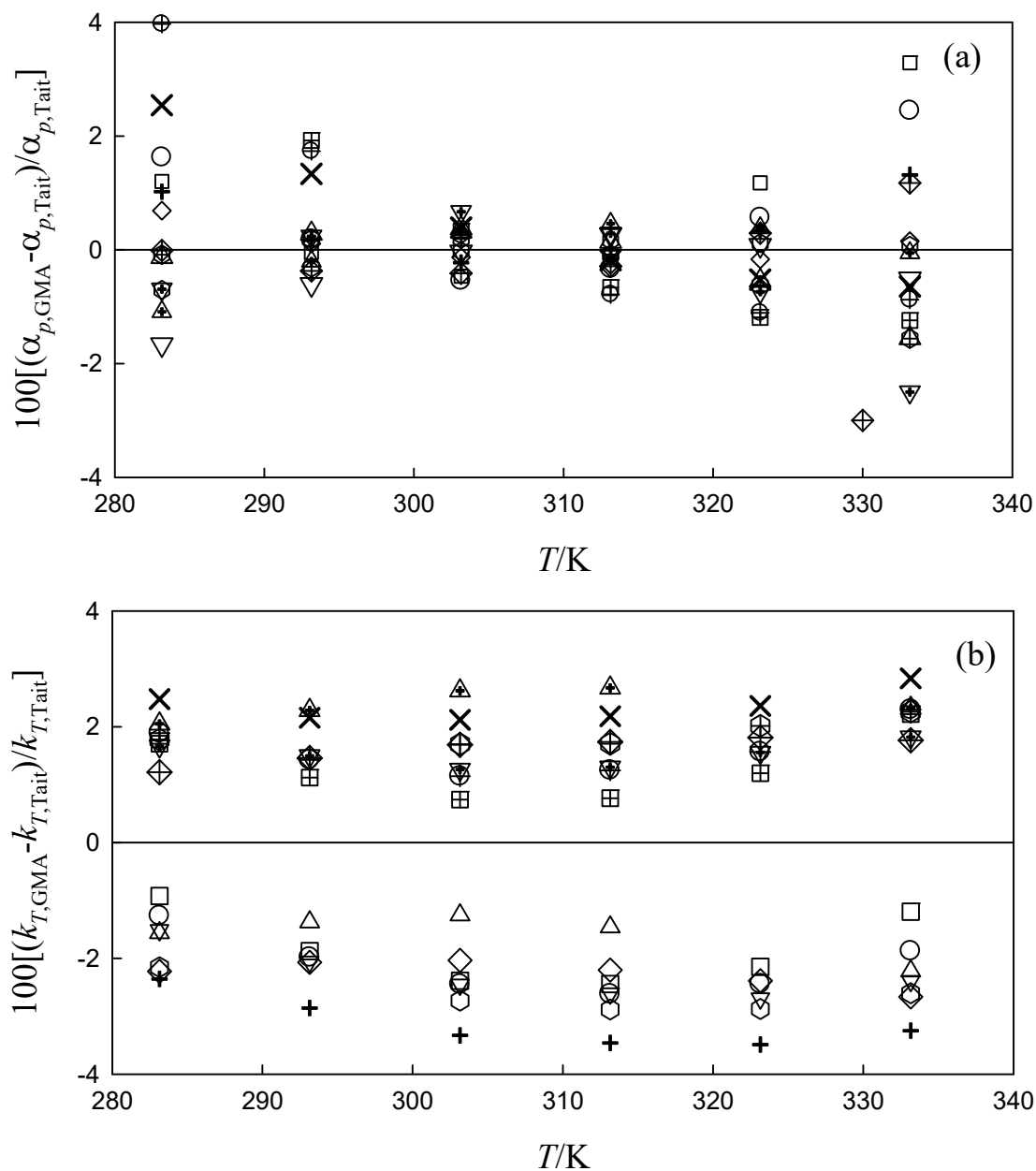


Figure B.7. Relative deviations of thermal expansivity (a) and isothermal compressibility (b) found between GMA and Tait EoS as function of temperature for the set (R, P, S, SR, RP, SP, SRP) at 0.1 MPa and 40 MPa. At 0.1 MPa: Δ , R; ∇ , P; \circ , S; \square , SR; \diamond , RP; $+$, SRP; At 40 MPa: \blacktriangle , R; \blacktriangledown , P; \oplus , S; \boxplus , SR; \boxplus , RP; \boxplus , SRP; \times , SRP.

C Data for chapter 4**Table C.1.** Parameters of Zong model [9].

Fragmentent	Symbol	Carbon	$C_{1,A}$ (Pa.s)	$C_{2,A}$ /K	$C_{3,A}$
glycerol	Gly-frag		96.530	-3009.6	-57.439
butyric	Bu-frag	C4:0	-51.003	2546.1	21.264
caproic	Co-frag	C6:0	-51.864	2627.6	21.387
caprylic	Cy-frag	C8:0	-55.104	2867.5	21.843
capric	C-frag	C10:0	-54.786	2919.1	21.784
lauric	L-frag	C12:0	-56.622	3060.8	22.045
myristic	M-frag	C14:0	-59.334	3259.8	22.425
palmitic	P-frag	C16:0	-60.312	3339.1	22.567
palmitoleic	Po-frag	C16:1	-60.312	3339.1	22.567
stearic	S-frag	C18:0	-67.306	3813.5	23.543
oleic	O-frag	C18:1	-53.789	2911.7	21.653
linoleic	Li-frag	C18:2	-39.270	2216.4	19.488
linolenic	Ln-frag	C18:3	-28.757	1491.5	18.027
arachidic	A-frag	C20:0	-66.197	3790.7	23.385
behenic	B-frag	C22:0	-68.231	3954.4	23.669
erucic	E-frag	C22:1	-68.231	3954.4	23.669

Table C.2. Parameters of Yuan model [11].

FAME	A	B	C	FAME	A	B	C
C8	-3.476	859.303	68.948	C18:2	-2.618	733.236	119.641
C10	-3.316	814.674	93.317	C18:3	-2.997	904.378	91.882
C12	-3.089	767.388	112.267	C20	-3.074	967.596	115.000
C14	-3.124	837.282	112.358	C20:1	-2.545	733.804	137.194
C16	-2.808	746.528	132.676	C22	-2.528	768.640	145.057
C16:1	-2.867	748.275	118.441	C22:1	-2.409	715.397	143.268
C18	-2.985	876.221	122.303	C24	-2.870	951.526	127.000
C18:1	-2.700	748.184	129.249				

Table C.3. Parameters of Ceriani model [10].

Group	A_{1k}	B_{1k}	C_{1k}	A_{2k}	B_{2k}	C_{2k}
CH ₃	-1.1369	83.6969	-72.3043	-0.00003	0.0109	-3.439
CH ₂	-0.0691	54.7992	2.7245	0.00003	-0.0101	4.2745
COOH	-0.6459	108.8	-102.2	-0.0104	13.1121	828.0
CH=	0.0472	12.9121	3.272	-0.00021	0.0518	8.2213
OH	-2.9095	704.5	-58.3105	0.00162	-0.1905	0.0
COO	-0.2149	16.8636	16.4977	-0.00089	0.6796	-115.4
CH ₂ -CH-CH ₂	2.2105	-128.9	21.8036	0.00149	-1.807	85.1661
Compounds	f_0	f_1		s_0	s_1	
Fatty acids	-3.5733	0.2758				
Alcohols	-23.4011	3.4594				
Esters	-0.6442	0.0479		0.0747	0.0478	
Acylglycerol	13.9884	-0.0681				
q	α	β		γ		
	0.00127	0.6458		-273.5		

D Data for chapter 5**Table D.1.** Parameters of Eq. 5-3 for the surface tension of FA as function of temperature [13].

Fluid	T_c / K	T range / K (ΔT_r)	AARD %	% RD_m	Coefficients γ_i	Coefficients n_i
Myristic acid	763	327.4 – 422.45 (0.22)	0.78	2.25	0.05805	1.247
Palmitic acid	785	335.9 – 423.15 (0.19)	0.65	1.92	0.05728	1.232
Stearic acid	803	342.75 – 685.51 (0.74)	1.16	3.07	0.04246 0.03285	1.052 3.243
Oleic acid	781	293.15 – 453.15 (0.32)	0.79	2.36	0.0538	1.05
Linoleic acid	775	268.15 – 688.15 (0.83)	0.17	0.55	0.04836 0.018996	1.0454 3.8152
Linoenic acid	780	262.05 – 692.05 (0.83)	0.15	0.49	0.048928 0.024378	1.1374 3.5932

Table D.2. Parameters of Eq. 5-3 for the surface tension of FAMES as function of temperature [12].

Fluid	T_c / K	T range / K (ΔT_r)	AARD %	% RD_m	Coefficients γ_i	Coefficients n_i
Methyl palmitate	755	303.05 – 685.98	0.54	2.18	0.025025 0.044435	3.039 1.1653
Methyl stearate	755	312.15 – 702.99	1.65	11.84	0.02313 0.04567	3.242 1.163
Methyl oleate	782	293.05 – 683.05	3.72	7.98	0.0565	1.31
Methyl linoleate	799	294.85 – 333.35	0.34	0.82	0.072487	1.9014

E Data for chapter 7

Table E.1. Selection criteria for density and NMR monitoring.

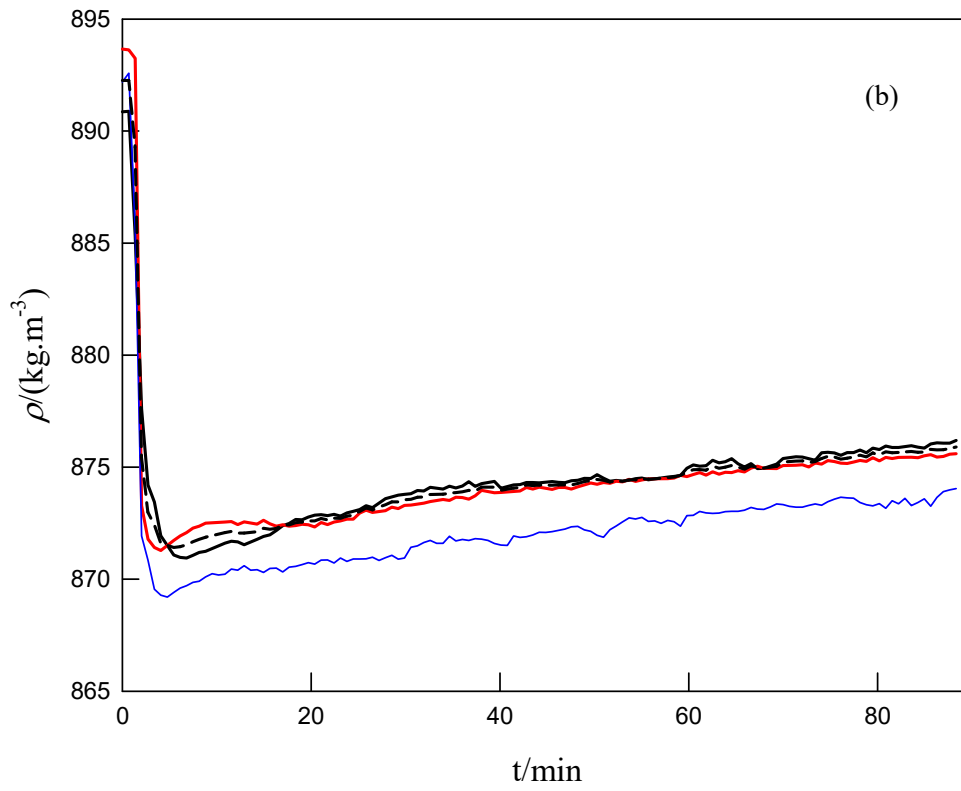
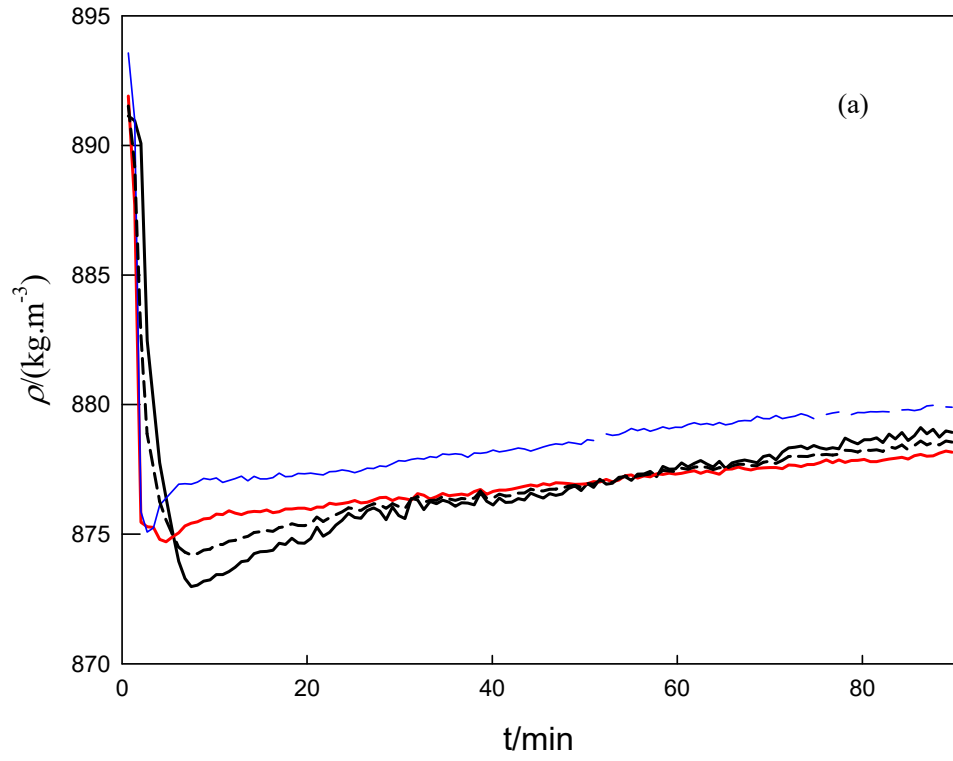
$T = 323.15; r = 4.5$				
Experiment	Selected (ρ , t) profile*	Justification	Selected (%C, t) profile	Justification
1 st	✓	The density for the 3 rd experiment was very close to the ρ axis and also as reaction time increases the values deviate from the others.	✓	The 1 st experiment was selected because it presents a very regular shape in the time. The 2 nd is in good agreement with the first except at intermediate time. The 3 rd shows a very irregular behaviour.
2 nd	✓			
3 rd				
$T = 323.15; r = 6.0$				
Experiment	Selected (ρ , T) profile*	Justification	Selected (%C, t) profile	Justification
1 st	✓	The density for the 3 rd experiment deviates from the others, after the ρ_{\min} is reached as reaction time increases. The 1 st and 2 nd run closely	✓	Two experiments were made. The 1 st experiment was selected because the results for the 2 nd experiment were very similar to the experiment for $r = 4.5$.
2 nd	✓			
3 rd				
$T = 323.15; r = 7.5$				
Experiment	Selected (ρ , T) profile*	Justification	Selected (%C, t) profile	Justification
1 st	✓	The 1 st and 3 rd experiments have wide and poorly defined ρ_{\min} .	✓	The 1 st experiment gives low values compared to what it is expected for $r = 7.5$. The 2 nd experiment was selected because it provides higher conversions than the one selected for $r = 6$.
2 nd				
3 rd				

Appendix

Continued

$T = 343.15; r = 4.5$				
Experiment	Selected (ρ, T) profile*	Justification	Selected (%C, t) profile	Justification
1 st		The 2 nd and 3 rd experiments run closely over all the reaction time. The 3 rd deviates appreciably.	✓	Two experiments were made. The 1 st experiment was selected because the values for 2 nd experiment are higher than it is expected.
2 nd	✓			
3 rd	✓			
$T = 343.15; r = 6.0$				
Experiment	Selected (ρ, T) profile*	Justification	Selected (%C, t) profile	Justification
1 st		The 2 nd and 3 rd experiments run closely over all the reaction time. The 3 rd deviates appreciably.		Two experiments were made. The 2 st experiment was selected because it presents a very regular shape over time. The 1 nd is in good agreement with the second except at intermediate time.
2 nd	✓		✓	
3 rd	✓			
$T = 343.15; r = 7.5$				
Experiment	Selected (ρ, T) profile*	Justification	Selected (%C, t) profile	Justification
1 st		The 2 nd and 3 rd experiments run closely over all the reaction time. The 3 rd has a non sharp ρ_{\min} .		The 3 rd experiment was selected because it presents very regular shape with values in agreement to what it is expected.
2 nd	✓		✓	
3 rd	✓			

* For the selected (ρ, T) profiles, the mean of densities was calculated and used..



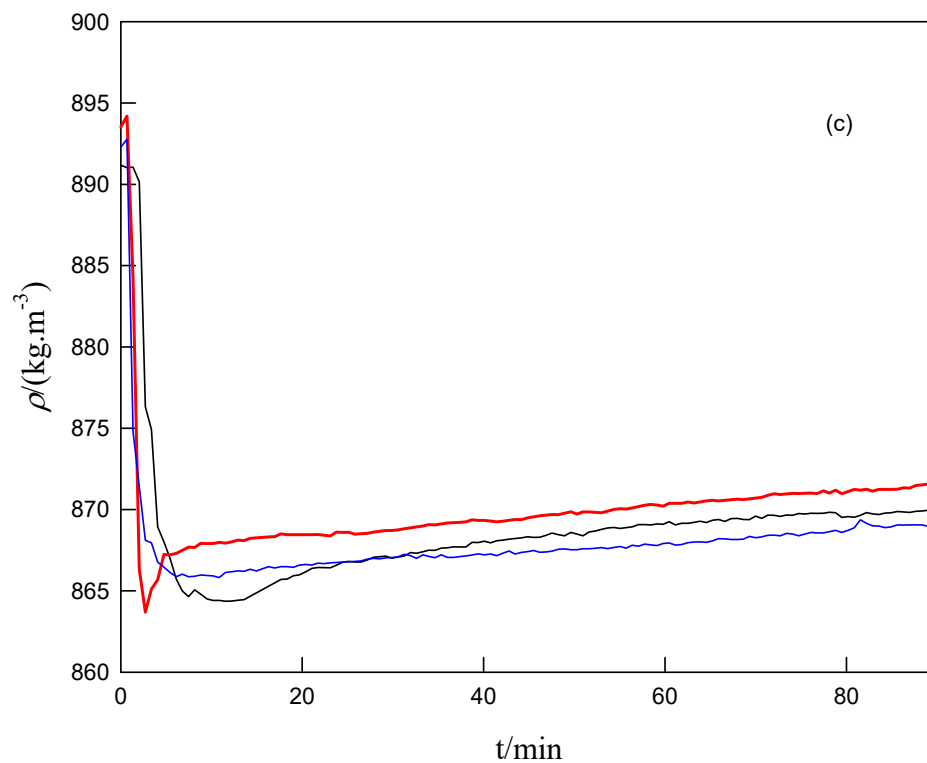


Figure E.1. Density, ρ , of the reaction medium as function of time, t , at $T = 323.15$ K. (a) $r = 4.5$; (b) $r = 6$ and (c) $r = 7.5$. Black, red and blue represent the 1st, 2nd and 3rd experiments, respectively. Thicker lines correspond to the selected experiments. --- represent the mean density-time profile.

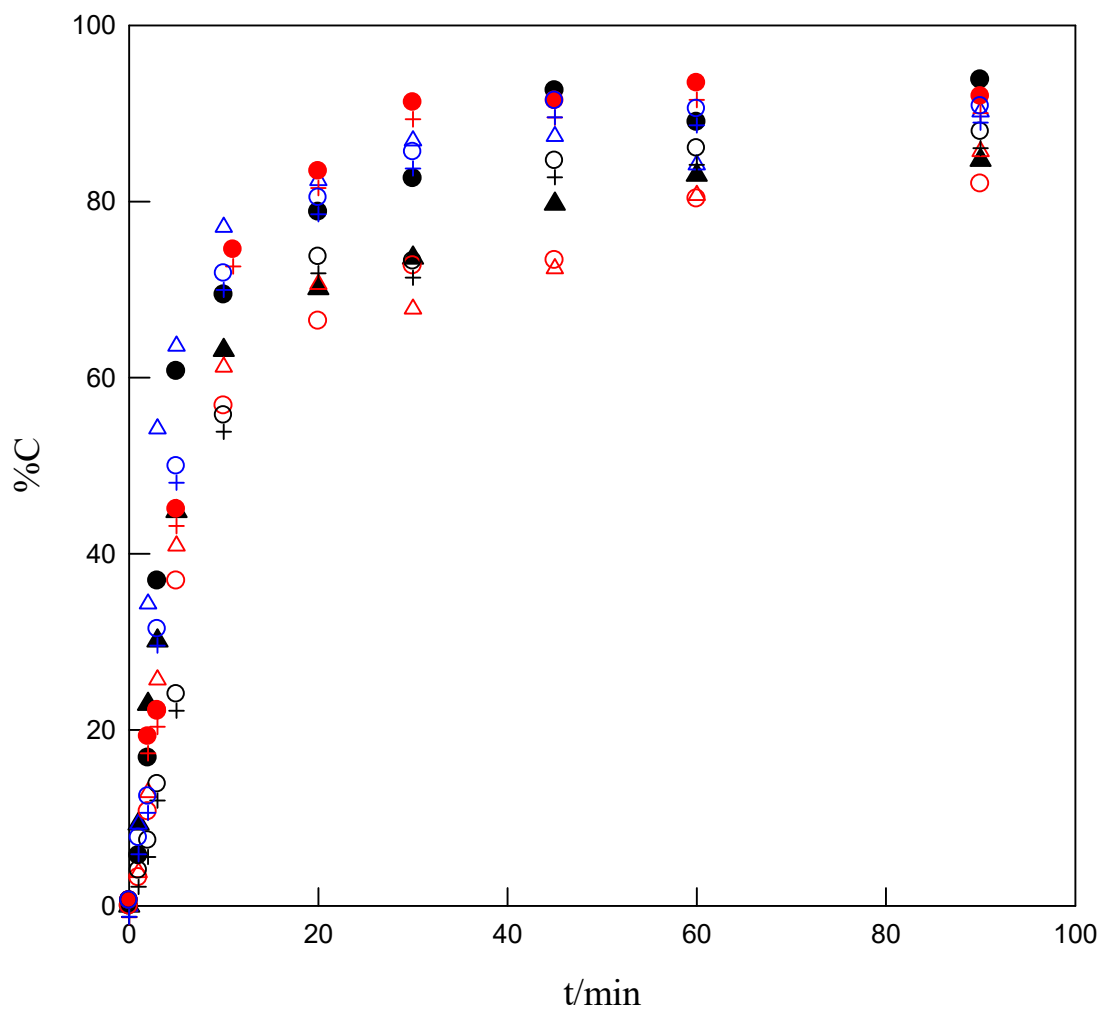
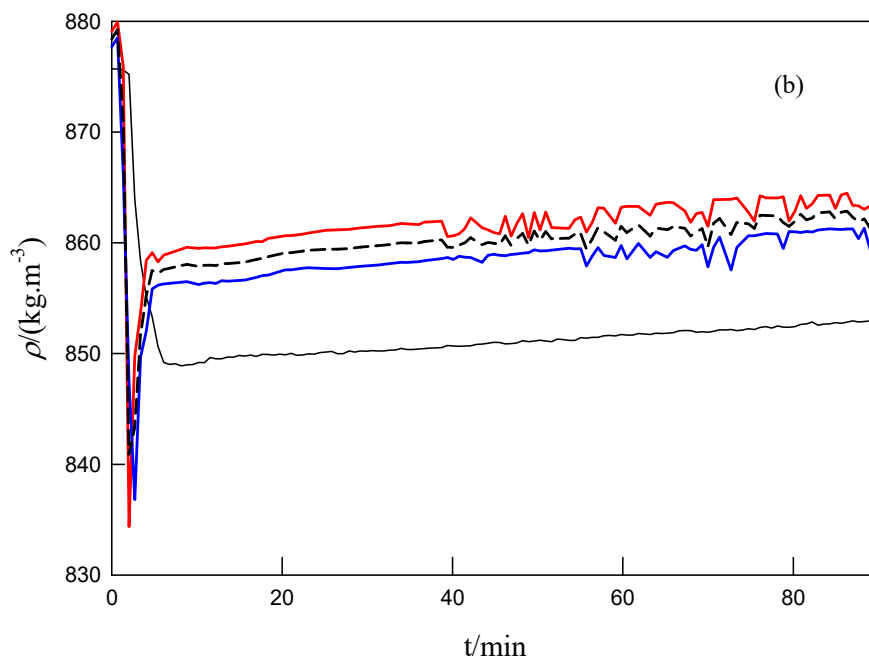
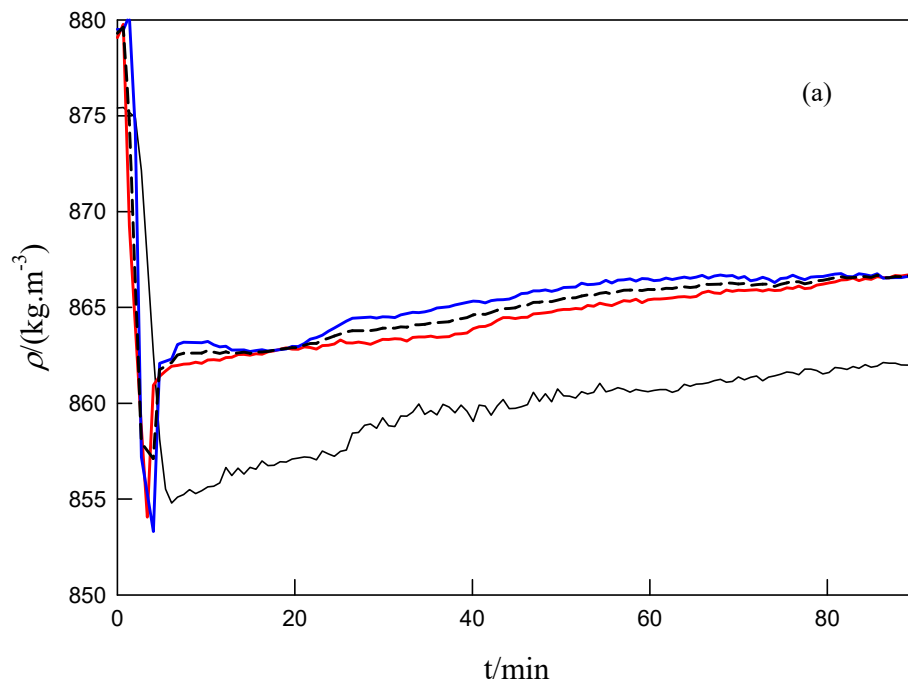


Figure E.2. ^1H NMR conversion at $T = 323.15$ K. Symbols represent experimental data: Δ , $r = 4.5$; \circ , $r = 6$ and \square , $r = 7.5$. Black, red and blue correspond to 1st, 2nd and 3rd experiments, respectively. Full symbols were for the selected experiments.



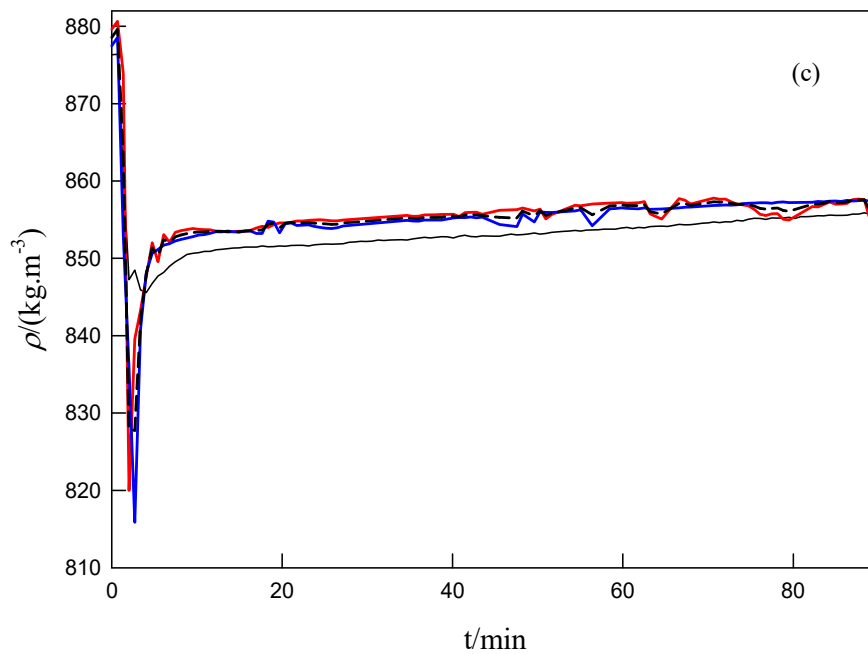


Figure E.3. Density, ρ , of the reaction medium as function of time, t , at $T = 343.15$ K. (a) $r = 4.5$; (b) $r = 6$ and (c) $r = 7.5$. Black, red and blue represent the 1st, 2nd and 3rd experiments, respectively. Thicker lines correspond to the selected experiments. --- represent the mean density-time profile.

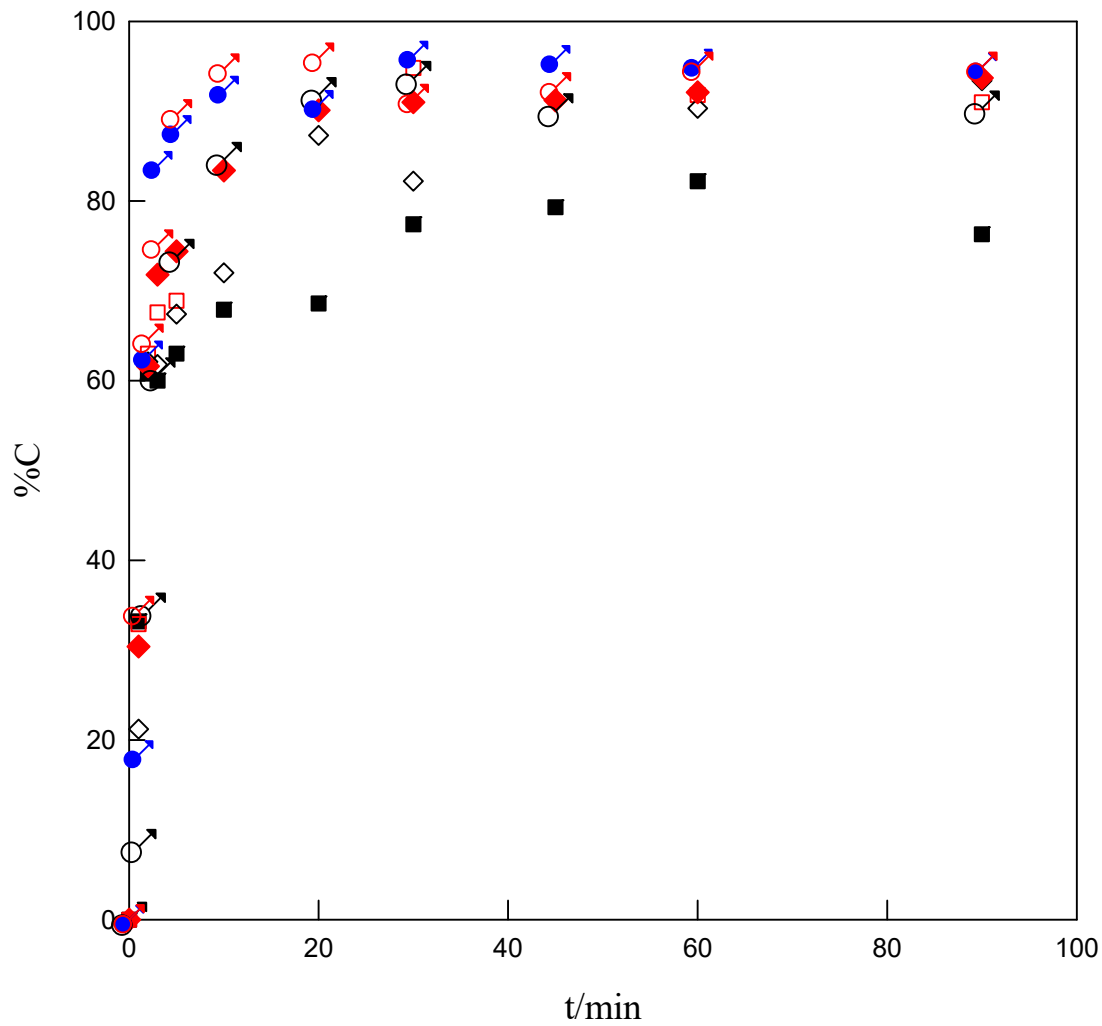


Figure E.4. ^1H NMR conversion at $T = 343.15$ K. Symbols represent experimental data: Δ , $r = 4.5$; \circ , $r = 6$ and \square , $r = 7.5$. Black, red and blue correspond to 1st, 2nd and 3rd experiments, respectively. Full symbols are for the selected experiments.